New techniques in liquid-phase ultrafast spectroscopy

Dissertation zur Erlangung des naturwissenschaftlichen Doktorgrades der Julius-Maximilians-Universität Würzburg

vorgelegt von
Florian Langhojer
aus Lichtenfels

Würzburg 2009

Eingereicht am 01.04.2009
bei der Fakultät für Physik und Astronomie

1. Gutachter: Prof. Dr. T. Brixner
2. Gutachter: Prof. Dr. T. Hertel
3. Gutachter: Prof. Dr. E. Riedle
der Dissertation

1. Prüfer: Prof. Dr. T. Brixner
2. Prüfer: Prof. Dr. T.Hertel
3. Prüfer: Prof. Dr. C. Honerkamp
im Promotionskolloquium

Tag des Promotionskolloquiums: 19.10.2009

Doktorurkunde ausgehändigt am: _____

List of Publications

Parts of this work have been published in the following references:

D. Cardoza, F. Langhojer, C. Trallero-Herrero, O.L.A. Monti, and T. Weinacht,
Changing pulse-shape basis for molecular learning control,
Phys. Rev. A **70**, 053406 (2004).

F. Langhojer, David. Cardoza, M. Baertschy, and T. Weinacht,
Gaining mechanistic insight from closed loop learning control: The importance of basis in searching the phase space,
J. Chem. Phys. **122**, 014102 (2005).

D. Cardoza, C. Trallero-Herrero, F. Langhojer, H. Rabitz, and T. Weinacht,
Transformations to diagonal bases in closed-loop quantum learning control experiments,
J. Chem. Phys. **122**, 124306 (2005).

F. Langhojer, F. Dimler, G. Jung, and T. Brixner,
Accumulative quantum control of photochemical reactions,
In P. Corkum, D. Miller, A.M. Weiner, D. Jonas (Eds.), *Ultrafast Phenomena XV*, volume 88 of *Springer Series in Chemical Physics,* pp. 285–287, Springer, Berlin (2007).

F. Langhojer, F. Dimler, G. Jung, and T. Brixner,
Product accumulation for ultrasensitive femtochemistry,
Opt. Lett. **32**, 3346 (2007).

R. Selle, P. Nuernberger, F. Langhojer, F. Dimler, S. Fechner, G. Gerber, and T. Brixner,
Generation of polarization-shaped ultraviolet femtosecond pulses,
Opt. Lett. **33**, 803 (2008).

D. Wolpert, M. Schade, F. Langhojer, G. Gerber, and T. Brixner,
Quantum control of the photoinduced Wolff rearrangement of diazonaphthoquinone in the condensed phase
J. Phys. B: At. Mol. Opt. Phys. **41** (2008) 074025.

U. Selig, F. Langhojer, F. Dimler, T. Löhrig, C. Schwarz, B. Gieseking, and T. Brixner,
Inherently phase-stable coherent two-dimensional spectroscopy using only conventional optics,
Opt. Lett. **33**, 2851 (2008).

F. Langhojer, F. Dimler, G. Jung, and T. Brixner,
Ultrafast photoconversion of the green fluorescent protein studied by accumulative femtosecond spectroscopy,
Biophys. J. **96**, 2763 (2009).

P. Nuernberger, R. Selle, F. Langhojer, F. Dimler, S. Fechner, G. Gerber, and T. Brixner,
Polarization-shaped femtosecond laser pulses in the ultraviolet
J. Opt. A: Pure Appl. Opt. **11**, 085202 (2009).

F. Langhojer, U. Selig, F. Dimler, and T. Brixner,
Criteria for phase stability in optical two-dimensional spectroscopy,
submitted to J. Opt. Soc. B (2009).

Contents

1 Introduction

Πάντα ῥεῖ
(*Panta rhei*)
Everything is in a state of flux.

Heraclitus, Greek philosopher

Very early in the history of science and philosophy, change was realized to be a fundamental and omnipresent process in nature. The observation and accurate description of not only static situations but also of dynamic processes quickly became a goal of scientific research. Macroscopic and microscopic objects were subjects of such observation. In physics the motion of bodies was first described by Newtonian mechanics. Later the advent of modern quantum mechanics allowed a mathematical description of the dynamics of microscopic particles and led to a fundamentally new understanding of motion and change. At the same time, it was realized that the microscopic changes in matter come about on timescales much shorter than timescales of classical motions. Chemical reactions in particular were found to occur on the "ultrafast" (femtosecond to picosecond) timescale. The observation of such fast processes was rendered possible by the development of ultrafast laser technology. Ultrashort light pulses are the shortest man-made events that can be used as a tool in scientific research. They allow the study of chemical reactions and the mapping of molecular processes – changes – on their natural timescale.

The question is "why does anything ever change in a quantum mechanical system?" After all, quantum mechanical eigenstates do not change as a function of time. One can distinguish two kinds of causes for change: couplings and interactions. No quantum system is truly isolated from its surroundings and therefore couplings to the larger environment that contains the system are always present. In molecules such couplings cause the dynamics of the system. Energy redistribution and energy transfer are common molecular phenomena that are ultimately caused by *intra*molecular couplings and *inter*molecular couplings, respectively. Researching both types of couplings is essential for the understanding of the processes they cause. Time-resolved spectroscopic techniques that make use of femtosecond pulses have excelled at mapping the dynamics of chemical reactions. Depending on the particular goal and molecular system, different spectroscopy techniques such as transient absorption, photo-electron spectroscopy, photon echo, or four-wave mixing have been used with great success. In recent years the development of coherent optical two-dimensional (2D) spectroscopy has provided a new tool for studying quantum systems on the femtosecond timescale. With this method couplings can be measured and visualized directly. In other words, 2D spectroscopy does not only yield information about "what changes on which timescale" but it also reveals

information about "why does it change". Currently, optical 2D spectroscopy has been implemented in the infrared wavelength region for measuring couplings between vibrations and in the visible wavelength region for measuring electronic couplings. However, this vastly promising spectroscopic technique involves some experimental challenges and, judging from the prospects it entails, it is not yet as widespread as one could hope. Especially with excitation in the visible wavelength region the technological requirements are severe. In chapter 4 of this thesis a new approach to 2D spectroscopy which simplifies the experimental setup is presented. This implementation uses only conventional optics and delay lines to create the light pulses that are necessary for the spectroscopy. The robustness and relative simplicity of this approach may help to propagate optical 2D spectroscopy as a general tool to measure couplings in quantum systems.

The second reason mentioned above for change in a quantum system is interaction. Ultrashort laser pulses are not only used for observation but additionally their interaction with a molecule changes the system itself and thereby induces chemical or physical reactions. A few possible photoinduced reaction channels of molecules are: internal conversion, fluorescence, inter-system crossing, isomerization, dissociation, ionization, bond breaking, and bond formation. All of these have been studied successfully using femtosecond laser pulses. However, for a given molecular system each of these possible reaction pathways will only occur with a certain quantum efficiency. Low efficiencies may impede an accurate measurement of the photoinduced changes in a molecular system with the majority of the conventional femtosecond spectroscopy techniques. Focusing on photoreactions that yield stable products, a new method has been developed in this work to allow femtosecond time-resolved observation of minute reaction channels. This novel accumulative method for photoproduct detection offers extreme sensitivity even to small quantum efficiencies. The ideas, technical details, and the calibration of this detection method are presented in chapter 5 along with demonstration experiments that examine the photobleaching of a dye molecule.

The application of the newly introduced method to a biological system, the green fluorescent protein, is described in chapter 6. This molecule is the most important genetic marker used in the life sciences. The ultrafast photoconversion of the protein that leads to its permanent alteration was studied in a time-resolved experiment using the accumulation technique to detect the small yields of photoproducts. Our findings are relevant with respect to the use of green fluorescent protein in multiphoton fluorescence microscopy in the life sciences. Further, shaped femtosecond pulses were used to map the dependence of the permanent photoconversion on the shape of the electric field that interacts with the molecule.

The concept of quantum control that was developed in the last 15 years exploits the interaction of light with a molecule not only to observe but to actively and deliberately change the system. Shaped laser pulses can be used to "steer" a system into a desired reaction channel and many types of reactions have been controlled up to date. These previous experiments have realized many parts of the dream to control chemistry with light. Yet, femtosecond control of a fundamental asymmetry in chemistry, chirality, has still not been demonstrated. The existence of two enantiomeric forms of amino acids illustrates the importance of this type of stereochemistry for all biological life. Although even fairly complex reactions such as the synthesis of larger molecules from

smaller molecules have been recently controlled with femtosecond pulses, only the *cis–trans* isomerization yield of a stereochemical reaction has been subject to such control to date. Enantiomeric selectivity has not yet been accomplished. The stereochemical properties of molecules are paralleled by the polarization of the electric field of light. In recent years the possibility to shape this polarization on a femtosecond timescale has emerged and theoretical investigations have revealed that these polarization-shaped laser pulses are a crucial component for achieving enantiomeric selectivity in quantum control. Nevertheless, an experimental demonstration of chiral control is outstanding. One important reason for this is that, not only must chiral control of the molecular system be achieved. A suitable method for detection that distinguishes between two enantiomers that exhibit nearly identical chemical and physical properties in an achiral environment must also be developed. The final part of this thesis (chapter 7) describes the first steps toward enantioselective quantum control by combining the accumulative detection method with a fast and precise polarimeter setup. Furthermore, several molecular systems are reviewed as potential precursor molecules for chiral control. In particular the spiropyran/merocyanine system is discussed. A photoinduced ring closure of the planar merocyanine form produces a chiral spiropyran form and control over this process could lead to enantioselectivity.

The described ultrafast technologies require the understanding of some basic concepts. These are first described in chapter 2 following this introduction. Chapter 2 also includes the description of a general software framework for scientific data acquisition and simulation which allowed us to perform all experiments presented in this thesis and which is also applied for all experiments in our research group.

As a prerequisite for the 2D electronic spectroscopy experiments, a means to generate, compress, and characterize broadband visible laser pulses was required. A noncollinear optical parametric amplifier in combination with a liquid crystal pulse shaper for pulse compression was used to generate these short pulses with spectra spanning the wavelength region from 500 nm to 750 nm. The technical details of this experimental setup that leads to versatile, shaped pulses, that can be used in both spectroscopy and quantum control experiments, are described in chapter 3.

2 Basic concepts and instrumentation

For the application and development of femtosecond spectroscopy techniques and ultrafast processes described in this thesis it is essential to understand the tools used for their theoretical description and experimental exploration. This chapter summarizes a number of concepts that are of importance for the following chapters. Further, the general software framework for scientific data acquisition and simulation that we have developed is described at the end of this chapter.

2.1 Mathematical description of femtosecond laser pulses

All femtosecond spectroscopies exploit the fact that modern-day laser technology allows the production of ultrashort laser pulses. First we need to describe these pulses themselves before we can investigate the phenomena they induce, such as nonlinear processes.

We start from the electromagnetic wave equation in homogeneous nonmagnetic media [1]

$$-\nabla \times \left(\nabla \times \vec{E}(t,\vec{r})\right) - \frac{1}{c^2}\frac{\partial^2}{\partial t^2}\vec{E}(t,\vec{r}) = \mu_0 \frac{\partial^2}{\partial t^2}\vec{P}(t,\vec{r}), \tag{2.1}$$

where $\vec{E}$ is the electric field vector, $\vec{P}$ is the polarization, c is the speed of light in vacuum, and μ_0 is the magnetic permeability of vacuum. The polarization $\vec{P}(t,\vec{r})$ on the right hand side represents the source term that generates electromagnetic fields. The homogenous wave equation results from the case with no polarization ($\vec{P} = 0$) and describes the spatio-temporal propagation of electromagnetic fields. For simplification purposes that will suffice for this thesis we can separate the spatio-temporal dependencies of solutions to the wave equation,

$$\vec{E}(t,\vec{r}) = u(\vec{r})\ \vec{E}(t,z), \tag{2.2}$$

into a part $u(\vec{r})$ that describes the transversal amplitude distribution (i.e., the laser beam profile), and into $\vec{E}(t,z)$ that describes the polarization of the electric field and its propagation along the z-axis. We can further consider the field at one certain point in space ($z = 0$) and neglect the vectorial character; this leaves the temporal dependence of the electric field

$$E(t) = 2A(t)\cos\Phi(t) = A(t)\ \mathrm{e}^{\mathrm{i}\Phi(t)} + c.c. = E^{+}(t) + c.c. = E^{+}(t) + E^{-}(t). \tag{2.3}$$

Here, *c.c.* denotes the complex conjugate of the previous terms. The complex notation consisting of an amplitude $A(t)$ and a phase $\Phi(t)$ is often used for practical reasons

because the complex function $E^+(t)$ describes the field unambiguously. Included in the phase function $\Phi(t)$ is a term that increases linearly with time and proportional to the central angular frequency ω_0 of the laser pulse. This term results in the fast oscillations of the electric field under its envelope that is determined by $A(t)$. One can divide the overall phase into two parts

$$\Phi(t) = \varphi(t) + \omega_0 t \tag{2.4}$$

so that the nonlinear phase terms are contained in a temporal phase function $\varphi(t)$. Then the field is written as

$$E^+(t) = A(t)\, \mathrm{e}^{\mathrm{i}\varphi(t)}\, \mathrm{e}^{\mathrm{i}\omega_0 t} = \tilde{A}(t)\, \mathrm{e}^{\mathrm{i}\omega_0 t} \tag{2.5}$$

where the function $\tilde{A}(t)$, called the complex amplitude, is separated from the carrier frequency ω_0.

The phase is often expanded in a Taylor series

$$\Phi(t) = \sum_{j=0}^{\infty} \frac{a_j}{j!}\, t^j \tag{2.6}$$

with the coefficients

$$a_j = \left.\frac{\mathrm{d}^j \Phi(t)}{\mathrm{d}t^j}\right|_{t\,=\,0}. \tag{2.7}$$

Without loss of generality the pulse is assumed to be centered around $t = 0$ and the expansion is also carried out around this point. The physical meaning of the zeroth term in the expansion is the so-called carrier–envelope phase (CEP) or absolute phase. It describes by how much the maximum of the fast oscillating electric field is shifted with respect to $t = 0$ which is usually the maximum of the envelope function $A(t)$. For the light–matter interaction of very short pulses the effects of the CEP can be significant [2]. However, for the pulse durations used in this thesis the effects of a_0 are negligible due to the large number of field oscillations under the pulse envelope. The term a_1 simply represents the carrier frequency ω_0 and higher order terms describe the temporal change of the oscillations under the pulse envelope.

In general, the momentary frequency $\omega_m(t)$ is defined as the derivative of the phase with respect to time

$$\omega_m(t) = \frac{\mathrm{d}\Phi(t)}{\mathrm{d}t} = \omega_0 + \frac{\mathrm{d}\varphi(t)}{\mathrm{d}t}. \tag{2.8}$$

Hence it is clear that the higher order terms absorbed in $\varphi(t)$ lead to a time-dependent deviation of the field oscillation frequency ω_m from the center frequency ω_0 of the pulse. One speaks of a "chirped" pulse if the momentary frequency changes with time (and of an "unchirped" pulse if $\omega_m(t) = \text{const.}$). Pulses with increasing momentary frequency ($\mathrm{d}\omega_m(t)/\mathrm{d}t > 0$) are called "upchirped" pulses. Vice versa, a "downchirped" pulse follows from a decreasing momentary frequency ($\mathrm{d}\omega_m(t)/\mathrm{d}t < 0$).

It should be mentioned here that the well-established methods of femtosecond pulse shaping [3] can create complex pulses and Eqs. 2.6 and 2.8 are the basis for the description and analysis of complicated pulses as well as simple pulses. However, usually

femtosecond pulse shaping is accomplished in frequency domain. The electric field is readily transferred into frequency space via the Fourier transform

$$E(\omega) = \mathcal{F}\{E(t)\} = \frac{1}{\sqrt{2\pi}} \int_{-\infty}^{+\infty} E(t) \mathrm{e}^{-\mathrm{i}\omega t} \mathrm{d}t. \tag{2.9}$$

Even though the functional dependencies are different in time and frequency space we do not use separate function symbols. The space in which the function is valid is rather clear from its argument t or ω.

The Fourier-transformed field $E(\omega)$ satisfies the symmetry relation

$$E(\omega) = E^*(-\omega) \tag{2.10}$$

because the temporal field $E(t)$ is real-valued. This implies that the field is unambiguously defined using the information from the positive-frequency half-space only:

$$E^+(\omega) = \begin{cases} E(\omega) & \text{if} \quad x \geq 0, \\ 0 & \text{if} \quad x < 0. \end{cases} \tag{2.11}$$

In fact, the complex temporal field $E^+(t)$ and the positive half space part $E^+(\omega)$ are related to each other by Fourier transformation

$$E^+(\omega) = \mathcal{F}\left\{E^+(t)\right\}. \tag{2.12}$$

Again, we can separate the spectral amplitude $A(\omega)$ and the spectral phase $\Phi(\omega)$:

$$E^+(\omega) = A(\omega) \mathrm{e}^{-\mathrm{i}\Phi(\omega)}. \tag{2.13}$$

The phase can be expanded in a Taylor series. Ultrashort laser pulses have a spectral amplitude distribution that is centered around a frequency ω_0 and zero for frequencies far from ω_0. It is sensible to expand the spectral phase around the central frequency

$$\Phi(\omega) = \sum_{j=0}^{\infty} \frac{b_j}{j!} \left(\omega - \omega_0\right)^j \tag{2.14}$$

with the coefficients

$$b_j = \left. \frac{\mathrm{d}^j \Phi(\omega)}{\mathrm{d}\omega^j} \right|_{\omega = \omega_0}. \tag{2.15}$$

Here, the zeroth coefficient also represents the absolute phase, as seen for the Taylor expansion of the temporal phase, hence $b_0 = a_0$. The linear term with coefficient b_1 gives rise to a shift of the electric field in time as can be seen from the Fourier shift theorem. Higher order terms ($j \geq 2$) will in general lead to complex and chirped pulses. It should be noted that for Gaussian-shaped spectra pure second order spectral phase ($b_2 \neq 0$ and $b_j = 0 \; \forall \; j > 2$) transforms to second order temporal phase as well [1]. This fact is especially important for creating linearly chirped pulses with pulse shapers that operate in the spectral domain. Using pulse shapers almost arbitrarily complex spectral phase functions that are not limited to the first few Taylor coefficients can be applied to alter the phase of the pulse.

2.2 Optical quantities and measurements

Optical spectroscopy requires definitions of the quantitative properties of light. This is essential for the right choice of measurement apparatus and calibration of the instrumentation.

2.2.1 Intensity

The high intensities of ultrashort laser pulses concentrated in a short period of time make them a versatile tool to induce many nonlinear phenomena. The temporal intensity of an ultrashort laser pulse may be derived from the average of the squared temporal electric field $E^2(t)$ over one cycle

$$I(t) = 2\epsilon_0 cn \frac{1}{T} \int_{t-T/2}^{t+T/2} E^2(t')\mathrm{d}t' = 2\epsilon_0 cnA^2(t). \tag{2.16}$$

The rightmost identity is only valid within the slowly varying envelope approximation, i.e., if the envelope function $A(t)$ changes slowly compared to the oscillations of the carrier wave ($|\mathrm{d}A(t)/\mathrm{d}t| \ll |\omega_0 A(t)|$). Intensities are usually given in units of Watts/cm^2.

The exact experimental determination of the temporal intensity $I(t)$ requires more sophisticated means than linear electronic devices which are too slow to measure femtosecond pulses. (For measurement methods see e.g. section 3.5.) At the same time, in many applications of femtosecond pulses that exploit nonlinear phenomena (or where those are to be suppressed) the peak intensity is the decisive figure of merit that is often reported. Usually, and throughout this thesis, the peak intensity is defined as the total energy of the pulse E_t divided by its full width at half maximum (FWHM) duration Δt and the area of the pulse intensity profile D:

$$I_{\mathrm{peak}} = \frac{E_t}{\Delta t D}. \tag{2.17}$$

Note that D is often simply taken as the area of a disk with a diameter that corresponds to the FWHM of the spatial intensity profile $u(x, y)$. This definition results in a good figure of merit for applications such as multiphoton microscopy or multiphoton ionization which use short pulses of durations close to the Fourier limit and approximately Gaussian beam profiles. Shaped laser pulses with highly structured temporal envelopes result in an I_{peak} that does not sufficiently describe the pulses.

The intensity can also be formulated in frequency space, analogous to Eq. 2.16

$$I(\omega) = 2\epsilon_0 cnA^2(\omega). \tag{2.18}$$

Due to the equivalency of the frequency and time representations the total fluence

$$F = \int_0^\infty 2\epsilon_0 cnA^2(\omega)\mathrm{d}\omega = \int_{-\infty}^\infty 2\epsilon_0 cnA^2(t)\mathrm{d}t \tag{2.19}$$

is equal in both domains. In the laboratory laser pulse spectra are usually measured with spectrometers yielding spectra

$$S(\lambda)\mathrm{d}\lambda = Q(\lambda)\ I(\lambda)\mathrm{d}\lambda \tag{2.20}$$

as a function of wavelength λ. The transmission of the spectrometer and the efficiency of the detector are absorbed in the factor $Q(\lambda)$. Even though for extremely broad spectra this factor has to be included in quantitative considerations, in this work we can assume $Q(\lambda)$ to be constant. More important is the fact that the spectrum $I(\omega) \propto S(\omega)$ must be evaluated as the Jacobi transformation of the spectral distribution

$$I(\omega)\mathrm{d}\omega = I(\omega(\lambda))\left|\frac{\mathrm{d}\omega}{\mathrm{d}\lambda}\right|\mathrm{d}\lambda = I\left(\frac{2\pi c}{\lambda}\right)\frac{2\pi c}{\lambda^2}\,\mathrm{d}\lambda. \tag{2.21}$$

In particular, the proportionality to λ^{-2} must be accounted for when transforming between measured spectra $S(\lambda)$ and spectra as a function of angular frequency $I(\omega)$.

2.2.2 Absorbance and Beer-Lambert law

Femtosecond spectroscopies rely on definitions of the optical absorption properties as much as classical absorption spectroscopy. Hence a short summary of measurement quantities is given here.

The intensity of a collimated probe beam that passes through a homogeneous sample and is weak enough so that it does not influence the sample follows the Beer-Lambert law

$$\begin{aligned} I(\lambda, z) &= I_0(\lambda)\ \mathrm{e}^{-\sigma(\lambda)Nz} \\ &= I_0(\lambda)\ 10^{-\varepsilon(\lambda)cz}. \end{aligned} \tag{2.22}$$

The first formulation is usually used for gases with N as the absorbing particle density in cm^{-3} and $\sigma(\lambda)$ as the absorption cross section. (σ is usually given in cm^2.) The second formulation is more common for describing the absorption of sample solutions. There, c is the sample concentration and $\varepsilon(\lambda)$ is the molar absorptivity given in $\mathrm{M}^{-1}\mathrm{cm}^{-1}$ or in L $\mathrm{mol}^{-1}\mathrm{cm}^{-1}$. ε is sometimes also called the (decadic) molar extinction coefficient. Exploiting the identity in Eq. 2.22 the conversion between extinction coefficient ε and absorption cross section σ and can be made via

$$\sigma = \ln 10\ N_A\ \varepsilon = 3.824 \times 10^{-21}\ \mathrm{cm}^2\ \left(\varepsilon/\left(\mathrm{M}^{-1}\mathrm{cm}^{-1}\right)\right) \tag{2.23}$$

with Avogadro's constant $N_A = 6.022 \times 10^{23}\mathrm{mol}^{-1}$ [4].

In liquid-phase spectroscopy the absorbance of a sample of thickness d is defined as

$$A(\lambda) = -\log_{10}\left(\frac{I(\lambda)}{I_0(\lambda)}\right) = \varepsilon(\lambda)cd \tag{2.24}$$

with the advantage of proportionality to the concentration of the absorbing species as well as the path length. The optical density is defined as the absorbance per unit path length

$$\mathrm{OD}(\lambda) = \frac{A(\lambda)}{d} = \varepsilon(\lambda)c. \tag{2.25}$$

However, a somewhat confusing use of the terms "absorbance" and "optical density" became common practice: the absorbance of the sample with constant thickness d is given for instance as a function of pump–probe delay in a transient absorption experiment and the term "optical density" is used as a synonym instead of "absorbance". Furthermore, although $A(\lambda)$ is dimensionless 1 OD or 1 mOD are often used as units of the absorbance A. It is important to keep in mind that in the vast majority of publications "optical density" refers to the quantity A defined in Eq. 2.24 resulting from a certain sample thickness in the experimental setup.

Transient absorption (TA) spectroscopy experiments typically determine the difference of absorbance ΔA (or ΔOD)

$$\Delta A(\tau) = A(\tau) - A_{\mathrm{ref}} = \left[\varepsilon(\tau)c(\tau) - \varepsilon_{\mathrm{ref}}c_{\mathrm{ref}}\right] d = -\log_{10}\left(\frac{I(\tau)}{I_{\mathrm{ref}}}\right) \tag{2.26}$$

between an experiment with pump pulse and an experiment without pump pulse by measuring the transmitted intensities $I(\tau)$ and I_{ref} as a function of pump–probe time delay τ. The dynamics of this signal $\Delta A(\tau)$ include the differences that are due to changes in the concentration (or population) of a certain species as well as the differences that are due to a laser-induced change in the absorptivity (e.g. as a result of molecular dynamics). This description applies to a particular wavelength. Usually, TA experiments are performed at a set of different wavelengths to characterize different (transient) molecular species of interest.

2.3 Laser system

Femtosecond laser pulses are the basis for the time-resolved spectroscopy experiments in this work. An overview of the whole system is given in Fig. 2.1. In our laboratory the ultrashort pulses are generated by a home-built Kerr-lens mode-locked Titanium:sapphire oscillator. The active medium is pumped by a commercial continuous-wave (CW) Nd:YVO_4 laser (Coherent Verdi V6) at 532 nm and dispersion compensation is achieved by an intracavity prism compressor. Output pulses exiting the oscillator at a repetition rate of 90 MHz have a central wavelength of 800 nm and an energy of 2.5 nJ. The pulses have a bandwidth of typically $\Delta\lambda_{\mathrm{FWHM}} \approx 12$ nm and are close to their transform-limited duration of $\Delta t_{\mathrm{FWHM}} \approx 80$ fs (Gaussian pulse shape). As indicated by the dashed lines in Fig. 2.1 a small fraction of the output beam is split off to constantly monitor the pulse characteristics in a spectrometer and an intensity autocorrelator.

To gain pulses with intensities high enough for frequency conversion (see section 3.3) or for highly nonlinear optical experiments a regenerative amplifier based on chirped pulse amplification (CPA) is used [5]. First positive dispersion is introduced to the oscillator pulses by an Öffner-type stretcher and the pulse duration is lengthened to several hundred picoseconds. The Ti:sapphire gain medium in the amplifier cavity is pumped at 527 nm by a commercial nanosecond Nd:YLF laser (Coherent Evolution 15) that is pulsed at ≈ 1 kHz repetition rate. An appropriate trigger signal for this pump laser is gained by detecting the pulse train from the oscillator with a photodiode and frequency-dividing the signal by a factor of 90,000. Pulse picking from the oscillator

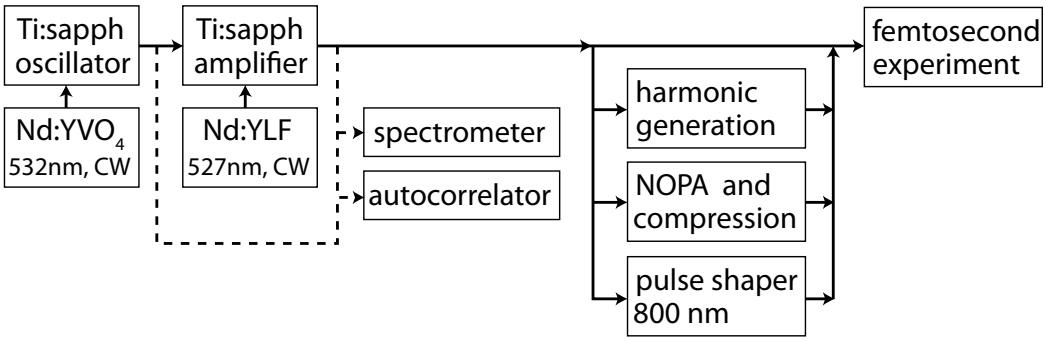

Figure 2.1: Femtosecond laser system. Left to right: A femtosecond oscillator seeds a regenerative amplifier. Both seed and amplified pulses are characterized by a spectrometer and an autocorrelator. Further methods such as pulse shaping or frequency conversion are employed before finally directing the pulses to the experiment.

pulse train is accomplished by an intracavity Pockels cell in combination with a dielectric thin film polarizer. After ca. 14 cavity round trips a second polarization switching of the same Pockels cell couples the amplified pulse (1 mJ) out of the regenerative amplifier cavity. The amplified pulses are recompressed in a Treacy-type grating compressor that introduces the appropriate amount of negative dispersion to yield pulses of < 100 fs duration and 650 μJ energy. The characterization and optimization when tweaking the alignment of the system can be achieved with the same setup as for the oscillator pulses (Fig. 2.1). Spectrum and pulse duration can be monitored online with the spectrometer and autocorrelator during an experiment.

The output pulses of the amplifier system can either be used in the femtosecond experiments directly or they can be further modified. In particular, we frequently use pulse shapers at 800 nm to fine-tune the pulse compression for time-resolved experiments or to influence the pulse shape in general for quantum control experiments. Alternatively, all or just a part of the pulse energy is used for harmonic generation in frequency-mixing crystals for multicolor experiments (see e.g. chapter 6). Another possible beam path pumps the NOPA for frequency conversion and bandwidth broadening in the visible wavelength region (see section 3.3). To accurately measure the pulse parameters at the location of the experiment, suitable pulse characterization methods such as frequency-resolved optical gating (FROG) are employed.

2.4 General software framework for scientific data acquisition and simulation

The success of scientific projects depends upon the formulation of a goal, researching existing achievements in the field, careful planning of experiments, proper and efficient execution of measurements, and finally good scientific data evaluation and interpretation. In particular the experiments themselves demand complex everyday tasks from the experimenter in the laboratory because the entire experiment usually involves a se-

quence of measurements following an adjustment of parameters. Most of the equipment is controlled electronically and yields a digital data output. Even a piece of equipment as simple as a laser power meter can be read out digitally and integrated in the whole measurement process. The ubiquity of the electronic and digital control and read-out in combination with computer systems allows scientists to achieve unprecedented flexibility and productivity in acquiring experimental data. Therefore the software that is used on the laboratory computer system to control equipment and acquire data plays a decisive role in present-day scientific projects.

A considerable number of different pieces of equipment should be integrated into preferably one general program structure that allows the users to perform nearly arbitrarily complex measurement sequences. This facilitates carrying out experiments that have not even been conceived yet by only making use of the software user interface and without the need for additional programming when changing the measurement process. For long-term usability new equipment and simulations must be integrated without difficulty. In addition to taking a single measurement point (a single experiment) that may consist of a sequence of several instrument operations (including simulations), it is often necessary to vary experimental parameters systematically in a scan or an automated optimization algorithm.

The choice of programming language is determined by a number of factors. First, the ease of use for both the programmer and the user is essential. Naturally, the control over the laboratory equipment must be sufficient and preferably simple to implement using the chosen language. Further, calculations, mathematics, and simulations should be included in the program structure as well and hence a simple interfacing with other programming and simulation languages is desired. The LabVIEW [6] platform was chosen for the implementation of the general laboratory software framework.[1] The development environment for the data-flow-oriented visual programming language G and its resulting programs (called virtual instruments or VIs) provide several advantages with respect to our purposes. Drivers for laboratory hardware that come in the form of (wrapper) VIs can be purchased along with the equipment or written via integration of other drivers into a LabVIEW VI with relative ease. In fact, the drivers for the vast majority of our equipment were already at hand before beginning this software project. LabVIEW further allows the fast creation of graphical user interfaces (GUIs). Even complex input- and output structures can be visualized for the user in clearly arranged input fields and data representations such as graphs and charts. While the visual programming is efficient for most tasks and LabVIEW provides a large number of built-in libraries, some problems can be solved more efficiently with conventional code-based languages. Particularly issues that include many mathematical operations and numerical simulations might be easier to implement in languages like C or MATLAB. For such cases LabVIEW allows the integration of foreign language programs into VIs. It should be noted that the choice of LabVIEW as the programming language also entails some disadvantages. The language lacks truly object-oriented features of modern languages such as C++ or JAVA. One manifestation of this lack is the fact that every variable must be typed at compile time. Unfortunately, this greatly reduces the flexibility

[1] LabVIEW is an acronym for “Laboratory Virtual Instrument Engineering Workbench”.

of data structures in LabVIEW VIs. Native recursion is also missing and can only be implemented using loop constructs. Nevertheless, LabVIEW can be considered a "general purpose" programming language and it features decisive advantages for the realization of a general laboratory software.

The program package that we created rendered the experiments presented in the later chapters of this thesis possible and should prove useful for future experiments. It includes the general data acquisition module that executes a sequence of hardware and simulation operations, a single experiment program (with GUI), a 2D scan program that varies parameters systematically, and an optimization program that employs an evolutionary algorithm to optimize experimental parameters with respect to a user-defined goal.

2.4.1 Core components

First, this section will describe the data structure and the program components crucial to the package. The most basic concept for the framework is that we define a single experiment as consisting of a sequence of data acquisitions. The term "data acquisition" will refer to addressing a hardware item with certain parameters and yielding an output, or, to performing a simulation (calculation) and yielding a result.

Data structure

Each data acquisition can yield two-dimensional data. This design decision (and restriction) had to be made because in LabVIEW the data type and the dimensionality of an array must be determined before the compile time, unless one uses the "variant" data type which entails other complications, such as the need for excessive type checking and casting. However, in practice, two-dimensional output arrays have proven to be sufficient for all data acquisitions.

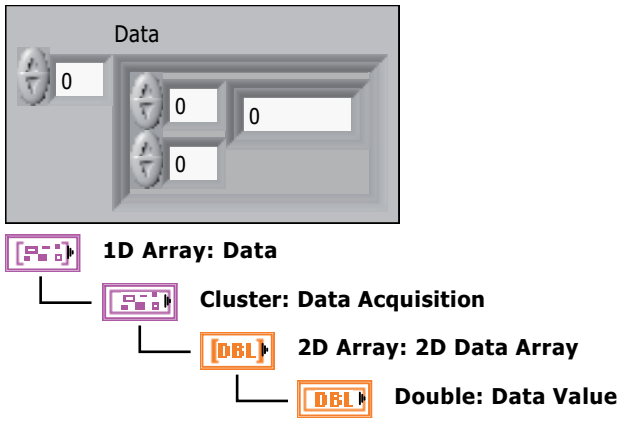

Figure 2.2: Type definition of the basic data type used throughout the software framework. Each hardware item (or "data acquisition") can yield a two-dimensional array of double precision numbers. Further, the 2D data array is clustered and used as the element of an outer array which represents the sequence of different data acquisitions.

This basic data structure is depicted in Fig. 2.2. Each data acquisition can yield a 2D array of real-valued double precision numbers (inner array). The sequence of the data acquisitions, i.e., the experiment, is represented by the outer one-dimensional (1D) array, where the wrapping cluster is necessary to allow varying 2D data sizes. Thus, the entire data from a single experiment, defined as a sequence of data acquisitions with

different hardware or simulation items, is contained in this data structure. A LabVIEW type definition was used for this data structure as well as all other relevant input and output data structures. How the data is combined into bigger structures when many experiments are performed automatically will be described in sections 2.4.3 and 2.4.4.

Data acquisition VI

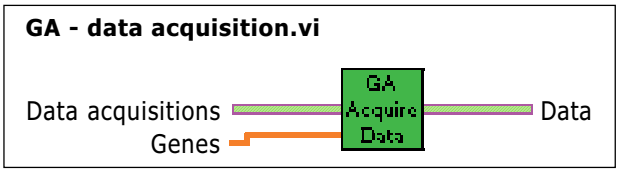

Figure 2.3: Inputs and output of "GA - data acquisition.vi". The inputs 'Data acquisitons' and 'Genes' contain all experimental parameters. The output is the data structure shown in Fig. 2.2.

The VI that actually executes a single experiment and outputs the described kind of data is called "GA - data acquisition.vi".[2] Its input and output connections are shown in Fig. 2.3. The output simply consists of the basic data structure. The inputs on the other hand have to contain all necessary parameters for an experiment: The 'Genes' are a 1D array of double precision numbers between 0 and 1. They represent the degrees of freedom that can be varied by our optimization algorithm (see section 2.4.4) and are mostly used when a parameter (e.g. of a laser pulse shape) is to be changed automatically between several experiments. The 'Genes' array can be accessed by each data acquisition in the experiment sequence. The experiment sequence itself is defined by the input array 'Data acquisitions'.

As mentioned, the 'Data acquisitions' array contains the instructions of how to measure with the different hardware items that constitute the experiment sequence. The data type of the array is sketched in Fig. 2.4. Within the 1D array, a cluster 'hardware parameters' is contained. The latter aggregates the settings for a single measurement. At the top of the cluster control the enum 'Use device' functions as a selector for which hardware item to use in the current data acquisition step, which is indicated by the array index. Additionally, the 'hardware parameters' cluster contains all the settings for all hardware and simulation items as individual clusters. Only the cluster that is currently selected by 'Use device' is regarded by the data acquisition VI. All hardware items must be included in the hardware parameters control because, again, LabVIEW variables must be typed at compile time. We have implemented a workaround for this drawback. Even though all the hardware item clusters are contained in 'hardware parameters', we have programmed a subVI ("GA - control visibility.vi") for use within all VIs that have GUIs for user interaction. This subVI hides all hardware clusters except for the one selected by the 'Use device' control. In this fashion, the user can virtually switch the contents of the 'hardware parameters' cluster control in a convenient way.

[2] "GA" is a file name prefix used throughout the general data acquisition framework for unambiguousness of VI names.

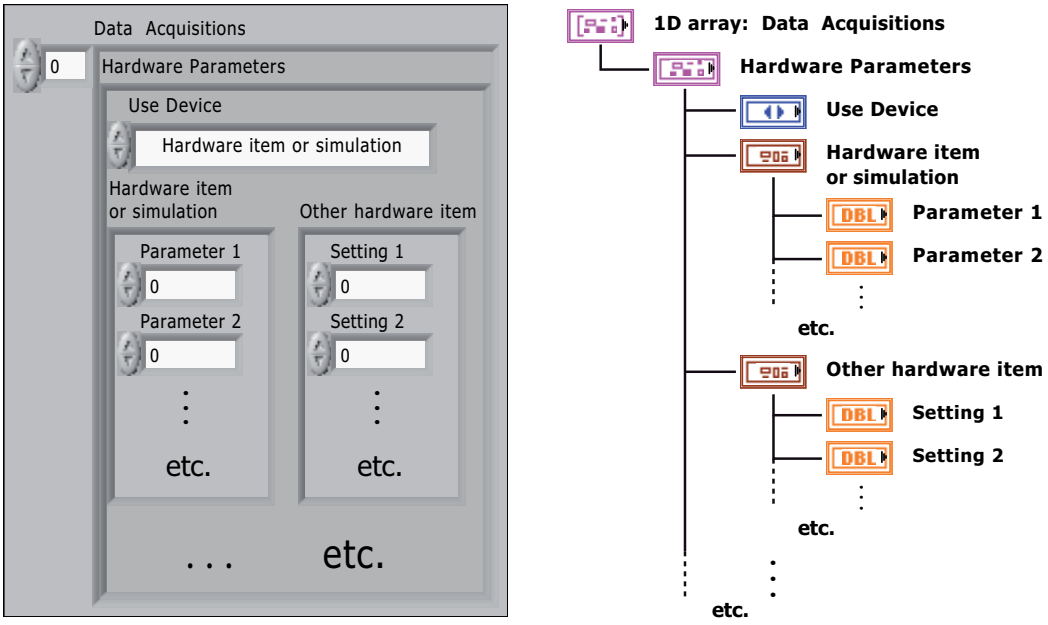

Figure 2.4: 'Data acquisitions' array defining the experiment. The sequence of measurements and simulations is determined by the 1D array of the cluster 'hardware parameters'. Each cluster contains the necessary parameters for all possible hardware and simulation items and, additionally, a selector called 'Use device' that specifies which hardware to use for the current element in the data acquisitions sequence.

The control visibility VI processes the tree structure of controls recursively so that more complex structures can be contained in a single hardware settings cluster. For example, in our implementation the simulation item contains several different types of simulations and the respective controls are switched on and off by a selector (in this case called 'type of simulation'). It should be noted that the data acquisition VI is not intended for use as a stand-alone program because neither the visibility of the different hardware items is controlled nor is there a means to display the output data. A suitable GUI for the data acquisition VI is provided by the "GA - data acquisition tool.vi" described in section 2.4.2 below.

The program "GA - data acquisition.vi" executes an experiment simply by looping over the 'data acquisitions' array. For each index the respective hardware item (selected by 'Use device') is controlled with the given parameters and the resulting 2D data is clustered and appended to the 1D data array of the experiment. With respect to preliminary data evaluation or similar purposes, it is important that each iteration of the loop, i.e. each data acquisition, has access to all data from the previous data acquisitions. We have for instance implemented an item called "data processing" that calculates averages, transposes or shifts data, or accomplishes more complex tasks such as calculating the absorbance change from the raw data of a transient absorption experiment.

For various reasons some hardware items and even some simulations require an initialization of some sort before being used in an automated, repeated experimental sequence. Computer oscilloscope cards for instance have to allocate space in their on-board buffers

according to the size of the expected data. Similarly, before starting a simulation, some data might be loaded from the hard drive or some data common to all simulation iterations can be pre-calculated. To make the fast iteration of experiments and simulations possible, we use a LabVIEW global variable called "GA - global hardware parameters.vi". There, each hardware or simulation item can store common data of arbitrary structure. Additionally, for each hardware there is a Boolean variable that indicates whether the hardware has been 'initialized' or not. This Boolean is checked every time before the hardware or simulation is executed; if it is 'false' then usually an additional initialization VI is called that loads data, performs pre-calculations, or demands user interaction. Subsequently, the pertinent data is entered in the global variable for later use and the Boolean 'initialized' is set to 'true'. Then the first measurement or simulation is performed with the given parameters. If the Boolean is 'true' then the initialization is simply skipped and the measurement is performed immediately. Thus, the first execution of an experiment sequence will usually take longer and may require further user interaction due to these initializations. After the first execution, a fast and automated experiment is possible.

Feedback, fitness, and cost functional VIs

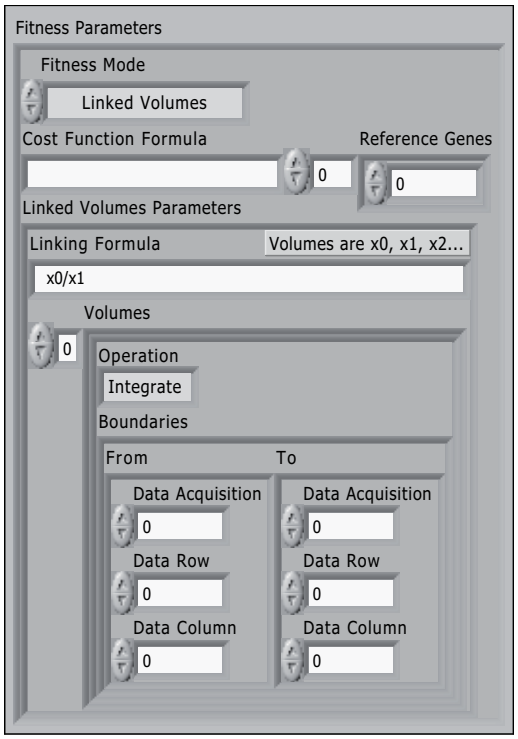

Figure 2.5: Fitness and cost functional parameters. Up to now, only the 'linked volumes' fitness mode has been implemented. A single fitness value is gained from the three dimensional data by defining a set of cuboid 'volumes' together with an operation ('integrate', 'mean', or 'standard deviation') that is to be performed on the contained data. The linking formula allows a large number of mathematical operations for processing the volume values $\{x_0, ..., x_n\}$, resulting in a fitness value. Further, an additional cost functional with respect to the reference genes can be defined through another formula.

Very often, it is necessary to gain a single value from the acquired data online, i.e., *during* the experiment. This value, that we will call "fitness" in analogy to the terminology of evolutionary algorithms (see section 2.4.4), can then determine the further course of an optimization or serve as the single-valued ordinate of a scan. Therefore, in

a VI called "GA - feedback.vi" we have combined the data acquisition VI with a "GA - fitness.vi" and a "GA - cost functional.vi".

This feedback VI first calls the data acquisition VI with all the necessary experimental parameters. Then all data is handed to the fitness VI and a fitness value is calculated with the help of 'fitness parameters' (shown in Fig. 2.5). Briefly, this is done by regarding the data from an experiment as three-dimensional and defining a set of cuboid volumes, to which one of the operations 'integrate', 'mean', or 'standard deviation' is applied. This yields the set of values $\{x_0, ..., x_n\}$ which can be used in the 'linking formula' that combines the values into a single fitness value. The formula string is entered in standard MATLAB or C notation and allows a large number of mathematical operations on the volume values. A simple example for the use of multiple volumes is the evaluation of the ratio A/B of two photochemical processes A and B that are measured in an experiment [7, 8]. However, much more complex fitness functions are possible as well.

After the calculation of the fitness value a cost functional can be applied that allows an additional alteration of the fitness value in relation to the genes. This is in contrast to the raw fitness value which only depends on the data from the data acquisitions. The cost functional can serve to normalize data or to bias a fitness landscape and thus identify extraneous degrees of freedom in an evolutionary algorithm optimization [9–11]. Note that the cost functional value is *subtracted* from the fitness. This results in the final fitness value as the output of "GA - feedback.vi". As alluded to above, in practice, the calculation of the fitness value is always advantageous. Hence, we never use the data acquisition VI by itself but always the feedback VI that includes the data acquisition and its processing to yield a meaningful fitness value.

2.4.2 Program for executing a single measurement sequence

With the components presented in the previous section it is now possible to perform an experiment in an automated fashion and obtain the data as well as a fitness value. For simple measurements, we have programmed a functional GUI, "GA - data acquisition tool.vi," as a front end for the feedback VI. It allows the convenient definition of a measurement sequence, which is executed on the click of a button. The data from the experiment can then be plotted in the same window with multiple graphical options such as single and multiline graphs, x-y-graphs, or intensity graphs for 2D data. For later analysis, the displayed data can be saved and exported as text in a spreadsheet file. Further, the controls for fitness definition are provided on the VI front panel and the resulting fitness value is displayed and adapted constantly. This data acquisition VI is usually used for simple, single measurements (e.g. the recording of a single laser spectrum) or to test out a complex data acquisition sequence.

2.4.3 Scan program

A typical laboratory project will require a series of experiments and a variation of the experimental parameters between these single experiments. Such a systematic variation of parameters and the pertaining measurements is called a "scan". The program "Scan -

parameter scan 2.0.vi" implements this using the data acquisition framework, i.e., using the feedback VI with data acquisitions, genes, and fitness parameters.

This program allows two-dimensional scans of arbitrary experimental parameters. These 'scan parameters' simply consist of the data acquisitions, the genes, and the fitness parameters. The most important notion for the scan program is that the 'scan parameters' span a high-dimensional space, and that the scan samples a 2D hyperplane in this space. The scanning plane is defined by a 'starting point' $\vec{S}$ and two 'increment vectors' $\vec{I}_1$ and $\vec{I}_2$. Hence, the points $\vec{P}_{jk}$ at which experiments are performed are given by

$$\vec{P}_{jk} = \vec{S} + j\, m_{1j}\, \vec{I}_1 + k\, m_{2k}\, \vec{I}_2, \tag{2.27}$$

where the indices j and k range from 0 to $(N_1 - 1)$ and $(N_2 - 1)$, respectively. N_1 and N_2 are the number of points in the two scanning dimensions. The multipliers m_{1j} and m_{2k} can be chosen to change the sampling of the rectangular scanning area. Fig. 2.6 illustrates the 2D scan. The two dimensions, or axes, are defined by the increment vectors $\vec{I}_1$ and $\vec{I}_2$. All measurement points $\vec{P}_{jk}$ are marked as dots. The first point $\vec{P}_{00}$ is equal to the starting point that also defines one corner of the total scanning area which is shown in gray. In dimension 1, the sketch also shows that the spacing of the measurement points can be increased or decreased. In this case the multipliers m_{1j} were doubled for the last three points in dimension 1. In total, $N_1 \times N_2$ points are taken and $\vec{P}_{N_1-1,N_2-1}$ marks the last point of the scan.

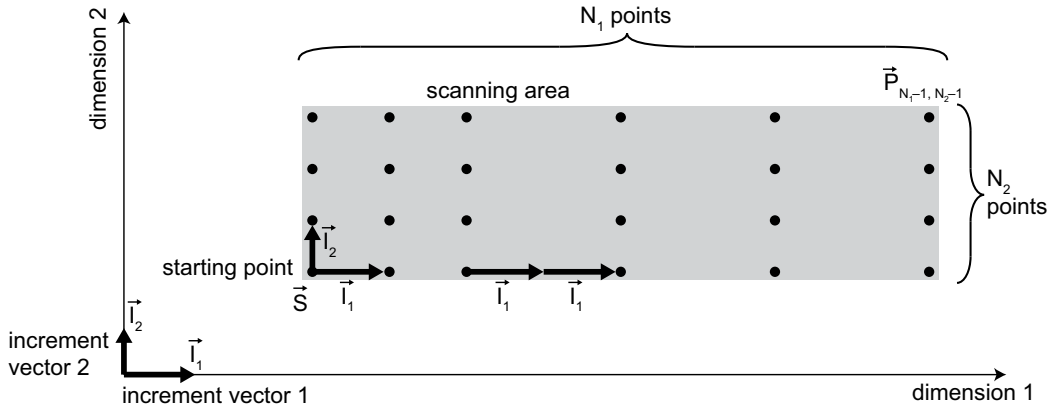

Figure 2.6: Illustration of a 2D scan with the program "Scan - parameter scan 2.0.vi". The increment vectors 1 and 2 span the experimental plane. The points where measurements are taken, are marked with dots. Starting from the point $\vec{S}$, a total number of $N_1 \times N_2$ points is taken with different sampling. See text for further explanation.

This somewhat abstract representation of an experimental scan in the laboratory, or of a systematic variation of parameters in a simulation, has the great advantage that it encompasses all possible scans with all hardware that is incorporated in the data acquisition framework. Not only very simple scans like moving a delay stage are possible, but also more complicated scans such as changing the laser pulse with a femtosecond pulse shaper while translating the sample with a stepper motor. Since only a few of the many possible experimental parameters are varied during a scan, usually the increment

vectors $\vec{I}_{1,2}$ are sparse vectors. In practice, this simplifies the definition of the increment vectors.

After defining the starting point, increment vectors, numbers of steps, and multipliers, or loading them from a saved XML file, the experimenter can pick single points of the scan and execute the pertaining experiments in order to test the settings or make further adjustments. The scan itself runs automatically and first loops over all steps in dimension 2 before proceeding to the next step in dimension 1. All the data taken at each point can be saved during the scan. The single fitness value gained at each point is also saved and displayed in a graph that is updated during the course of the scan. This allows online monitoring of the experimental results and it can also be used as a feedback signal for manual adjustments such as beam alignment.

Naturally, the scan program can be used to perform a 1D scan, simply by setting the number of steps in either dimension 1 or dimension 2 to $N = 1$. Conversely, in the very rare case where scans in 3 or more dimensions are required, "Scan - parameter scan 2.0.vi" can be used as a subVI that accepts all the settings for a 2D scan and returns the data and fitness values of this scan to the caller VI, which can execute the third dimension of the scan.

2.4.4 Evolutionary algorithm optimization program

For complex problems where the search space is large and may depend on multiple variables, it is often not possible to find the optimal solution by simply varying the parameters in a deterministic way as it is done, for instance, with our scan program. A more advanced optimization algorithm is required for these types of problems. Evolutionary algorithms have been developed and used for many purposes. In particular in ultrafast optics and optimal control experiments this class of optimization algorithms has been applied very successfully to find optimal solutions to a wide range of problems [12–17].

In principle, any kind of optimization algorithm, such as gradient search, simulated annealing, genetic algorithms, could be implemented and draw upon the advantages of our software framework for data acquisition and simulation. The algorithmic details and the measurement are independent from each other. The feedback VI controls the experiment and the evaluation of a set of parameters as described above. Any optimization algorithm could process the output data and iterate the variation of parameters to finally find the optimal solution. Currently, we have implemented an evolutionary algorithm which proved to be suitable for many applications (see e.g. section 3.8.1).

In general evolutionary algorithms mimic biological evolution. In particular, selection ("survival of the fittest"), heredity transmission, and reproduction are the principles that are translated into components of the algorithm. A pool of a certain number of initially randomly selected potential solutions – called "individuals" – form a "population". Each individual consists of a number of parameters, the "genes". The goal of the optimization is defined as maximization of a "fitness" value or minimization of a cost. Thus, each individual in the population is tested by this fitness function. Only a certain percentage of the best in the population survives to reproduce. This selection favors the fit individuals and helps convergence of the algorithm. The surviving individuals reproduce via various processes (see below) and their offspring form a new population. Then

the process of fitness evaluation, selection, and reproduction repeats and each repetition is called a "generation". After a number of iterations the fitness reaches an optimum value and the best individual corresponds to the optimal solution. Since evolutionary algorithms have been described comprehensively elsewhere [18], we will not go into further detail here, but rather outline the special features of our implementation.

First of all, our program "GA - simultaneous optimizations.vi" has the ability to perform an arbitrary number of evolutionary optimizations with different settings in parallel. In the implementation this is accomplished simply by defining all necessary parameters as an array over the different optimizations. The individuals of all the populations from the different optimizations are interleaved before calling the feedback VI for each one of them. After sequentially being assigned a fitness value, the individuals are collected again in their respective population. This method allows us to perform parallel optimizations with different settings or experiments and directly compare the results, because the external conditions are the same for all optimizations.

The reproduction mechanisms we use are mutation, two-point crossover, and cloning (or elitism). The latter only promotes a few of the very best individuals to the next generation without alteration so that the best solution cannot be discarded, even in the presence of noise. Mutation changes a number of genes of an individual in a random fashion. For the new gene value, we use a normal distribution, centered around the old gene value. The adjustable parameters of the mutation mechanism are the fraction of all individuals that are to be mutated, the probability for each gene to be mutated, and the width of the random distribution for the new values. In general, mutation introduces new genetic material into the population. Depending on the width of the mutation, it can also sample the search space locally by creating small variations of individuals. Finally, two-point crossover switches a randomly determined part of all genes between two individuals. This allows the combination of "good traits" of two individuals into a new individual. Here, the parameters we use are the fraction of all individuals of the next generation that is to be created by two-point crossover and a mating selection factor. This factor determines whether a good individual is combined with another good individual, or if a good individual is rather combined with a more unfit individual. For complex problems with a high-dimensional or very complicated search space, our algorithm allows the automatic variation of all above-mentioned parameters. This corresponds to an automatic change of search strategies and helps convergence even with complicated optimizations.

In practice, our optimization program first demands the definition of all optimization parameters from the user. These parameters include the data acquisitions, the parameters for the algorithm itself, and the fitness parameters. All of these can be changed at each step of the program, even while the algorithm is running. After the initial definition a test individual can be defined and a measurement can be taken with this individual. This aides with the definition of the fitness function. It should be noted that the GUI for this part of the program is virtually identical to the GUI used in the scan program and in the single experiment program. Further, a reference individual is defined. This serves as benchmark to judge the fitness improvement that is achieved during the optimization and also to monitor the stability of the experimental conditions. After setting up all parameters for all parallel optimizations, the algorithm runs automatically. Determination

of the convergence and ending the optimization is at the discretion of the user. As a final step, the best individuals which represent the solution to the optimization problem are evaluated again and this data is saved. The solution can be the goal of a scientific problem or be used as input for further experiments.

2.4.5 Applications of the software framework

The software frame work and the programs that were presented in the last sections are applied extensively for many purposes in our research group. The evolutionary optimization program is used as an everyday tool for adaptive compression of laser pulses with femtosecond pulse shapers (see for instance section 3.8.1). In quantum control experiments on photoinduced reactions the algorithm was employed to find optimally shaped laser pulses (see for instance the Wolff rearrangement reaction of diazonaphthoquinone [19]). Recently, we have started to use the optimization algorithm to find the proper absolute phase of two-dimensional correlation spectra (for 2D phasing see chapter 4). The evolutionary algorithm was also used in a simulation to find optimal polarization-shaped pulses that control the propagation of plasmonic energy in a nanostructure [20]. First experiments on this topic were also conducted [21].

The scan program on the other hand is used for the deterministic variation of parameters. In particular, various time-resolved spectroscopy techniques benefit from the scan program. The realization of the 2D spectroscopy experiments presented in chapter 4 was facilitated by the scan program. The technique of accumulation for femtosecond spectroscopy, that is presented in chapters 5 and applied to a biological system in chapter 6, was rendered possible by the scan program and the capability of the data acquisition program to define and perform a complex measurement sequence. Transient absorption spectroscopy experiments are also routinely conducted with the help of the scan program. Ultraviolet or visible pump pulses were used in combination with time-delayed visible or midinfrared pulses [8, 19, 22, 23].

This list of applications is not comprehensive. New hardware and simulation modules are being added constantly to the software framework. Therefore new applications to everyday laboratory tasks and to scientific questions are devised as well. The flexible framework creates a prolific basis for novel experiments and techniques.

2.5 Summary

In this chapter the basic description of laser pulses has been outlined. This is a prerequisite for the application of shaped pulses and the description of nonlinear spectroscopies in subsequent chapters. Further, optical quantities that are important for femtosecond spectroscopy such as intensity, absorbance, and optical density have been defined here. The primary elements and the setup of our femtosecond laser system were described. This system was used in the projects presented in the subsequent chapters. Finally, a general software framework for scientific data acquisition and simulation was described. It allows the definition of an arbitrary experimental sequence of measurements or simulations. All laboratory equipment can be controlled by the framework and computations or

simulations can be included in the sequence. New components can be easily integrated. The main programs based on this framework are a scan program and an optimization program. The scan program allows the deterministic variation of arbitrary parameters in a 2D scan. The optimization program is based on an evolutionary algorithm. It allows the flexible definition of a goal and finds the optimal solution to this problem. Both programs are applied not only to the scientific projects presented in this thesis but also to many other projects in our research group.

3 Generation of ultrabroadband femtosecond pulses in the visible

Many modern day ultrafast applications require a broad spectrum to both provide short pulses and to tailor the spectrum to the molecular systems to be studied. At the same time frequency conversion of widely used 800 nm Ti:Sapphire laser systems is necessary to access the frequency bands of interesting sample systems such as biological complexes, organic dyes, aggregates, polymers that are generally located in the visible spectral range. The focus of the present work is on the development of experimental methods and applications to these kinds of systems and therefore means to generate, manipulate, and measure broadband ultrashort visible laser pulses were built. This chapter deals with the principles of nonlinear optics, frequency conversion, and optical parametric amplification. The experimental implementation of the noncollinear optical parametric amplifier is presented, as is the liquid crystal pulse shaper to compress the pulses. Finally, the characterization of these pulses is described along with results of the pulse compression.

3.1 Nonlinear optics

For both the generation and the characterization of the pulses nonlinear optical effects are exploited and a brief introduction is given here.

3.1.1 Nonlinear polarization and frequency conversion

High intensities, common when dealing with ultrashort laser pulses, can cause the induced polarization in traversed material to be not only linearly proportional to the electric field strength but to also have nonlinear components [24]

$$P(\omega) = \epsilon_0 \sum_{j=0}^{\infty} \chi^{(j)} E(\omega)^j. \tag{3.1}$$

Here we simply write the electric field E and the polarization P as scalars. The susceptibilities $\chi^{(j)}$ determine the response of the material to the electric field and since in general polarization and electric field are vector quantities, the susceptibilities are generally tensors. For a qualitative understanding of many nonlinear optical phenomena we can restrict ourselves to only the term of second order in E,

$$P_i^{(2)}(\omega_q) = \epsilon_0 \sum_{j,k} \chi_{ijk}^{(2)}(-\omega_q, \omega_n, \omega_m) E_j(\omega_m) E_k(\omega_n). \tag{3.2}$$

The indices i, j, k take the values of the spatial directions x, y, z and the three frequencies $\omega_q, \omega_m, \omega_n$ must meet the condition $\omega_q = \omega_m + \omega_n$. It is important to note that $\chi^{(2)}$, the second order susceptibility, is only non-vanishing in media which lack inversion symmetry.

Neglecting the spatial indices and assuming electric fields of the form $E = E_0 \mathrm{e}^{-\mathrm{i}\omega t} +$ c.c., it can be easily seen that time-dependent polarizations are created at different frequencies than the fundamental. For example, given a field consisting of two distinct frequencies ω_1 and ω_2

$$E = E_1 \mathrm{e}^{-\mathrm{i}\omega_1 t} + E_2 \mathrm{e}^{-\mathrm{i}\omega_2 t} + \text{c.c.} \tag{3.3}$$

the second order nonlinear polarization results as

$$\begin{aligned} P^{(2)} = \epsilon_0 \chi^{(2)} \left(E_1^2 \mathrm{e}^{-2\mathrm{i}\omega_1 t} + E_2^2 \mathrm{e}^{-2\mathrm{i}\omega_2 t} + 2E_1 E_2 \mathrm{e}^{-\mathrm{i}(\omega_1+\omega_2)t} + 2E_1 E_2^* \mathrm{e}^{-\mathrm{i}(\omega_1-\omega_2)t} + \text{c.c.} \right) \\ + 2\epsilon_0 \chi^{(2)} \left(E_1 E_1^* + E_2 E_2^* \right). \end{aligned} \tag{3.4}$$

The terms in Eq. 3.4 can be identified as a multitude of nonlinear optical effects of different frequencies. Their complex amplitudes are given as

$$P(2\omega_1) = \epsilon_0 \chi^{(2)} E_1^2 \tag{3.5}$$
$$P(2\omega_2) = \epsilon_0 \chi^{(2)} E_2^2 \tag{3.6}$$
$$P(\omega_1 + \omega_2) = 2\epsilon_0 \chi^{(2)} E_1 E_2 \tag{3.7}$$
$$P(\omega_1 - \omega_2) = 2\epsilon_0 \chi^{(2)} E_1 E_2^* \tag{3.8}$$
$$P(0) = 2\epsilon_0 \chi^{(2)} \left(E_1 E_1^* + E_2 E_2^* \right). \tag{3.9}$$

According to the wave equation of classical electrodynamics any oscillating polarization acts as a source for the emission of new fields [25]. Therefore the polarizations in eqns. 3.5–3.8 give rise to frequency-converted fields at $2\omega_1$, $2\omega_2$, $\omega_1 + \omega_2$, and $\omega_1 - \omega_2$. The respective effects are called second harmonic generation (SHG) of ω_1 and ω_2, sum frequency generation (SFG), and difference frequency generation (DFG). Eqn. 3.9 on the other hand describes a non-oscillating, constant polarization of the optical material and the effect is called optical rectification (OR) [24].

3.1.2 Phase matching

For the process of generating the frequency-converted emitted fields in a bulk medium one has to take the propagation of these fields as well as the propagation of the original fields into account. Efficient frequency conversion processes in materials are only possible if the fields that generate the nonlinear polarization propagate with the same phase velocity through the material as the resulting frequency-converted field. Otherwise there would be destructive interference between parts of the resulting field that were generated earlier and parts that were generated later. This condition can be expressed in terms of the wave vectors as

$$\Delta\vec{k} = \vec{k_q} - \vec{k_m} - \vec{k_n} = 0. \tag{3.10}$$

In the case of SHG, e.g., this corresponds to $\vec{k_2} - 2\vec{k_1} = 0$ with the wave vectors $\vec{k_1}$ of the fundamental and $\vec{k_2}$ of the second harmonic. Accordingly, $\vec{k_3} - \vec{k_1} - \vec{k_2} = 0$ holds for

DFG of the two frequencies ω_1 and ω_2 with wave vectors $\vec{k_1}$ and $\vec{k_2}$, creating frequency ω_3 with wave vector $\vec{k_3}$. In fact, this phase matching condition can also be interpreted as the law of momentum conservation in nonlinear optics because the photon momentum is given as $\vec{p} = \hbar\vec{k}$.

For three frequencies $\omega_q > \omega_m > \omega_n$ Eq. 3.10 can be cast as

$$n_q\omega_q = n_m\omega_m + n_n\omega_n \tag{3.11}$$

with the refractive indices of the respective frequencies n_j. However, in the normal dispersion regime of bulk isotropic material where $n_1 < n_2 < n_3$ this condition cannot be fulfilled. One therefore generally uses birefringent crystals as nonlinear media where phase matching can be achieved by choosing the polarizations of the different frequencies such that the higher frequencies have a lower refractive index due to the birefringence. A typical example is type I phase matching in a negative uniaxial crystal ($n_e < n_o$) where ω_q is polarized in the extraordinary direction and ω_m and ω_n are of equal and ordinary polarization. For other types of phase matching see e.g. Ref. [26]. The index of refraction for the extraordinary component can be tuned by adjusting the angle of propagation with respect to the optical axis of the crystal. For type I phase matching Eq. 3.11 becomes

$$n_{eq}(\theta)\omega_q = n_{om}\omega_m + n_{on}\omega_n \tag{3.12}$$

with the additional indices e and o for extraordinary and ordinary polarization. The angle between the propagation direction and the optical axis θ determines changes in the index of refraction of the extraordinary component n_{eq} according to

$$\frac{1}{n_{eq}^2(\theta)} = \frac{\sin^2\theta}{n_{eq}^2} + \frac{\cos^2\theta}{n_{oq}^2}. \tag{3.13}$$

Therefore the type I phase matching angle is given by

$$\theta = \arcsin\left(\frac{n_{eq}}{n_{eq}(\theta)}\sqrt{\frac{n_{oq}^2 - n_{eq}^2(\theta)}{n_{oq}^2 - n_{eq}^2}}\right). \tag{3.14}$$

The program SNLO, originally developed at Sandia National Labs [27], is a convenient way to calculate phase matching angles. The software contains a database with many common optical crystal materials and can assist with calculations of different nonlinear processes under different phase matching conditions.

3.2 Optical parametric amplification

Optical parametric amplification (OPA) can in fact be described in a very similar manner to DFG. In DFG two beams of different frequencies ω_1, ω_2 but comparable intensities generate a third beam at the difference frequency $\omega_1 - \omega_2$. In OPA, on the other hand, one strong beam of frequency ω_p ("pump") and a weak beam at ω_s ("signal", sometimes also called "seed") irradiate the nonlinear crystal and the signal is amplified while the pump is depleted. At the same time a third frequency $\omega_i = \omega_p - \omega_s$ is generated ("idler").

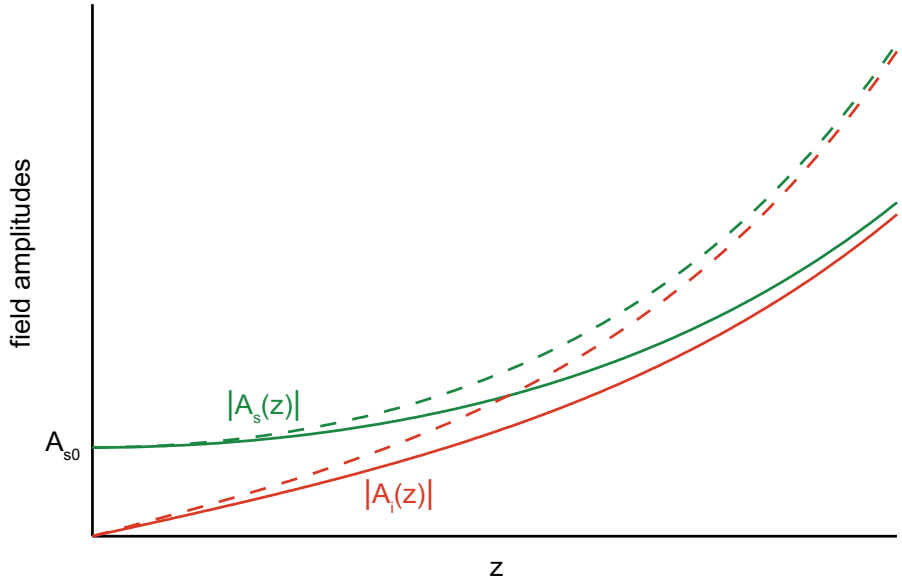

Figure 3.1: OPA: As the waves propagate along z, the signal amplitude $|A_s(z)|$ starting with A_{s0} is amplified and the idler amplitude $|A_i(z)|$ is generated. In the approximation that the pump amplitude remains constant and that all waves are monochromatic and perfectly phase matched ($\Delta k = 0$) the amplitudes grow like cosh and sinh. The coupling constant κ is 1.2 times bigger for the dashed curves than for the solid curves.

The seed for an OPA is usually obtained via white light generation [28]. A relatively small fraction of the Ti:Sapphire amplifier system output is focused tightly into a $\chi^{(3)}$ material. Self-focusing creates a stable filament of a few micron in diameter and the extremely high intensities give rise to spectral broadening through effects such as self-phase modulation and Raman scattering. White light generation is not fully understood and the involved processes are a matter of current investigations [29]. The stable filaments, primarily created in Sapphire, CaF_2, or even in photonic crystal fibers, are used for many purposes, e.g. as a broadband probe in transient absorption spectroscopy [30], as a source for broad spectra to generate few cycle pulses after compression [31], and as seed pulses for OPAs [32, 33].

To evaluate the OPA process quantitatively one has to derive three coupled differential equations from the wave equation describing the amplification of the signal, the generation of the idler, and the weakening of the pump (see e.g. Ref. [33] or Ref. [24]). Approximating the pump intensity as constant and all waves as perfectly phase matched (which also requires them to be monochromatic), the amplification of the signal and the generation of the idler can be expressed as

$$A_s(z) = A_{s0} \cosh \kappa z \tag{3.15}$$

$$A_i(z) = \mathrm{i}\sqrt{\frac{n_s \omega_i}{n_i \omega_s}} \frac{A_p}{|A_p|} A_{s0}^* \sinh \kappa z \tag{3.16}$$

during the propagation along z with the coupling constant

$$\kappa = \frac{[\chi^{(2)}]^2 \omega_s^2 \omega_i^2}{k_s k_i c^4} \ |A_p|^2 \tag{3.17}$$

that is proportional to the intensity of the pump [24]. Fig. 3.1 illustrates the continuous generation of the signal and idler from the pump for two different pump intensities.

The first optical parametric oscillator (which is basically a self-seeded OPA) exploiting this process in continuous wave operation was presented by Giordmaine and Miller [34] in 1965. Thereafter OPA has been used extensively for frequency conversion purposes.

3.3 Noncollinear optical parametric amplifier

When using ultrashort pulses in the OPA process, more effects have to be taken into account. First, only one set of frequencies can be phase matched simultaneously and there will always be a remaining phase mismatch for all other frequencies in the broadband pulse. This results in a frequency-dependent parametric gain of the OPA. Second, and more importantly, group velocity dispersion (GVD) has the effect that pump, signal, and idler pulses all propagate through the medium at different velocities (see Fig. 3.2(a) for illustration). The difference in group velocity between the pump and the other two beams results in a maximum crystal length over which parametric gain can be achieved, namely the distance of propagation L_{sep} after which the pump and the signal (or idler) are spatially separated from each other. The difference in group velocity between the signal and the idler, on the other hand, (Fig. 3.2(b)) limits the amplification matching bandwidth because the bigger the difference between their frequencies is, the bigger the difference between their group velocities will be. (A quantitative treatment of this effect can be found in Ref. [33].)

While the problem of the limited interaction length of the pump and the generated light cannot be removed, there is a rather elegant way of making signal and idler appear having the same group velocity: It was first observed by the group of Hache that choosing an appropriate angle of noncollinearity Ψ between signal and pump allows a broader amplification bandwidth than that of collinear OPAs [35, 36]. Fig. 3.2(c) shows the geometry of such a noncollinear optical parametric amplifier (NOPA). The pump beam propagates through the medium at the phase matching angle θ with respect to the optical axis of the birefringent crystal. Usually the crystal surface is cut at this angle so that the pump impinges perpendicularly onto the surface. The angle of the seed with respect to the pump outside of the crystal is adjusted such that the internal angle between these two beams is equal to Ψ. The phase matching or momentum conservation condition then dictates the angle Ω at which the idler is generated. Since the $\vec{k}$ vectors of the signal vary in length with their respective frequencies the angle Ω is frequency dependent and the idler is emitted with angular dispersion. Choosing the noncollinearity angle Ψ gives an additional degree of freedom that can be used to effectively match the group velocities of signal and idler. Fig. 3.2(d) shows how the projection of the group velocity v_{gi} of the idler beam onto the propagation direction of the signal beam is equal to the group velocity of the signal and therefore these two pulses propagate at equal longitudinal

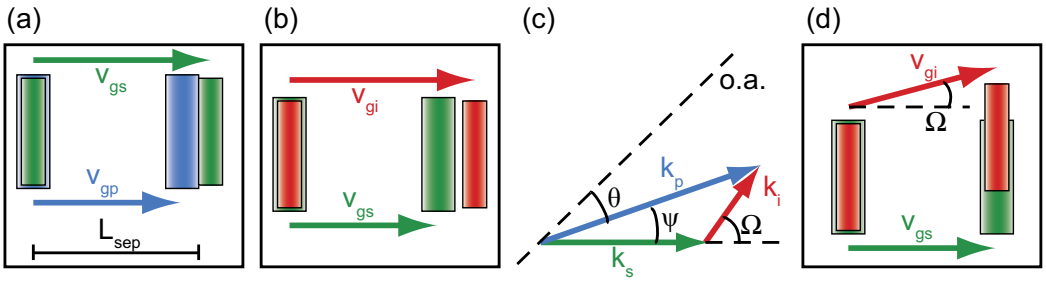

Figure 3.2: OPA and noncollinear OPA. **(a)** After propagating over a distance L_{sep} in the crystal the pump pulse is separated spatially from signal and idler, thus there can be no further parametric amplification. **(b)** Group velocity mismatch between signal and idler leads to separation of these two pulses in the material as well and effectively results in a limited phase matching bandwidth. **(c)** A noncollinear geometry allows broad phase matching: The pump propagates at a the phase matching angle θ with respect to the optical axis (o.a.) of the crystal. The seed (signal) propagates at the noncollinearity angle Ψ with respect to the pump. Conservation of momentum dictates the frequency-dependent angle Ω at which the idler is generated. **(d)** In a correctly chosen noncollinear geometry signal and idler propagate at the same longitudinal group velocity and overlap across the full length of the crystal.

(horizontal in the picture) speed throughout the crystal. Note that the lateral shift after traversing the crystal of length $\approx L_{sep}$ due to the vertical component between signal and idler is only on the order of a few tens of microns while the diameter of the beams is a few hundred microns.

From Fig. 3.2(d) it can easily be seen that for optimal group velocity matching

$$v_{gs} = v_{gi} \cos \Omega. \tag{3.18}$$

Within the approximation (good to 4%) that the refractive indices of the pump, signal, and idler are all equal [37] the angle of noncollinearity is given by

$$\Psi(\lambda_s) \approx \frac{\Omega(\lambda_s)}{1 + \frac{\lambda_i}{\lambda_s}}. \tag{3.19}$$

The condition in Eq. 3.18 for Ω can be rewritten in a more practical form that relates Ψ to the dispersive properties of the crystal [33]:

$$\Psi = \arcsin \left\{ \frac{1 - v_{gs}^2/v_{gi}^2}{1 + 2v_{gs}n_s\lambda_i/v_{gi}n_i\lambda_s + n_s^2\lambda_i^2/n_i^2\lambda_s^2} \right\}^{1/2}. \tag{3.20}$$

For the commonly used β-barium borate (BBO) with type I phase matching pumped at $\lambda_p = 400$ nm the angle Ψ for a (center) signal wavelength $\lambda_s = 600$ nm can be calculated as 3.7°. Furthermore, in the signal wavelength region from 500 nm to 700 nm Ψ varies only slightly between 3° and 4° and broadband phase and group velocity matching can be achieved in this region [38].

Given a spectrally broad source for the seed light, such as a supercontinuum generated in sapphire, the NOPA phase matching geometry can lead to amplified ultrabroadband

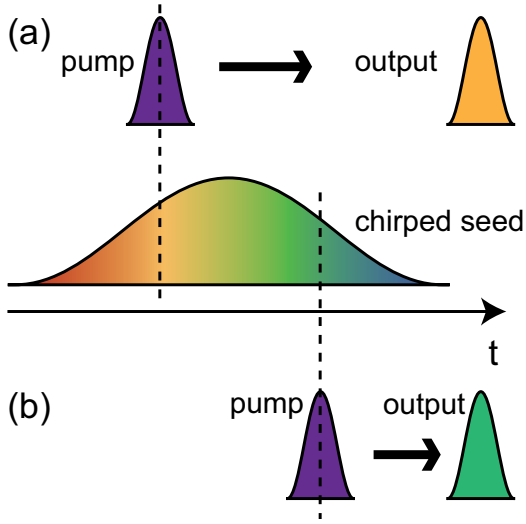

Figure 3.3: Frequency selection in OPA and NOPA. The supercontinuum that acts as seed is chirped (middle). **(a)** If the relatively short pump pulse comes at an early time, the red orange part of the seed frequencies is amplified. **(b)** If the pump pulse comes at later times, the blue/green parts of the seed spectrum are amplified.

pulses ranging from 480 nm to 750 nm. The lower wavelength limit results from the increasing dispersion of BBO in this region and the upper limit is due to degeneracy of the amplification process at 800 nm. However, this kind of bandwidth requires the signal and the pump to overlap completely. As illustrated in Fig. 3.3 chirped seed pulses can be used to tune the central wavelength of the NOPA by changing the time delay of pump and seed, thus changing the temporal overlap of the pump with different subsets of colors in the seed.

The first experimental realization of a NOPA was reported by the group of Riedle [38] in 1997. They created frequency-tunable 16 fs pulses of 11 μJ energy with a single stage NOPA. The theoretically attainable ultrabroadband spectra in the visible gave rise to many studies in different groups worldwide, seeking to broaden the NOPA output spectra and, with suitable compression methods, shorten the pulse duration more and more. By using reflective optics for manipulating (especially focusing) the seed light only and thus avoiding chirping the supercontinuum further Cerullo *et al.* [39] were able to compress the obtained broad spectra to $\approx$ 11 fs. In the group of Kobayashi a pulse-front matched geometry was employed to avoid spatial chirp or pulse front tilt [40–42] and Shirakawa *et al.* [43] were able to measure clean sub-10 fs pulses down to 6.1 fs. In the same group the temporal overlap of pump and seed pulses was further improved by precompressing the seed with chirped mirrors resulting in sub-5-fs pulses [44]. Fine tuning of the pulse phase using adaptive pulse compression with a deformable mirror pulse shaper following a grating compressor, Baltuška *et al.* were able to reduce the pulse duration to 3.7 fs [45, 46]; these represent the shortest NOPA pulses in the visible that have been reported so far. The latter experimental setup also used two sequential amplification stages that facilitated shaping of the spectral contents according to the principle sketched in Fig. 3.3. Other notable NOPA implementations were published by the groups of Miller [47], Cerullo [48, 49], and Wachtveitl [50].

3.4 Considerations and experimental design of NOPA

For the purposes of the present work, i.e., broadband 2D spectroscopy in the visible regime and quantum control, one has to consider a number of possibilities for the generation of the visible laser pulses with a NOPA. A reasonable compromise between day-to-day usability and extraordinarily broad spectra and short pulses has to be found.

3.4.1 Options for broadening the NOPA bandwidth

A number of techniques that modify the original simple NOPA design [38] in order to broaden the resulting spectra or shorten the visible pulses have been reported in the literature.

Temporal pump–seed overlap: seed compression

As described in section 3.3 (Fig. 3.3) the temporal overlap of pump and seed pulses in the BBO crystal largely determines the amplified spectrum if the optimal angles for phase matching and group velocity matching are met. Since the seed white light continuum is chirped [51] and the spectral components of interest here (500 – 750 nm) are estimated to extend over a time period of $\approx$ 500 fs, one option to increase the temporal pump–seed overlap is to (pre)compress the seed pulses before sending them to the amplification stage. This has been done using chirped mirrors [44] or a prism compressor [46]. A pair of chirped mirrors must match the dispersion to be compensated by design, i.e., the phase after a certain number of reflections off the mirrors must be equal to the inverse of the phase to be compensated and there is not much flexibility in the phase curve after the mirrors have been produced. With a prism compressor on the other hand it is possible to influence the temporal frequency sweep of the seed pulses so that the amplified frequency range in the NOPA process can be chosen. In the commonly used two-stage setup the amplification can be chosen for each NOPA stage separately, e.g., the wings of the seed spectrum or the central part can be amplified, and an optimally broad output spectrum can be achieved by balancing the amplified spectra of both stages carefully [46]. This situation is illustrated schematically in Fig. 3.4. The graph on the left shows the group delay of the seed pulses (e.g. after passing through a prism compressor with only some residual higher order phase on the pulses). In a two stage NOPA the two pump pulses can be delayed such that they overlap with the wings and the center of the spectrum and the respective resulting amplified spectra are depicted on the right hand side. Fig. 3.5 shows the experimental realization of this frequency selection. The amplified spectra of one stage were recorded at two different delay times of the UV pump pulse with respect to the seed pulses that passed through a prism compressor (see section 3.4.2). The fact that the extreme wavelengths are amplified at one delay position (dashed line) and the center wavelengths at the other (solid line) demonstrates that the group delay of the precompressed seed pulse indeed follows a curve as it is depicted on the left hand side of Fig. 3.4.

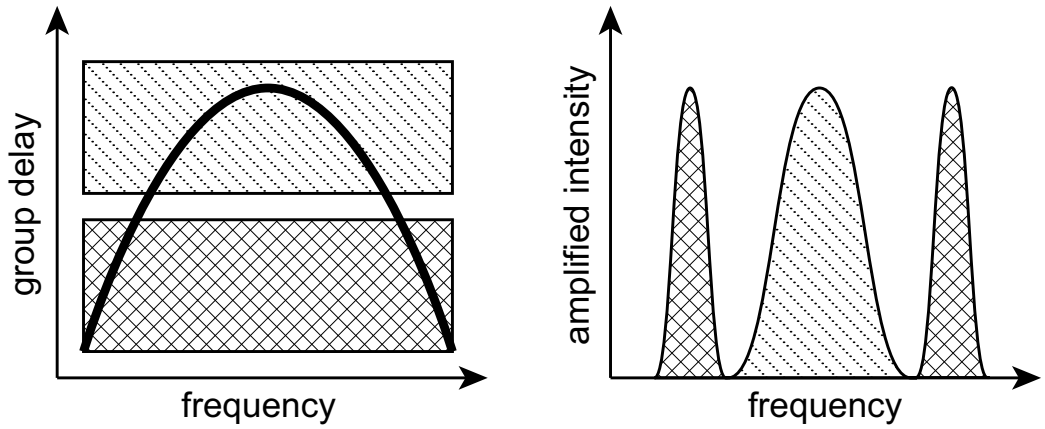

Figure 3.4: Temporal overlap of NOPA seed and pump pulses and resulting amplified spectra. **Left:** The thick line represents an exemplary group delay of the seed light. In a two stage NOPA the two pump pulses (indicated by the two hatched areas) are delayed so that they overlap with different spectral regions. **Right:** The resulting amplified spectra are sketched as hatched areas. While the cross-hatched pump pulse amplifies the wings of the seed spectrum only, the diagonally hatched pump amplifies the center part of the spectrum. (Note that this is a strongly simplified sketch and in an experiment one would make the pump pulses, and therefore the amplified spectra, overlap.)

Temporal pump–seed overlap: pump stretching

Conversely, to increase the temporal overlap of pump and seed it is also possible to stretch the pump pulses. The material dispersion of a long glass rod is sufficient to lengthen (and chirp) the pump pulses to a few hundred femtoseconds. However, one has to take care that the used material is suitable for high intensity UV pulses at 400 nm because many highly dispersive types of glasses exhibit strong absorption (also multiphoton absorption) and fluorescence upon irradiation with 400 nm pulses from a femtosecond laser and are also easily destroyed. Fused silica is the best suited material for our purposes and shows only minimal fluorescence. Knowing the bandwidth of the 400 nm pump pulses (≈ 4 nm), the pulse duration as a function of length of the rod can simply be calculated through a numerical simulation using the Sellmeier coefficients [52] for fused silica. Some rod lengths and their corresponding pulse durations are listed in table 3.1. The optimal glass length must be chosen such that the pump and seed pulse durations match best.

rod length (cm)	0	1	3	5	10	15	20
pulse duration (fs)	78	85	129	189	323	522	694

Table 3.1: Calculated pump pulse durations (full width at half maximum) after passing through a glass rod. The numerical simulations were performed with the refractive indices of fused silica gained through the Sellmeier equation and the pulses were assumed to be of transform-limited, Gaussian shape before passing through the material.

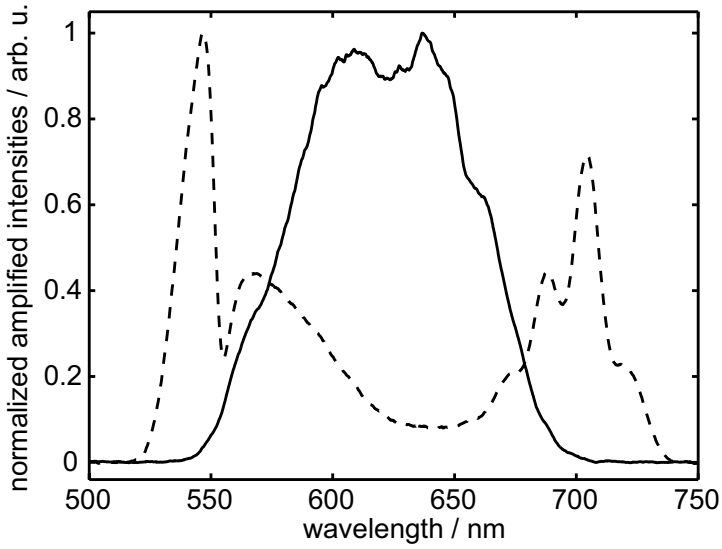

Figure 3.5: Frequency selection with precompressed seed pulses. The NOPA pump pulses can be set at a time delay such that the center part of the spectrum is amplified (solid line) *or* such that the extreme wavelengths are amplified (dashed line). See text and Fig. 3.4 for explanation.

Pulse front matching

The first sub-5-fs pulses in the visible were achieved in a NOPA that made use of pulse front matching [43, 44]. Due to the noncollinear geometry of a NOPA, the seed pulses have a pulse front tilt after entering the crystal. Shirakawa *et al.* have shown that it is possible to counteract the resulting pulse front mismatch between the pump and the signal in the NOPA crystal by tilting the pulse front of the pump accordingly. The internal tilt angle between pump and seed corresponds to the angle of noncollinearity $\Psi = 3.7°$. A prism in the beam path of the pump and focusing optics or a telescope can provide the right pulse front tilt in front of the NOPA crystal such that the pulse fronts will match inside the crystal.

This addition to a standard design NOPA adds significant complication. The angles and distances for the additional optics in the pump beam have to be calculated and aligned precisely. In multistage NOPAs the pulse front matching condition must be ensured for each stage separately, therefore the tilting setup takes away from the flexibility and complicates day-to-day alignment of the NOPA. Furthermore, when using relatively small beam diameters at the nonlinear crystal, the pulse front mismatch is less pronounced [37]. This is why for our purposes the pulse front matching has been omitted in the present design of our NOPA.

Angular dispersion of pump

The phase matching angle θ for OPA in a noncollinear geometry at $\Psi \approx 3.7°$ is almost constant over a wide range of signal frequencies. Nevertheless there is some residual variation of θ for the different frequencies in the pump pulse. Introducing a prism into the pump beam before focusing it onto the NOPA crystal allows an adjustment of the angle of incidence for each pump frequency such that the entire bandwidth (particularly the amplification of the wings) is maximized [45, 46]. However, as with the pulse front matched geometry, this addition to a NOPA must be considered carefully, as it takes

away from the flexibility and adds complications in multistage setups.

3.4.2 Experimental setup

All the options for generating extremely broad spectra presented in section 3.4.1 were considered thoroughly. For reasons of day-to-day usability the best compromise was found to be a NOPA setup that includes pump stretching as well as white-light seed precompression but omits angular dispersion and pulse front matching of the pump.

Fig. 3.7 shows a sketch of the setup. The entire NOPA is pumped by $\approx 500\ \mu$J, 800 nm pulses at 1 kHz with the electric field vector polarized parallel to the breadboard/drawing plane. The incoming beam is split into two parts: 10% is used for supercontinuum generation in a 2 mm sapphire plate cut at $\theta = 0^\circ$ (c-cut) and 90% is sent to a frequency doubling crystal (BBO) to generate the 400 nm pump pulses.

The fraction for continuum generation is further attenuated by a variable wheel and the beam is clipped by an aperture in front of the 5 cm focusing lens. These additional degrees of freedom, choosing the clipping by closing or opening the aperture and increasing or decreasing the attenuation via the filter wheel allow to create a white light beam of high spatial mode quality, which is essential for a good NOPA output. To avoid astigmatism the seed beam is recollimated and reflected off a spherical mirror ($f = 5$ cm) at a shallow angle. Precompression and dispersion management of the seed beam is accomplished using a prism compressor built with fused silica prisms with 69.1° apex angles and 69 cm prism separation. The first prism is mounted on a micrometer stage so that material dispersion can be added or subtracted by translating it in and out of the beam. Furthermore, the spatially dispersed colors at the symmetry mirror of the prism compressor can be used to tailor the bandwidth of the seed and suppress the remaining fundamental light. Simply inserting a blackened piece of metal on either side of the spectrum can block the unwanted frequency components. A polarization rotating periscope is used to adjust the polarization of the seed so that its electric field vector is perpendicular to the drawing plane or the surface of the breadboard. This way it is possible to keep all beams around the NOPA crystals in one plane and no vertically inclined beams are necessary. Tuning of the noncollinearity angle is thus simplified and dangerous stray beams are avoided. The external angle of noncollinearity $\Psi_{ext} = 6.4^\circ$ of the seed with respect to the pump and the seed–pump overlap is adjusted via the two mirrors in front of the BBO crystal. The seed recollimation mirror is mounted on a micrometer stage and it is slightly detuned from actual collimation so that a long and loose focus is located in the crystal of the first NOPA stage.

The major fraction of the 800 nm light is sent to a 0.6 mm thick type I BBO crystal cut at 29.2°. The unfocused geometry results in a frequency-doubling yield of $\approx 15\%$ and 400 nm pump pulses of 70 μJ energy [53]. Due to the relatively small phase matching bandwidth of the 0.6 mm crystal the angle must be adjusted carefully and the compression of the 800 nm pulses must be optimal. Both the crystal angle and the 800 nm pulse compression should be attended to when starting the NOPA alignment because the pulse shape of the 800 nm pump will affect the white light generation as well as the seed dispersion. The UV light passes through a fused silica (Schott Lithotec SQ1) glass rod of 10 cm length to stretch the pump pulses (see also table 3.1). Before splitting

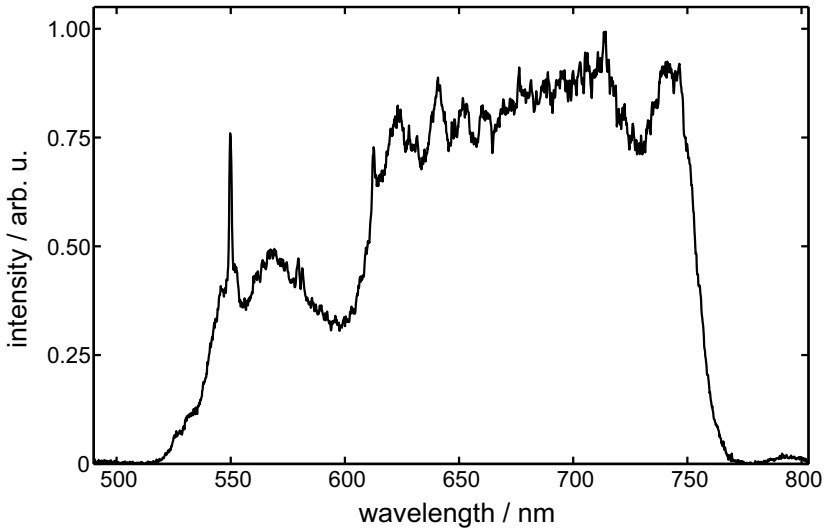

Figure 3.6: Broad amplified NOPA spectrum with a pulse energy of about 4.6 μJ. The narrow peak at 550 nm is due to stray light from the fluorescent room lighting.

the pump pulses into two fractions of 35% and 65% for the first and second NOPA amplification stage respectively, the polarization is rotated with a $\frac{\lambda}{2}$ wave plate to be parallel to the breadboard. For both amplification stages the pump beams are focused with 15 cm lenses. The BBO crystals are not placed at the exact focus of these beams, but a few millimeters behind the focus, thus the intensity at the crystals is well below their damage threshold and the diverging beam minimizes disadvantageous self focusing effects in the BBO [39, 54].

Amplification in the first NOPA stage yields pulses of about 1.5 μJ. Typically, in broadband operation, the time delay of the pump pulses in the first stage is adjusted so that the wings of the seed spectrum are amplified (see cross-hatched areas in Fig. 3.4). Then the amplified pulses are imaged from the first NOPA stage crystal into the second stage crystal via a 12.5 cm focal length mirror and a folding mirror. As in the first stage the combination of these two mirrors allows adjusting the angle of noncollinearity between seed and pump in the second stage. Here the pump pulse delay is typically set so that the central part of the spectrum is amplified. After the second stage the pulse energy can be up to 10 μJ, depending on the bandwidth and/or spectral shape. A broad spectrum with 4.6 μJ energy is shown in Fig. 3.6. Finally, a spherical mirror of 25 cm focal length collimates the NOPA output and the beam is directed to the compression setup. The pulse duration at this stage is about 800 fs.

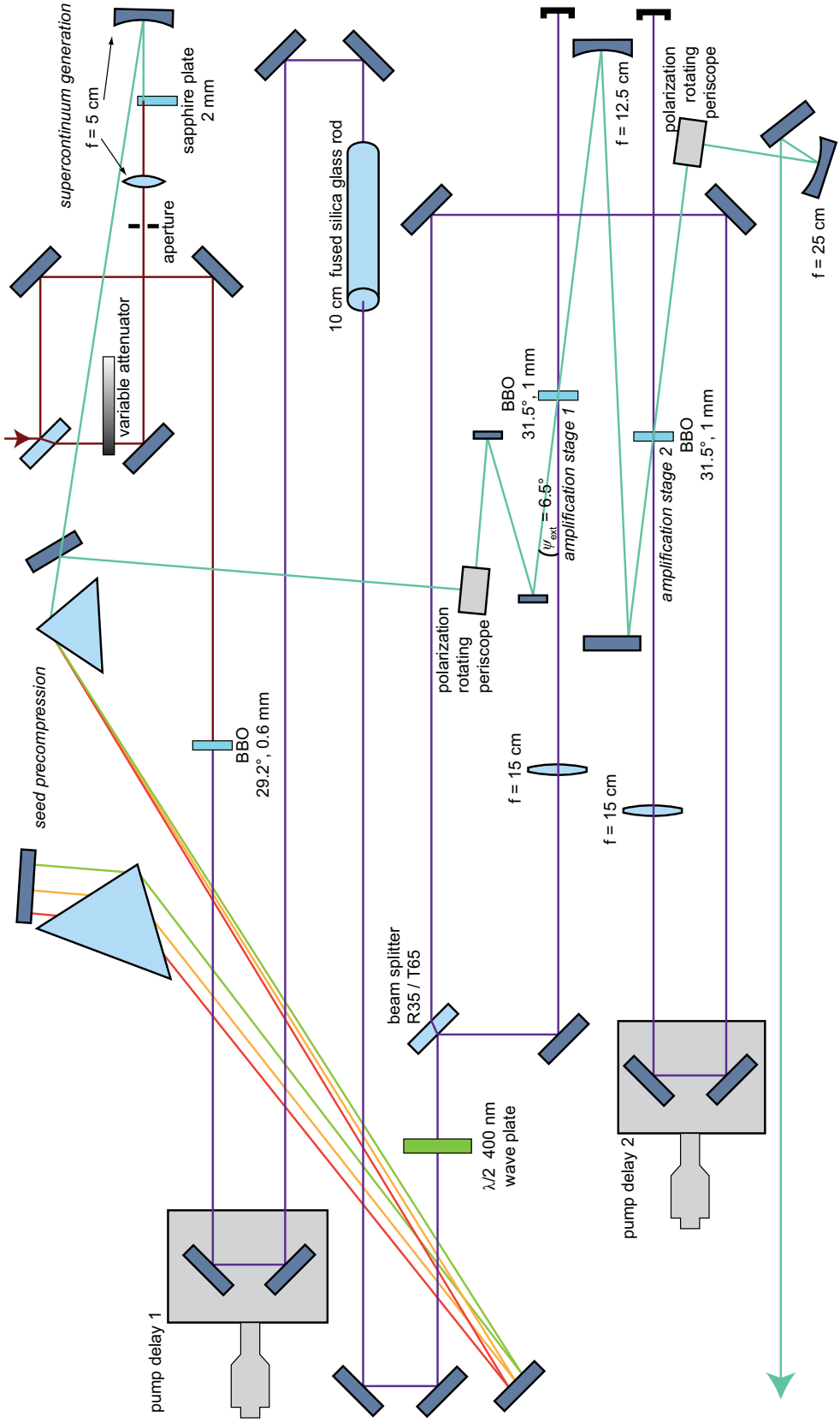

Figure 3.7: Experimental NOPA setup. A white light supercontinuum is created and precompressed. The 800 nm pump light is frequency-doubled to 400 nm and delayed. The polarizations of both, seed and pump beams are adjusted. Amplification takes place in a two stage setup in two separate BBO crystals with imaging optics for the (preamplified) seed beam and an additional variable delay for the second pump beam. The entire setup is built on a 45 × 80 cm^2 breadboard.

3.5 NOPA pulse characterization

For the use in any experiment, a knowledge of the temporal structure of the visible pulses generated by the NOPA is essential. Further, any pulse compression, i.e., the reduction of the pulse duration to the Fourier limit, also requires a means for pulse characterization. There are many established methods of pulse characterization for different spectral regimes, pulse durations, and energies.

However, with ultrabroadband NOPA pulses only a few of the standard methods can be used. If only the time duration is to be determined, a simple nonlinear autocorrelation (with a suitable nonlinearity) can be employed. To determine the phase and thus the full temporal structure of the NOPA pulses two general methods can be applied: spectral interferometry for direct electric field reconstruction (SPIDER) and frequency-resolved optical gating (FROG).

SPIDER and its derivatives have been used for NOPA pulses mostly by the groups of Cerullo [49] and Riedle [55, 56]. The method is based on the spectral interference of two time-delayed pulse copies with a spectral shear created by sum frequency mixing with the different spectral components of a very long, chirped pulse [57]. SPIDER retrieves the spectral phase of the laser pulses in a non-iterative way and can be used in real-time, e.g. for constantly monitoring the pulses used in an experiment. Since it is an interferometric technique, however, SPIDER is not sensitive to spatial distortions of the ultrashort laser pulses. Even in the presence of spatial chirp, angular dispersion, or pulse front tilt SPIDER can yield results resembling those of a perfectly short and compressed pulse shape.

FROG has been used for the characterization of NOPA pulses by many groups as well [58, 59]. As the name already implies FROG [60] is a derivative of optical gating, i.e. nonlinear auto- or cross-correlation, with the difference that the signal is spectrally resolved. Therefore the FROG data or "FROG trace" corresponds to a spectrogram $S(\omega, \tau)$ of the electric field $E(t)$ with an unknown gate function $G(t)$

$$S(\omega, \tau) = \left| \int_{-\infty}^{+\infty} E(t)\, G(t-\tau)\, \mathrm{e}^{-\mathrm{i}\omega t}\, \mathrm{d}t \right|^2 . \tag{3.21}$$

There are a number of different subtypes of FROG that are mostly termed according to the type of nonlinear process they exploit as gate, e.g. second harmonic generation (SHG FROG), polarization gating (PG FROG), transient grating (TG FROG), third harmonic generation (THG FROG), or self diffraction (SD FROG) [61, 62]. Common to all FROG types is the iterative reconstruction algorithm that finds the electric field that would create the measured FROG trace [63].

It is worth mentioning that FROG is sensitive to spatial distortions of the input pulses and that these distortions can even be measured using FROG [64, 65]. This is especially interesting if pulses are to be characterized that will be used for nonlinear spectroscopy experiments. The FROG measurement can then be taken *in* the same spectroscopy setup. The experimenter then gains insight into not only the temporal structure of the pulses (amplitude and phase) but also if there is spatio-temporal distortion present at the position where the spectroscopy measurement is made. For example, the trace of

an SHG FROG must be perfectly symmetric with respect to $\tau = 0$, if this is not the case and the setup is otherwise perfectly aligned, spatial chirp or angular dispersion can be the reason for the signal distortion and the quality of the light source needs to be improved.

Two FROG methods that are suitable for visible NOPA pulses and that were used in this work are presented in the following sections: SHG FROG and TG FROG.

3.5.1 Second harmonic generation frequency-resolved optical gating

SHG FROG has been shown to be a viable characterization method for very broadband pulses approaching the single cycle regime. The method has been applied to fiber-compressed Ti:Sapphire oscillator pulses [66] as well as supercontinuum pulses centered around 800 nm [67]. Closely related to the purposes of this work, Ref. [46] reports on the characterization of visible NOPA pulses centered around 600 nm.

SHG FROG makes use of the cooperative SHG (or perhaps more precisely the SFG) of two time-delayed pulse replica. The probe and the gate pulses are identical in this setup and the signal spectrogram is given by

$$S_{\mathrm{SHG}}(\omega,\tau) = \left| \int_{-\infty}^{+\infty} E(t)\; E(t-\tau)\; \mathrm{e}^{-\mathrm{i}\omega t}\; \mathrm{d}t \right|^2 . \tag{3.22}$$

The signal can easily be measured in a noncollinear two-pulse setup, such as that used for pump–probe or transient absorption measurements, without the need to add additional optics or delay lines. For this reason and, in order to characterize the pulses *in situ* for some of the experiments presented in this thesis, the FROG measurements were taken in the 2D spectroscopy setup (see section 4.4.2) using beams number 1 and 2.

A few peculiarities with respect to SHG FROG arise from the fact that we attempt to characterize ultrabroadband visible pulses. In general, the SHG medium should be phase matched for the full bandwidth of the measured pulses. If this is not the case the actual FROG signal can be written as

$$S_{\mathrm{measured}}(\Omega,\tau) = R(\Omega)\; S_{\mathrm{SHG}}(\Omega,\tau) \tag{3.23}$$

where $S_{\mathrm{SHG}}(\Omega,\tau)$ is the ideal FROG signal at frequency Ω and time delay τ and

$$R(\Omega) = Q(\Omega)\; \frac{\Omega^3}{n_e(\Omega)} \left[(n_e^2(\Omega)-1)(n_o^2(\Omega/2)-1)^2\right]^2\; \mathrm{sinc}^2\left(\frac{\Delta k(\Omega/2)L}{2}\right) \tag{3.24}$$

is the spectral filter function that alters the measured FROG trace [66]. Here, $Q(\Omega)$ is the spectral sensitivity of the detector (spectrometer + CCD array), n_o and n_e are the refractive indices of the SHG crystal, L is the crystal length, and

$$\begin{aligned} \Delta k(\Omega/2) &= 2k(\Omega/2) - k(\Omega) \\ &= 2\frac{n_o\left(\frac{\Omega}{2}\right)\frac{\Omega}{2}}{c} - \frac{n_e(\Omega,\theta)\Omega}{c} \\ &= \frac{\Omega}{c}\left[n_o\left(\frac{\Omega}{2}\right) - n_e(\Omega,\theta)\right] \end{aligned} \tag{3.25}$$

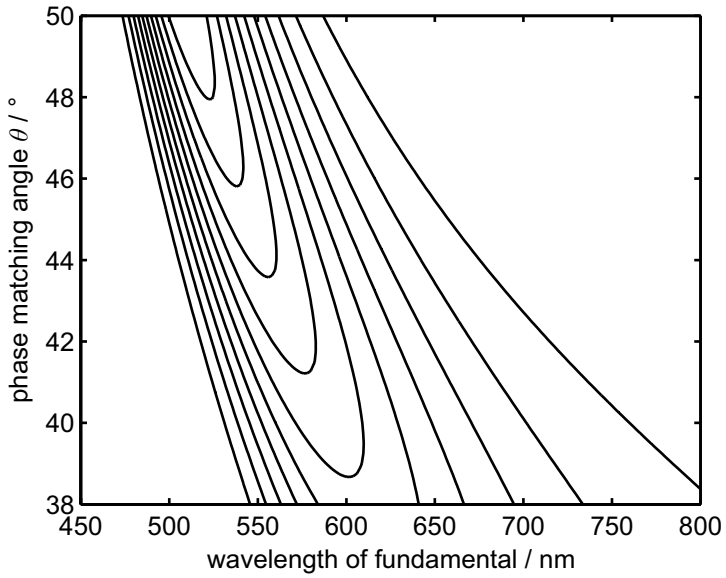

Figure 3.8: Contour plot of filter function $R(\Omega)$ (see Eq. 3.24) as a function of the fundamental wavelength $\lambda = 4\pi c/\Omega$. The second order response of BBO and the spectrometer sensitivity are assumed to be spectrally uniform ($Q(\Omega) \equiv 1$). Equidistant contour lines are drawn from 9% to 91% of the maximum which is located at 515 nm and 50° in this graph.

is the wave vector mismatch in (approximate) collinear type I phase matching. The sinc^2 factor of Eq. 3.24 thus represents the phase-matching-governed part of the SHG efficiency, while the remaining factors are due to the frequency-dependent emission of the second order nonlinear polarization as well as the different spot sizes of the different frequencies in focused geometry [67].

The filter function Eq. 3.24 of a $L = 10$ μm thin BBO crystal is shown as a function of wavelength of the fundamental and of the phase matching angle in Fig. 3.8. It is clear that for NOPA pulses of broad bandwidth this filter will have a significant impact on the FROG trace. Note that due to factors such as dispersion of $n(\omega)$ and the Ω^3 dependence, the slope of $R(\Omega)$ with respect to the wavelength is far less pronounced in the red part of the fundamental spectrum. Especially when tuning the phase matching angle to be optimal for shorter wavelengths (increasing θ) the effective SHG phase matching bandwidth narrows. Therefore an SHG FROG characterization of visible pulses is more difficult compared to an SHG FROG of pulses centered around 800 nm, the Ti:Sapphire central wavelength.

Within the approximations [67] the filter $R(\Omega)$ only affects the frequency dimension of the measured spectrogram (Eq. 3.23) and it is therefore possible to correct the measured FROG trace numerically (scale the measured "single frequency autocorrelation") at each frequency Ω if $R(\Omega)$ is known quantitatively. This has been done in Refs. [66, 67] and allows additional validation of the experimental FROG trace by comparing the frequency marginal to the autoconvolution of the linear spectrum. However, this kind of correction requires a quantitative knowledge of the filter $R(\Omega)$ which can be hard to obtain. In particular, measuring the angle to which the SHG crystal is tuned can be non-trivial.

Another way of compensating for $R(\Omega)$ is through the comparison of the frequency marginal of the measured FROG trace with the autoconvolution of the fundamental spectrum. If one is certain that the experimental setup is aligned well, i.e., all signal frequencies are observed, $R(\Omega) \neq 0$ for all signal frequencies, the intensities are not too

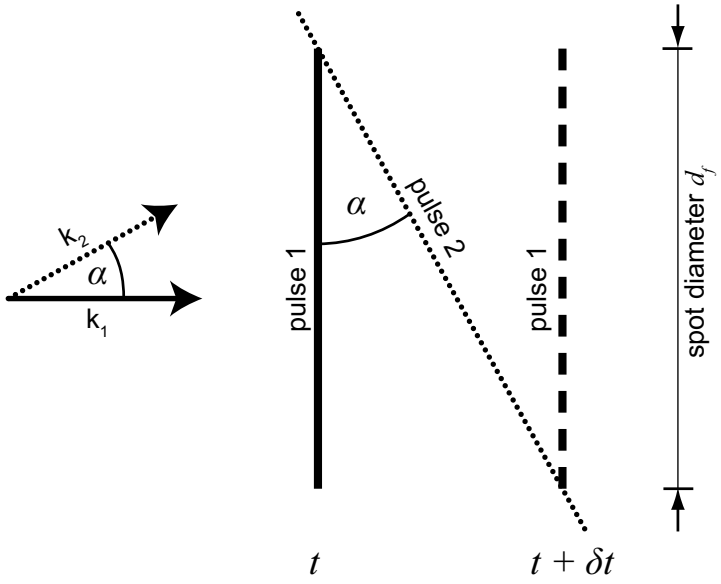

Figure 3.9: Temporal smearing occurs because of noncollinear beam crossing in the focus. Two beams propagate and intersect at an angle α as shown on the left. As pulse 1 is delayed with respect to pulse 2 they overlap with each other during a period of time δt.

high, etc., the FROG trace may be scaled. For this purpose a fundamental spectrum is measured separately and the redundancy of information contained in the FROG trace can be used by scaling each frequency to be equal to the autoconvolution of the fundamental spectrum. The commercial electric field reconstruction software used in our laboratory, FROG 3.2.2 [68], provides this option in a convenient way. It accepts both the FROG trace and the fundamental spectrum, compares them, and applies the correction as described. Even though this procedure prevents FROG trace validation through marginal comparison, after reconstruction of the electric field in amplitude and phase the FROG error can provide a measure for how well the reconstructed trace agrees with the measured (and scaled) trace. If this error is small one should compare the reconstructed spectrum with the fundamental spectrum. The agreement between these two is strong evidence that the measurement, the correction, and the electric field reconstruction were carried out correctly.

So far the filter function $R(\Omega)$ has only been treated in collinear approximation here, and this is sufficient to describe the effects incorporated in Eq. 3.23. An effect inherent to the noncollinear autocorrelation however is the so-called temporal smearing caused by the intersection of the short pulses in the SHG crystal at a finite angle α and their finite spot diameters d_f [69]. The geometry is sketched in Fig. 3.9. Even for an infinitely short pulse the spatial overlap of the two pulses leads to a time period δt during which a nonlinear, cooperative signal is generated by both pulses. Within the small angle approximation δt can be expressed as

$$\delta t = \frac{d_f \alpha}{c} \tag{3.26}$$

where c is the speed of light. In case when the two pulses are initially parallel to each other with a distance d and a beam diameter x, and are then focused by a common optic

of focal length f, the temporal smearing can be written as

$$\delta t = \frac{4\lambda d}{\pi x c} \tag{3.27}$$

within the small angle approximation [70]. If the beams are as close as possible to each other in front of the focusing optic (the distance d between their centers is equal to their beam diameters x), Eq. 3.27 simplifies to

$$\delta t = \frac{4\lambda}{\pi c}. \tag{3.28}$$

Interestingly this is independent of the focal length and therefore constitutes a fundamental limit for the time resolution that applies to all nonlinear spectroscopies, pulse characterizations etc. carried out in a noncollinear geometry.

Assuming both a Gaussian beam profile in the focus and a temporal Gaussian pulse shape of duration τ_{real} the measured effective duration is given by

$$\tau^2_{\mathrm{measured}} = \tau^2_{\mathrm{real}} + \delta t^2. \tag{3.29}$$

The limit δt itself is rather low: it is only 0.4 fs at $\lambda = 800$ nm. Nevertheless, the technically challenging task in the laboratory is bringing the beams as close together as possible without causing any clipping or diffraction, while still being able to adjust the overlap in the interaction region. Therefore in most experiments the distance d and angle α between the beams, and thus the temporal smearing, is much bigger than stated by Eq. 3.28. The problem can be overcome by using a pulse-front matched setup which is easiest to implement with diffractive optics. However, this solution cannot be applied to any kind of setup without considerable effort. Usually, one merely tries to minimize the effects by choosing small angles. Temporal smearing due to the noncollinearity of the interacting beams is an issue that one has to be aware of.

3.5.2 Transient grating frequency-resolved optical gating

TG FROG is a pulse characterization method that overcomes the problem of phase matching that exists with SHG FROG. It makes use of a $\chi^{(3)}$ process known as transient grating where two temporally coincident pulses that intersect at an angle create a phase grating in a $\chi^{(3)}$ medium and a third, time delayed pulse is diffracted off this grating [71]. Phase matching in this case is simply accomplished by selecting the signal detection direction as $\vec{k_s} = -\vec{k_1} + \vec{k_2} + \vec{k_3}$, where $k_{1,2,3}$ are the wave vectors of the three incident beams (all involved frequencies are equal to the fundamental frequency).

The TG FROG trace takes the mathematical form of the trace of a PG FROG

$$S_{\mathrm{TG}}(\omega,\tau) = \left| \int_{-\infty}^{+\infty} E(t)\ |E(t+\tau)|^2\ \mathrm{e}^{-\mathrm{i}\omega t}\ \mathrm{d}t \right|^2. \tag{3.30}$$

with only an additional reversal of the time delay τ [71]. Thus, the electric field of a TG FROG can also be reconstructed with the commercial software, using the algorithm

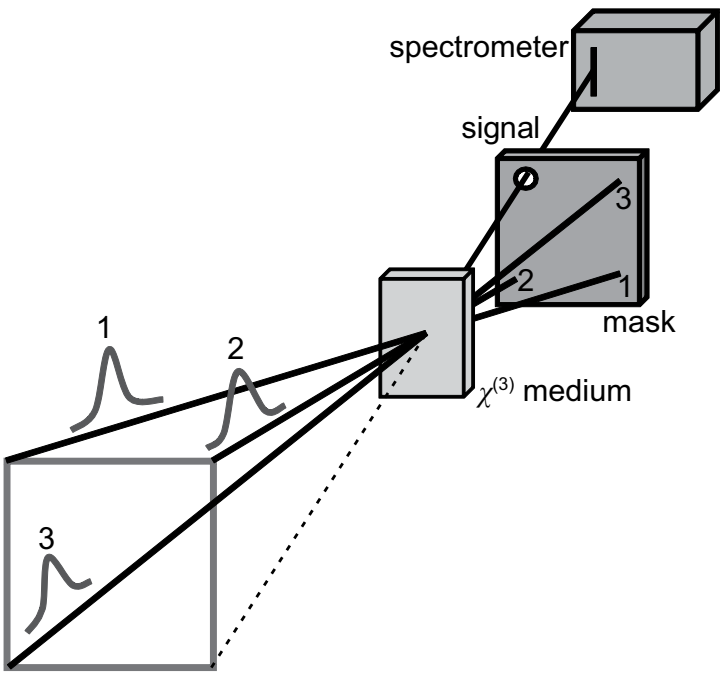

Figure 3.10: Measurement geometry for TG FROG. Three beams start on three corners of a square and converge onto the same spot in a transparent medium where the temporally coincident pulses 1 and 2 create a transient phase grating. Pulse 3 is time delayed with respect to 1 and 2. A signal is generated in the direction of the fourth corner of the square. A mask spatially filters this signal from stray light and a spectrometer records it.

for PG FROGs. Then the reconstructed E-field needs to be reversed in time once. Nevertheless, TG FROG has the advantage of an unambiguous time direction over SHG FROG.

Typically the TG signal is measured in a box geometry shown in Fig. 3.10. The setup for two-dimensional spectroscopy (see section 4.4.2) can easily be used for TG FROG measurements and the built-in positioners can provide accurate time delays. Before conducting an actual TG FROG measurement the zero delay positions for all three pulses have to be found. A two-dimensional scan of the total TG signal as a function of the two delays between the three pulses is performed. The maximum of the total signal indicates the best temporal overlap between all pulses and determines the zero delay positions.

The nonlinear medium can consist of any amorphous or crystalline material, with the condition that the $\chi^{(3)}$ response is instantaneous, i.e., the material is perfectly transparent at the wavelengths that are to be measured. The nonlinear material should also be thin so that the signal is generated before material dispersion due to the propagation through the medium broadens the pulses significantly, thereby distorting the FROG trace. Since the nonresonant $\chi^{(3)}$ process intrinsically yields low signal intensities, relatively high pulse energies compared to other pulse characterization methods, like for instance SHG FROG, have to be employed in TG FROG. Another result of the low signal intensities is the requirement to eliminate practically all scattered light which interferes with the FROG signal and therefore cannot easily be removed from the FROG trace. Thus the optical surfaces of the medium must be of excellent quality.

3.6 Compression and shaping methods for NOPA pulses

The NOPA output pulses are not transform-limited and, in order to achieve the shortest possible pulses or to have the "raw material" for complex shaped pulses, a compression setup needs to be implemented.

This section will discuss a number of techniques that can be employed to compress or shape visible NOPA pulses. The goal of a pulse compression is to achieve a transform-limited pulse at the sample position of the experimental setup by means of dispersion management, i.e., introduction of the right amount of dispersion to compensate for the phase on the input pulses. Pulse shaping on the other hand describes the creation of potentially complex temporal phase and amplitude evolutions of the electric field, ideally also at the position of the sample. Therefore any means of pulse shaping can also be used as a means of pulse compression when an appropriate amount of phase is imprinted onto the input pulses. Thus, the terms "pulse shaping" and "pulse compression" are interchangeable to a certain extent.

The temporal structure of the straight NOPA output is determined by the initial chirp of the white light continuum and the sum of the dispersion introduced by the optical elements in the NOPA, i.e., the prism compressor, the two amplification stages in the BBO crystals, and the air through which the pulses propagate. For a suitable compression setup one must compensate not only for dispersion of these aforementioned elements but also for the dispersion of the beam path to the sample in an experimental setup (like 2D spectroscopy). For instance an autocorrelation measurement[1] in the 2D setup revealed a pulse duration of $\approx$ 400 fs and the dispersion has to be compensated correspondingly; group delays of up to a few hundred femtoseconds over the NOPA bandwidth have to be compensated.

3.6.1 Grating compressor

The grating compressor as introduced by Treacy [72, 73] is, alongside the prism compressor, the most common compression method in ultrafast laser technology, especially after chirped pulse amplification. With respect to their use for NOPAs however there are a number of disadvantages. While in typical setups and applications grating compressors can easily introduce group delays of tens to hundreds of picoseconds, for a visible NOPA the required group delays are orders of magnitude smaller. Furthermore, in a Treacy-type grating compressor four reflections off a grating are necessary. This reduces the overall efficiency of the compressor to a maximum of around 70% when extremely good gratings are used. Probably the biggest issue when using gratings for the compression of NOPA pulses is the limited bandwidth of diffraction gratings. Even the custom designed volume phase holographic gratings for use with the NOPA pulse shaper (see section 3.7.2) have a nonuniform efficiency over the bandwidth of the NOPA pulses (see also Fig. 3.15). The efficiencies at the edges of the NOPA bandwidth are $\approx$ 75%

[1] The piezo actuators in this setup can only introduce a limited delay so that the autocorrelation is truncated at the edges. Due to this incomplete measurement, the data is not shown here. However, since the data are background-free, the FWHM duration of the input pulses can be estimated to be around 400 fs. Pre- or post-pulses are also evident.

compared to ≈ 90% at the center of the spectrum. Therefore, after four reflections the wings of the spectrum would be significantly suppressed with respect to the center wavelengths (32% vs. 66% effective throughput); this would result in a reduction of the NOPA bandwidth.

3.6.2 Prism compressor

Prism compressors [74] on the other hand do not alter the spectral contents of the input pulses and they have a nearly 100% throughput efficiency if Brewster prisms are used. The introduced group delay can be adjusted by selecting the separation of the prisms and by selecting an appropriate prism material.

However, a constant drawback of prism compressors in general is the fact that they introduce a fairly high amount of third order phase (which corresponds to the curvature of the group delay). In contrast, the experimenter in the laboratory usually wants to compensate the dispersion from passing through bulk (glass) material and the third order component of this dispersion is comparably small. Fig. 3.11 illustrates this situation: the group delay of a prism compressor made of fused silica prisms at a distance of 1 m from each other was simulated using the optical path differences calculated from geometric optics considerations (solid line). It is obvious that the delay for the red part of the NOPA spectrum is almost constant whereas the delay curve has a substantial slope on the blue part. This nonlinear behavior can be understood in the following simple picture: due to the nonlinear material dispersion the first prism introduces much more angular dispersion for the blue components and the second prism "amplifies" this effect by letting the blue frequencies pass through even more material. Therefore this fairly big effect of higher order phase distortion is inherent to prism compressors. In fact, higher dispersive prism materials can only increase the higher order components of the introduced group delay.

As an example for material dispersion compensation, Fig. 3.11 shows the inverse of the group delay introduced by passing through 2 cm of fused silica as dashed line. Note that the material causes mostly linear group delay. While at edges of the spectrum the group delay is well compensated (the two lines are close to each other), the center of the spectrum cannot be compressed with a prism combination.

In its current configuration the NOPA includes a prism compressor for precompression of the seed light. As a result the seed pulses have a mostly parabolic group delay as sketched in Fig. 3.4 left. Thus, using a prism compressor for the compression at the sample position of an experiment is not a viable option because this would only increase the third order phase distortion further.

3.6.3 Chirped mirrors

Chirped mirrors [75] have been used by a few groups as an exclusive means for compression of NOPAs [49, 55, 76, 77] or also in combination with other pulse compression methods [46, 47, 58]. These dispersion compensating mirrors have to be custom-designed according to the exact compression requirements in a particular setup. In general ultrabroadband chirped mirrors can support the bandwidths of visible NOPA pulses, however,

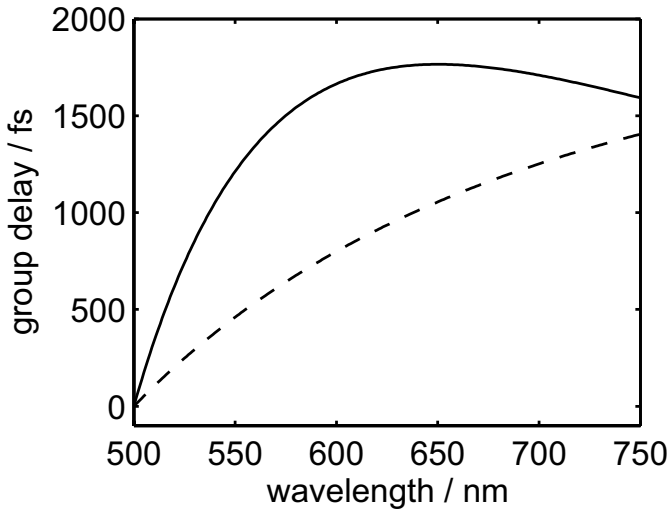

Figure 3.11: Group delay of a prism compressor. The group delay over the NOPA bandwidth was calculated for fused silica Brewster prisms at 1 m separation (solid line). For comparison the group delay introduced by 2 cm fused silica bulk material is plotted with reversed sign (dashed line). The prism compressor introduces much more nonlinear group delay than what needs to be compensated.

only about 40 fs group delay per reflection of such a mirror were accomplished in designs up to date. Therefore 10 to 30 bounces have been used in applications of chirped mirrors to NOPA pulse compression. If the experimental conditions change, i.e. the dispersion the pulses collect in the setup becomes different, only a different number of bounces can help to compensate for the change. Alternatively chirped mirrors can be used in combination with a flexible compression technique like a pulse shaper.

3.6.4 Detuned zero dispersion compressor

A $4f$-type zero dispersion setup used in all frequency-domain pulse shapers ideally does not introduce any dispersion into the pulse. In reality, the amount of dispersion is nonzero and very susceptible to the exact alignment and placement of the optics. The setup is shown schematically in Fig. 3.12. It can be modeled by the extended $ABCD$ matrix formalism as presented by Martinez in Ref. [78]. This formalism allows a calculation of the resulting dispersion in the setup when the parameters a, a', and b are detuned.

Fig. 3.13 shows the result of such a calculation, with the parameters grating, focal length, and bandwidth of our pulse shaper setup. It is obvious that the zero-dispersion compressor at perfect alignment ($a = b = 0$) is not entirely dispersion-neutral but instead introduces about -1800 fs^2 and -400 fs^2 at the red and blue edges of the spectrum, respectively. This corresponds to a significant negative second order and positive third order spectral phase. Comparison with the expected spectral phase of the NOPA pulses due to material dispersion shows that the optimal detuning to compensate the phase distortions of the pulse is close to the optimum alignment ($a = 0.001$) and the remaining nonlinear components of the spectral phase after passing through the material of the NOPA, the experimental setup and through the $4f$ setup itself should be only a few tens of radians [79]. Therefore, a slight detuning of the parameter a can provide flexible dispersion compensation at the cost of little spatial distortions [46, 80].

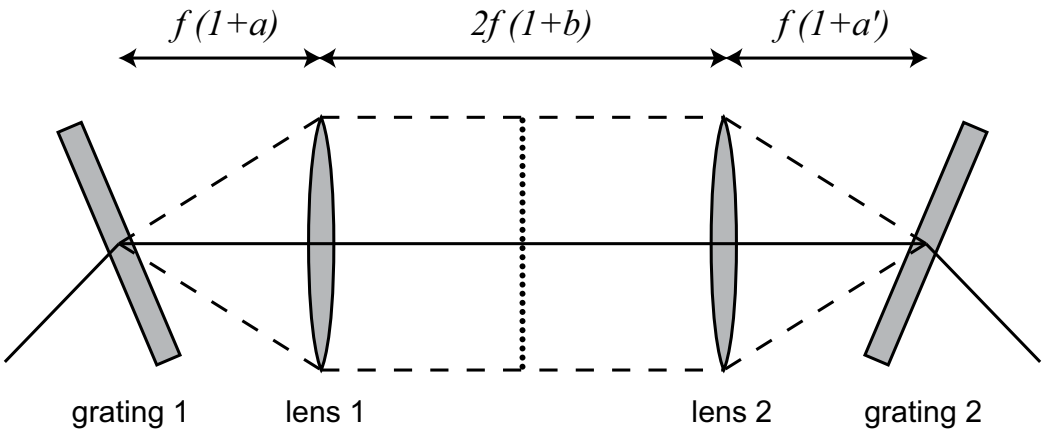

Figure 3.12: Schematics of a $4f$ zero dispersion compressor. The detuning parameters a, a' and b are indicated. Folding the setup at the dotted line, i.e. at the Fourier plane, results in $a = a'$.

It should be noted that the analysis applies to a linear setup only, and that any detuning from perfect alignment results in spatial chirp or angular dispersion of the output beam. Investigations of the spatial effects in planar and non-planar folded arrangements using advanced ray tracing software are under way.

3.6.5 Deformable mirror pulse shaper

Deformable mirrors are flexible, reflective membranes whose surface can be influenced by a number of high voltage electrodes or piezo actuators behind the membrane. Placed in the Fourier plane of a $4f$ compressor or as a symmetry mirror at the end of a prism compressor deformable mirrors can be used as active elements for pulse compression [81, 82] and shaping for quantum control purposes [59].

Typical deformable mirrors can introduce only 40 fs group delay because of the limitation of the surface deflection to a maximum of 6 μm [83]. Thus, for NOPA compression deformable mirrors need to be used in combination with more powerful compression techniques such as prism compressors, $4f$ setups, or chirped mirrors. In combination they can provide the fine tuning of the dispersion to yield close to transform-limited pulses [55, 58, 84].

While deformable mirrors have a high damage threshold and a fast response time, they are limited in the pulse shapes they can produce. The membrane cannot take arbitrary surface shapes and there is always a certain degree of coupling between the areas addressed by neighboring actuators or electrodes. This is also a reason why calibration of the optical delay as a function of applied voltage is not easy to accomplish and the deterministic generation of particular pulse shapes is hindered. Further, the bending of the membrane in the direction perpendicular to the dispersed spectrum could potentially have a negative impact on the spatial mode of the output beam.

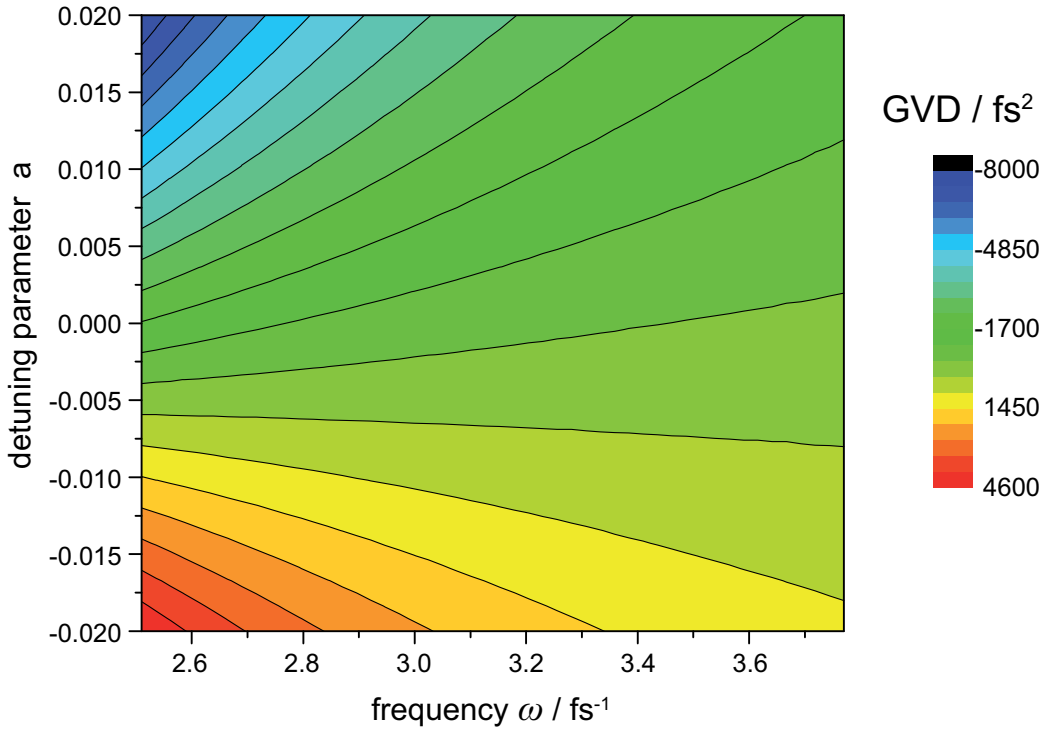

Figure 3.13: Group velocity dispersion (GVD) as a function of detuning parameter a. b was found to have little effect on dispersion (data not shown) and therefore $b = 0$ in this graph. All other parameters (grating line frequency, lens focal length, bandwidth) were kept at the values of our actual implementation. The frequency axis limits correspond to 750 nm and 500 nm. Graph adapted from Ref. [79].

3.6.6 Liquid crystal pulse shaper

Liquid crystal pulse shapers have been employed as a flexible compression method for NOPA pulses yielding sub-16 fs pulses [85]. The possibility of calibration and deterministic generation of nearly arbitrary pulse shapes are particularly attractive for use in our setup. Furthermore, by wrapping the total phase curve for dispersion compensation into intervals of multiples of 2π, relatively large group delays can be introduced (about 2000 fs^2 in our setup). LC pulse shapers can not only compress pulses by shaping spectral amplitude and phase, but also generate polarization-shaped pulses for various interesting applications (see also chapter 7).

Given the plans for future experiments and the arguments presented in the previous sections, we opted to build a liquid crystal pulse shaper with a detuned $4f$ setup to have a flexible means of compression and the possibility of versatile pulse shaping.

3.7 Liquid crystal pulse shaper

3.7.1 Femtosecond pulse shapers

Modern femtosecond pulse shaping techniques most commonly rely on manipulation of the laser pulses in the frequency domain [3, 86]. These techniques are standard methods that are presently used in most femtosecond laboratories for various purposes like adaptive pulse compression, creation of shaped pulses for coherent control, dispersion compensation, or delay generation.

In a $4f$ setup, as described in section 3.6.4, the frequencies are dispersed along a spatial coordinate. There, an active usually computer-controlled mask or spatial light modulator (SLM) can imprint a spectral phase or amplitude onto the input pulses. The most common SLMs are liquid crystal (LC) arrays and acousto-optical modulators (AOMs). AOMs have the advantage of very fast update rates [87] and with the right choice of crystal they can also be used in the ultraviolet [88] and in the infrared [89, 90] wavelength region. LC SLMs, on the other hand, feature high transmission. If they are constructed with several (usually two) layers they can not only change the spectral phase but also the amplitude of the different spectral components. Alternatively, a modulation of the polarization state is possible, leading to complex output pulses with polarization states that change on a femtosecond timescale [91].

3.7.2 Experimental design and parameters

When designing a pulse shaper setup, the most basic considerations are the following parameters (see Fig. 3.14): focal length of the focusing elements, line density of the gratings (angular dispersion), length of the active parts of the SLM, bandwidth of the laser system, and input beam size w_{in}. These parameters are given by the experimental conditions or have to be chosen for optimum performance of the shaper.

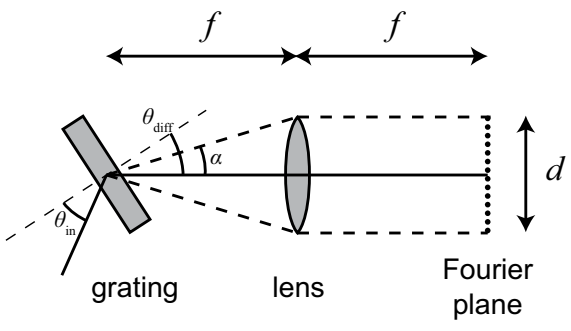

Figure 3.14: Geometry and important design parameters of a $4f$ zero dispersion compressor. The figure is drawn for a transmission grating in Bragg configuration. The angle of incidence and the diffraction angle of the center wavelength are indicated as θ_{in} and θ_{diff}; the half angle of the dispersion of the spectrum is indicated as α. In the Fourier plane the length d is given by the dimensions of the SLM in the pulse shaping setup.

The NOPA pulse shaper uses a dual mask 640 element LC SLM that is commercially available from Cambridge Research & Instrumentation, Inc. For reference the parame-

ters of this SLM are given in table 3.2. The focusing optics and the grating are chosen to be optimal for the dimensions of the SLM.

number of elements (pixels)	640
pixel height	5.0 mm
pixel pitch	(100 ± 0.005) μm
inter-pixel gap	2 μm
inter-mask separation	1.02 mm
transmission over spectral range 488–900 nm	94%

Table 3.2: Data of the LC SLM for shaping visible NOPA pulses.

Spectral resolution and focal length

For pulse shaping in the frequency domain using a $4f$ setup, the important notion is that every single color has a focus or beam waist in the Fourier plane [3], which allows independent manipulation of the colors (limited by their spot size) by an amplitude and/or phase mask. The radius of the focal spot w_0 is given by

$$w_0 = \frac{\cos\theta_{\text{in}}}{\cos\theta_{\text{diff}}} \frac{f\lambda}{\pi w_{\text{in}}} \tag{3.31}$$

where w_{in} is the radius of the input beam, f is the focal length of the focusing elements, λ is the wavelength, θ_{in} is the angle of incidence on the grating, and θ_{diff} is the angle of diffraction off the grating (see Fig. 3.14). The first factor is due to geometric effects in non-Littrow or non-Bragg configuration of reflection or transmission gratings, respectively. It can be neglected for close to Littrow or Bragg configurations and wavelengths close to the center wavelength. The actual spectral modulation is given by the convolution of the SLM pattern with the beam profile [92] and thus, to make use of all of the potential spectral resolution of a spatial light modulator (SLM), the spot diameter $2w_0$ should be smaller than the size Δx of the elements of the SLM. A further benefit of a small w_0 is the avoidance of severe space–time coupling [93, 94]. Note, that due to the nonzero inter-mask separation of the SLM, it is not possible to bring both SLM masks exactly into the Fourier plane and w_0 is effectively bigger than the best case estimate of Eq. 3.31. This also occurs in folded geometries where the symmetry mirror is located at the exact position of the Fourier plane.

Cylindrical focusing optics are widely used in order to keep intensities at the SLM low and still make use of the maximum possible resolution. The input beam size is chosen such that the full height of the SLM pixels (5 mm) is illuminated and the focusing along the direction of the pixel array assures high spectral resolution. Thus, assuming an input beam size of $2w_{\text{in}} = 4$ mm cylindrical mirrors with $f = 20$ cm lead to a spot diameter $2w_0 = 40$ μm at the design central wavelength $\lambda_0 = 630$ nm, with larger and smaller w_0 toward the red and blue edges of the spectrum, respectively.

Grating line density

The spectral range of the pulse shaper is designed to be from 500 nm to 750 nm. The employed gratings have to disperse the spectrum so that the spectrum fills the aperture of the SLM ($d = 64$ mm). This determines that the required angular dispersion

$$\alpha = \arctan \frac{d}{2f} \tag{3.32}$$

between the central wavelength and the edges of the spectrum is $\alpha = 9.1°$.

Using the standard grating equation for first order diffraction

$$g\left(\sin\theta_{\text{in}} + \sin\theta(\lambda)\right) = \lambda \tag{3.33}$$

and the approximation that all angles are small the required grating constant can be calculated as

$$g \approx \frac{\lambda_{\text{edge}} - \lambda_0}{\alpha} \tag{3.34}$$

where λ_{edge} is the wavelength at the (red or blue) edge of the spectrum. The given spectral range and the required angular dispersion result in a desired value of $g = 760$ nm or a grating frequency of $g^{-1} = 1300$ mm^{-1} in the current experimental setup.

Volume phase holographic gratings

As mentioned in section 3.6.1 the narrow bandwidth and low efficiency of regular diffraction gratings are crucial issues for their use with ultrabroadband visible NOPA pulses. Contrary to surface relief gratings where the diffraction is due to path differences of the impinging wave, volume phase holographic (VPH) gratings imprint a phase (or optical path difference) onto the wave through a modulated index of refraction in bulk material.

In contrast to surface gratings, volume holograms have the additional effect of possible Bragg reflection analogous to Bragg reflection in X-ray crystallography; this effect can be used for the "super-blazing" of such transmission gratings. The depth of the index modulation and the thickness of the modulation layer represent two additional degrees of freedom compared to surface gratings. Precise control of these two parameters during the production process allows for control over the polarization-dependent efficiencies and over the bandwidth of the gratings. A review of the design and production processes together with a basic theory of VPH gratings can be found in Ref. [95].

VPH gratings have several advantages over surface gratings with respect to their use with femtosecond laser pulses. The efficiency can be designed such that it is close to 100% over the bandwidth of the laser pulses. Further, the alignment of compressors is simplified due to the transmissive geometry. VPH gratings have been used for the compression of amplified pulses [96] and their design can be adjusted to the requirements of different broadband laser systems [97].

For use in our NOPA pulse shaper special VPH gratings were designed by Philippe Lemaire of ATHOL, Liège, Belgium. The gratings were holographically recorded in dichromated gelatin [98], which is the standard material for VPH gratings, and feature a high damage threshold. Sealed holograms last for decades. Due to the production

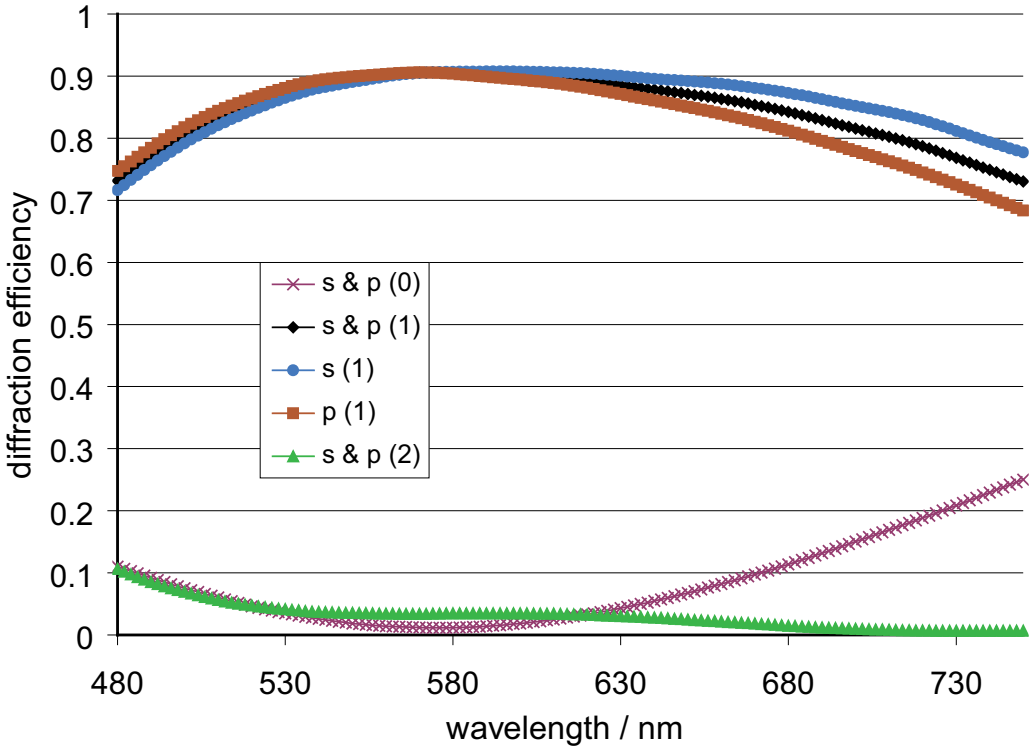

Figure 3.15: Calculated efficiencies of the custom designed VPH gratings in the NOPA pulse shaper for different polarizations and diffraction orders. The line frequency of the gratings is $g^{-1} = 1000\ \mathrm{mm}^{-1}$. s (p) means that the electric field vector oscillates perpendicular (parallel) to the plane of incidence defined by the surface normal and the k-vector of the incidence beam. The angle of incidence for this simulation is set to the Bragg angle for 615 nm, i.e., $\theta_{\mathrm{in}} = 18°$.

process, the calculated optimal grating frequency (1300 mm^{-1}) could not be met with sufficient quality because the required grating structures are too small for reliable holographic recording. Instead, gratings with a line density of 1000 mm^{-1} were produced. This results in a slightly larger throughput bandwidth of the pulse shaper. The requirement of high efficiency over all of the NOPA bandwidth is met by using a high modulation depth for the index of refraction and at the same time using only a thin layer of dichromated gelatin. The resulting diffraction efficiencies are shown in Fig. 3.15. First order diffraction is high for both polarization directions over all of the NOPA bandwidth. This insensitivity to polarization is especially valuable for polarization pulse shaping [99].

3.7.3 Optical setup of the LC pulse shaper

The pulse shaper setup has been designed according to the parameters discussed in the previous section. We chose a geometry that is folded in the Fourier plane (Fig. 3.16) which allows the use of fewer optics and simplifies alignment of the $4f$ setup. The input and output beam must impinge on the grating slightly vertically displaced, but with no horizontal displacement. In this configuration, the angles at the gratings are adjusted

optimally, and no angular dispersion of the output beam should remain. Furthermore we use a vertical folding mirror between the grating and the cylindrical mirror. This kind of folding avoids any astigmatic aberration that would occur in a horizontally folded geometry.

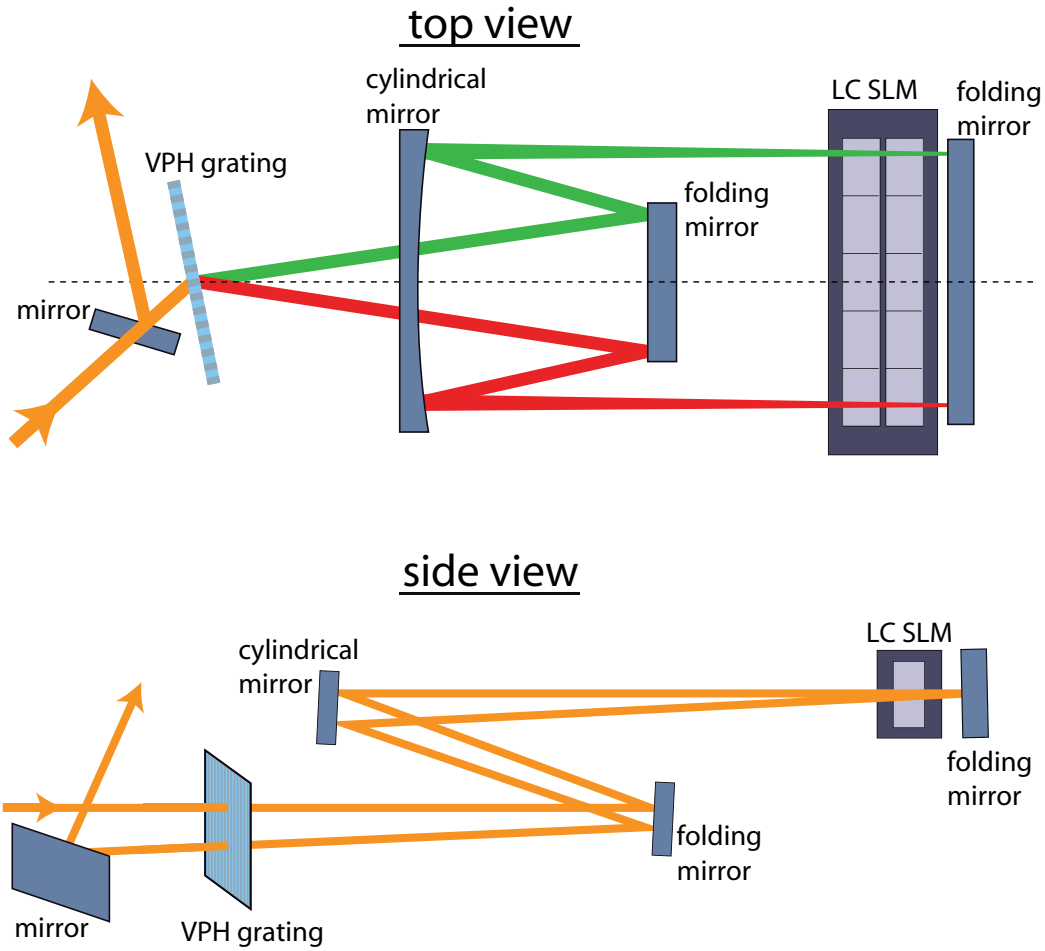

Figure 3.16: Optical setup of the LC pulse shaper for NOPA pulses. Top view: The input beam hits the VPH grating under the Bragg angle. A folding mirror directs the dispersed spectrum to the cylindrical mirror. The second folding mirror (on the right hand of the drawing) is placed in the Fourier plane of the setup and the SLM is placed as close as possible to this mirror. Side view: The input beam is parallel to the optical table and passes through the VPH grating. Folding mirror and cylindrical mirror direct the beam in a vertical Z shape. The second folding mirror is slightly tilted so that the output beam leaves the $4f$ arrangement lower than the input and is picked off by a mirror.

3.7.4 Calibrations of the pulse shaper

For the deterministic generation of output pulse shapes the pulse shaper must be calibrated. The frequency or wavelength distribution along the SLM must be known and

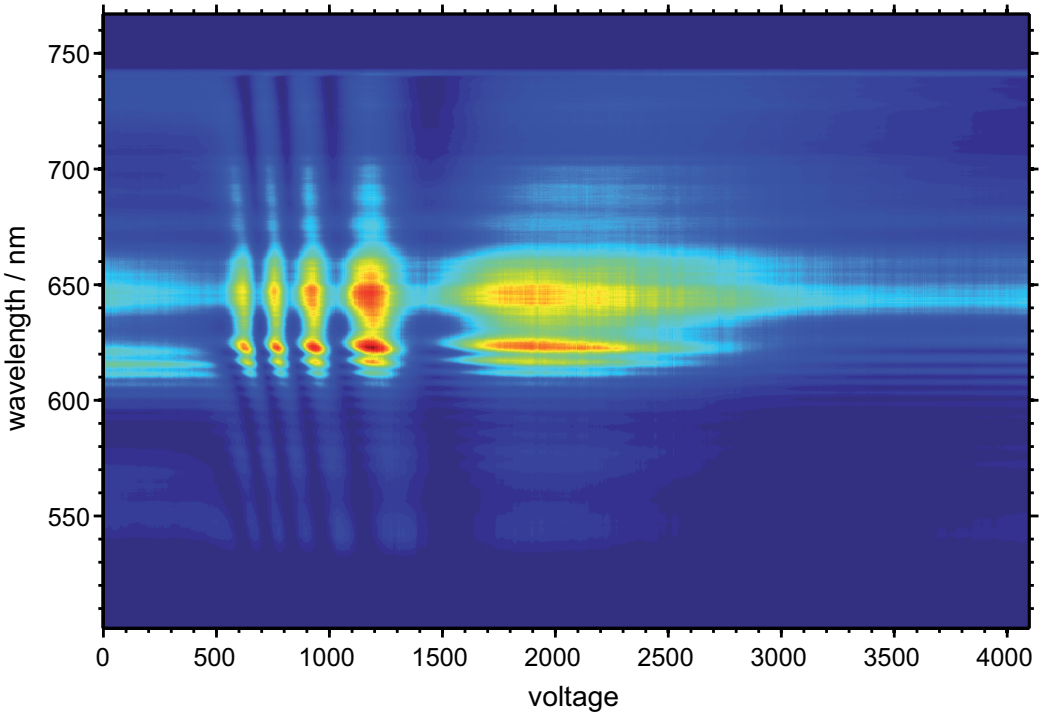

Figure 3.17: Raw data for phase calibration of the 640-pixel SLM. The SLM is operated in amplitude modulation mode and a broad laser spectrum is used for calibration. For each mask, spectra are recorded as a function of applied voltage, while the other mask is kept at a constant voltage of usually 2000.

the amount of phase that is introduced as a function of voltage applied to the pixels needs to be measured. While for more narrow-band pulse shapers the latter type of calibration can usually be done with only one pixel (one laser frequency), our setup that spans more than 200 nm in the visible requires us to take the dispersion of the liquid crystals themselves into account.

Measurement of calibration data

The calibration data for the phase calibration is measured first because it is required for the wavelength calibration. Contrary to previous approaches to calibration methods in our group, we calibrate each SLM pixel with the wavelength which it will modulate in regular operation as well. Hence, for the calibration we have to use a laser spectrum that at least covers all the pixels that are to be used in an experiment, i.e., the calibration spectrum $I_0(\omega)$ has to be as wide as the desired width in an experiment. First, the mask that is *not* to be calibrated is set to a constant voltage value U_{const} (usually 2000). Note that all voltages given here do not have units because the controller of the LC SLM accepts 12-bit numbers (0...4095) and automatically translates them into voltages that are applied to the LC array. A polarizer is attached to the SLM and used for amplitude

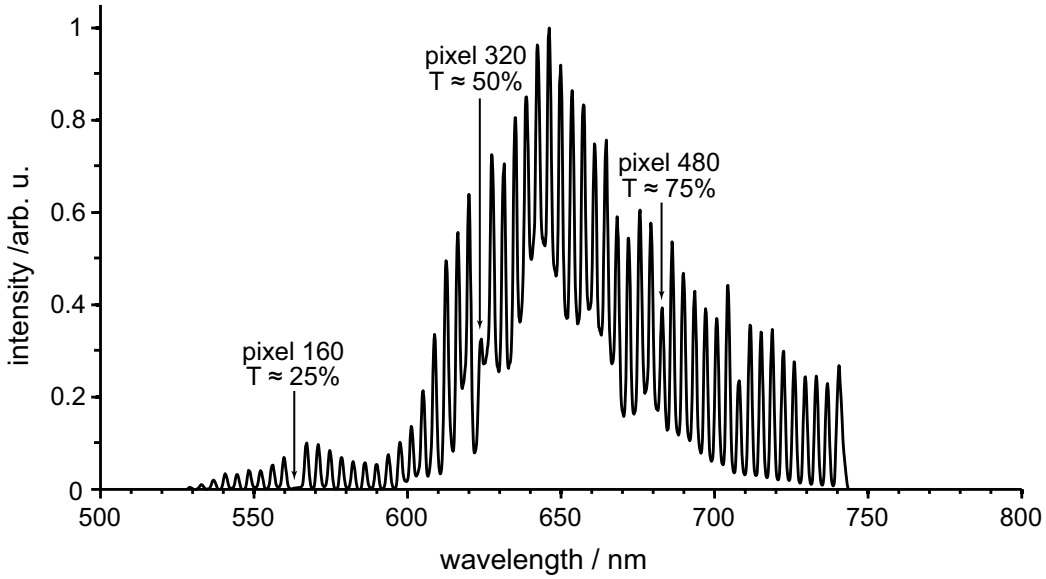

Figure 3.18: Data for wavelength calibration of the pulse shaper. Using the phase calibration data, the amplitudes of all pixels are set such that every tenth pixel has a transmission close to $T = 1$ and all other pixels are set to $T \approx 0$. The positions indicated with arrows are "special" pixels with different transmissions that are used to identify the center pixel and the directionality of the calibration.

modulation. Then the transmitted spectrum

$$I_j(U, \omega) = I_0(\omega) \left(1 + \cos \phi_j(U, \omega)\right) / 2 \tag{3.35}$$

is recorded by a spectrometer located after the pulse shaper [79, 100]. In this equation the index $j = \{1, 2\}$ refers to the mask that is to be calibrated. The voltage applied to this mask is varied from 0 to 4095 and spectra are recorded in suitable steps. Then the procedure is repeated for the other mask. Fig. 3.17 shows a plot of an example data set against wavelength and voltage. The data are modulated along the voltage axis and exhibit several maxima and minima. For different wavelengths these extrema are shifted because the modulation of the index of refraction, introduced by the LC crystals, causes a phase shift $\phi \propto 1/\lambda$. In addition, the dispersion of the liquid crystals, as well as potential imperfections like inhomogeneous layer thickness over the length of the SLM, are contained within the data in Fig. 3.17.

Then the data for the wavelength calibration is recorded. One picks a pair of corresponding maximum and minimum in the calibration data (i.e. a ridge and a valley in roughly vertical direction in Fig. 3.17). The respective mask is now used to create an intensity pattern across the SLM from which the wavelength calibration can be reconstructed. Typically, every tenth pixel is set to the voltage value that corresponds to maximum transmission and all other pixels are set to minimum transmission (while the other mask is kept at the constant value $U = 2000$). The resulting spectrum is recorded and an example is shown in Fig. 3.18.

Wavelength calibration

Obviously, the wavelengths of the peaks in Fig. 3.18 correspond to the wavelengths of the pixels that were set to high transmission. However, the spectrum illuminating the SLM does not extend all the way to its edges. Thus, it is not clear *a priori* which pixel corresponds to which peak. In order to make this assignment and also to identify the directionality ("low pixel number $\sim$ small wavelengths" vs. "low pixel number $\sim$ large wavelengths"), we use three pixels that are set to approximately 25%, 50%, and 75% transmission (see Fig. 3.18). This assignment is made by a LabVIEW program using a combination of automatic peak detection and manual fine adjustment. The found wavelength values are fit with a second order polynomial. This polynomial is the final wavelength calibration that assigns a wavelength to each pixel of the SLM.

Phase calibration

The reconstruction of the phase that each pixel introduces as a function of applied voltage can in principle be done by inverting Eq. 3.35, i.e., solving the equation for ϕ. In reality however, there are some complications that do not allow this direct approach. First, the laser spectrum $I_0(\omega)$ that is used for calibration is subject to noise. Further, the inversion of the cosine function has to be done over multiple periods and the joining of the different periods is done in places where the cosine function is shallow (maxima or minima). This leads to special susceptibility of the inverted function $\phi(U)$ to noise in these places and often unwanted phase jumps occur [101]. Hence we usually use a more complicated method instead of direct inversion to recover $\phi(U)$.

First, the wavelength calibration is used to assign a curve $I_j(U, \omega = \omega_k)$ to each pixel k. These curves $I_j(U, \omega = \omega_k)$ that are a function of U are then "normalized" such that each period of the modulations in U ranges from -1 to 1. This procedure compensates for the nonuniform spectrum $I_0(\omega)$ and it also partially compensates for laser power variations over the measurement period. All normalized curves are then inverted and unwrapped using another LabVIEW program. Due to a number of factors [101] not every single curve is inverted and unwrapped successfully. Thus one picks the curves where the data quality was satisfactory. Also, the data for small voltages, for example $U < 500$ in Fig. 3.17, where the liquid crystals don't respond to the applied voltages is dropped from further processing. The dots in Fig. 3.19 represent those selected data. The idea now is to calibrate the whole SLM – including the parts where no calibration raw data could be gained – by fitting a model function that interpolates and extrapolates the characteristics of the phase calibration. The important notion is that the model function only needs to reproduce the data and have good inter- and extrapolation properties (i.e. no oscillatory or diverging behavior). Due to the different contributions to the characteristics of the data, it is reasonable to use a model function

$$\phi(U, \omega) = F(U) + D(U, \omega) \tag{3.36}$$

where the major voltage-dependent contribution $F(U)$ is separated from the somewhat smaller voltage- and pixel-dependent contribution $D(U, \omega)$ that results from dispersion and bandwidth effects. $F(U)$ simply contains the general trend that the phase ϕ decreases with increasing voltage for all pixels. This approach corresponds to a separate

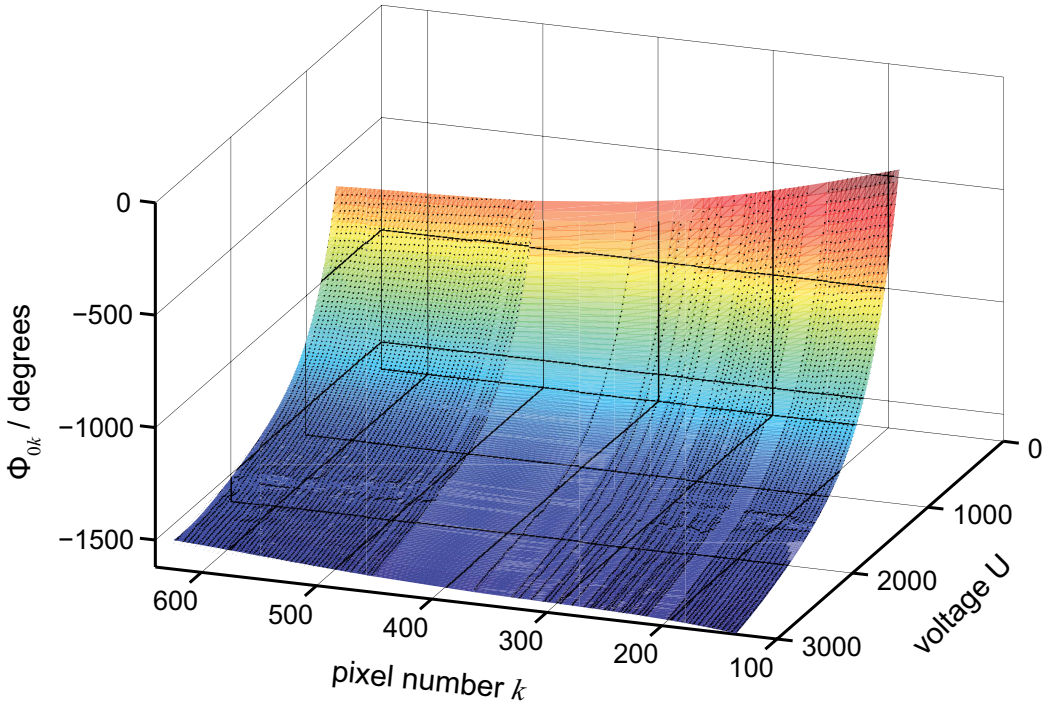

Figure 3.19: Phase calibration data and best fit. The automatically processed data for all pixel are plotted as dots together with a best fit (shaded surface). The fit routine (described in the text and Eqs. 3.36–3.38) interpolates the data and compensates for imperfections of the inversion of Eq. 3.35.

treatment of the average phase, similar to previous calibrations with smaller bandwidths [92, 102], and a two-dimensional "correction" term $D(U,\omega)$ that includes the dependence on the wavelength and the dispersion. In this way, the data fitting process itself can be separated into two steps: (a) finding the optimal parameters for $F(U)$ with the data that is averaged over all pixels $\overline{\phi}(U)$ and (b) finding the optimal parameters for $D(U,\omega)$ by fitting the residual data $\phi(U,\omega) - F(U)$.

When we restrict ourselves to the voltage range shown in Fig. 3.19, a suitable fit model for the average voltage-dependent part is a biexponential function

$$F(U) = \phi_0 + \phi_1 \, \mathrm{e}^{-U/U_1} + \phi_2 \, \mathrm{e}^{-U/U_2} \tag{3.37}$$

with a constant offset ϕ_0 and two decays with constants U_1, U_2 and amplitudes ϕ_1, ϕ_2. It should be stressed again that this function has no physical meaning and must only reproduce and interpolate the data. Therefore, in the future, other functions that also serve this purpose might be used.

The two-dimensional residual fit by the term $D(U,\omega)$ does not exhibit any large trends along either axis but rather reflects the slow variations of ϕ with the voltage and pixel number. Here, the fit model that we chose is a two-dimensional polynomial

$$D(U,\omega) = \sum_{m=0}^{N} \sum_{n=0}^{m} a_{mn} (U - U_0)^n \, (p - p_0)^{m-n} \tag{3.38}$$

of the order N in voltage U and pixel number p with the coefficients a_{mn} centered around U_0 and p_0. The experimenter chooses the order of the polynomial N high enough so that the features in the data can be captured but also low enough so that the number of fit parameters is not too large. [The number of coefficients is $(N+1)(N+2)/2$.] Our experience with the 640-pixel SLM and a broad visible spectrum shows that an order of $N = 4$, or sometimes even $N = 3$, is sufficient.

The color-shaded surface in Fig. 3.19 is the result of such a two-step fitting procedure. In this graph, it can be seen that the data is reproduced well. Additionally, the area where there are almost no useable data points ($\approx$ pixels 330 through 450) is interpolated smoothly in both directions, U and p. In practice it is useful to look at the residual in order to determine the magnitude of the deviations and also to check that there are no systematic deviations from features in the data that are not captured by the model function.

If the fit is satisfactory, the best parameters and the model function are next used to compute a two-dimensional array of $\phi_j(U, p)$ for $U = [0, 1, ..., 4095]$ and $p = [0, 1, ..., 639]$. The procedure is done for both SLM masks. When calibrating one mask, it is intrinsic to the calibration procedure that the other mask introduces an additional (small) phase. Using the two sets of calibration data for the two masks, this effect is taken into account by subtracting the phase values $\phi_2(U_{\text{const}}, p)$ of one mask from all phase data $\phi_1(U, p)$ of the other mask (see Ref. [79] for details). Finally, the data is entered into our software framework which also controls the pulse shapers. Only the area that was modeled well by the fitting procedure can be used. The total usable modulation depth results from the minimum range on the ϕ-axis that is spanned by all pixels. In Fig. 3.19, e.g., pixel 639 spans the smallest range in ϕ and thus determines the modulation depth. In the case of our 640-pixel pulse shaper that operates in the visible and is built in reflective, folded geometry, a modulation depth of 4π is possible.

3.8 Adaptive pulse compression

After setting up the zero-dispersion compressor the NOPA pulses passing through the setup were characterized with TG FROG and SHG FROG. The first stage of compression was accomplished by detuning the $4f$ setup (see section 3.6.4). The feedback signal that was maximized in order to shorten the pulses while adjusting the $4f$ setup was the TG or SHG signal at $\tau = 0$ or the SHG signal of a single beam. The final stage of the pulse compression was the adaptive adjusting of the SLM mask in the pulse shaper. There are two approaches to adaptive pulse compression: open loop and closed loop. In our experiments we used both and examples are shown in the following sections.

3.8.1 Closed loop pulse compression

In the case of unknown phase distortions on the laser pulses the closed loop approach can be an excellent means to compress the pulses [12–15]. In this approach a feedback signal guides a "learning algorithm" such as a genetic or an evolutionary algorithm [14] or simulated annealing [12].

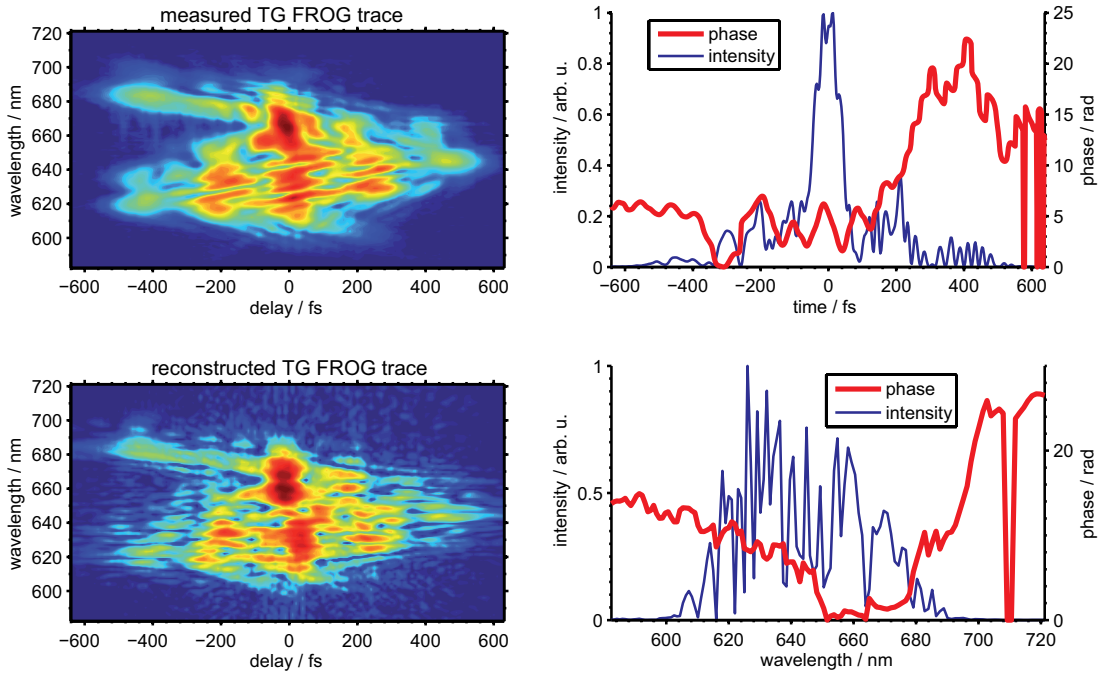

Figure 3.20: TG FROG results of NOPA pulses before adaptive compression. Left: measured FROG trace and reconstructed FROG trace. Right: reconstructed electric field in time and frequency domain.

A particularly attractive signal for use as feedback in our setup is the third order nonlinear signal from the TG FROG at zero time delay between all three generating pulses. The signal can be detected with a photodiode or spectrometer and maximizing the integrated signal or the photodiode signal leads to compressed pulses. Afterward it is simple to record a TG FROG in the same setup and characterize the resulting pulse shapes.

An example of closed loop adaptive pulse compression is shown in Figs. 3.20 and 3.21. The TG FROGs were recorded as described in section 3.5.2. In both figures the measured and the reconstructed FROG traces are represented on the left and the reconstructed fields are represented in time- and frequency-domain on the right.

To compress the pulses, the distances of the elements in the $4f$ setup were first adjusted such that the integrated signal from the spectrometer at $\tau = 0$ was maximized. This corresponds to the shortest possible pulse using detuning of the $4f$ setup only. With these adjustments a FROG was recorded and the results are shown in Fig. 3.20. From the highly structured FROG trace it is clear that complex phase distortions are present. The FROG reconstruction algorithm did not reconstruct the field perfectly. Due to the complex temporal structure the algorithm finds a structured spectrum that exhibits "holes", in contrast to the rather smooth, independently recorded linear spectrum (see also comparison between these spectra in Fig. 3.22). Therefore only a small amount of confidence can be placed in the reconstructed phase.

Next, the evolutionary algorithm was used to compress the pulses automatically by

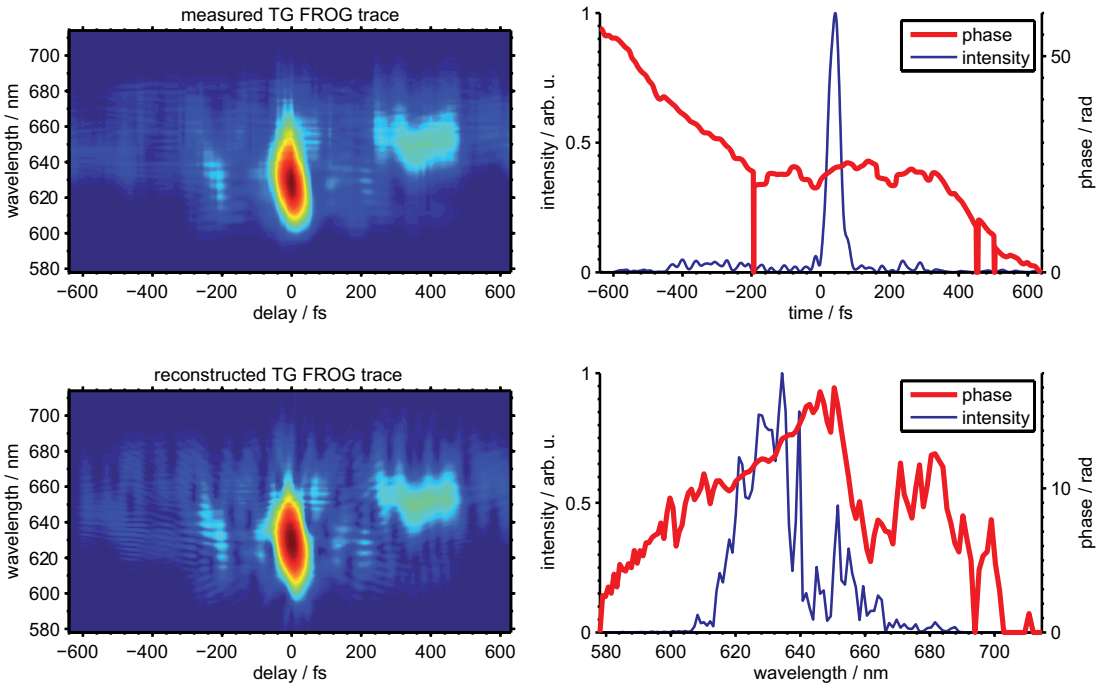

Figure 3.21: TG FROG results of NOPA pulses after adaptive compression. Left: measured FROG trace and reconstructed FROG trace. Right: reconstructed electric field in time and frequency domain.

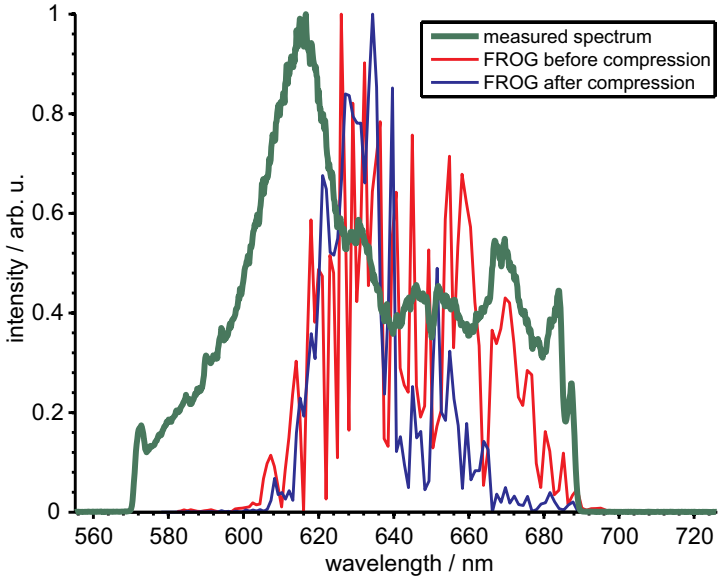

Figure 3.22: Comparison of the reconstructed spectra from the TG FROGs before and after closed loop compression with the directly measured linear spectrum.

maximizing the TG FROG signal at $\tau = 0$. After convergence the best phases of the optimization were applied to the SLM and another TG FROG was recorded (Fig. 3.21) to determine the outcome of the compression. The reconstructed trace is in very good agreement with the original trace. The adaptive compression was successful: the temporal width was reduced to 39 fs (FWHM) and the energy is concentrated in one main pulse. Yet, the spectrum is not reproduced well here either (see Fig. 3.22). Even though the holes in the reconstructed spectrum are not as pronounced as in the reconstructed field of the pulse before optimization, in both cases the blue edge of the spectrum is not reproduced in the reconstruction and, in fact, there is no signal at those wavelengths in the measured trace. A possible explanation could be that competing three-photon absorptions distort the $\chi^{(3)}$ transient grating signal, especially at short wavelengths where the energy of three photons corresponds to the energy of photons in the deep UV to which fused silica is not transparent. Despite these remaining inconsistencies, the success of the compression procedure is obvious from the comparison of the FROG traces before and after the evolutionary algorithm optimization.

3.8.2 Open loop pulse compression

The complementary approach is open loop pulse compression. The phase of the uncompressed pulses is measured precisely and the inverted spectral phase is then applied to the LC pulse shaper to cancel the phase distortions on the input pulses.

An example of adaptive pulse compression using this method with SHG FROG is shown in Figs. 3.23–3.24. We used a BBO crystal that has a thickness of only 10 μm in the setup for 2D spectroscopy for this experiment. Similar to the closed loop approach, first the SHG FROG signal at $\tau = 0$ was maximized by adjusting the $4f$ setup only, during which time a flat spectral phase was applied to the SLM. The fundamental spectrum of the pulses was recorded in an independent measurement. Then a FROG trace was recorded and reconstructed after correction of the marginals for nonuniform SHG efficiency of the crystal over the full bandwidth. The results are shown in Fig. 3.23. On the left hand side the reconstructed FROG trace shows excellent agreement with the measured trace, despite the complexity. The reconstructed temporal electric field displayed on the top right of Fig. 3.23 reveals a relatively short main pulse and a few pre- and post-pulses, demonstrating that the compression using the $4f$ setup only was successful at eliminating the second order spectral phase and produced pulses with only higher order phase distortions. The reconstruction of the spectral phase (bottom right of Fig. 3.23) shows that there is about 10 rad of phase distortion left over the bandwidth of the NOPA pulses. Furthermore, the comparison of the reconstructed spectrum with the linear spectrum in Fig. 3.25 corroborates that we have an accurate reconstruction of the electric field; thus, the reconstructed phase can be employed to compress the pulses.

The process of open loop compression using SHG FROG is, in general, a multi step process for two reasons. First, the direction of the time axis (and the sign of the spectral phase) of the SHG FROG reconstruction is intrinsically ambiguous. Therefore, both possible spectral phases have to be applied and the outcome must be measured to find the true sign of the spectral phase. Secondly, a more complex residual spectral phase leads to a less accurate reconstruction. After finding the right sign of the spectral phase

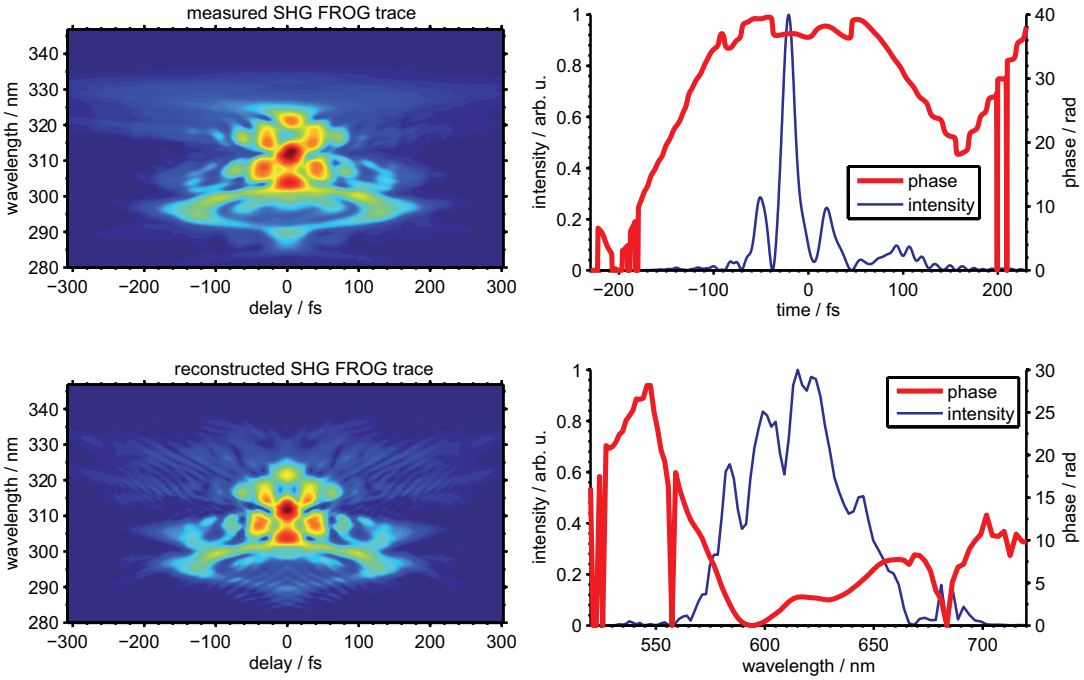

Figure 3.23: SHG FROG results of NOPA pulses after adjusting the $4f$ setup manually. Left: measured FROG trace and reconstructed FROG trace. Right: reconstructed electric field in time and frequency domain.

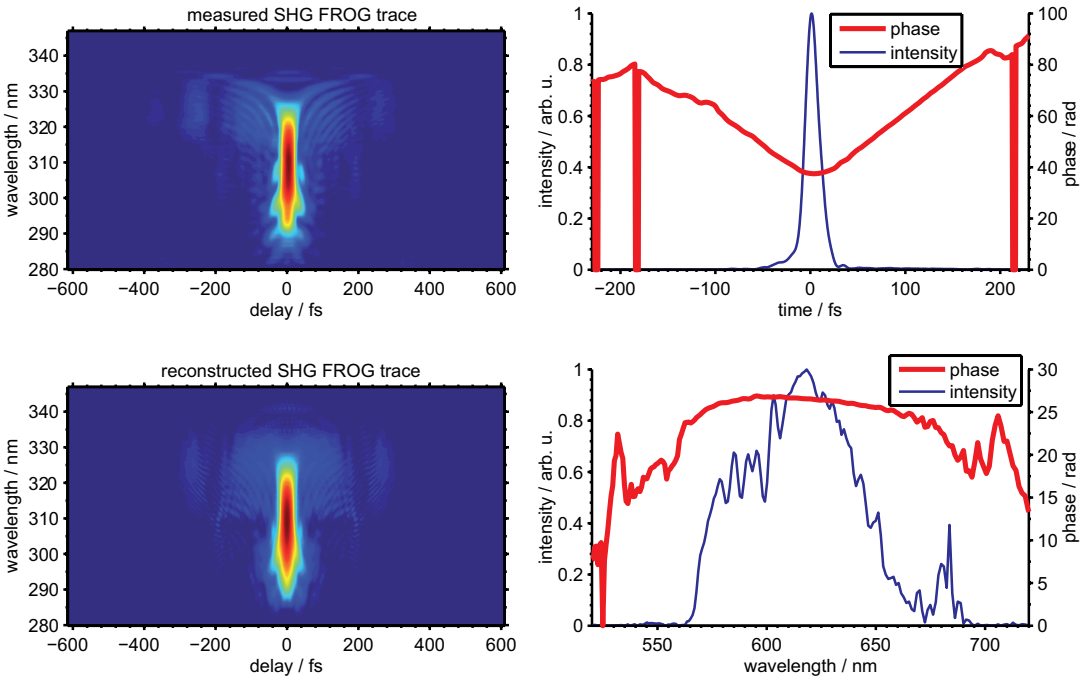

Figure 3.24: SHG FROG results of NOPA pulses after applying the reconstructed phase from Fig. 3.23, leading to compressed pulses. Left: measured FROG trace and reconstructed FROG trace. Right: reconstructed electric field in time and frequency domain.

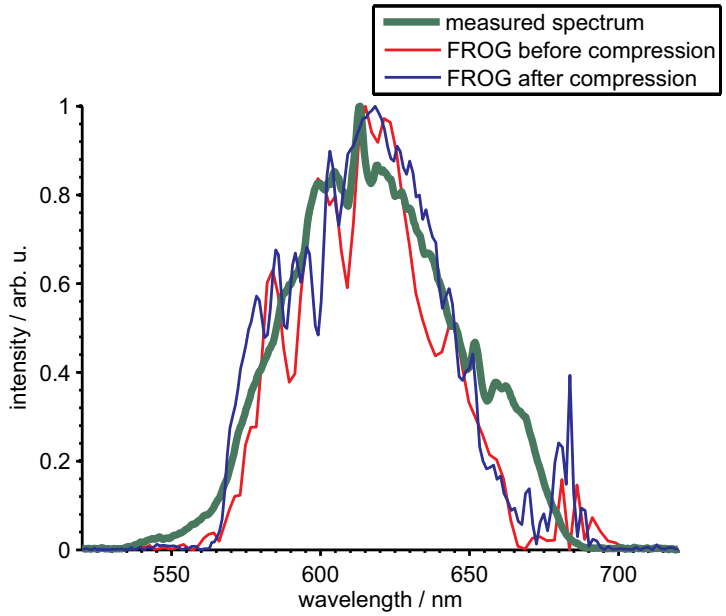

Figure 3.25: Comparison of the reconstructed spectra from the SHG FROGs before and after open loop compression with the directly measured linear spectrum.

one or two more iterations of recording and reconstructing a FROG trace and adding or subtracting the reconstructed spectral phase to the SLM mask can be necessary to reach the optimal compression.

Fig. 3.24 shows the final result of this iterative compression method. Again the FROG trace was corrected for the SHG efficiency and reconstructed. Here also we see excellent agreement of the reconstructed and experimental traces as well as of the reconstructed spectrum and the measured spectrum (see Fig. 3.25). The energy is now concentrated in one short pulse of 17 fs duration (FWHM) with small residual phase distortions.

3.9 Conclusions

In summary, within the work of this thesis means to generate, measure, and compress broadband pulses in the visible wavelength region have been implemented. A NOPA generates spectra spanning the region from 500 nm to 750 nm. Phase distortions on the generated pulses including the dispersion from the 2D spectroscopy setup are compensated mainly by detuning a $4f$ zero dispersion compressor. Together with a 640 pixel LC SLM this $4f$ setup also provides a means for flexible compression and pulse shaping of the broadband pulses. For characterization of the pulses in the setup for 2D spectroscopy, i.e., at the sample position of an experiment, both SHG FROG and TG FROG can be used. The FROG signals represent a good feedback for adaptive compression using the SLM in open or closed loop optimization approaches. This combination results in short pulses at 630 nm with 17 fs duration that can be employed in a variety of applications such as quantum control and femtosecond spectroscopy.

4 Coherent optical two-dimensional spectroscopy

4.1 Introduction

Throughout the history of science, gaining deeper understanding of atomic and molecular structure and processes has always been linked to advances in spectroscopic techniques. While the static structure of molecules is now routinely determined via X-ray scattering or nuclear magnetic resonance (NMR) techniques, the development of ultrafast spectroscopic techniques has improved the time resolution on which molecular processes can be observed down to a few femtoseconds. In particular nonlinear optical spectroscopies, such as transient absorption, have made it possible to measure molecular dynamics on the femtosecond timescale. The insights needed for designing artificial functional molecules and understanding the elementary processes of life like photosynthesis include energy transfer and couplings between functional units of molecules and aggregates.

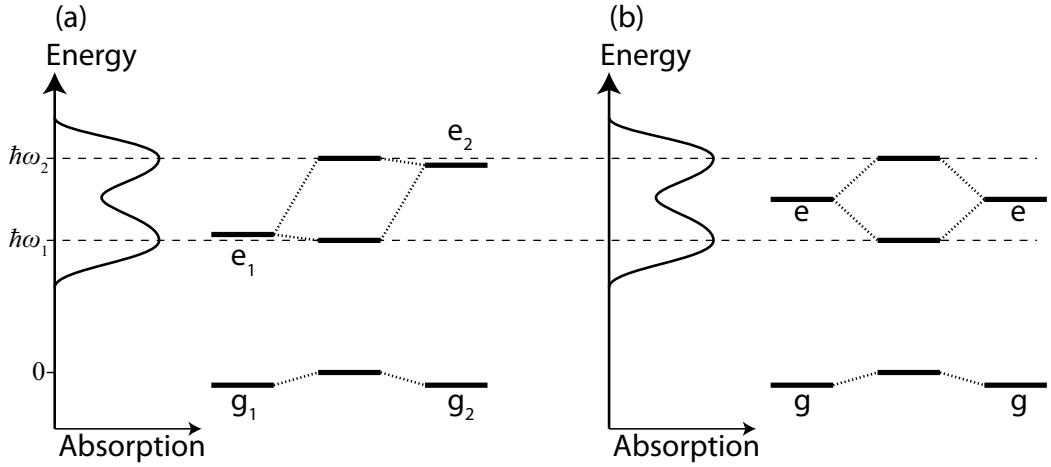

Figure 4.1: Identical linear absorption spectra of a strongly coupled dimer and of two different, weakly coupled chromophores. (a) Two weakly coupled chromophores with different (site) energies have an absorption spectrum of the overall system depicted on the left. (b) Two equal chromophores that are strongly coupled lead to the same overall absorption spectrum.

Energy transfer and couplings are particularly difficult to measure with linear spectroscopy or even conventional transient absorption spectroscopy. Fig. 4.1 illustrates the spectroscopy of a system containing two chromophores. Two situations are depicted: (a) Two different chromophores only interact minimally. The spectrum of the system

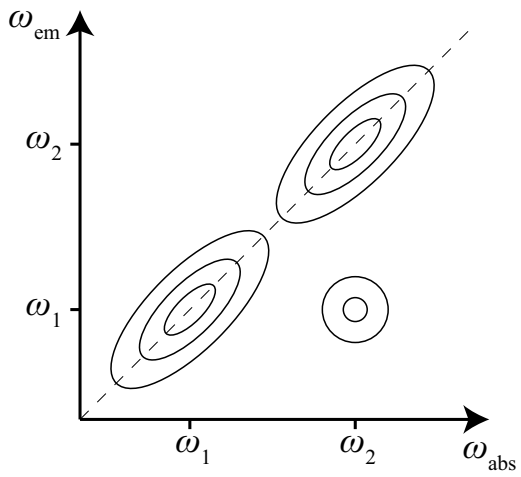

Figure 4.2: Schematic 2D spectrum. The axes of the contour graph represent the absorption and emission frequencies. It can be interpreted as a probability distribution. Hence, the peak off the diagonal (cross peak) indicates coupling between the two states with ω_1 and ω_2.

drawn on the vertical axis on the left is almost identical to a simple superposition of the spectra of the isolated chromophores. (b) Two identical chromophores couple to each other strongly and the level splitting results in the spectrum of the whole system on the vertical axis. Note that both cases (a) and (b) have the same linear absorption spectrum rendering their distinction with linear spectroscopy impossible.

It is however possible to resolve these situations using multidimensional spectroscopy. Two-dimensional spectroscopy reveals invaluable information by resolving excitation and emission on two separate energy axes as sketched schematically in Fig. 4.2. The graph can be interpreted as a probability distribution for absorption at frequency ω_1 and emission at ω_2 [103]. Obviously, every optically accessible state will have a contribution on the diagonal. Any peak off the diagonal (a so-called cross peak) results from a process where $\omega_1 \neq \omega_2$ and thus indicates coupling or energy transfer. Hence, the two situations from the example in Fig. 4.1 can be distinguished in a 2D spectrum by the presence (situation (b)) or absence (situation (a)) of a cross peak. This very simplified fictional molecular system and its 2D spectrum should only serve as an example to show the potential of 2D spectroscopy. In reality many more features can be observed and interpreted in 2D spectra; for a detailed treatment of these one may refer to the textbook on nonlinear optical spectroscopy by Shaul Mukamel [104] and a number of review articles about optical 2D spectroscopy [105, 106].

This chapter first briefly sketches the theoretical treatment of third order nonlinear optical spectroscopy. Then the experimentally important implications in terms of the requirements for phase stability are derived. A number of experimental methods to overcome this and to acquire 2D spectra has been reported in the literature and will be summarized here. We will present our approach which uses only conventional optics and describe the setup in detail. Finally, the first results on the dye Nile blue, including proof for the phase-stability of the setup, will be presented and an outlook for future experiments will be given.

4.2 Theory of third order nonlinear optical spectroscopies

4.2.1 Response function, electric fields, and signal field

The theory of nonlinear optical spectroscopy [104] is an extensive topic and cannot be treated with any claim of completeness here. Thus only the necessary ideas and principles needed for understanding the experimental setup presented in this work will be described here.

Using perturbation theory with the density formalism in Liouville space one can derive the time-dependent third order nonlinear polarization

$$P^{(3)}(t) = \int_0^\infty \int_0^\infty \int_0^\infty S^{(3)}(\tau_a, \tau_b, \tau_c) E(t-\tau_a-\tau_b-\tau_c) E(t-\tau_b-\tau_c) E(t-\tau_c) \mathrm{d}\tau_a \mathrm{d}\tau_b \mathrm{d}\tau_c \quad (4.1)$$

of a system caused by three interactions with the electric field $E(t')$. The third order response function $S^{(3)}(t_1', t_2', t_3')$ includes all the information about the system. It is related to the third order susceptibility $\chi^{(3)}(\omega_a, \omega_b, \omega_c)$ via inverse Fourier transformation.[1] The three-fold convolution with the electric fields represents the interaction of the system with the field at three previous points in time $\tau_a+\tau_b+\tau_c$, $\tau_b+\tau_c$, and τ_c. For a definition of the time variables see Fig. 4.3. The total electric field $E(\vec{r}, t')$ can be written as a sum of three electric fields

$$E(\vec{r}, t') = \tilde{A}(t'-t_1)\mathrm{e}^{-\mathrm{i}\omega_0(t'-t_1)+\mathrm{i}\vec{k_1}\vec{r}} + \tilde{A}(t'-t_2)\mathrm{e}^{-\mathrm{i}\omega_0(t'-t_2)+\mathrm{i}\vec{k_2}\vec{r}} + \tilde{A}(t'-t_3)\mathrm{e}^{-\mathrm{i}\omega_0(t'-t_3)+\mathrm{i}\vec{k_3}\vec{r}} + c.c. \quad (4.2)$$

with identical complex pulse envelopes $\tilde{A}(t') = A(t')\exp[-\mathrm{i}\varphi(t')]$ including amplitude and phase. The measurement of $S^{(3)}(t_1, t_2, t_3)$ or $\chi^{(3)}(\omega_1, \omega_2, \omega_3)$ may be termed the "goal" of 2D spectroscopy. One can see from Eq. 4.1 that, hypothetically, one can obtain $S^{(3)}$ from a measurement with three infinitely short pulses ($\tilde{A}(t') = \delta(t')$) and a characterization of the resulting polarization $P^{(3)}(t)$. However, in reality finite pulse lengths lead to an uncertainty of the interaction times and a smoothing of the resulting spectrum $S_{2\mathrm{D}}$ compared to $S^{(3)}(t_1, t_2, t_3)$. This is mediated by the convolution with the actual fields in Eq. 4.1. In an experiment one delays the pulse centers with respect to each other and thus varies the time periods τ and T. τ is called "coherence time" because the system density matrix is in a state of coherence during this time $\tau \approx \tau_a$. T is called "population time" because only density matrix entries on the diagonal are nonzero during this time $T \approx \tau_b$.

Since $P^{(3)}(t)$ is not directly accessible experimentally, one has to obtain an equivalent information. The inhomogeneous electromagnetic wave equation

$$\nabla \times \nabla \times \vec{E}_s(\vec{r}, t) + \frac{n^2}{c^2}\frac{\partial^2}{\partial t^2}\vec{E}_s(\vec{r}, t) = -\mu_0 \frac{\partial^2}{\partial t^2}\vec{P}(\vec{r}, t) \quad (4.3)$$

[1] Here the vector character of the electric fields and the polarization is neglected and hence the tensors $S^{(3)}$ and $\chi^{(3)}$ are written as scalars only.

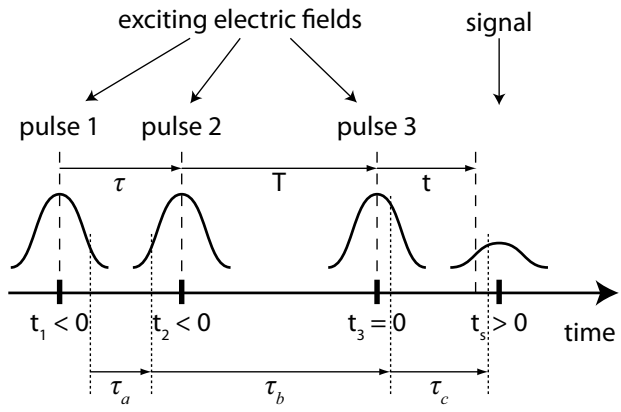

Figure 4.3: Definition of time variables for response function formalism. Three pulses with centers at t_1, t_2, and t_3 interact with the system. The time periods between the interactions are τ_a, τ_b and between pulse 3 and the signal emission τ_c. Experimentally, the times between the pulse centers τ, T, and t are varied and measured, respectively.

shows that the induced nonlinear polarization is a source term for an emitted signal wave $\vec{E}_s(\vec{r}, t)$. c is the speed of light and n is the refractive index of the medium. We consider only solutions that represent a signal propagating in the direction in which the measurement is performed, $\vec{k}_s = -\vec{k}_1 + \vec{k}_2 + \vec{k}_3$. Thus, due to this phase matching we also only need to consider terms in the polarization $\vec{P}(\vec{r}, t)$ that will generate a signal in the direction $\vec{k}_s$ of the form $P_s(t) \exp[\mathrm{i}\vec{k}_s\vec{r} - \mathrm{i}\omega_s t]$. Note that P_s is a complex quantity. Given that there is no reabsorption or propagation effects and within the slowly varying envelope approximation the solution for the signal field is

$$E_s(l, t) = \frac{\mu_0 c \omega_s l}{2n(\omega_s)} \ \mathrm{i} \ P_s(t). \tag{4.4}$$

l is the propagation length through the region where the nonlinear polarization was induced. This means the polarization is linearly proportional to the emitted, and experimentally detected, signal field. The actual measurement is carried out in a spectrometer (see next section) and therefore the frequency domain representation of this relation is useful:

$$E_s(\omega_t) \propto \frac{\omega_t}{n(\omega_t)} \ \mathrm{i} \ P^{(3)}(\omega_t). \tag{4.5}$$

A spectrum $E_s(\omega_t)$ is measured for each setting of τ and T. As both $P^{(3)}$ and E_s are complex, this measurement must be phase-sensitive.

4.2.2 Signal detection with spectral interferometry

The commonly used phase-sensitive method for detecting signal fields in four wave mixing and 2D spectroscopy in particular is "spectral interferometry" (SI) [107, 108]. This heterodyne detection additionally allows amplification of small signals, therefore provides a high sensitivity at small signal levels. In spectral interferometry the interference spectrogram of a superposition of a known and an unknown pulse is recorded. If the amplitude and phase of the reference pulse (also called the "local oscillator", LO) is known the unknown pulse can be retrieved in amplitude and phase.

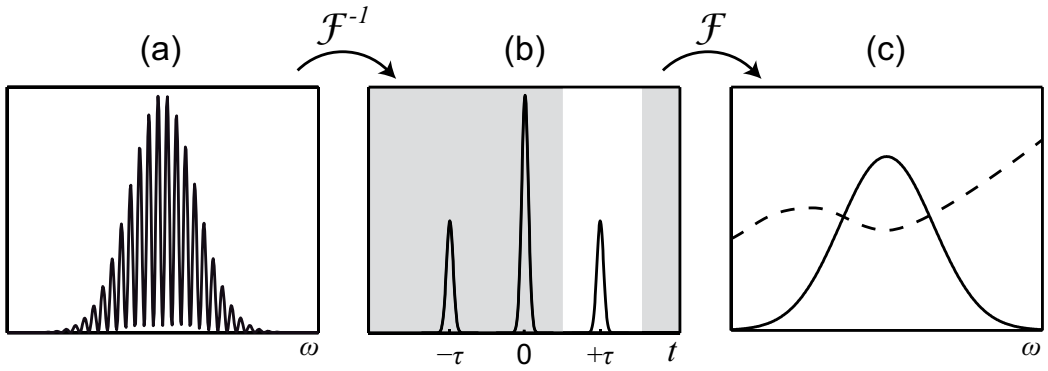

Figure 4.4: Evaluation of spectral interferometry data. (a) Raw modulated spectrum. Inverse Fourier transformation leads to (b) where one can see three peaks in the absolute value at $-\tau, 0$, and $+\tau$. Everything but the third peak is filtered out (indicated by the gray-shaded area) and Fourier transformation leads back to frequency domain. After dividing by the known reference spectrum the unknown spectrum and the phase difference between the unknown and the reference pulse are recovered in (c).

The SI interference intensity spectrum $I_{SI}(\omega)$ is calculated from the superposition of the two electric fields

$$\begin{aligned} I_{SI}(\omega) &= |E_s + E_{LO}|^2 \\ &= \left| \tilde{E}_s(\omega)\ \mathrm{e}^{\mathrm{i}\phi_s(\omega)} + \tilde{E}_{LO}(\omega)\ \mathrm{e}^{\mathrm{i}(\phi_{LO}(\omega)+\omega\tau)} \right|^2 \\ &= I_s + I_{LO} + 2\sqrt{I_s I_{LO}}\ \cos(\phi_s - \phi_{LO} - \omega\tau) \end{aligned} \tag{4.6}$$

as the sum of the intensities plus an interference term that depends on the phases of the signal field ϕ_s, of the LO field ϕ_{LO}, and on the time separation τ (for an illustration see Fig. 4.4 (a)). To obtain the signal field in amplitude and phase from Eq. 4.6 usually the following procedure is used. First the whole spectrum $I_{SI}(\omega)$ is inversely Fourier transformed:

$$\begin{aligned} I_{SI}(t) &= \mathcal{F}^{-1}\left\{I_{SI}(\omega)\right\} = \\ &= \mathcal{F}^{-1}\left\{I_s(\omega)\right\} + \mathcal{F}^{-1}\left\{I_{LO}(\omega)\right\} + \mathcal{F}^{-1}\left\{2\sqrt{I_s I_{LO}}\ \cos(\phi_s - \phi_{LO} - \omega\tau)\right\}. \end{aligned} \tag{4.7}$$

Using the convolution theorem it can easily be shown that this can be written as

$$\begin{aligned} I_{SI}(t) = \mathcal{F}^{-1}\left\{I_s(\omega)\right\} &+ \mathcal{F}^{-1}\left\{I_{LO}(\omega)\right\} \\ &+ \mathcal{F}^{-1}\left\{2\sqrt{I_s(\omega) I_{LO}(\omega)}\ \mathrm{e}^{\mathrm{i}\Delta\phi(\omega)}\right\}(t-\tau) \\ &+ \mathcal{F}^{-1}\left\{2\sqrt{I_s(\omega) I_{LO}(\omega)}\ \mathrm{e}^{-\mathrm{i}\Delta\phi(\omega)}\right\}(t+\tau) \end{aligned} \tag{4.8}$$

where $\Delta\phi(\omega)$ is the phase difference $\phi_s - \phi_{LO}$ between the signal field and the local oscillator field. Because $\Delta\phi(\omega), I_s(\omega)$, and $I_{LO}(\omega)$ are slowly varying functions in ω (compared to $1/\tau$), $I_{SI}(t)$ has three peaks centered at $t = -\tau, 0$, and $+\tau$ (see also

Fig. 4.4 (b)). The transformed data is next filtered using a simple time window that only retains the peak at $+\tau$ (Fig. 4.4 (b)) that corresponds to the third term of Eq. 4.8. Fourier transformation of the filtered signal back to the frequency domain yields

$$\begin{aligned} I_{SI,\ \mathrm{filtered}}(\omega) &= \mathcal{F}\left\{\mathcal{F}^{-1}\left\{2\sqrt{I_s(\omega)I_{LO}(\omega)}\ \mathrm{e}^{\mathrm{i}\Delta\phi(\omega)}\right\}(t-\tau)\right\} \\ &= 2\sqrt{I_s(\omega)I_{LO}(\omega)}\ \mathrm{e}^{\mathrm{i}(\Delta\phi(\omega)+\omega\tau)}. \end{aligned} \tag{4.9}$$

After division by $2\sqrt{I_{LO}(\omega)}$ and subtraction of the linear phase term $\omega\tau$ the signal amplitude $\sqrt{I_s(\omega)}$ and the phase difference $\Delta\phi(\omega)$ are retrieved (see Fig. 4.4 (c)). The phase of the LO is determined in an independent measurement.

4.2.3 Evaluation of two-dimensional spectra and phasing

Having fully characterized the signal field $E_S(\tau, T, \omega_t)$ for each coherence time setting τ, the two-dimensional spectra can be calculated as the Fourier transform along τ

$$S_{\mathrm{2D}}(\omega_\tau, T, \omega_t) = \int_{-\infty}^{+\infty} \mathrm{i}P^{(3)}(\tau, T, \omega_t)\mathrm{e}^{\mathrm{i}\omega_\tau\tau}\mathrm{d}\tau \tag{4.10}$$

with the population time T as a constant parameter for each 2D spectrum. The third order polarization $P^{(3)}$ is obtained from the measured signal field via Eq. 4.5 and can be substituted so that finally

$$S_{\mathrm{2D}}(\omega_\tau, T, \omega_t) = \int_{-\infty}^{+\infty} \frac{n(\omega_t)}{\omega_t} E_s(\tau, T, \omega_t)\mathrm{e}^{\mathrm{i}\omega_\tau\tau}\mathrm{d}\tau. \tag{4.11}$$

This is the complex 2D spectrum that can be plotted as real part $\mathrm{Re}(S_{\mathrm{2D}})$ and imaginary part $\mathrm{Im}(S_{\mathrm{2D}})$ or, alternatively, as amplitude $|S_{\mathrm{2D}}|$ and phase φ_{2D}. While the real part represents the change in absorption after interaction of the sample with the first two pulses the imaginary part represents the change in refractive index.

However, the phase of the spectrum is only determined up to a constant phase φ_0:

$$S_{\mathrm{2D}}(\omega_\tau, T, \omega_t) = |S_{\mathrm{2D}}|\,\mathrm{e}^{\mathrm{i}(\varphi_{\mathrm{2D}}(\omega_\tau, T, \omega_t)+\varphi_0)}. \tag{4.12}$$

Usually, φ_0 is determined by measuring a transient absorption spectrum $S_{\mathrm{TA}}(T, \omega)$ at the corresponding population time T with pulse 1 or 2 as pump and pulse 3 as probe pulse. One then exploits the property that the real part of the ω_t-marginal corresponds to the transient absorption spectrum [109]

$$S_{\mathrm{TA}}(T, \omega_t) \propto \mathrm{Re}\left[\omega_t \hat{E}_{pr}(\omega_t) \int_{-\infty}^{+\infty} S_{\mathrm{2D}}(\omega_\tau, T, \omega_t)\mathrm{d}\omega_\tau\right]. \tag{4.13}$$

Here, $\hat{E}_{pr}(\omega_t)$ is the complex probe field. To be more precise, this "transient absorption spectrum" is the modified probe intensity and *not* the change in optical absorbance.

The independently measured $S_{\mathrm{TA}}(T,\omega_t)$ and the pump–probe spectrum obtained from the 2D spectrum must match. Therefore $S_{\mathrm{2D}}(\omega_\tau,T,\omega_t)$ is "rotated" by changing φ_0 until the shapes of the data match best. In addition to the phase factor of $\exp[\mathrm{i}\varphi_0]$ it might sometimes be necessary to include a small timing offset correction between pulse 3 and the LO $\exp[\mathrm{i}(\omega_t-\omega_0)\delta t]$ [109, 110]. The whole procedure, called the "phasing" of a 2D spectrum, is done for each population time T.

4.2.4 Selection and classification of terms in induced nonlinear polarization

It is worth taking a closer look at the mathematical formulation of the induced nonlinear polarization in Eq. 4.1. On the one hand, different terms of the product describe different physical processes, and on the other hand, the involved phase factors together with the SI method are important from the experimental point of view.

When substituted with the sum of the incident fields (Eq. 4.2) the product of the three electric fields under the integrals yields $(3+3)^3 = 216$ terms (3 single electric fields and 3 conjugations). They each consist of a product of three amplitude functions (or their complex conjugate) at different points in time and three complex phase factors that describe the respective frequency and direction dependencies. Thus, each term corresponds to a certain time ordering and direction of interactions of the fields with the system. As a typical example one can consider the term

$$\begin{aligned}&\tilde{A}(t-t_2-\tau_a-\tau_b-\tau_c)\;\tilde{A}^*(t-t_1-\tau_b-\tau_c)\;\tilde{A}(t-t_3-\tau_c)\times\\&\mathrm{e}^{-\mathrm{i}\omega_0(t-t_2-\tau_a-\tau_b-\tau_c)}\;\mathrm{e}^{\mathrm{i}\omega_0(t-t_1-\tau_b-\tau_c)}\;\mathrm{e}^{-\mathrm{i}\omega_0(t-t_3-\tau_c)}\;\mathrm{e}^{\mathrm{i}(-\vec{k}_1+\vec{k}_2+\vec{k}_3)\vec{r}}.\end{aligned} \tag{4.14}$$

It describes the interaction of the system with pulse 2 at time $t-\tau_a-\tau_b-\tau_c$, then interaction with pulse 1 at time $t-\tau_b-\tau_c$, and another interaction with pulse 3 at the time $t-\tau_c$. For each of the 216 terms the last phase factor that includes the k vectors indicates the direction in which a signal can be expected from this particular sequence of interaction with the electric fields. In total, six terms are "selected" by choosing the detection direction as $\vec{k}_s=-\vec{k}_1+\vec{k}_2+\vec{k}_3$. From this selection it follows that all remaining terms have the common phase factors $\mathrm{e}^{-\mathrm{i}\omega_0 t}\;\mathrm{e}^{\mathrm{i}\omega_0\tau}$ (with $\tau=-t_1+t_2+t_3$). Additionally, they can be divided into three categories with the phase factor $\mathrm{e}^{\mathrm{i}\omega_0(\tau_c-\tau_a)}$, $\mathrm{e}^{\mathrm{i}\omega_0(\tau_a+\tau_c)}$, or $\mathrm{e}^{\mathrm{i}\omega_0(\tau_a+2\tau_b+\tau_c)}$.

For a further simplification we now move our attention from the electric field part of Eq. 4.1 to the response function $S^{(3)}(\tau_a,\tau_b,\tau_c)$. The latter can be regarded as a sum

$$S^{(3)}(\tau_a,\tau_b,\tau_c)=\sum_j S_j^{(3)}(\tau_a,\tau_b,\tau_c) \tag{4.15}$$

of terms $S_j^{(3)}(\tau_a,\tau_b,\tau_c)$ that represent different pathways in Liouville space [104]. Some of these terms have phase factors similar to those of the electric field terms. One can next apply the rotating-wave approximation. Only those terms where the contributions of phase factors from the electric field terms and from the response function cancel will yield a significant value after evaluation of the integral. Terms with phases that oscillate

with τ_i will be negligible. For the six terms in the detection direction $\vec{k}_s$ we can therefore write

$$
\begin{aligned}
P^{(3)}(\tau,T,t) = \mathrm{e}^{-\mathrm{i}\omega_0 t+\mathrm{i}\omega_0\tau} \int_0^\infty\int_0^\infty\int_0^\infty \mathrm{d}\tau_a\mathrm{d}\tau_b\mathrm{d}\tau_c \\
\Big\{ S_R^{(3)}(\tau_a,\tau_b,\tau_c)\mathrm{e}^{\mathrm{i}\omega_0(\tau_c-\tau_a)}\big[\tilde{A}^*(t-t_1-\tau_a-\tau_b-\tau_c)\tilde{A}(t-t_2-\tau_b-\tau_c)\tilde{A}(t-t_3-\tau_c)+ \\
+\tilde{A}^*(t-t_1-\tau_a-\tau_b-\tau_c)\tilde{A}(t-t_3-\tau_b-\tau_c)\tilde{A}(t-t_2-\tau_c)\big]+ \\
S_{NR}^{(3)}(\tau_a,\tau_b,\tau_c)\mathrm{e}^{\mathrm{i}\omega_0(\tau_a+\tau_c)}\big[\tilde{A}(t-t_2-\tau_a-\tau_b-\tau_c)\tilde{A}^*(t-t_1-\tau_b-\tau_c)\tilde{A}(t-t_3-\tau_c)+ \\
+\tilde{A}(t-t_3-\tau_a-\tau_b-\tau_c)\tilde{A}^*(t-t_1-\tau_b-\tau_c)\tilde{A}(t-t_2-\tau_c)\big]+ \\
S_{DC}^{(3)}(\tau_a,\tau_b,\tau_c)\mathrm{e}^{\mathrm{i}\omega_0(\tau_a+2\tau_b+\tau_c)}\big[\tilde{A}(t-t_2-\tau_a-\tau_b-\tau_c)\tilde{A}(t-t_3-\tau_b-\tau_c)\tilde{A}^*(t-t_1-\tau_c)+ \\
+\tilde{A}(t-t_3-\tau_a-\tau_b-\tau_c)\tilde{A}(t-t_2-\tau_b-\tau_c)\tilde{A}^*(t-t_1-\tau_c)\big]\Big\}
\end{aligned}
\tag{4.16}
$$

where the terms of the response function that are retained by the rotating-wave approximation are written as $S_R^{(3)}$, $S_{NR}^{(3)}$, and $S_{DC}^{(3)}$. $S_R^{(3)}$ contains the so-called rephasing pathways where the phase gained during τ_c is equal but of opposite sign of the accumulated phase during τ_a. The phase factor $\exp[\mathrm{i}\omega_0(\tau_c-\tau_a)]$ leads to a large contribution in $P^{(3)}$ when $t \approx \tau$. This is usually called the photon echo. For the $S_{NR}^{(3)}$ term on the other hand such a rephasing is not possible but the phases add up $\exp[\mathrm{i}\omega_0(\tau_a+\tau_c)]$. These "non-rephasing pathways" contribute to the signal as the free induction decay only. Finally, the "double coherence" part $S_{DC}^{(3)}$ has a phase factor of $\exp[\mathrm{i}\omega_0(\tau_a+2\tau_b+\tau_c)]$. To what extent the different pathways contribute and if they are present at all depends on the system under study. As a simple example one can imagine a system that couples strongly to a bath; there rephasing of the system as a whole is strongly suppressed and $S_R^{(3)}$ is small. The experimental timings τ and T are contained implicitly in the arguments of the field amplitudes: $\tau = -t_1 + t_2 + t_3$ and $T = -t_2 + t_3$ (the time origin is set at $t_3 = 0$).

4.2.5 Oscillatory character of measured signal

Even though 2D spectroscopy represents a powerful spectroscopic tool and provides a wealth of information about a molecular system, experimentally, it can be challenging to carry out. The major experimental issue is the appropriate signal measurement.

2D spectroscopy is a Fourier method and as stated before, the frequency axis in ω_τ is obtained through Fourier transformation of data collected as a function of τ (see Eq. 4.11). As with any Fourier method, the times τ of the data points (or in this case whole signal spectra) must be known precisely. If there is a slight drift or random deviation of the actual measurement times the resulting transformed spectrum will suffer distortion or unwanted signal decrease [111]. Therefore, the time delay τ between the pulses 1 and 2 has to be introduced precisely, ideally [111], with a deviation of less than $\frac{1}{50}\frac{2\pi}{\omega_0}$ corresponding to a timing jitter of only 0.04 fs at $\lambda_0 = 600$ nm.

Conversely, the phase-sensitive measurement of the signal spectra itself entails the requirement of precise control over the time delay between pulse 3 (which represents

$t = 0$) and the local oscillator pulse. If unwanted drifts or jitters are introduced, the recovered signal field absorbs the mistimed pulse arrival in an additional, inappropriate phase (see Eq. 4.9). Provided that the additional delay is constant for all recorded spectra, this effect can partly be compensated in the phasing procedure after acquisition of the whole 2D spectrum [110]. Drifts and jitters, however, cannot be compensated and again lead to distortions and signal decrease.

These two requirements, extreme precision in τ and extreme precision in t, are often paraphrased as the requirement of interferometric phase stability between the pulses in a 2D spectroscopy setup. The shorter the wavelength the more severe this requirement becomes and, unfortunately, in general it cannot be met using simple setups that split, delay, and recombine the pulses in a conventional way. This poses a major obstacle to easy collection of 2D data. This is also probably the most important reason why implementations of 2D spectroscopy for the visible and shorter wavelength regime are not spread as widely as one would expect based on the wealth of information that can be gained through 2D spectroscopy. This obstacle was the main motivation for the present work to improve on the available techniques and to devise an experimentally simple setup for easy collection of 2D spectra.

4.3 Previous experimental implementations

Experimental development of 2D spectroscopy for electronic excitation in the near infrared spectral region has been lead by the groups of Jonas [112] and Hochstrasser [113]. Hamm [113, 114], and Tokmakoff [115] developed 2D spectroscopy with vibrational excitation in the MIR region. In the visible range, 2D spectroscopy was implemented by the groups of Fleming [110, 116] and Miller [117].

As detailed in the previous section, one of the most challenging requirements of coherent multidimensional spectroscopy in a non-collinear photon-echo geometry is the relative phase stability of the laser pulses that generate and measure the nonlinear signal. Small drifts or vibrations of beam splitters and mirrors lead to drifts or oscillations in the signal phase and therefore, after Fourier transformation, to distortions in the measured 2D trace. Nevertheless, 2D spectroscopy in the optical regime has been demonstrated successfully. For these breakthroughs and subsequent demonstrations that established 2D spectroscopy as an experimental method the phase stability requirements had to be met by special measures.

Passive phase stabilization was obtained using diffractive optics [110, 116–119] as beam splitters. In these schemes, small vibrations of the diffractive beam splitter do not change the phase between the two resulting pulses significantly, because both beam paths change by the same amount. After splitting the beams with diffractive optics it is especially advantageous to manipulate them with common optics so that the additionally introduced time delays are common to both split beams. To precisely introduce the deliberate delays Brixner *et al.* [116] used movable glass wedges (see schematic setup in Fig. 4.5). Recently, this kind of setup was also implemented in the group of Kauffmann [120, 121].

However, the disadvantage of diffractive optics based setups is that the diffraction

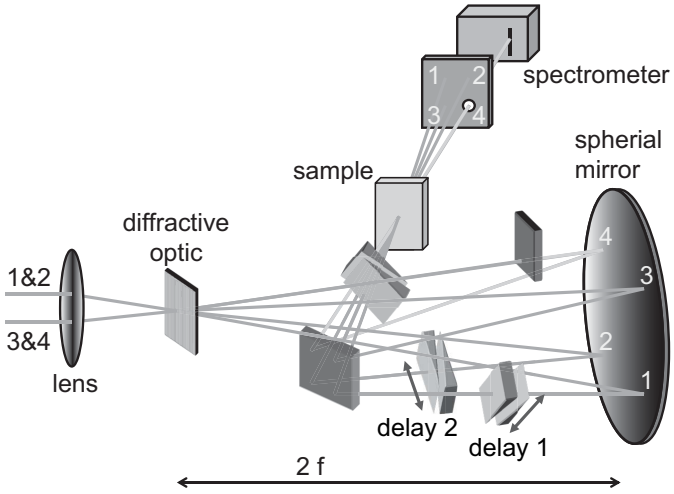

Figure 4.5: Setup for 2D spectroscopy by Brixner *et al.* [110, 116]. Beams 1,2 and 3,4 are split conventionally (not shown) and then split into 1, 2, 3, and 4 by a diffractive optic. The beams are all manipulated only by the same optics and delays are introduced via movable glass wedges. (Figure adapted from Ref. [116].)

introduces angular dispersion. This can make the propagation and manipulation of the widened, dispersed beams impracticable. The diffractive optic approach can thus be unsuitable for the bandwidths already used in current 2D-IR experiments or for future ultrabroadband applications in the VIS. Even for narrowband applications, tuning the wavelength requires realigning the setup (due to the varying diffraction angles) and even exchanging the diffractive optics that are custom-designed for a particular central wavelength. The drawback that arises from the use of glass wedges for introducing the time delays is that the varying material thickness over the experiment can cause significant changes of the pulse shape, in particular if very broad spectra are used. This can also lead to distortions of the measured 2D spectra.

As a different approach, femtosecond pulse shaping was used by Warren and coworkers [87] to provide the pulse sequences with inherent phase stability in an all-collinear beam geometry. Their technique incorporates phase cycling and is the direct optical analogue of 2D nuclear magnetic resonance spectroscopy. Damrauer and Zanni [122, 123] used a pulse shaper in a transient absorption setup to modulate the pump pulses and create a time-delayed pulse pair. The detection is facilitated via the probe beam that acts as LO as well. The overall geometry of this setup is hence partially collinear. This makes setting up the experiment easy, however, the contributions of many copropagating nonlinear signals such as signals of rephasing and non-rephasing pathways are inevitably recorded simultaneously in (partially) collinear geometries. While the latter can be an advantage in some cases, the specific insight provided by the separate analysis, e.g. when studying electronic coherences in multichromophoric systems, is no longer possible. Furthermore, in noncollinear setups the local oscillator strength can be independently adjusted to accommodate small signal levels. The need for phase cycling is eliminated in a noncollinear geometry which further enhances the applicability. Depending on the particular application, a non-collinear geometry can therefore be preferred.

Feurer and Nelson [124] were able to create four noncollinear but phase-stable beams with a two-dimensional LC array in a 4f pulse-shaper setup. The respective time delays were introduced by applying the proper phase masks to the LC array. The authors also extended their setup and showed that it is possible to independently control the phase

and the spectrum of all excitation pulses [125]. This is the basis for future combinations of coherent control schemes with two-dimensional spectroscopy.

These pulse shaper-based schemes provide flexibility in the ways the spectra are collected and allow for varying excitation pulse shapes. However, one has to consider the limitations due to pulse-shaper resolution, limited temporal scanning range, finite pixel sizes, inter-pixel gaps, pre and post pulses, and space-time coupling, among others, along with a reduced energy throughput.

A third technique for achieving phase stability is active stabilization. The groups of Cundiff [126] and Hamm [127] demonstrated that the phases of the excitation pulses can be kept constant with a feedback loop via continuous adjustment of path length. It has been shown that this is a good and very effective means, but it requires additional interferometers, reference lasers, and electronics for determining the phases of all beams.

4.4 Inherently phase-stable setup using conventional optics only

With the goal in mind to make 2D spectroscopy easy to implement it is obvious from the previous section that there is room for improvement on how to achieve a phase-stable setup. Our novel approach that has partly been developed within this thesis work facilitates easy collection of two-dimensional spectra and is simple to implement because it only uses conventional optics and no active components.

4.4.1 Manipulation of pulse pairs as a basis for stability

The basic idea that allows us to achieve passive phase stability has been introduced by the group of Miller. In combination with beam splitting using diffractive optics they manipulated only pairs of the beams that create and detect the nonlinear signal [117]. Here we show that passive phase stability can even be achieved using only conventional beam splitters and without the need for diffractive beam splitting.

To motivate how the manipulation of pulse pairs can lead to passive phase-stability we will calculate the changes in signal phase (fast oscillations) that result from small changes of the experimental timings t_1, t_2, and t_3. Afterwards we will combine this result with the detection of the signal phase via spectral interferometry and deduce the conditions under which phase stability is possible.

We start from the third order polarization $P^{(3)}(\tau, T, t)$ in Eq. 4.1. Again we only consider the terms in the electric fields that will cause a signal in the detection direction. Here however, the third order response function is not split into the sum defined in Eq. 4.15, i.e., the different Liouville pathways need not be distinguished. Unlike in

Eq. 4.16, we will not factor out common phases at this point. Hence, we can write

$$P^{(3)}(\tau,T,t) = \int_0^\infty \int_0^\infty \int_0^\infty \mathrm{d}\tau_a\,\mathrm{d}\tau_b\,\mathrm{d}\tau_c \left\{ S^{(3)}(\tau_a,\tau_b,\tau_c) \sum_{j=1}^{6} B_j(t,t_1,t_2,t_3,\tau_a,\tau_b,\tau_c) C_j(t,t_1,t_2,t_3,\tau_a,\tau_b,\tau_c) \right\} \tag{4.17}$$

where the sum is over the six electric field terms that cause emission in the detection direction. These terms are separated into amplitude and phase. B_j are the amplitudes that result from the multiplication of the envelope functions $\tilde{A}$ and their complex conjugates. The phases are contained within the functions C_j with $|C_j| = 1$. It should be noted that if the laser pulses possess a nonzero temporal phase $\varphi(t')$ in $\tilde{A}(t')$, B_j will also contain phase factors. The term from Eq. 4.14 can serve as an example again:

$$\begin{aligned} B_3(t,t_1,t_2,t_3,\tau_a,\tau_b,\tau_c) &= \tilde{A}(t-t_2-\tau_a-\tau_b-\tau_c)\ \tilde{A}^*(t-t_1-\tau_b-\tau_c) \\ &\quad\times\ \tilde{A}(t-t_3-\tau_c) \\ C_3(t,t_1,t_2,t_3,\tau_a,\tau_b,\tau_c) &= \mathrm{e}^{-\mathrm{i}\omega_0(t-t_2-\tau_a-\tau_b-\tau_c)}\ \mathrm{e}^{\mathrm{i}\omega_0(t-t_1-\tau_b-\tau_c)}\ \mathrm{e}^{-\mathrm{i}\omega_0(t-t_3-\tau_c)}. \end{aligned} \tag{4.18}$$

Since the signal will be detected in the frequency domain, $P^{(3)}(\tau,T,t)$ must be Fourier transformed with respect to the detection time t to yield the signal field

$$E_s(\tau,T,\omega_t) \propto \mathcal{F}\left\{P^{(3)}(\tau,T,t)\right\} \propto \int_{-\infty}^{+\infty} \mathrm{d}t\ \mathrm{e}^{\mathrm{i}\omega_t t}\ P^{(3)}(\tau,T,t). \tag{4.19}$$

Note that, contrary to the usual convention used throughout the rest of this thesis, in the 2D spectroscopy field the Fourier transform is defined as $f(\omega) = \mathcal{F}\{f(t)\} = \int f(t)\exp[\mathrm{i}\omega t]\mathrm{d}t$. This convention [104, 110, 128] will be used in this chapter. Instead of using the time periods τ and T we rather write the signal field as a function of the experimentally varied pulse centers (t_1,t_2,t_3)

$$E_s(\omega_t,t_1,t_2,t_3) \propto \int_{-\infty}^{+\infty} \mathrm{d}t\ \mathrm{e}^{\mathrm{i}\omega_t t} \int_0^\infty \int_0^\infty \int_0^\infty \mathrm{d}\tau_a\mathrm{d}\tau_b\mathrm{d}\tau_c \left\{ S^{(3)}(\tau_a,\tau_b,\tau_c) \sum_{j=1}^{6} B_j(t,t_1,t_2,t_3,\tau_a,\tau_b,\tau_c) C_j(t,t_1,t_2,t_3,\tau_a,\tau_b,\tau_c) \right\}. \tag{4.20}$$

The next step is to identify and quantify all dependencies of E_s on t_1, t_2, and t_3 that have an oscillatory character, i.e., all phase terms that can be written in a form $\exp[\mathrm{i}X(t_1,t_2,t_3)]$ on the right hand side of Eq. 4.20. It is clear that the C_j phase terms will lead to such phases that can be factored out of the sum and the integrals. This was, for instance, done for the term $\exp[\mathrm{i}\omega_0\tau] \equiv \exp[\mathrm{i}\omega_0(-t_1+t_2+t_3)]$ in Eq. 4.16. Additionally, the B_j terms will also give rise to phases of the total signal field because the Fourier transform $\hat{f}$ of a complex function in general results in a phase that depends on both

the amplitude and the phase of the original function f. The Fourier shift theorem states that additional phase terms in the transformed function may result from the argument of the original function. Thus, for quantifying the phase terms $X(t_1, t_2, t_3)$ fully, it is necessary to consider the entire electric field terms $B_j C_j$.

We now assume that the electric field is described by a real-valued Gaussian envelope function

$$\tilde{A}(t) = \mathrm{e}^{-2\ln 2 \frac{t^2}{\Delta t^2}} \tag{4.21}$$

with zero phase and a duration of Δt (FWHM of intensity). Further we can use Fubini's theorem which states that one can change the order of the integrations in Eq. 4.20 because the integrand is continuous and the integration will yield a finite result. Reordering results in

$$\begin{aligned} E_s(\omega_t, t_1, t_2, t_3) \propto \mathrm{e}^{\mathrm{i}\omega_0(-t_1+t_2+t_3)} \int_0^\infty \int_0^\infty \int_0^\infty \mathrm{d}\tau_a \mathrm{d}\tau_b \mathrm{d}\tau_c \; S^{(3)}(\tau_a, \tau_b, \tau_c) \times \\ \left\{ \sum_{j=1}^{6} \mathrm{e}^{\mathrm{i}\omega_0 P_j(\tau_a,\tau_b,\tau_c)} \int_{-\infty}^{+\infty} \mathrm{d}t \; \mathrm{e}^{\mathrm{i}(\omega_t-\omega_0)t} \tilde{A}(t-\tilde{t}_{j1}) \tilde{A}(t-\tilde{t}_{j2}) \tilde{A}(t-\tilde{t}_{j3}) \right\}. \end{aligned} \tag{4.22}$$

Here we have omitted the complex conjugation because of the real-valued envelopes. Further, the common phase terms were factored out and the τ_k-dependent phase terms were absorbed into a function $P_j(\tau_a, \tau_b, \tau_c)$ that is different for each Liouville pathway. The term for $j = 3$, for instance, has $P_3(\tau_a, \tau_b, \tau_c) = \tau_a + \tau_b$. The time arguments of the envelopes are abbreviated as $t - \tilde{t}_{jk}$. The term $j = 3$ (see Eq. 4.18) would, for instance, have $\tilde{t}_{31} = t_2 + \tau_a + \tau_b + \tau_c$, $\tilde{t}_{32} = t_1 + \tau_b + \tau_c$, and $\tilde{t}_{33} = t_3 + \tau_c$. The goal to separate out all t_k dependencies hence requires us to Fourier transform the product of three Gaussians with different centers.

The identity

$$\mathrm{e}^{-a(x-x_a)^2} \, \mathrm{e}^{-a(x-x_b)^2} \, \mathrm{e}^{-a(x-x_c)^2} = \mathrm{e}^{-\frac{2}{3}a(x_a^2+x_b^2+x_c^2-x_a x_b-x_a x_c-x_b x_c)} \, \mathrm{e}^{-a[x-\frac{1}{3}(x_a+x_b+x_c)]^2} \tag{4.23}$$

shows that the product of three equally wide and intense Gaussians centered at x_a, x_b, and x_c is equal to another, scaled Gaussian of the same width with a shifted center at $(x_a + x_b + x_c)/3$. Applying this identity to Eq. 4.22 results in

$$\begin{aligned} E_s(\omega_t, t_1, t_2, t_3) \propto \mathrm{e}^{\mathrm{i}\omega_0(-t_1+t_2+t_3)} \int_0^\infty \int_0^\infty \int_0^\infty \mathrm{d}\tau_a \mathrm{d}\tau_b \mathrm{d}\tau_c \; S^{(3)}(\tau_a, \tau_b, \tau_c) \times \\ \left\{ \sum_{j=1}^{6} \mathrm{e}^{\mathrm{i}\omega_0 P_j(\tau_a,\tau_b,\tau_c)} D(\tilde{t}_{j1}, \tilde{t}_{j2}, \tilde{t}_{j3}) \int_{-\infty}^{+\infty} \mathrm{d}t \; \mathrm{e}^{\mathrm{i}(\omega_t-\omega_0)t} \tilde{A}\left[t - (\tilde{t}_{j1} + \tilde{t}_{j2} + \tilde{t}_{j3})/3\right] \right\} \end{aligned} \tag{4.24}$$

where the constant scaling factor $D(\tilde{t}_{j1}, \tilde{t}_{j2}, \tilde{t}_{j3})$ was written in front of the Fourier integral. An inspection of all $\tilde{A}(t - \tilde{t}_{jk})$ terms shows that

$$\tilde{t}_{j1} + \tilde{t}_{j2} + \tilde{t}_{j3} = (t_1 + t_2 + t_3) + (\tau_a + 2\tau_b + 3\tau_c) \tag{4.25}$$

for all j. Using the Fourier shift theorem in the form

$$\int_{-\infty}^{+\infty} \mathrm{d}t\ \mathrm{e}^{\mathrm{i}(\omega_t-\omega_0)t}\tilde{A}(t-t') = \mathrm{e}^{\mathrm{i}(\omega_t-\omega_0)t'}\ \mathcal{F}\left\{\tilde{A}(t)\right\}[\omega_t-\omega_0] \tag{4.26}$$

for the last integral in Eq. 4.24 we can finally write

$$E_s(\omega_t,t_1,t_2,t_3) \propto \mathrm{e}^{\mathrm{i}\omega_0(-t_1+t_2+t_3)}\ \mathrm{e}^{\mathrm{i}\frac{1}{3}(\omega_t-\omega_0)(t_1+t_2+t_3)} \int_0^\infty\int_0^\infty\int_0^\infty \mathrm{d}\tau_a\mathrm{d}\tau_b\mathrm{d}\tau_c \times$$

$$\left\{S^{(3)}(\tau_a,\tau_b,\tau_c)\mathrm{e}^{\mathrm{i}\frac{1}{3}(\omega_t-\omega_0)(\tau_a+2\tau_b+3\tau_c)}\sum_{j=1}^{6}\mathrm{e}^{\mathrm{i}\omega_0 P_j(\tau_a,\tau_b,\tau_c)}D(\tilde{t}_{j1},\tilde{t}_{j2},\tilde{t}_{j3})\mathrm{e}^{-\frac{\Delta t^2}{8\ln 2}(\omega_t-\omega_0)^2}\right\}. \tag{4.27}$$

This form of E_s illustrates that the oscillatory behavior of the signal as a function of the pulse arrival times t_k is caused by two exponential factors that we have isolated from all other dependencies of E_s.

Besides causing the oscillatory behavior of the signal E_s, the pulse arrival times t_k also affect the accurate measurement of the third order response $S^{(3)}$. The factors $D(\tilde{t}_{j1},\tilde{t}_{j2},\tilde{t}_{j3})$ are of Gaussian form (see Eq. 4.23) in the times $\tilde{t}_{jk}$ and thus also in the pulse arrival times t_k. The multiplication of $S^{(3)}$ with $D(\tilde{t}_{j1},\tilde{t}_{j2},\tilde{t}_{j3})$ and the integration over the variables τ_a,τ_b, and τ_c hence corresponds to a "sampling" of the response function $S^{(3)}$. For an accurate measurement of the response function of a molecular system, the restriction that results from the term $D(\tilde{t}_{j1},\tilde{t}_{j2},\tilde{t}_{j3})$ on the pulse arrival times is therefore the following. The uncertainty of the pulse arrival times must be less than the timescale of the fastest dynamics of the molecular system under study. However, this requirement also applies to other kinds of time-resolved techniques such as transient absorption spectroscopy and is not specific to 2D spectroscopy. Optical delay lines for delay generation of femtosecond pulses generally meet this requirement.

In order to lessen the effects of the oscillatory behavior of the signal as a function of the pulse arrival times – the requirement of phase stability – we can exploit the separation of the phase factors in Eq. 4.27. We consider the actual experimentally measured signal, i.e. the SI spectrum

$$I_{SI}(\omega_t) = \left|E_s(\omega_t) + E_4(\omega_t)\right|^2. \tag{4.28}$$

Now we introduce small shifts of the arrival times of pulses 1–3 and of the LO (pulse 4)

$$t_k \to t_k + \Delta t_k \tag{4.29}$$

as they would arise from small instabilities or vibrations in an experimental setup. In air the group velocity dispersion is negligible and the small path length changes regarded here only affect the arrival times of the pulses. Small vibrations do not change the pulse shape (such as the carrier–envelope offset) significantly. Thus the signal changes its phase according to the first two factors in Eq. 4.27 and the LO acquires an additional phase $\exp[\mathrm{i}\omega_t\Delta t_4]$ so that the measured interferogram changes to

$$I_{SI}(\omega_t) = \left|E_s(\omega_t)\,\mathrm{e}^{\mathrm{i}\omega_0(-\Delta t_1+\Delta t_2+\Delta t_3)+\frac{1}{3}\mathrm{i}(\omega_t-\omega_0)(\Delta t_1+\Delta t_2+\Delta t_3)} + E_4(\omega_t)\mathrm{e}^{\mathrm{i}\omega_t\Delta t_4}\right|^2. \tag{4.30}$$

	pulse 1	pulse 2	pulse 3	pulse 4
Δ_{12}	$\rightarrow$	$\rightarrow$		
Δ_{13}	$\rightarrow$		$\rightarrow$	
Δ_{24}		$\rightarrow$		$\rightarrow$
Δ_{34}			$\rightarrow$	$\rightarrow$
Δt_j	$\Delta_{12}+\Delta_{13}$	$\Delta_{12}+\Delta_{24}$	$\Delta_{13}+\Delta_{34}$	$\Delta_{24}+\Delta_{34}$

Table 4.1: Pairwise correlated fluctuations of pulse arrival times. The timing fluctuations Δ_{jk} affect the pulses j and k that are marked with "$\rightarrow$" in the table. The resulting total timing shifts Δt_j are given for each pulse in the bottom row. This pairwise correlation of timing shifts results in cancellation of unwanted signal phase terms of zero order in ω_t (see text).

Hence the detected phase change of the fringe pattern in the spectrometer is

$$\begin{aligned}\varphi_{SI} &= \omega_0(-\Delta t_1+\Delta t_2+\Delta t_3)+\frac{1}{3}(\omega_t-\omega_0)(\Delta t_1+\Delta t_2+\Delta t_3)-\omega_t\Delta t_4\\ &= \omega_0(-\Delta t_1+\Delta t_2+\Delta t_3-\Delta t_4)+\frac{1}{3}(\omega_t-\omega_0)(\Delta t_1+\Delta t_2+\Delta t_3-3\Delta t_4).\end{aligned} \tag{4.31}$$

It is obvious that $\omega_0 > |\omega_t-\omega_0|$, especially for small to moderate bandwidths, and therefore the major contribution to the unwanted phase shift φ_{SI} results from the first term that is constant with respect to ω_t. This contribution will vanish if

$$-\Delta t_1+\Delta t_2+\Delta t_3-\Delta t_4=0. \tag{4.32}$$

If we now assume that all path-length fluctuations are correlated in a pairwise fashion such that

$$\begin{aligned}\Delta t_1 &= \Delta_{12}+\Delta_{13}\\ \Delta t_2 &= \Delta_{12}+\Delta_{24}\\ \Delta t_3 &= \Delta_{13}+\Delta_{34}\\ \Delta t_4 &= \Delta_{24}+\Delta_{34}\end{aligned} \tag{4.33}$$

and no other timing fluctuations are possible, the condition in Eq. 4.32 will always be met. This pairwise correlation given in Eq. 4.33 is illustrated in table 4.1. In other words, pairwise correlations of drifts and jitters of the pulse arrival times result in complete cancellation of the unwanted zero order phase shift of the SI signal.

The phase shift that is linear in ω_t,

$$\varphi_{SI,\text{remaining}}=\frac{2}{3}(\omega_t-\omega_0)(\Delta_{12}+\Delta_{13}-\Delta_{24}-\Delta_{34})=\frac{2}{3}(\omega_t-\omega_0)(\Delta t_1-\Delta t_4), \tag{4.34}$$

is partially compensated. With the assumption that a successful 2D measurement requires the uncompensated phase to remain smaller than $|\varphi_{SI}|<2\pi/50$ one can further quantify the stability requirement on the optics to

$$|\Delta t_1-\Delta t_4|<\frac{3}{2}\,\frac{2\pi}{50}\,\frac{1}{|\omega_t-\omega_0|}. \tag{4.35}$$

This requirement holds for the full bandwidth over which a 2D spectrum is to be measured. When transform-limited Gaussian pulses of bandwidth $\Delta\omega$ (FWHM) and duration Δt (with a time–bandwidth product $\Delta\omega\Delta t = 0.441 \times 2\pi$) are used to detect SI fringes over ca. $2\Delta\omega$, one can also reduce the stability requirement resulting from the linear, uncompensated phase part to

$$|\Delta t_1 - \Delta t_4| < \frac{3}{2}\,\frac{1}{50}\,\frac{\Delta t}{0.441} = 0.07\ \Delta t. \tag{4.36}$$

On the other hand without the pairwise manipulation of pulses, the fluctuations of the pulse arrival times must meet the condition

$$|\Delta t_j| < \frac{2\pi}{50}\,\frac{1}{\omega_0} = 0.02\ T \tag{4.37}$$

where T is the oscillation period of the electric field. Hence, the difference between the stability conditions provided by our passive stabilization method (Eq. 4.36) and the unstabilized version (Eq. 4.37) can be illustrated as follows. Pairwise manipulation only requires the pulse arrival times to be kept constant to 7% of the pulse *duration* Δt while without stabilization they have to be constant to 2% of the carrier frequency *oscillation period* T. This represents a great relaxation of the often quoted "interferometric" phase stability requirements.

4.4.2 Experimental setup

The presented principle was used to design an inherently phase-stable experimental setup for measuring 2D spectra in the visible spectral regime. This setup uses only conventional optics and is simple to construct.

The pulses entering the setup (shown in Fig. 4.6) are derived from the NOPA and their phases are precompensated for the dispersion of the 2D setup so that they are as short as possible at the sample position. The pairwise manipulation is realized by first splitting the incoming beam into the two beams "1/2" and "3/4" with the vertically arranged beam splitter and mirror combination BS1/M1. (An inset in the bottom left of Fig. 4.6 shows this combination from the side.) In the whole setup the beams are guided on two levels that are indicated by dashed lines for laser beams on the top level and solid lines for laser beams on the bottom level. A time delay between the initially split beams "1/2" and "3/4" is introduced by delay stage DS1. DS1 is a combination of a motorized linear translator (Newport UTM-50) and a high precision piezo element (Piezosysteme Jena PX 200 CAP DIG) that allows the coarse adjustment of the position between 0 and 50 mm as well as its precise variation in a range of 160 μm with a resolution of 1 nm. Note that contrary to usual laboratory practice the bottom beam "1/2" is not further delayed after redirection by mirror M1 but the zero delay position of DS1 instead compensates for the optical path length between BS1 and M1. This makes the setup more compact and fewer optics can be used and also contributes to the stability. The distance BS1–M1 (and hence the beam distance in the box geometry) is 3 cm in our setup. In the sense that the pair "1/2" will later form the pulses 1 and 2 and the pair "3/4" will form the pulses 3 and 4, the manipulation of beam "1/2" and "3/4" is

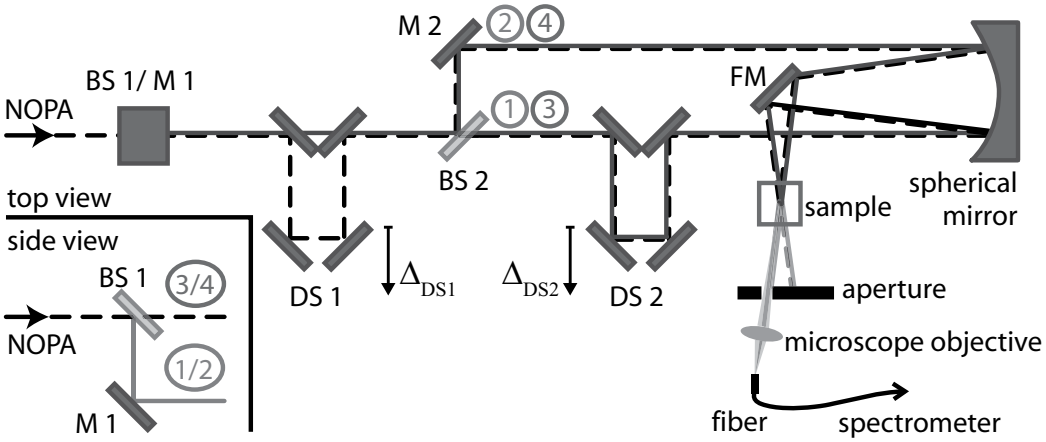

Figure 4.6: Inherently phase-stable setup for 2D spectroscopy in the visible. Beam splitting is facilitated by conventional metal-coated optics in the combinations BS1/M1 and BS2/M2. The respective time delays are introduced by stages DS1 and DS2. The four parallel beams are focused into the sample by a spherical mirror via the folding mirror FM. The third order signal and the LO are selected by an aperture and coupled into a single mode fiber.

equivalent to a pairwise (correlated) manipulation that introduces the time shifts Δ_{12} and Δ_{34}, respectively, as defined in Eq. 4.33.

Then the combination BS2/M2 splits the beams "1/2" and "3/4" further. Both beams hit the beam splitter BS2 vertically displaced and are split in the respective horizontal planes, creating the reflected beams 2 and 4 as well as the transmitted beams 1 and 3. Pairwise manipulation, in this case correlated manipulation of beams 2 and 4, is achieved by using a single tall beam splitter and a single mirror, meaning that both beams are manipulated by the same optics. In analogy to the delay between "1/2" and "3/4" delay stage DS2 creates the necessary time difference between the beam pairs "1/3" and "2/4". Here however, tall mirrors reflect both vertically displaced beams 1 and 3 in order to maintain the correlation of their timings. DS2 is a combination of a manual linear translator and another piezo element of the same type as the one used in DS1.

Finally, all four parallel beams impinge upon a spherical focusing mirror in straight back reflection geometry. The converging beams are picked off by the folding mirror FM and directed into the sample cell. This arrangement eliminates the need for an off-axis parabolic mirror that is in general more complicated to align. The resulting spot size in the sample is approximately 100 μm. Behind the sample, an aperture selects the signal and the local oscillator (beam 4) and blocks all other beams, including potentially scattered light. Then the signal and the LO are focused onto a single mode fiber by a 10x microscope objective. The back-propagation of the small transversal mode of the fiber into the sample results in a small volume from which the signal and the LO are collected. Ideally, this should result in the selection of a homogenous area where any spatial effects on the third order signal (resulting for example from spatial chirp or a poor spatial intensity profile) are mitigated. However, it should be noted that this spatial (especially angular) selection can also lead to a certain loss of features in

the 2D spectrum [129]. For signal detection the fiber is connected to a high-resolution spectrometer (Acton SpectraPro 2500i) fitted with a 16-bit 2D charge-coupled-device (CCD) camera with 512×2048 pixels (Roper Scientific PIXIS 2K).

The setup also includes compensation glass plates (not shown in Fig. 4.6) that offset the dispersion caused by the beam splitters. Further, with the assistance of a variable attenuator wheel the intensity of the LO is adjusted to a suitable level with respect to the third order signal intensity. A final compensation plate in the LO beam path can be chosen such that the combined glass thickness that it passes through causes the LO to either arrive after the other beams or to arrive before all other beams. The latter case implicates limitations to the scanning range of the population time; see section 4.4.3. In order to avoid local air currents that can affect single beams and thus destroy the pairwise correlation the entire setup as shown in Fig. 4.6 is enclosed in a plexiglass box. The stability of the piezo elements is also improved by this measure because their calibration is not perturbed by external influences such as temperature fluctuations. Four automated, computer-controlled rotary solenoids are mounted on the lid of the box. These move four beam blocks that extend into the beam path in the box and that are used for acquiring spectra of different combinations of excitation beams to correct the signal spectra for scattered light (see section 4.4.4). The solenoids are mounted outside of the box because when in operation they create heat that would cause dilations of the setup and thus destroy the phase stability [111].

Our current setup is designed for visible excitation with a very broad spectrum. Therefore we used silver coatings with a flat and high reflectance for the bending and focusing mirrors. It is important that the different excitation pulses have an equal spectrum. This is very hard to accomplish with dielectric (or Bragg) partial reflectors for a broad spectral range when at the same time the introduced dispersion has to be kept as low as possible. Thin metallic coatings however can provide both low dispersion and a spectrally flat splitting ratio. Since the penetration depth of light into the metal layer is only on the order of the wavelength, the technical challenge during the production of metallic beam splitters is to achieve exactly the right thickness that results in the desired splitting ratio. The reflectivity of the coating further depends strongly on the polarization of the incident beam. The electric field of the pulses entering our setup are polarized parallel to the optical table which corresponds to *s*-polarization at the beam splitter BS1. A spectrally flat splitting ratio of close to 50/50 between "1/2" and "3/4" is accomplished by employing a thin silver coating on a fused silica substrate as BS1 (custom-made by LINOS Photonics). The further division of the beams at BS2 on the other hand requires the use of a different coating because the horizontal splitting means that the beams are *p*-polarized with respect to BS2. In order to maintain the spectral flatness of the splitting we had to use chromium as the coating material (also on a fused silica substrate and custom-made by LINOS Photonics). This has the slight drawback that about 50% of the incident visible light is absorbed in the metallic coating and the splitting ratio of BS2 is about 25/25. The overall splitting of the incident light by BS1 and BS2 yields four beams containing roughly the same spectra and 1/8 of the input energy each.

4.4.3 Measurement procedure

The actual measurement of the raw data for a 2D spectrum involves several steps and usually some data corrections are made before the evaluation of the data. The pairwise manipulation of beams in our setup causes some peculiarities with respect to the variation of the time delays of the excitation beams and the LO beam.

Before acquisition of the necessary scans for the 2D measurement the complete temporal overlap of all three excitation pulses must be determined precisely. In particular the timing between the pulses 1 and 2 is critical because it determines the coherence time τ. First, both piezo elements on DS1 and DS2 are positioned in the center of their scanning ranges. There are several methods for finding $t_1 = t_2 = t_3 = 0$ at the sample position [110, 111] but the details are excluded here.

As mentioned before, even when the excitation pulses coincide, the local oscillator pulse (pulse 4) is delayed to a time $t_{4,0}$ due to a different material thickness in its optical path. The time $t_{4,0}$ is also determined via SI before the 2D measurements so that pulses 3 and 4 have a good separation that makes the reconstruction of E_s from the SI data possible.

To describe how the scanning of the time delays T and τ is realized with our setup we will now consider the definition of the time variables (Fig. 4.3) in combination with the pairwise manipulation of the pulses. While Fig. 4.3 applies to the shown pulse order $t_1 < t_2 < t_3$ only, in general the population time T is defined as the shortest time difference between pulse 3 and pulse 1 or 2

$$T = \begin{cases} t_3 - t_2 & \text{if} \quad t_1 \leq t_2, \\ t_3 - t_1 & \text{if} \quad t_1 > t_2. \end{cases} \tag{4.38}$$

Together with the definition of $\tau = t_2 - t_1$ this means that the first case of Eq. 4.38 applies to positive coherence times $\tau \geq 0$ and the second case to negative coherence times $\tau < 0$. The actual time delays of the single pulses caused by the movements of the delay stages DS1 and DS2 can be regarded analogous to Eq. 4.33. DS1 shifts pulses 3 and 4 by a time Δ_{DS1} but leaves pulses 1 and 2 unaltered ($\Delta_{12} = 0$). DS2 shifts pulses 1 and 3 by a time Δ_{DS2} but leaves pulses 2 and 4 unchanged ($\Delta_{24} = 0$).[2] Hence the arrival times of all pulses are

$$\begin{aligned} t_1 &= \Delta_{\mathrm{DS2}} \\ t_2 &= 0 \\ t_3 &= \Delta_{\mathrm{DS1}} + \Delta_{\mathrm{DS2}} \\ t_4 &= \Delta_{\mathrm{DS1}} + t_{4,0}. \end{aligned} \tag{4.39}$$

The coherence and population times result as

$$\begin{aligned} \tau &= -\Delta_{\mathrm{DS2}} \\ T &= \begin{cases} \Delta_{\mathrm{DS1}} + \Delta_{\mathrm{DS2}} & \text{if} \quad \tau \geq 0, \\ \Delta_{\mathrm{DS1}} & \text{if} \quad \tau < 0. \end{cases} \end{aligned} \tag{4.40}$$

[2] Here the Δ variables stand for the deliberate time shifts in contrast to unwanted fluctuations discussed before.

Conversely, the instructions for how to move the two delay stages as a function of T and τ are given by

$$\Delta_{\mathrm{DS1}} = \begin{cases} T+\tau & \text{if} \quad \tau \geq 0 \\ T & \text{if} \quad \tau < 0 \end{cases} \qquad (4.41)$$
$$\Delta_{\mathrm{DS2}} = -\tau.$$

At the beginning of the measurement for a 2D spectrum the desired population time T is set by moving DS1 to the respective position (further away from the other beams for larger T) while the coherence time τ is kept at zero. Then, the piezo element on stage DS2 is moved to the most negative coherence time of the scan $\tau = -|\tau_{\mathrm{max}}|$, i.e., to $\Delta_{\mathrm{DS2}} = |\tau_{\mathrm{max}}|$. This corresponds to moving DS2 away from the beams (see Fig. 4.6 and Eq. 4.41 for the definitions of the signs and directions of movements). To obtain a continuous set of data and avoid artifacts in the 2D spectrum that can result from discontinuities during the τ-scan, DS2 is scanned from the most negative coherence time to the most positive coherence time in equidistant steps of typically 2 fs. Sensible values for these time steps depend on the width of the excitation spectrum. They should be chosen such that the Fourier transform $\tau \rightarrow \omega_\tau$ is somewhat broader than the excitation spectrum. As soon as $\tau = 0$ is crossed and positive τ are measured, the piezo on stage DS1 has to start moving with the same step size in the $+\Delta_{\mathrm{DS1}}$ direction to keep the population time constant (see Eq. 4.41).

The time difference Δt_{LO} between the LO and pulse 3 is essential for the signal recovery via SI. Our scanning method implies that this time changes over the τ scan

$$\Delta t_{\mathrm{LO}} = t_4 - t_3 = t_{4,0} + \tau. \qquad (4.42)$$

This time shift has to be accounted for when windowing the SI data in the signal reconstruction process. As mentioned before, the glass thicknesses in the beam paths can be chosen such that the LO arrives after all other pulses ($\Delta t_{\mathrm{LO}} > 0$) or before all other pulses. The later case has the advantage that the local oscillator will only experience the linear optical properties of the sample and will not be "pump–probe-contaminated" [110]. This case however can only be applied for very short population times because longer population times would result in an arrival of the LO after the pulses 1 or 2. It is possible to chose the "right" thickness of the glass in the beam path of the LO for each particular population time T. Then however, not only does the setup have to be altered but also the timing calibration for $t_{4,0}$ has to be repeated for each setting of T. In the experiments presented in this thesis we have used the case $t_{4,0} > 0$. This has the advantage that due to the correlated delay of pulse 3 and pulse 4 the time difference $\Delta t_{\mathrm{LO}} > 0$ that enters in the SI evaluation is equal for arbitrary population times T.

Scanning the coherence and population times, activating the beam shutters, recording and saving the necessary spectra for the 2D measurement is facilitated by our scan program (see section 2.4.3). The typical sequence of data acquisitions for each setting of T and τ is detailed in table 4.2. The two-dimensional scan then uses dimension 1 to scan the desired population times (or repetitions of the same population times) and dimension 2 is used to scan the coherence times. At each position the SI of the signal

index	hardware	description
0	XPS Controller	move UTM-50 stage on DS1 to population time T (do nothing *during* a τ scan because it is already there)
1	Piezo	move both piezo elements (in the "tau mode" of the program) to their positions described by Eq. 4.41
2	Shutters	open all beam shutters
3	2D Spectrometer	record SI spectrum of LO and signal with appropriate integration time
4	Shutters	block beams 1 and 2
5	2D Spectrometer	record scattering contribution I_{34} (with same settings as in index 4)
6	Shutters	block beam 3, unblock beams 1 and 2
7	2D Spectrometer	record scattering contribution I_{124}
8	Shutters	block excitation pulses 1,2, and 3
9	2D Spectrometer	record LO spectrum

Table 4.2: Sequence of data acquisitions used in scan program for measuring 2D spectra.

with the LO is measured and the scattering contributions (I_{34} and I_{124}) are measured with the help of the beam shutters. These will be used for scattering correction in the data evaluation process (see section 4.4.4). Further, a local oscillator spectrum is recorded at the end of each data point. This spectrum can also be used to correct for scattering. In the case of drifts in the laser power it can be used to partially compensate for the different LO power in the SI signal reconstruction. The scan program can append all τ scans (and thus all data for the different 2D spectra) to one file during the data recording, or each τ scan can be saved to a separate file, depending on the experimenter's choice and on the expected amounts of data.

4.4.4 Data evaluation

Within the Diplom thesis work of Ulrike Selig [111] a LabVIEW program was developed with which the data obtained from the procedure in the previous section can be analyzed and transformed into an intuitive 2D spectrum.

First, the data is read and extracted from the saved file. After specification of the indices where which data is located in the overall data structure (see also section 2.4.1) the raw SI data can be plotted and viewed as a function of wavelength and coherence time for each population time. Then the residual spectrometer background signal and noise can be subtracted from all data.

Before actually reconstructing the amplitude and phase of the signal field from the SI data one has to consider potential signal distortions due to scattered light. The sample itself, the surfaces of the sample holder, and other media can scatter some of the excitation beam light in the detection direction so that it contributes to the recorded SI

spectrum via a coherent superposition with the desired signal. Hence, the measured signal I_{SI} is not the one defined in Eq. 4.6 but it contains contributions from the excitation beams as well [110]:

$$\begin{aligned} I_{1234} &= |E_1 + E_2 + E_3 + E_4 + E_s|^2 \\ &= (E_1 + E_2)^* E_3 + (E_1 + E_2) E_3^* + |E_1 + E_2|^2 + |E_s|^2 \\ &\quad + (E_1 + E_2)^* E_s + (E_1 + E_2) E_s^* + E_3^* E_s + E_3 E_s^* \\ &\quad + (E_1 + E_2)^* E_4 + (E_1 + E_2) E_4^* + |E_3 + E_4|^2 \\ &\quad + E_4^* E_s + E_4 E_s^*. \end{aligned} \tag{4.43}$$

Here each complex electric field term E_j is of the form

$$E_j = \sqrt{I_j(\omega)}\ \mathrm{e}^{\mathrm{i}\Phi_j(\omega) + \mathrm{i}\omega t_j} \tag{4.44}$$

where t_j represents the arrival time of the signal E_j. Without any scattered light, only the terms in the last line of Eq. 4.43 would be relevant. In reality however, the detected signal contains all terms. During the SI evaluation the Fourier transform of I_{1234} is computed and each of the terms in Eq. 4.43 appears at a different time according to the sum of its phase factors. The windowing filter keeps only terms that approximately occur at times $t_4 - t_s$. These are collected in the second to last line and the terms on the other lines are eliminated by the SI evaluation itself. The idea is now to record suitable spectra and subtract the terms that can coincide with the Fourier window [110]. As indicated in the measurement sequence (table 4.2) we record the spectra

$$\begin{aligned} I_{34} &= |E_3 + E_4|^2 \qquad \text{and} \\ I_{124} &= |E_1 + E_2 + E_4|^2 \\ &= (E_1 + E_2)^* E_4 + (E_1 + E_2) E_4^* + |E_1 + E_2|^2 + |E_4|^2 . \end{aligned} \tag{4.45}$$

It can be seen from Eq. 4.39 that the relative timings between pulses 1 and 2 as well as those between pulses 3 and 4 change as a function of the coherence time τ. For this reason neither of these scattering contributions can be assumed to be constant and they are recorded for each setting of T and τ. The SI data I_{1234} can now be corrected with the two scattering spectra by simply subtracting them $I_{\text{corrected}} = I_{1234} - I_{34} - I_{124}$ which cancels the terms in the second last line of Eq. 4.43 so that only the desired signal term remains in the Fourier window of the SI evaluation. It was found that the scattering correction can be further improved by adding the separately recorded LO spectrum $I_{\text{corrected}} = I_{1234} - I_{34} - I_{124} + I_4$. This cancels the "accidentally" introduced term $|E_4|^2$ (very last term of Eq. 4.45). While the term $|E_4|^2$ by itself would not have any contribution in the Fourier window, the local oscillator can be scattered several times during its propagation through the sample and the sample cell. Hence there is a scattering contribution on the LO signal itself.

After the scattering correction is applied to all spectra of a τ scan, the Fourier evaluation of the SI data is the next step. The experimenter inspects a set of the inversely Fourier-transformed data and chooses suitable edges of the square-windowing filter. The

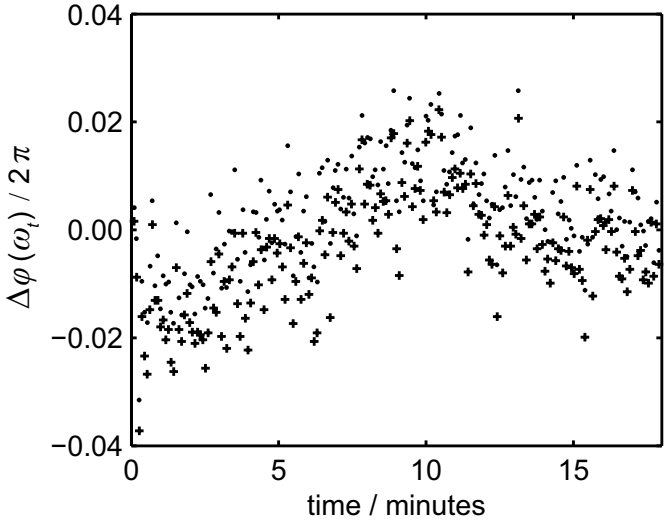

Figure 4.7: Proof of phase stability over a time period of 18 minutes. The SI signal between LO and E_s was recorded for $T = \tau = 0$. The spectral phase was reconstructed via Fourier evaluation and the deviation from the first measured point is shown for two spectral regions (+ and •). The total standard deviation is $2\pi/92$.

window is shifted automatically when looping over the different Fourier evaluations for the entire τ scan according to Eq. 4.42. Then the signal $E_s(\tau, T, \omega_t)$ is reconstructed for all population and coherence times. This data is next Fourier transformed along the τ-axis (see Eq. 4.11) yielding a complex-valued 2D spectrum with amplitude and phase. Only the regions on the ω_t- and ω_τ-axes where the laser spectrum has significant nonzero intensity are meaningful. This area is used for the phasing of the 2D spectrum with separately recorded pump–probe data according to the procedure described in section 4.2.3.

4.5 First experimental results

4.5.1 Demonstration of phase stability

Our first experimental goal was to demonstrate the inherent phase stability of the novel setup. It is necessary to analyze the residual phase drifts over all relevant timescales for 2D measurements. The necessary measurements were conducted on the dye molecule Nile Blue in acetonitrile pumped through a standard flow cell at room temperature.

First, we measured the signal and scattering terms (table 4.2) over a period of 18 minutes which is a typical timescale for a τ scan. No delay stage was moved during the measurement and the population and coherence times were set to $T = 0$ and $\tau = 0$. We calculated the phase difference $\Delta\varphi(\omega_t)$ between the LO and the nonlinear signal from the scattering-corrected spectra for each data point. Fig. 4.7 shows the differences of the reconstructed phases with respect to the first recorded spectrum so that only the important residual phase fluctuations are visible. Two spectral regions were evaluated exemplarily and the mean values of the phase differences in these two regions are plotted with two different symbols. Both regions show the same behavior with no major phase drifts. In fact, the standard deviation of the entire data set is $2\pi/92$ and the maximum deviation over the measurement period is less than $2\pi/30$. This stability is very much comparable to previous implementations that used diffractive optics.

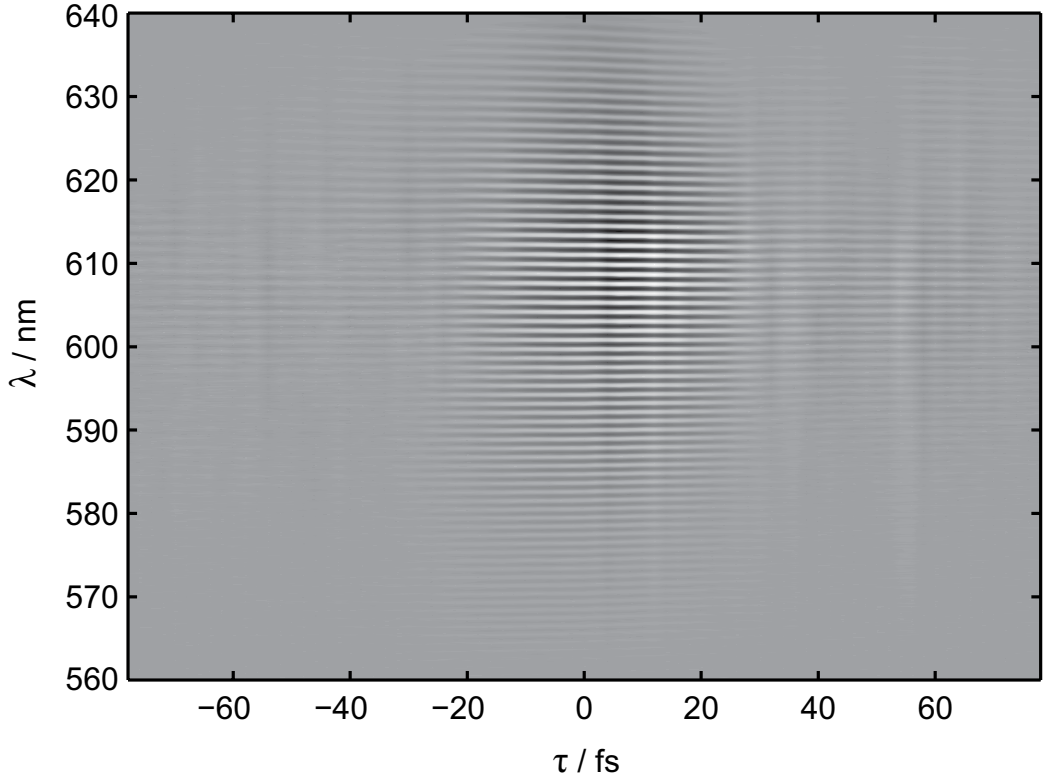

Figure 4.8: Raw data of a τ scan at $T = 0$. The scattering contributions were subtracted so that only the heterodyne component of the spectral interference pattern remains. The continuous interference fringes without distortions further demonstrate the stability of the setup.

While the experiment in Fig. 4.7 did not involve any stage movement, we have also recorded an entire τ scan. The heterodyne component of the signal and LO spectral interference (after scattering correction) are shown in Fig. 4.8. The fringes of the scattering corrected spectra oscillate between positive and negative values. This results in the black and white representation of the maxima and minima; zero intensity is represented by medium gray color. Notice the very regular fringe pattern. The maxima and minima do not shift with respect to each other over the entire τ scan and each fringe is continuous over the scan with a changing intensity. This change is due to the dynamics of the sample molecule itself and not to instabilities. For larger τ the fringe spacing decreases slightly, resulting in a different slant angle for the fringes at different wavelengths. This can be explained by the changing temporal separation of the LO and the signal which causes a change of the linear phase.

The data in Fig. 4.8 was taken with steps of $\Delta\tau = 2$ fs. Subinterferometric precision is not required in our novel scheme. In an earlier diffractive-optics-based implementation [110, 116], $\lambda/100$ precision was achieved using pairs of movable glass wedges to introduce time delays. However, the varying glass thickness introduces varying dispersion which can be problematic for broadband applications. The horizontal fringes shown

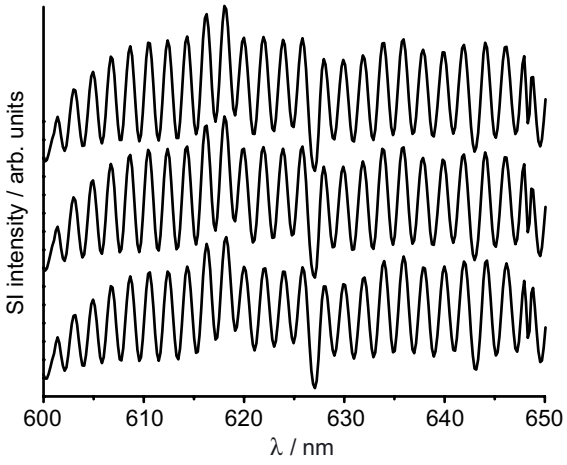

Figure 4.9: Comparison of fringe patterns at long timescales. Interference spectra are shown for $T = \tau = 0$ fs from three separate τ scans; the second (middle) and the third one (bottom) were recorded 38 and 117 minutes after the first one (top).

in Ref. [116] were due to precise undersampling. In the scheme presented here, such precision is unnecessary, because the signal does not oscillate when either delay stage is moved on the order of the wavelength of the laser pulses. Instead, the mentioned slow change in the fringe spacing is observed and a time-delay accuracy on the order of the quantum system dynamics (ca. 5 fs) is sufficient to capture all the information contained in the third order response $S^{(3)}$.

A third stability check was conducted by comparing fringe spectra over longer time scales. It might be necessary to average several 2D spectra recorded at the same population time or to compare spectra taken at different population times. In these cases the stability has to be given over a timescale of hours rather than minutes. Fig. 4.9 shows a set of three vertically offset fringe patterns taken at $T = \tau = 0$. All delay stages were moved between the recording of each of the spectra. Even though the time between the acquisition of the first and the last spectrum is about two hours, all fringe positions remain constant. This demonstrates the excellent phase stability of our setup even over a period of hours.

4.5.2 2D spectrum of Nile Blue at room temperature

Having shown the phase stability of the setup, we will now demonstrate its function, the measurement of a 2D spectrum. The dye Nile Blue in acetonitrile serves as test system for this purpose. Its molecular structure is shown in Fig. 4.10(a). Brixner *et al.* [110, 116] have conducted the experimental demonstration of their setup and some 2D spectrum simulations on the same system. This molecule is well suited for a broadband excitation in the visible because it has a very broad vibronic absorption with a maximum at 630 nm (see linear absorption spectrum, solid line in Fig. 4.10(b)). For the 2D experiment the sample solution was pumped through a 200 μm thick flow cell so that the resulting absorbance was 0.3 OD at the maximum. The excitation pulses from the NOPA were compressed and characterized as described in chapter 3. The reconstructed intensities and phases from the FROG measurement are shown in Fig. 3.24. The spectrum (drawn as dotted line in Fig. 4.10(b)) is centered around the molecular absorption maximum at 630 nm and matches the absorption almost exactly. The pulses have a duration of 17 fs

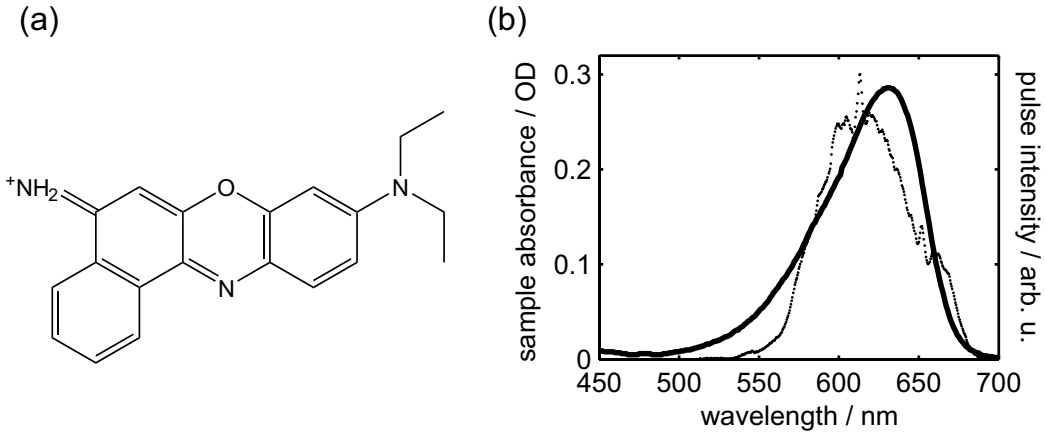

Figure 4.10: (a) Molecular structure of Nile Blue. (b) Linear absorption spectrum of Nile Blue in acetonitrile (solid line) and laser pulse spectrum used in the 2D experiment (dotted line).

and little residual phase. With these short pulses the third order signal from the sample was comparatively strong and we were able to reduce the pulse energies down to ≈ 1 nJ and still attain sufficient signal to noise (or scattering) ratio. The low energy suppresses higher order processes that could distort the 2D spectrum.

After the data corrections and Fourier evaluations that were performed as described in the earlier sections of this chapter we obtained the 2D spectrum shown in Fig. 4.11. The complex-valued coherence spectrum ($T = 0$) is represented as contour plots of the absolute value in (a) and phase in (b). The 2D spectrum consists of a broad, mostly featureless absorption peak that seems to be somewhat stretched below the diagonal. This might indicate the intramolecular coupling between higher- and lower-lying vibronic states. However, the data presented here merely serves to illustrate that the new setup is functional and yields good 2D spectra. Thus, further analysis of the presented spectrum will not be pursued here. The residual distortions that we see on the 2D spectrum might be explained by the fact that the excitation spectrum is not entirely smooth (see dotted line in Fig. 4.10(b)) and the sharp variations in intensity of the excitation pulses are reflected in the 2D spectrum. Nevertheless, the experiment and the figure demonstrate clearly that the setup is operational, it provides phase stability, and 2D spectra can be recorded and evaluated.

4.6 Summary and outlook

Optical 2D spectroscopy can reveal a wealth of details about photoprocesses in complex molecular systems. This chapter first outlined the theory of third order nonlinear spectroscopy. The molecular third order response function $S^{(3)}$ was introduced and used to describe the signal generation that is exploited in optical 2D spectroscopy. Further, the principles of the complete signal characterization via spectral interferometry and the computation of the final 2D spectrum from the data were discussed. Due to the

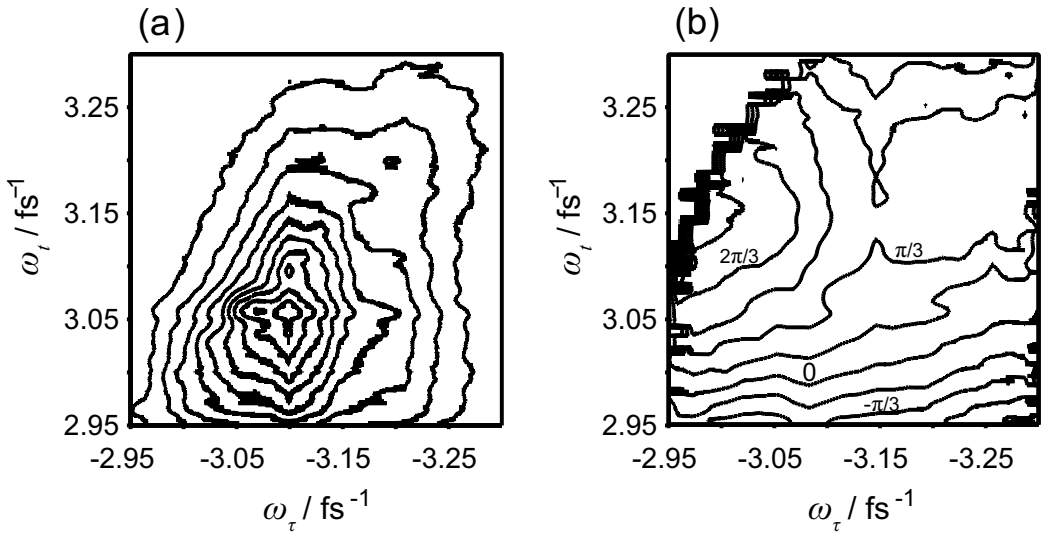

Figure 4.11: 2D spectrum of Nile Blue at $T = 0$ fs in acetonitrile: (a) absolute magnitude and (b) phase. Contour lines are drawn in steps of 10% for the absolute magnitude and in steps of $\pi/6$ for the phase.

fast oscillatory character of the measured third order signal field with respect to the timings of the excitation pulses the realization of a 2D measurement can be challenging. The previous experimental implementations in other research groups were summarized briefly.

We have detailed the theoretical basis for inherent phase stability via the manipulation of pulse pairs. In this fashion, possible phase fluctuations are correlated and the zero order spectral phase distortion vanishes, leaving only a linear contribution. This residual linear contribution gives rise to greatly relaxed stability requirements on the experimental setup. Instead of keeping the beam path lengths constant to a small fraction of the wavelength, as required in conventional setups, one can use correlated manipulation of pulse pairs. Then the requirement is that the beam paths are kept constant only to a fraction of the pulse length.

Our novel setup was presented along with the description of the measurement and data evaluation process. Several experiments were conducted to prove the phase stability of the new setup. Even though the setup is much simpler and easier to build, our scheme is comparable in stability to previous diffractive optics-based setups. The standard deviation of the residual phase drifts is only $2\pi/92$ over a period of 18 minutes. We have used the new apparatus to measure a 2D spectrum of the dye Nile Blue in acetonitrile at room temperature. The data underlines that the new setup is ready for further applications.

Even though electronic 2D spectroscopy opens up a new route to gain insight into intra- and intermolecular couplings and energy transfer processes, the method is not yet widely used. We hope that by presenting our new simple scheme we can stimulate a more wide-spread use and adoption of 2D electronic spectroscopy. There are many potential applications for our setup in the near future. The broadband visible excitation

enables us to measure intramolecular vibronic coupling directly [130] and thus unveil this fundamental intramolecular process. For this purpose, low-temperature 2D experiments on Nile Blue are being prepared.

With the help of our setup, newly synthesized molecular compounds that could potentially be used for organic solar cells can be evaluated in detail. The efficiency and the timescale of energy transfer in these hetero compounds is essential for the function and design of the overall solar cell. With 2D spectroscopy we can visualize the energy transfer, its efficiency, and timescale in a 2D spectrum directly. The evaluation of these parameters provides a feedback to synthetic chemists who can then vary the chemical composition. Many parameters such as the chromophores, the substituents, side chains, bridging groups, or other functional groups can be varied in order to "tune" the properties of the compound and a 2D spectroscopy measurement can reveal the resulting changes in the photophysical properties. Therefore we have reason to hope that, in a tight collaboration with synthetic chemists, this iteration of 2D spectroscopy and synthesis steps might help the development of new hetero compounds for use in organic solar cells. In fact, first measurements on a donor–acceptor system are under way.

The medium-term plans for extending our 2D spectroscopy techniques include a pulse-front matched setup, where temporal smearing effects due to the noncollinearity of the excitation beams are eliminated. Our inherently phase-stable scheme will also be applied to the implementation of 2D spectroscopy with UV pulses which will further increase the spectral range and applicability of 2D spectroscopy.

5 Product accumulation for ultrasensitive femtochemistry

The field of femtochemistry has evolved from the early dreams of laser-induced selective chemistry and spectroscopy to present-day realizations of these dreams. Currently, time-resolved nonlinear spectroscopy techniques such as 2D spectroscopy provide insight into the dynamics of photochemical reactions on a femtosecond timescale (see chapter 4). Adaptive quantum control [131, 132] has become very successful in controlling various quantum-mechanical and photochemical phenomena. For both of these experimental techniques, signal detection is an issue under current investigations. Therefore, within the scope of this PhD work, a novel method for product detection has been developed.

5.1 The problem of sensitivity in femtochemistry

When studying femtochemistry there are often several issues with detection sensitivity. After inducing a photochemical reaction with a pulsed laser in the liquid phase, an optical absorption (in the UV, VIS, or IR spectral regimes) of the products or reactants is usually used to determine the effects of the first laser irradiation. The foremost example of this approach is the transient absorption method. Not taking any coherent effects or time-evolution into account, i.e., a long time after the pump pulse, the change in optical density is given by

$$\Delta\mathrm{OD} \propto \epsilon_\mathrm{p} Q \epsilon_\mathrm{r} \Phi c_\mathrm{r} \tag{5.1}$$

where Q is the energy of the reaction inducing laser pulses, ϵ_r and ϵ_p are the absorptivity of the reactant and the product, respectively, Φ is the quantum efficiency of the reaction, and c_r is the initial concentration of the reactant.

Photochemical reactions with permanent products are especially relevant in real-world applications. However, for this type of reaction, in contrast to photophysical reactions like fluorescence, the quantum efficiency Φ and the absorptivity ϵ_r needed for accessing the reactive state can be rather low. Therefore the expected signals are often small and difficult, or even impossible, to measure in a conventional setup. These drawbacks cannot be offset by increasing Q or c_r because in an experiment there are limitations on the pulse energy and on the concentration.

Conventional schemes employ identical starting conditions for each elementary experiment. An elementary experiment consists of the application of a particular configuration of ultrashort pulses to an ensemble of molecules and the result is determined by a measurement of the immediate light-induced effects. For example, in TA spectroscopy the pulse configuration consists of a pump and a probe pulse that detects the resulting change of absorption. In a quantum control experiment on the other hand, the pulse

configuration consists of at least one shaped laser pulse and detection afterwards. After each elementary experiment, the illuminated sample volume is exchanged against a fresh sample volume by means of rapid sample transport (flow cell or molecular beam). Then the pulse configuration, i.e. time delay (spectroscopy) or pulse shape (quantum control), is changed and the elementary experiment repeated.

Moreover, in a conventional setup neither photoinduced reverse-reaction effects nor consecutive reactions, i.e. secondary reaction steps via intermediates, can be studied because no further interaction of the laser with the previously illuminated molecules is possible.

Therefore a method is needed that provides high sensitivity to low yields of stable photoproducts and includes photoinduced reverse- and consecutive reaction effects.

5.2 Accumulation for increased sensitivity

To overcome the difficulties concerning signal detection in femtochemistry that were described in the previous section, a novel "accumulative" method which can be used both for quantum control and spectroscopy has been developed. Accordingly we call the schemes accumulative control and accumulative spectroscopy.

The general idea of accumulation is to increase the measurement sensitivity by taking a measurement after accumulating photoproducts over several interactions with the femtosecond laser instead of taking a measurement immediately after the exciting laser pulse. This is in contrast to conventional femtosecond spectroscopy, like TA spectroscopy, which usually measures immediately following excitation.

5.2.1 Comparison of conventional and accumulative sensitivity

The sensitivity of a measurement series of a quantity A can be expressed by its standard error σ_{A}

$$\sigma_{\mathrm{A}}(N) = \frac{\sigma_{\mathrm{A0}}}{\sqrt{N}} \tag{5.2}$$

where N is the number of statistically independent measurements in the series and σ_{A0} is the error of a single measurement [133].

A TA experiment can be regarded as such a series. The error of a single measurement σ_{A0} is determined by the error of measuring the probe pulses in a spectrometer at a certain wavelength or using a photodiode. The number of measurements is given by the number of pump–probe pulse combinations (i.e. the number of elementary experiments) and therefore it is determined by the repetition rate of the laser system and the averaging time.

The accumulative method on the other hand should be regarded as a series of elementary experiments and a single measurement after this series of laser–sample interactions. Within the approximation that the accumulation of photoproducts is linear with respect to the number of elementary experiments[1] the measured quantity increases like

[1] This approximation is valid only if both diffusion and saturation are neglected. Section 5.4 describes a calibration that includes both of these effects.

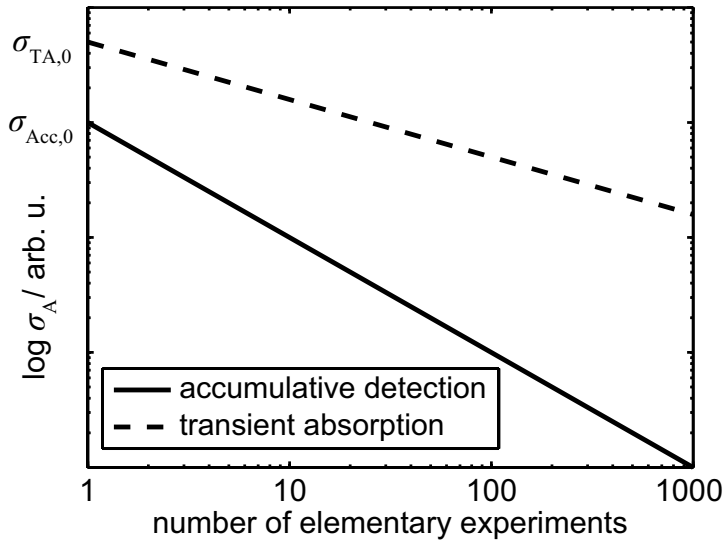

Figure 5.1: Comparison of measurement errors in TA and accumulative experiments. The initial error is smaller for the accumulative experiment due the use of a stable CW light source ($\sigma_{\mathrm{TA},0} = 5\sigma_{\mathrm{Acc},0}$, arbitrarily). The error of the accumulative measurement decreases faster than the error of the TA measurement.

$A = NA_e$, where A_e is the value resulting from the photoproducts of one elementary experiment. After product accumulation the measurement of A is performed once and the value A_e with respect to the elementary experiment is calculated simply as $A_e = A/N$. The overall determination of A_e after N elementary experiments therefore has a reduced error

$$\sigma_{\mathrm{A_e}}(N) = \frac{\sigma_{\mathrm{A0}}}{N}, \tag{5.3}$$

where σ_{A0} again represents the error of the single measurement. Using this formula, TA and accumulative experiments can be compared.

It should be noted that a further quantitative advantage of the accumulative measurement is the fact that the absorption measurement can be recorded with a very stable CW light source such as a light emitting diode (LED) and a low-noise photodiode. The signal can be integrated over a few hundred milliseconds and filtered if necessary to obtain only the constant part. In contrast to TA measurements, this approach does not suffer from the noise that arises from intensity fluctuations of the femtosecond probe pulses. Thus the error of a single measurement in an accumulative scheme $\sigma_{\mathrm{Acc},0}$ is in general smaller than the error of a single measurement in a TA experiment $\sigma_{\mathrm{TA},0}$.

A comparison of a conventional TA experiment with an accumulative experiment in Fig. 5.1 demonstrates that after a number of elementary experiments N the resulting standard error σ_{A} decreases with N for both types of measurements. However, due to the smaller error in the CW measurement of the accumulative method, even for small averaging or accumulation times, σ_{A} is smaller for the accumulation method than for TA. The accumulation itself makes the error also decrease faster compared to the error in a TA experiment.

5.2.2 Schematics and illustrative example

To illustrate the accumulative scheme and stress its advantages, we now consider the model reaction of a fictional system $\mathrm{ABC} \rightleftharpoons \mathrm{A} + \mathrm{BC} \rightleftharpoons \mathrm{A} + \mathrm{B} + \mathrm{C}$ in Fig. 5.2. Note

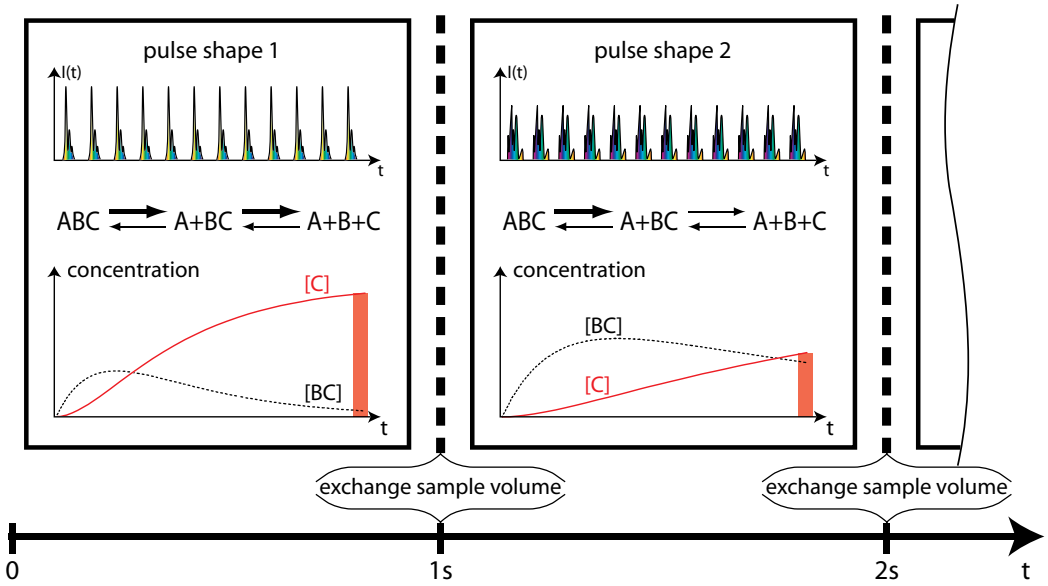

Figure 5.2: Schematics of the accumulative measurement. Each rectangular box represents a sample volume on which a single accumulative experiment is performed: The pulse configuration depicted on the top is applied repeatedly (with the laser repetition rate) and the concentrations (depicted on the bottom) of the reactants, intermediates, and products of the reactions depicted in the middle evolve according to the efficiencies of the applied pulses.

that for the two steps of the total reaction both forward and reverse reactions may be induced. The efficiency of each step is represented by the arrow thickness and depends on the pulse configuration. In the two cases of control and spectroscopy this corresponds to shaped laser pulses and time-separated pulses, respectively. One sample volume (rectangular box) interacts with a pulse train of 1 s duration with a constant pulse configuration, i.e. one particular pulse shape or one particular pump-dump delay time. For each pulse configuration, the concentrations in the volume evolve with a different effective rate for the intermediate [BC] and the final product [C]. Provided that all electronically excited species relax fully in between the pulses of the train, the accumulative scheme corresponds to a rapid sequence of conventional elementary experiments with changing initial concentrations, similar to the idea of "laser distillation" [134]. After a well-controlled exposure time the pump laser is blocked and the concentration of the final, stable product (shaded bar) is measured. Subsequently, the used sample volume is exchanged against fresh sample solution, the pulse configuration may be changed and the measurement cycle can be repeated many times in an automated fashion.

5.3 Experimental setup

The experimental setup for accumulative product detection is shown schematically in Fig. 5.3. The basic design is very similar to a conventional TA experiment, however, instead of a flow cell it employs a glass capillary with a square cross section of 250 ×

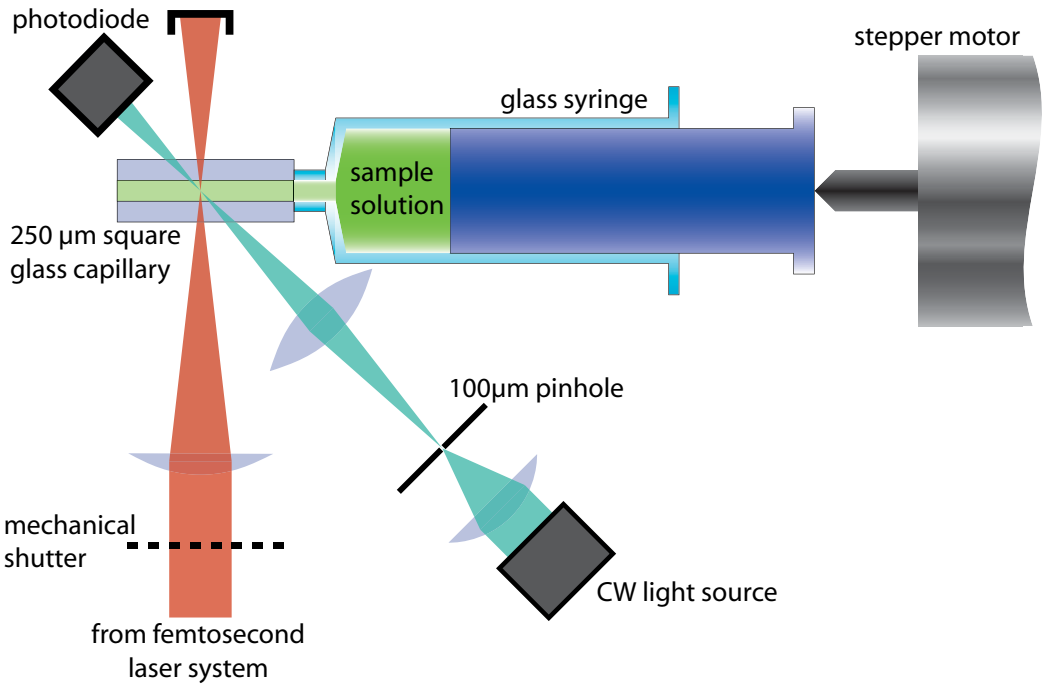

Figure 5.3: Experimental setup for accumulative measurement. The laser–sample interaction takes place in a glass capillary and the effects are probed by CW light. The source is collimated onto a pinhole which in turn is imaged into the interaction volume and the absorption is detected by a photodiode. The sample transport is facilitated by a glass syringe and a computer-controlled stepper motor.

250 μm^2 for the laser–sample interaction. These capillaries are commonly used in flow cell cytometry (counting of blood cells) and are commercially available e.g. from Hellma GmbH & Co. KG. The square cross section ensures that there are no aberrations when imaging the beams into the capillary. The femtosecond laser beam is focused into the capillary so that its beam diameter is approximately equal to the width of the capillary. From here on the laser that induces the photoreactions will be called "pump laser" and the affected volume of sample solution will be called the "pump volume". A mechanical shutter controls the exposure time and thus dictates the number of pulses from the pump laser impinging upon the sample. To probe the photoproducts, CW light from a stable source, such as a laser diode or LED, is collimated onto a 100 μm pinhole, imaged roughly 1:1 into the pump volume, and finally detected by a photodiode. The volume in the capillary where the measurement takes place is accordingly called the "probe volume".

After the measurement the used sample volume is exchanged against a fresh volume by means of a glass syringe and a stepper motor. The glass syringe has an inner diameter of 4.6 mm, thus moving the stepper motor by 1 μm translates the sample solution by $\approx$ 270 μm in the capillary which suffices to move the solution by a full pump beam diameter. To determine how far the stepper motor needs to be moved between experiments a scan of the step size was performed. The change in optical density $-\Delta$OD is plotted as a

function of the distance of movement of the stepper motor in Fig. 5.4. For movements of close to 0 μm there is a mostly constant offset in the change of optical density. This can be explained as follows: The piston inside the syringe glides on a liquid film between itself and the glass walls of the syringe and thus has very little friction. Nevertheless, for very small movements of the stepper motor (< 1 μm) the piston seems to remain stationary in the syringe and does not transport the sample at all. The remaining $-\Delta$OD is due to reactants diffusing into the interaction volume (see also next section) and not because of active sample transport. As the step size becomes larger the signal becomes rather erratic between 1 and 2 μm because the piston only moves some of the time. For step sizes bigger than 3 μm the piston moves reliably every single time and in an experiment we usually choose step sizes of around 5 μm or larger. The minor increase of the signal from 5 μm to 25 μm of 3.6% is due to the adhesion of the solution to the capillary walls. The further the piston is moved, the less residual previously illuminated sample solution stays at the capillary walls.

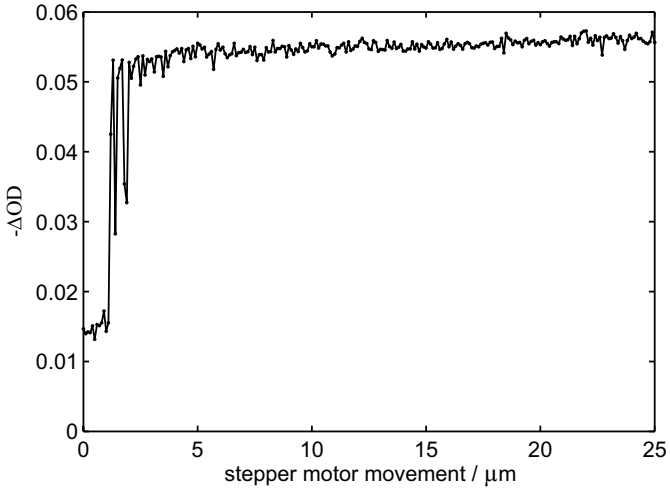

Figure 5.4: Accumulation signal as a function of the step size of the stepper motor driving the syringe. The motor movement was increased in steps of 0.1 μm, the minimum resolution of the motor. Typically, experiments were performed with step sizes of around 5 μm.

5.4 Calibration and modeling of accumulation

In order to deduce quantitative information from the accumulative experiment it is crucial to understand the accumulation process, especially the time evolution of the concentrations of all involved chemical species in the probe volume. Contrary to a conventional pump-probe experiment where the probe process follows the pump excitation on a timescale much shorter than the time for diffusion, here the effects of a pulse train that lasts for ca. one second are probed. Since the mean distance a traveled in a time $t \approx 1$ s by a chromophore due to diffusion is given by $a \sim \sqrt{2Dt}$, with the diffusion constant D, one can expect typical values of $a \approx 30$ μm during the accumulation process. Thus the measured optical density after exposure depends not only on the efficiency of the applied pulse configuration but also on the beam geometry and diffusion. We use a quantitative calibration procedure to take these effects into account and recover the single-pulse efficiency that corresponds to the result of an elementary experiment

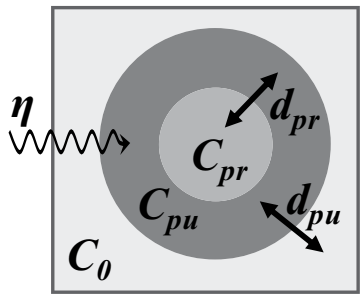

Figure 5.5: Simplified beam geometry in the accumulative setup. Throughout the capillary a the homogeneous concentration is equal to C_0. The femtosecond laser affects the pump volume (dark shaded area) with an efficiency η and the corresponding concentration is C_{pu}. The process is probed by CW light in the central shaded area, the probe volume with concentration C_{pr}. The arrows describe the diffusion exchange rates d_{pu} and d_{pr} between the different volumes.

in a conventional TA measurement. Therefore an accumulative experiment consists of a two-step process: first, experimental characterization of the diffusion as calibration of the setup, and second, the actual control or spectroscopic experiment.

The beam geometry in our experiments is shown in Fig. 5.5. A pump volume with concentration C_{pu} is defined by the femtosecond laser and a probe volume with concentration C_{pr} is defined by the CW light. Before the exposure the concentration of reactant molecules is homogeneous in the capillary:

$$C_{pu}(0) = C_{pr}(0) = C_0. \tag{5.4}$$

Even though a complete description of the concentration dynamics would have to use the diffusion equation and include the exact spatial intensity profiles of the beams [135], we reduce the problem by using simple exchange rates between the different volumes, marked as arrows in Fig. 5.5. As will be discussed, this suffices to describe the time evolution of the concentrations and can be used as a quantitative calibration of the setup.

The exposure of the pump volume to the femtosecond laser starts at $t = 0$ and lasts for an exposure time τ. The exposure to the femtosecond laser reduces the initial concentration of the irradiated sample solution. During the exposure ($0 \leq t \leq \tau$) we therefore arrive at

$$\dot{C}_{pu}(t) = d_{pu}(C_0 - C_{pu}(t)) - \eta C_{pu}(t) \qquad \text{and} \tag{5.5}$$
$$C_{pr}(t) \equiv C_{pu}(t), \tag{5.6}$$

where C_i and d_i are the concentrations and diffusion rates of volume i, η is the photoconversion efficiency of an elementary experiment, i.e. the fraction of converted molecules per unit time in the illuminated volume for a particular applied pulse configuration.

After the exposure ($t > \tau$) only diffusion persists:

$$\dot{C}_{pu}(t) = d_{pu}(C_0 - C_{pu}(t)), \tag{5.7}$$
$$\dot{C}_{pr}(t) = d_{pr}(C_{pu}(t) - C_{pr}(t)). \tag{5.8}$$

To characterize the diffusion rates d_i in the experimental setup, we record the change in optical density ΔOD in a two-dimensional scan as a function of exposure time τ and of an additional waiting time T after the exposure is finished. This means that the CW

probe signal is collected at a time T after the pump shutter has been closed. Thus with $t = \tau + T$ and $\Delta C(t) = C_{pr}(t) - C_0$, the solution to eqns. 5.4–5.8 is

$$\begin{aligned}\Delta C(\tau, T) = &\frac{C_0 \eta}{(d_{pr} - d_{pu})(d_{pu} + \eta)} \times \exp\left[-(d_{pr} + d_{pu})T - (d_{pu} + \eta)\tau\right] \\ &\times \left(d_{pu} \exp\left[d_{pu} T\right] - d_{pr} \exp\left[d_{pr} T\right]\right) \times \left(\exp\left[(d_{pu} + \eta)\tau\right] - 1\right).\end{aligned} \tag{5.9}$$

This represents the expected signal from a calibration experiment used to determine the relation between the accumulated signal $\Delta\mathrm{OD} \propto \Delta C$ and the elementary conversion efficiency η. It is obvious that this calibration model is a nonlinear function of the elementary efficiency η. The calibration data is usually recorded in a two-dimensional scan of exposure time τ and waiting time T. Then the model (Eq. 5.9) is fit to this data and the parameters d_{pu} and d_{pr} are determined by the best fit. These parameters are constant for a given beam geometry and alignment. The calibration is used in a spectroscopy experiment as follows. The data is recorded as the change in optical density $\Delta\mathrm{OD}$ and the elementary efficiency can then be recovered by solving Eq. 5.9 numerically for η while keeping the diffusion constants d_{pu} and d_{pr} at their previously determined values. Note that similar simple models can be found for cases in which more than one chemical species in the sample solution have to be considered (for an application to such a problem see chapter 6).

5.5 Experiments on indocyanine green

For a demonstration of both the calibration and pulse shaping experiments, we used indocyanine green (ICG), also known as the laser dye IR125. ICG is widely used in medical imaging applications and especially as a dye in ophthalmology [136]. ICG has a broad absorption maximum close to 800 nm. In aqueous solution it undergoes a photoreaction resulting in a decrease of absorption [137], which we here quantify with a 793 nm laser diode.

5.5.1 Calibration of the setup

The calibration experiment with 21×13 measurement points in the additional waiting time T and exposure time τ, respectively, is shown in Fig. 5.6. The data are marked with dots while the surface represents a best fit of the model function Eq. 5.9 with $C_0 = 0.19$ OD, $d_{pu} = 0.76\ \mathrm{s}^{-1}$, $d_{pr} = 3.4\ \mathrm{s}^{-1}$, and $\eta = 1.9 \times 10^{-3}$/pulse as the best values for the coefficients. Note that the parameters C_0, d_{pu}, and d_{pr} are constant for a given experimental setup consisting of a particular beam geometry, alignment, solvent, and solute. The simple model using diffusion rates describes the concentration dynamics well. Therefore the diffusion constant D and the details of the beam geometry do not need to be used in this treatment but the rather simple calibration model suffices to obtain quantitative information from the accumulative experiment.

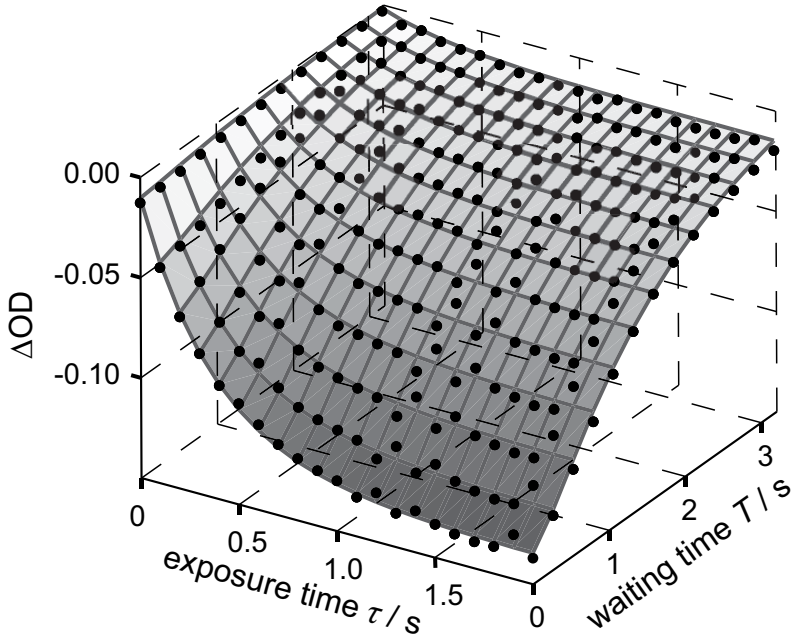

Figure 5.6: Calibration of accumulative setup. The ICG sample was irradiated for an exposure time τ and after an additional waiting time T the resulting change in absorbance was recorded (shown as •). The shaded surface represents a best fit of Eq. 5.9 to the data and the free parameters were determined as $C_0 = 0.19$ OD, $d_{pu} = 0.76$ s^{-1}, $d_{pr} = 3.4$ s^{-1}, and $\eta = 1.9 \times 10^{-3}$/pulse.

5.5.2 Chirped pulse excitation

The results reported in the next two sections demonstrate the applicability of the accumulative method to femtosecond pulse shaping experiments. For other possible applications of the accumulative measurement scheme such as one- or two-color pump-dump spectroscopy see chapter 6.

The 800 nm pulses from the laser system were chirped using the 128 pixel LC pulse shaper described in Ref. [100]. The chirped pulses were then coupled into the accumulative setup and the change of absorbance was recorded after an exposure time $\tau = 1$ s as a function of the second order spectral phase term between -20000 and $+20000$ fs^2. This change in optical density is shown in Fig. 5.7 as crosses. For each data point Eq. 5.9 was solved numerically for the elementary efficiency η using the best fit parameters determined in the calibration and results in the calibrated data shown as dots. In this case η is simply the fraction of all molecules in the pump volume which undergo the photolysis reaction upon irradiation with a single laser pulse.

The highest photoreaction efficiencies are obtained with short pulses and within the accuracy of the pulse shaper the curve is symmetric about zero chirp. This behavior points to a multiphoton absorption being responsible for the photobleaching of ICG.

Power studies which record many data points can be easily carried out using the accumulative setup. Further evidence that ICG is bleached through a multiphoton process

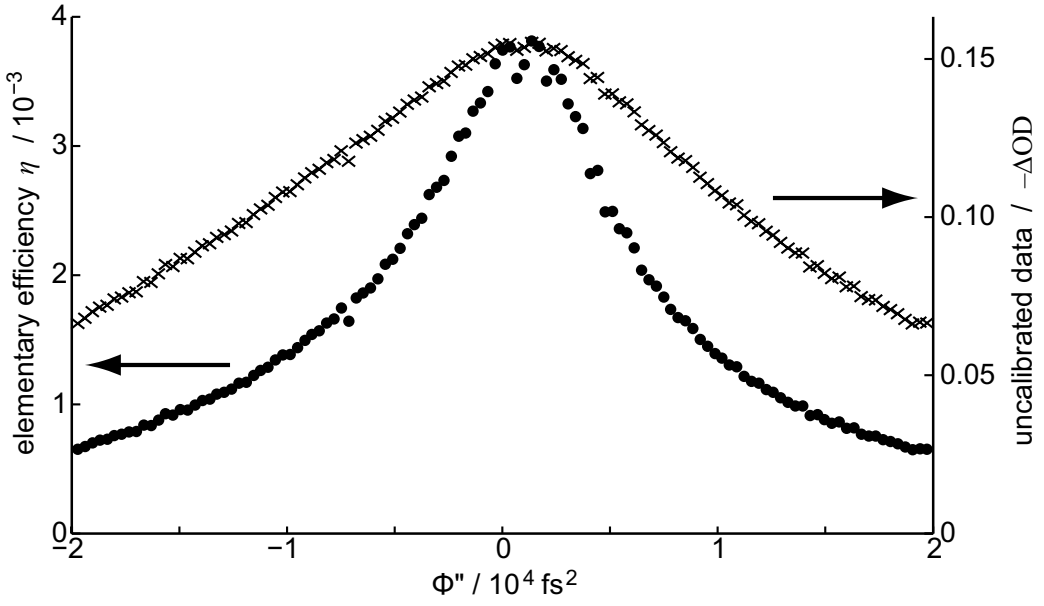

Figure 5.7: Chirped excitation of ICG. The second order spectral phase term of the exciting 800 nm pulses was varied using an LC pulse shaper. The raw data is shown as crosses. The calibration was applied and the diffusion corrected data is shown as dots.

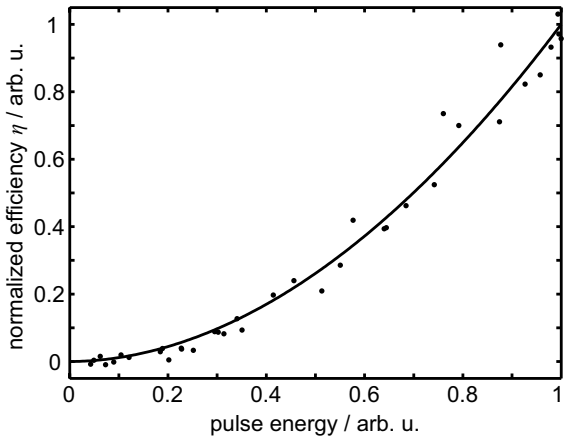

Figure 5.8: Power study of ICG photolysis. The change in optical density was recorded as a function of pulse energy and the nonlinear calibration was applied to the raw data. A fit of the function $\eta = \alpha\ P^{\beta}$ shown as solid line yields the exponent $\beta = 1.94 \pm 0.09$, providing further evidence that the photobleaching is induced by a multiphoton absorption.

was gained by scanning the power of the (unchirped) excitation pulses using a variable attenuator and recording both the excitation power with an additional photodiode as well as the resulting change in optical density. The calibrated data (the efficiency η) is plotted as dots versus the excitation power P in Fig. 5.8 and a fit of the form $\eta = \alpha\ P^{\beta}$ is drawn as a solid line. The exponent was determined to be $\beta = 1.94 \pm 0.09$ and therefore more than one photon seems to be required for efficient photobleaching of ICG.

However, we cannot draw any conclusions about the actual photochemical mechanism responsible for the bleaching. Further experiments, such as multipulse and multicolor time-resolved spectroscopy, together with a more detailed knowledge of the energy level structure of the molecule would be required. Nonetheless, this chirped pulse experi-

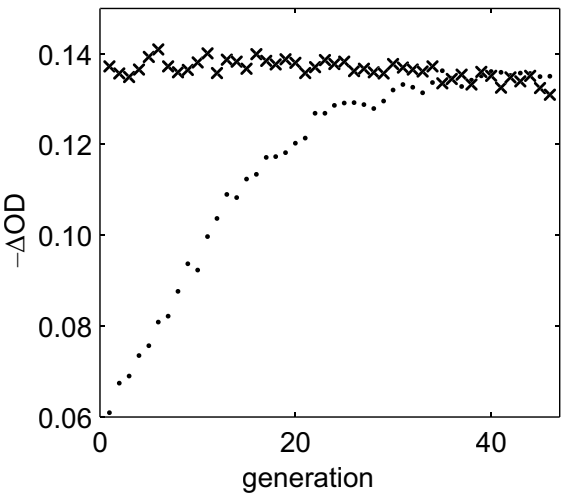

Figure 5.9: Adaptive optimization of photobleaching of ICG. Guided by the evolutionary algorithm the LC pulse shaper varied 64 degrees of spectral phase independently. The negative change in optical density $-\Delta$OD was used as feedback signal. After 40 generations the algorithm converged and the optimal pulse shape for photolysis was found to be the transform-limited shape. The average $-\Delta$OD of the best 10% of every generation is shown as dots and after each generation a transform-limited pulse was applied as a reference (shown as crosses).

ment and the power study show that a systematic study of pulse-shape effects on a photoreaction can be implemented in the accumulative scheme.

5.5.3 Adaptive pulse shaping

As mentioned above, the accumulative detection method can be used for both femtosecond spectroscopy and quantum control experiments [7, 138]. For demonstration purposes the evolutionary algorithm was used to find the pulse shape that optimally drives the photolysis of ICG. Again, the 128 pixel LC pulse shaper was used and 62 independent degrees of freedom in spectral phase were varied by the evolutionary algorithm. Each shaped electric field was tested for its effectiveness at driving the photolysis through the measurement cycle of sample exchange, illumination and accumulation, and finally product detection. In such an experiment the change in optical density ΔOD can be used as a feedback signal directly. In general the efficiency η is a nonlinear function of the detected ΔOD, nevertheless, this function is monotonic and a higher $|\Delta\text{OD}|$ means a higher η. The initial population of the evolutionary algorithm consisted of 40 random pulse shapes. After about 40 generations the algorithm converged and transform-limited pulses were found as the optimal solution (see fitness curve in Fig. 5.9). This experiment demonstrates that our setup is suited for adaptive quantum control with permanent products. The approach only consumes small volumes of sample solution (< 0.5 ml for the presented optimization). Hence, the method is ideally suited for the study of samples of which only small amounts are available.

5.6 Conclusions

In this chapter the accumulative method for achieving high sensitivity to stable photoproducts was introduced. When photoproducts that are stable on a timescale of seconds are to be measured, an optical absorption measurement after the interaction of the sample with a number of laser pulses can yield higher sensitivity than for instance conventional transient absorption spectroscopy. However, for a quantitative result, one must take diffusion into account. We have discussed the general method for the calibration of the experimental setup that includes diffusion and accumulation of the product and reactant molecules. The mathematical calibration model is applied to simple experiments on the photobleaching of indocyanine green upon irradiation with 800 nm pulses. We have demonstrated that our method can be used for power studies with high sensitivity, shaped-pulse excitation experiments, and adaptive pulse shaping experiments. Hence, our method of product accumulation can be applied to a variety of femtosecond experiments. In particular, systems with permanent photoproducts, that are available only in small quantities such as biological systems, can be studied with high sensitivity using only small volumes of sample solution (see e.g. chapter 6). Systems where the conventional techniques, such as transient absorption, do not yield a sufficient signal-to-noise ratio due to the small efficiency of a single laser pulse, can be studied with the accumulation technique. The femtosecond quantum control of chiral systems is discussed as another application of this method in chapter 7.

6 Ultrafast photoconversion of the green fluorescent protein

The newly developed accumulative measurement scheme has a broad range of potential applications. The study of photoreactions of biological molecules is one of these applications. Results on the photoconversion of a mutant of the green fluorescent protein (GFP) are presented in this chapter and demonstrate that accumulation can be used to obtain quantitative time-resolved spectroscopic information with extremely high sensitivity.

6.1 Green fluorescent protein

In the past two decades, fluorescence became the basis for many standard analytical tools in the life sciences because of its detection sensitivity and specificity toward analytes. The availability of compact and powerful laser sources triggered the development of new fluorophores and of detection schemes beyond ordinary luminescence excitation. Manipulating intervention into the emission process by stimulated emission was applied to localize cellular structures with unprecedented accuracy in optical microscopy [139]. Photoactivation was used to map proteins with temporal and spatial resolution [140]. While the first method repeatedly exploits the cyclic population of different photophysical states of a dye molecule, the latter technique is based on irreversible phototransformations [141, 142]. Especially autofluorescent proteins apply as effector molecules for these techniques.

The most well known representative among the autofluorescent proteins is green fluorescent protein from the pacific jellyfish Aequorea victoria (for a detailed review see e.g. Ref. [143]). The nucleotide sequence of GFP and the structure of its chromophore were unraveled in the 1990s [144, 145]. In its natural, fluorescent state the GFP chromophore is enclosed in a β-barrel [146, 147]. The *p*-hydroxybenzylideneimidazolinone chromophore and the tertiary β-barrel structure is shown in Fig. 6.1. Chalfie *et al.* [148] found experimental proof that the fluorescence is encoded genetically and, thus, opened up the possibility for genetically labeling proteins and studying them under the fluorescence microscope.

Upon excitation with light having $\lambda \approx 400$ nm, GFP exhibits green fluorescence peaking at approximately 510 nm. The absorption and fluorescence spectra of the T203V mutant are shown in Fig. 6.2. It was shown that the large Stokes shift results from an excited state proton-transfer reaction after excitation with $\lambda \approx 400$ nm. Herein, the neutral chromophore state RH releases a proton to the protein matrix, specifically the Glu222 residue, leaving a deprotonated, metastable anionic chromophore state R_I^{-*} [149–152]. After photon emission at 510 nm this intermediate state in the photocycle of GFP

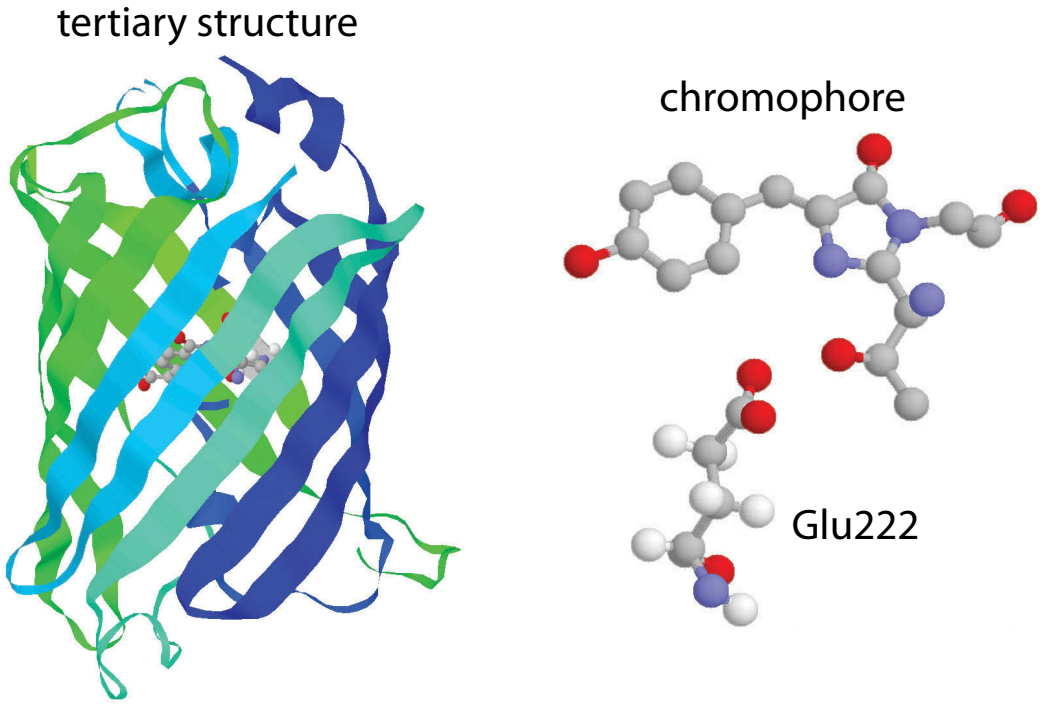

Figure 6.1: Structure of green fluorescent protein. The tertiary structure, a β-barrel with the chromophore at its center is shown on the left. On the right hand side, the p-hydroxybenzylideneimidazolinone chromophore is shown together with the Glu222 residue from a peptide strand of the surrounding barrel. This residue is the final acceptor of the excited state proton transfer and plays a crucial role in photoactivation of GFP. The figure was created from the Protein Data Bank file 1EMA [146].

undergoes reprotonation within less than 1 ns [153]. Fig. 6.3 b illustrates the photocycle of GFP. The intermediate state can be stabilized by site-directed mutagenesis [154].

Besides R_I^-, a stable, equilibrated anionic chromophore state, R_{eq}^-, exists in wild-type (wt)-GFP which absorbs at approximately 480 nm and fluoresces around 510 nm (Fig. 6.3 a). While for different mutants these two absorptions of wt-GFP around 400 nm and 480 nm are shifted in wavelength and of different strength, one finds both absorption maxima (usually denoted as A and B forms) in most GFP mutants [143].

In addition to creating these reversibly interconverting chromophore species, prolonged irradiation of the protein causes photoconversion, by which an anionic chromophore state R_{pc}^- (Fig. 6.3 c) – also with green fluorescence – is produced. The optical properties of this converted form are very similar to those of R_{eq}^- (the B form). Absorption and fluorescence of R_{pc}^- occur at 500 nm and 510 nm, respectively, for T203V GFP. Crystallography, mass spectrometry, optical and vibrational spectroscopy were used to unravel the underlying structural rearrangements. It was determined that this irreversible phototransformation is characterized by decarboxylation of Glu222 which is in close contact to the chromophore [156–158].

In previous studies [156–159] a strong dependence of the photoconversion of GFP on

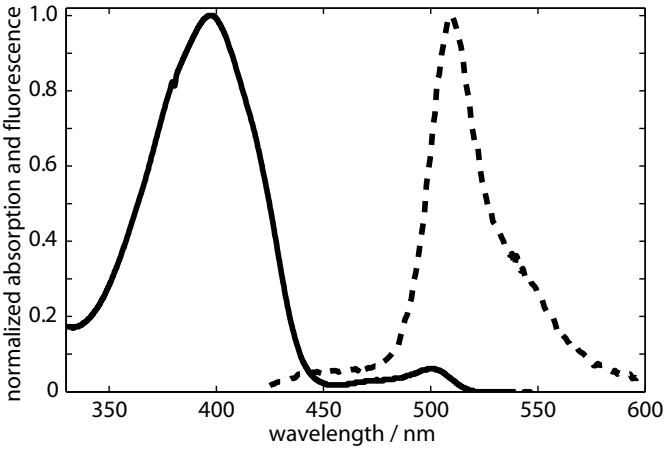

Figure 6.2: Absorption and fluorescence spectra of the T203V mutant of GFP.

the excitation wavelength was found; UV light proved to be more efficient at inducing photoconversion than visible light. Also, it was suggested that a Kolbe type mechanism is responsible for the photoconversion, starting with an excited chromophore that accepts an electron from the Glu222 rest which in turn is decarboxylated. Therefore the efficiency of UV light is explained by the higher oxidizing power of excited chromophore states higher than RH*. While that study was performed under CW conditions and the role of RH* in the photoconversion process remains ambiguous [158], many modern studies involving GFP use picosecond or femtosecond radiation for excitation, e.g. two-photon absorption (TPA) microscopy. The transient molecular species in combination with possible multiphoton absorptions constitute the basis for a potentially very different photochemical behavior of GFP under femtosecond excitation compared to CW excitation conditions. Conventional ultrafast spectroscopy for separating the competing photoreactions of photoconversion and excited state proton transfer is, however, hampered by the small quantum yield for the irreversible photoreaction.

In the study presented in the following sections, we compensate for the drawback of a low yield of photoproduct by employing the accumulative method for data collection. Using this technique, pump–probe transients can be measured even when the photochemical conversion efficiency is extremely low. We examine the GFP mutant T203V. This mutant is particularly appropriate for investigating photoconversion due to the predominance of RH (Fig. 6.2) and the detailed knowledge about its fluorescence dynamics [154, 155, 160, 161]. The GFP mutant T203V was kindly provided by J. Wiehler, Gene Center Munich. We used the undiluted sample which was buffered to physiological conditions with an optical density of $\approx 10/\mathrm{cm}$ at $\lambda_{\max}$.

6.2 Experimental setup for photoconversion of GFP

The general method for accumulative spectroscopy has been described in chapter 5. For the experiments on GFP the setup has been extended as shown in Fig. 6.4 to make experiments with 800 nm as well as 400 nm excitation pulses and time-resolved two-color experiments possible.

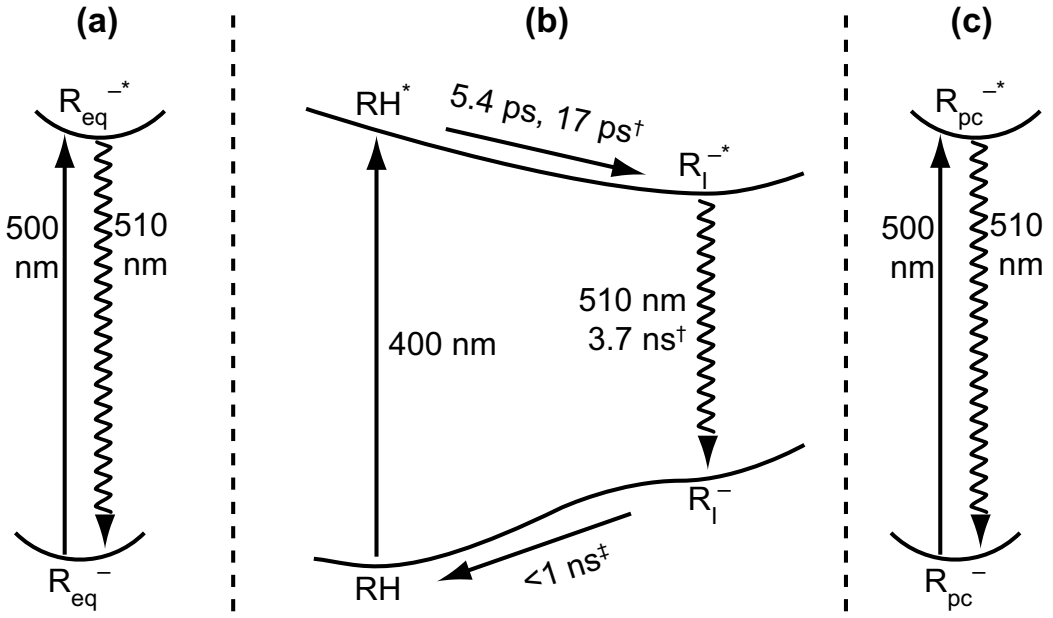

Figure 6.3: Simple potential energy scheme of T203V GFP. (a) Equilibrated anionic chromophore state R_{eq}^{-}. The T203V mutant exists in this form only to a very small fraction. (b) Photocycle of the RH form of GFP including excitation, excited state proton transfer, fluorescence and reprotonation. †, ‡Times taken from Refs. [153, 155]. (c) Photoconverted form R_{pc}^{-}.

The pulses from the Ti:sapphire laser system were used for these experiments directly. For the power studies of fluorescence and photoconversion these pulses were attenuated by a variable filter wheel and their energy was monitored by separating a small portion of the beam before sending them to the sample and measuring the energy with a photodiode. The fluorescence was collected by a microscope objective above the capillary, then passed through a green interference filter, and its intensity was measured with another photodiode. Due to the laser repetition frequency of 1 kHz the RH species completes a full photocycle of excitation, excited state proton transfer, fluorescence, and reprotonation between two consecutive laser pulses.

For the time-resolved two-color experiment the beam from the laser system was divided into two beam paths (Fig. 6.4); the pulses in one beam were time-delayed and frequency-doubled in a 100 μm BBO crystal. A short pass filter eliminates the remaining fundamental light and a dichroic mirror recombines the 400 nm pulses with the 800 nm pulses collinearly. In addition, the pulse energy in each beam can be adjusted independently with two variable attenuator wheels (not drawn). The diameter of the 800 nm beam was adjusted with an aperture so that after focusing both beams had a diameter of $\approx$ 200 μm inside the capillary. To ensure the best possible time resolution the input pulses were compressed as much as possible with the grating compressor at the CPA output such that the SHG in our setup yielded the highest power for the 400 nm pulses. After that, the pulse shaper in the 800 nm arm the setup was used to compress the 800 nm pulses adaptively. Finally, to avoid timing offsets between the 400 nm pulses

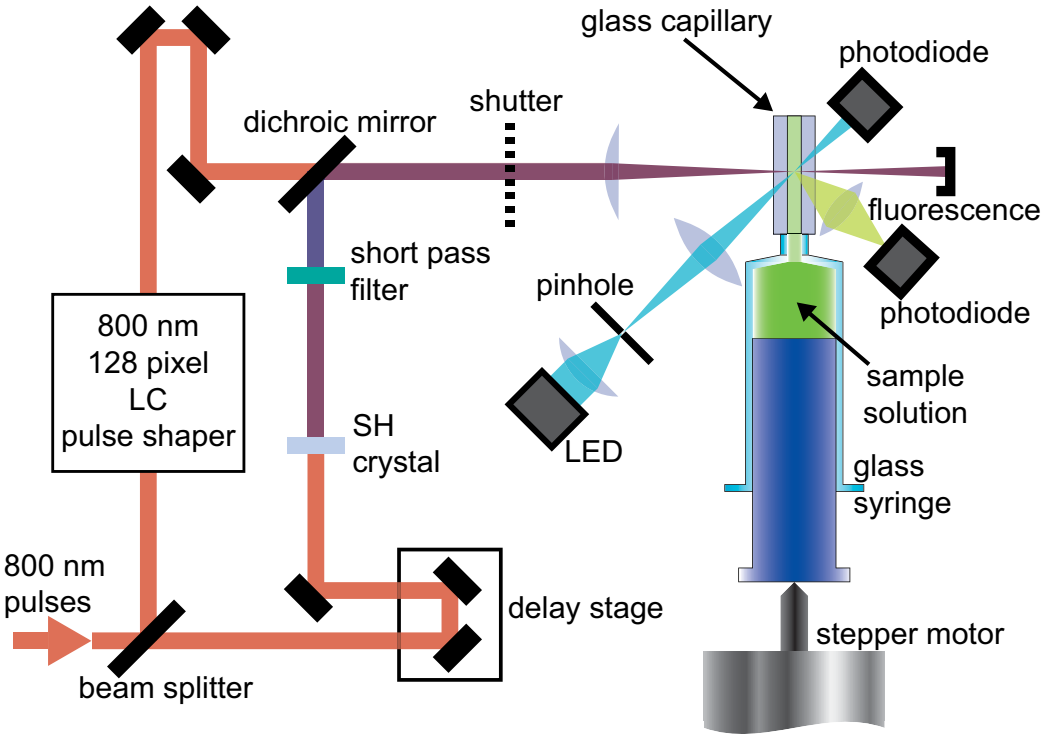

Figure 6.4: Setup for accumulative spectroscopy on GFP. The 800 nm input pulses are split into two time-delayed parts of which one is frequency doubled. The other part passes through the 128 pixel phase only pulse shaper. Both beams are recombined collinearly and focused into the capillary. The effects of the pump pulses are probed by an LED with emission around 504 nm.

and the 800 nm pulses and to determine the instrument response, a piece of glass as thick as the wall of the capillary holding the sample was placed into the common beam path. A cross-correlation of the two beams was performed in a sum-frequency mixing crystal (see Fig. 6.5). This procedure revealed a time-resolution of 165 fs.

The measurement sequence consisted of the following steps: First the stepper motor pushed the glass syringe forward to bring a fresh sample volume into the interaction region. Either the pulse configuration, i.e., the time delay between 400 nm and 800 nm pulses was adjusted (in the pump–repump experiments) or the energy or shape of the pulses was changed (in the power study and pulse shaping experiments). Then the shutter was opened and the exposure time started. The fluorescence signal was collected during the first few laser shots that impinged upon the sample. In all the experiments on GFP shown here we used an exposure time of 3 seconds, thus roughly 3000 pulses irradiated the pump volume. After closing the shutter again, the absorption of the pump volume at 504 nm was obtained through a measurement of the transmitted intensity of an LED. We used a 100 μm pinhole in front of the LED and imaged this pinhole into the pump volume. This defined the probe volume which was slightly smaller than the pump volume as described in chapter 5. Then the cycle started again with a fresh sample volume. This sequence is computer-controlled and can be repeated automatically many

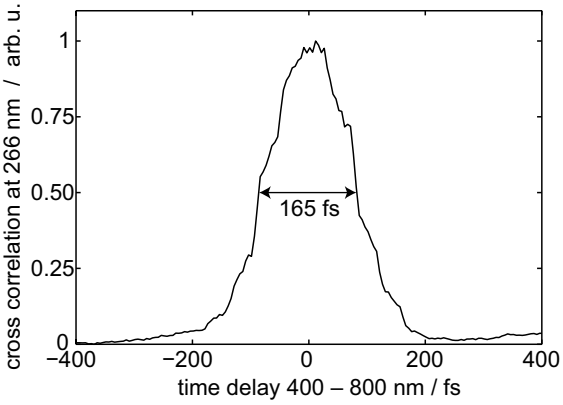

Figure 6.5: Instrument response for 400–800 nm two-color experiments. A collinear cross-correlation between the 400 nm and 800 nm pulses was taken in a sum-frequency mixing crystal. The frequencies were dispersed using a fused silica prism and the signal was detected with a photodiode at $\approx$ 266 nm. The full width at half maximum was 165 fs.

times. Due to the small cross section of the glass capillary small amounts of sample volume are sufficient for these types of measurements. A typical experiment, e.g. the one from Fig. 6.8, used only about 50 μl of sample solution.

6.3 Calibration of the setup for GFP

The model for diffusion used for the calibration of the experimental setup in chapter 5, where only one chemical species needed to be considered, namely, the reactant ICG itself, has to be extended for our GFP experiments. In general, obtaining the efficiency η is the goal of the measurement and the nonlinear calibration has to be applied to the raw data to obtain quantitatively correct data. The efficiency η can be regarded as the product of the quantum efficiency Φ and the probability for excitation. However, especially with possible multiphoton excitations the probability for excitation is not easy to determine and for studies of the efficiency of a process such as photoconversion of GFP under given conditions (as in this study) it is sufficient to consider the efficiency η only.

6.3.1 Model for concentration dynamics of involved GFP species

Here, three species have to be considered in the accumulation process: RH, R^-_{eq}, and R^-_{pc}. Since we only look at the photoconversion of RH which results in R^-_{pc}, the optical absorption properties of R^-_{eq} are equal to those of R^-_{pc} [142], and our laser is only resonant with RH, we consider the spectroscopically distinguishable species A and B with absorption maxima around 397 nm and 500 nm, respectively (Fig. 6.2). The geometry of pump and probe volumes including the constants describing the dynamics during exposure is shown schematically in Fig. 5.5 of the previous chapter. Using a simple exchange rate d_{pu} between the pump volume and the bulk sample solution one can attain the following differential equations to describe the concentration dynamics of A and B during the exposure ($0 \le t \le \tau$, the total exposure time is τ):

$$\dot{A}_{pu}(t) = -\eta A_{pu}(t) + d_{pu}(A_0 - A_{pu}(t)), \quad (6.1)$$

$$\dot{B}_{pu}(t) = \eta A_{pu}(t) + d_{pu}(B_0 - B_{pu}(t)). \quad (6.2)$$

A_{pu} and B_{pu} are the concentrations of A and B in the pump volume. The initial conditions are dictated by the homogeneous concentrations of both A and B throughout the capillary:

$$A_{pu}(0) = A_{pr}(0) = A_0, \tag{6.3}$$
$$B_{pu}(0) = B_{pr}(0) = B_0. \tag{6.4}$$

For determining the effects of the pump laser on the sample in the pump volume the probe light is focused on a volume smaller than the pump volume. During the exposure time τ, the concentrations in this probe volume, A_{pr} and B_{pr}, develop identically to the concentrations in the bigger pump volume because the probe volume is a subset of the pump volume:

$$A_{pr}(t) \equiv A_{pu}(t), \tag{6.5}$$
$$B_{pr}(t) \equiv B_{pu}(t). \tag{6.6}$$

In order to characterize the diffusion in the calibration experiment independent of the molecular dynamics, an additional waiting time T is introduced after the end of the exposure time τ and before measuring the absorption of B ($t > \tau,\ T = t - \tau$). Then B evolves according to

$$\dot{B}_{pu}(T) = d_{pu}(B_0 - B_{pu}(T)) - d_{pr}(B_{pu}(T) - B_{pr}(T)), \tag{6.7}$$
$$\dot{B}_{pr}(T) = d_{pr}(B_{pu}(T) - B_{pr}(T)). \tag{6.8}$$

Here, d_{pr} is the diffusion exchange rate between the pump and probe volume, analogous to d_{pu} (inset of Fig. 5.5).

The conditions for joining Eqs. 6.7–6.8 with Eqs. 6.1 and 6.2 are

$$B_{pu}(t = \tau) = B_{pu}(T = 0) \qquad \text{and} \tag{6.9}$$
$$B_{pr}(t = \tau) = B_{pr}(T = 0). \tag{6.10}$$

The differential Eqs. 6.1–6.8 were solved with the Mathematica software package and the solutions for times $0 < t < \tau$ during the exposure to the femtosecond pulses are

$$A_{pu}(t) = A_{pr}(t) = \frac{A_0}{d_{pu} + \eta}\left(d_{pu} + \eta\ \mathrm{e}^{-(d_{pu}+\eta)\ t}\right) \tag{6.11}$$

$$B_{pu}(t) = B_{pr}(t) = \frac{A_0\ \eta}{d_{pu} + \eta}\left(1 - \mathrm{e}^{-(d_{pu}+\eta)\ t}\right) + B_0. \tag{6.12}$$

The solutions for Eqns. 6.7–6.10 for non-zero waiting times T after the exposure ($T \equiv t - \tau$, $t > \tau$) are

$$\begin{aligned} B_{pu}(\tau, T) = \frac{1}{2s(d_{pu} + \eta)} \times \exp\left[-\frac{3}{2}(d_{pu} + 2d_{pr})\ T - \frac{1}{2}sT - (d_{pu} + \eta)\ \tau\right] \times \\ \Big\{ A_0\eta \exp\left[(d_{pu} + 2d_{pr})T\right] (\exp\left[(d_{pu} + \eta)\ \tau\right] - 1) \times \\ (d_{pu} + (s - d_{pu}) \exp[sT] + 2d_{pr}(\exp[sT] - 1) + s) + \\ +2B_0 s(d_{pu} + \eta) \exp\left[3d_{pr}T + \frac{3}{2}d_{pu}T + \frac{1}{2}sT + (d_{pu} + \eta)\tau\right] \Big\} \end{aligned} \tag{6.13}$$

and

$$\begin{aligned} B_{pr}(\tau,T) = \frac{1}{2s(d_{pu}+\eta)} \times \exp\left[-\frac{3}{2}(d_{pu}+2d_{pr})T - \frac{1}{2}sT - (d_{pu}+\eta)\tau\right] \times \\ \Big\{ A_0\eta \exp[(d_{pu}+2d_{pr})T](\exp[(d_{pu}+\eta)\tau]-1)\times \\ (-d_{pu}+(s+d_{pu})\exp[sT]+2d_{pr}(\exp[sT]-1)+s)+ \\ 2B_0 s(d_{pu}+\eta)\exp\left[3d_{pr}T+\frac{3}{2}d_{pu}T+\frac{1}{2}sT+(d_{pr}+\eta)\tau\right]\Big\} \end{aligned} \tag{6.14}$$

with

$$s = \sqrt{{d_{pu}}^2 + 4{d_{pr}}^2}. \tag{6.15}$$

So far the discussion here has dealt with the total number N of molecules of the A and B form in the pump and in the probe volume, i.e. the variable B_{pr} for instance denotes the number of molecules in the probed volume. To make the transition to absorbance OD (the signal from the experiment) we consider the proportionality

$$\mathrm{OD} \propto \epsilon N. \tag{6.16}$$

Thus, substituting

$$A \rightarrow \mathrm{OD_A}/\epsilon_A \tag{6.17}$$

$$B \rightarrow \mathrm{OD_B}/\epsilon_B \tag{6.18}$$

and defining

$$c \equiv \frac{\epsilon_B}{\epsilon_A} \tag{6.19}$$

as the ratio of the absorptivities of the two forms, we can write

$$\begin{aligned} \Delta\mathrm{OD_B}(\tau,T) &= \epsilon_B B_{pr}(\tau,T) - \mathrm{OD_{B0}} \\ &= \frac{1}{2s(d_{pu}+\eta)} \exp\left[-\frac{3}{2}(d_{pu}+2d_{pr})T - \frac{1}{2}sT - (d_{pu}+\eta)\tau\right] \times \\ &\Big\{ c\ \mathrm{OD_{A0}}\eta \exp[(d_{pu}+2d_{pr})T](\exp[(d_{pu}+\eta)\tau]-1)\times \\ &\quad (-d_{pu}+(s+d_{pu})\exp[sT]+2d_{pr}(\exp[sT]-1)+s)+ \\ &\quad 2\mathrm{OD_{B0}} s(d_{pu}+\eta)\exp\left[3d_{pr}T+\frac{3}{2}d_{pu}T+\frac{1}{2}sT+(d_{pr}+\eta)\tau\right]\Big\} - \mathrm{OD_{B0}}. \end{aligned} \tag{6.20}$$

Only the absorbance in the probe volume is of interest, therefore one can simply write $\Delta\mathrm{OD_B}$ instead of $\Delta\mathrm{OD_{B,pr}}$ to denote the change of absorbance measured at 504 nm in the experiment. We used the numeric values of the absorption cross sections of A and B from Ref. [154]. The initial absorbances $\mathrm{OD_A}(t \leq 0)$ and $\mathrm{OD_B}(t \leq 0)$ of the unexposed sample volume were recorded in an independent measurement. Thus, the function $\Delta\mathrm{OD_B}(\tau,T)$ has the three remaining free parameters d_{pu}, d_{pr}, and η. The last parameter depends on

the properties of the applied laser pulses that induce photoconversion, and the objective of the actual pump–repump and power study experiments is to obtain it. The first two parameters depend only on the measurement geometry and the diffusion properties of GFP in the buffer solution and are therefore constant for all experiments performed with different femtosecond pulse configurations.

The diffusion calibration experiment was conducted analogously to the experiments on ICG and the data is shown as a function of exposure and waiting time in Fig. 6.6. In order to retrieve the diffusion rates we fit the model function Eq. 6.20 to the calibration data. The best fit obtained from a least-squares optimization is represented by a shaded surface in Fig. 6.6. The best parameters are $d_{pu} = 0.487/\mathrm{s}$, $d_{pr} = 1.86/\mathrm{s}$ and $\eta = 4.06 \times 10^{-5}/\mathrm{pulse}$. We used the diffusion calibration for all experiments of the pump–repump and power study by using the obtained measurement data $\Delta\mathrm{OD_B}$ as a function of pulse configuration (e.g. pump–repump delay time) to solve the fit model for the efficiency η numerically for each data point. This calibration is a necessary nonlinear correction to the absorbance data and results in the diffusion-corrected efficiency of a certain pulse delay or a certain pulse energy for the time-resolved 400 nm plus 800 nm experiment and the power study.

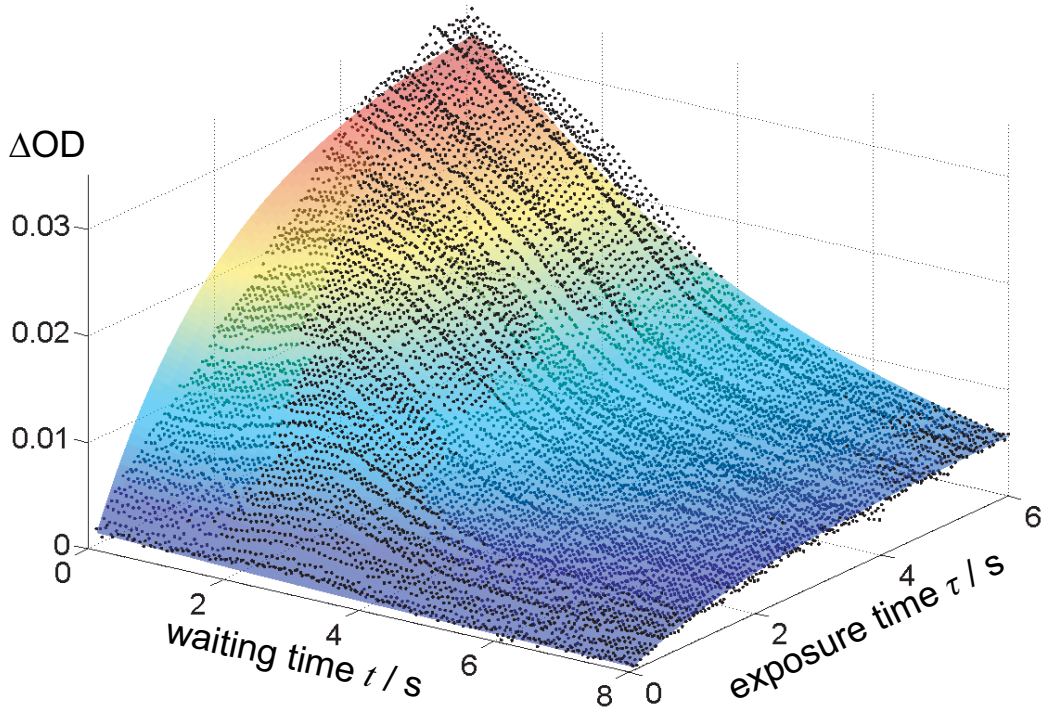

Figure 6.6: Calibration scan of the accumulation setup for GFP. The data is shown as • and the best fit to the model function 6.20 is shown as shaded surface. The best parameters are $d_{pu} = 0.487/\mathrm{s}$, $d_{pr} = 1.86/\mathrm{s}$ and $\eta = 4.06 \times 10^{-5}/\mathrm{pulse}$.

6.3.2 Estimate of sensitivity

In the previous chapter it was shown that for stable photoproducts one can obtain information with the accumulative method that corresponds to a conventional experiment, but with greatly enhanced sensitivity. The sensitivity can be expressed in terms of the change in the elementary efficiency $\Delta\eta$ or in terms of differences in the change of absorbance $\Delta(\Delta\mathrm{OD})$ per elementary experiment. Both have complex dependencies on the precise experimental conditions. Due to the nonlinear concentration dynamics, the sensitivity is nonuniform for different values of η. As mentioned before, for different magnitudes of η the exposure time can be adjusted such that there is an easy to measure change in absorption, yet no saturation.

For a given experiment under set conditions the sensitivities can be calculated simply from the standard deviation of the data. An appropriate example of such data is the part of the time resolved experiment in Fig. 6.8 where the time delay is negative. This part of the signal does not show any systematic modulations of η and the variations are caused only by noise. The standard deviation in this region is $\sigma_\eta = 2.27 \times 10^{-7}$/pulse, which corresponds to the sensitivity $\Delta\eta$ under these conditions. The sensitivity in change of absorbance $\Delta(\Delta\mathrm{OD})$ on the other hand can be simply calculated using

$$\Delta(\Delta\mathrm{OD}) = \frac{1}{2}\left[\Delta\mathrm{OD}_\mathrm{B}\left(\overline{\eta} + \Delta\eta\right) - \Delta\mathrm{OD}_\mathrm{B}\left(\overline{\eta} - \Delta\eta\right)\right] \tag{6.21}$$

derived from Eq. 6.20 with $\tau = 1$ ms, $T = 0$, and the average value of $\overline{\eta} = 1.3949 \times 10^{-5}$. The resulting sensitivity per pump–repump sequence is $\Delta(\Delta\mathrm{OD}) = 9.7 \times 10^{-8}$. Compared to conventional TA experiments this is an increase in sensitivity of several orders of magnitude.

6.4 Excitation power study

To investigate the photoconversion of GFP under femtosecond excitation, first we conducted a power study of the photoinduced reaction. While this is in general a rather simple experiment, to our knowledge it has not been previously performed on the efficiency of photoconversion of GFP, perhaps due to the low conversion efficiency in conventional flow-cell geometries. The accumulation setup facilitates an easy automated measurement with high sensitivity where many data points can be taken with different sample volumes.

The results of such a power study using 800 nm laser pulses for excitation are shown in Fig. 6.7; both the fluorescence (Fig. 6.7a) and the photoconversion (Fig. 6.7b) were measured simultaneously. For interpretation it should be considered that TPA microscopy with GFP as fluorescent marker is a common technique and exploits the fact that GFP (in its RH form) has a relatively strong TPA around 800 nm [162, 163]. One therefore expects a proportionality of the fluorescence yield to the squared intensity of the pulses (or pulse energy, since the duration and beam profile are not altered). The best fit of the function $f = \alpha\ I^\beta$ to the data (solid line in Fig. 6.7a) indeed reveals a quadratic dependence of the fluorescence on the excitation intensity. Moreover, even at the higher power levels there are no saturation effects. This confirms that the green fluorescence

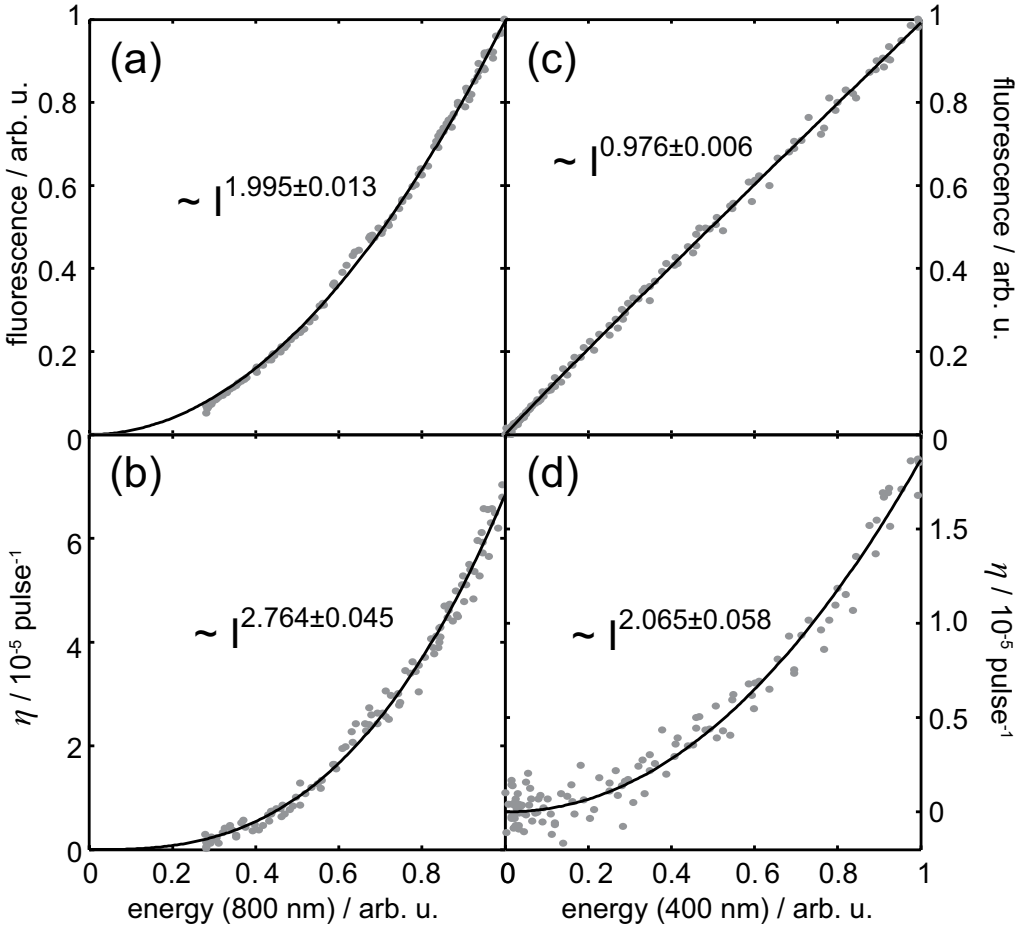

Figure 6.7: Power studies of GFP photoconversion and fluorescence. (a) Fluorescence yield after excitation with 800 nm pulses. (b) Photoconversion efficiency upon excitation with 800 nm pulses. Maximum intensity in (a) and (b) corresponds to 7×10^{11} Watt/cm^2. (c) Fluorescence yield after excitation with 400 nm pulses. (d) Photoconversion efficiency upon excitation with 400 nm pulses. Maximum intensity in (c) and (d) corresponds to 5×10^9 Watt/cm^2.

results purely from TPA of RH at 800 nm leading to RH* and excited state proton transfer.

For the photoconversion the situation is more complex. In the original experiments, where photoconversion of a GFP variant (PA-GFP) was introduced as a means to mark structures in a cell and track them under a microscope, high levels of CW light, resonant with the RH $\rightarrow$ RH* transition, were used to trigger photoconversion [141]. However, the nature of the reactive state remained unclear. Does photoconversion occur via TPA of RH into RH* as has been shown for a GFP variant [164]?

In our highly sensitive accumulative study we determined an exponent of the power dependence of 2.76 (Fig. 6.7b). The diffusion calibration has already been applied as described in section 6.3. The value of the exponent is significantly higher than what one would expect if photoconversion occurred from the same initial excited state (RH*) as fluorescence. Our data suggests that an efficient photoconversion can only be induced

by absorption of at least three 800 nm photons, exciting a higher state, RH^{**}, and that photoconversion predominantly starts from this RH^{**} state rather than from RH^{*} which is the excited state of the regular fluorescence photocyle of GFP.

This conclusion is further supported by data obtained with 400 nm instead of 800 nm excitation pulses. The fluorescence (Fig. 6.7c) shows a linear dependence on the excitation intensity as expected. However, the dependence of photoconversion on the excitation intensity (Fig. 6.7d) is ≈ 2, indicating that more than one photon is needed to induce photoconversion efficiently and that excitation to a higher excited state is needed for photoconversion. Two 400 nm photons most likely excite a state that is higher-lying than RH^{**} and can either lead to decarboxylation itself or undergo a fast conversion to the reactive RH^{**}. The evidence for a consecutive TPA being responsible for the photoconversion of another autofluorescent protein, DsRed, reported by Habuchi *et al.* [165] corroborates our interpretation of this data. In a study of fluorescence dynamics of super folder GFP upon TPA with 975 nm Cotlet *et al.* [166] suggested that the photoconversion, which they detected indirectly via fluorescence lifetime of single molecules, is due to a 2+1 photon absorption. Note that we do not exclude the possibility of photoconversion from R_I^-, but under our experimental conditions any resulting linear component of the power dependence is concealed under the vastly greater nonlinear component due to excitation of RH^{**}.

We did not perform any experiments using deep UV excitation; however, this has been reported to be a very efficient way of inducing photoconversion [159]. Presumably, wavelengths of around 267 nm, corresponding to three 800 nm photons, access RH^{**} directly and are therefore efficient at photoconverting the RH species.

6.5 Time-resolved two-color experiment

Although photoconversion must occur from the higher-lying RH^{**}, RH^{*} is a resonant intermediate state when exciting with either wavelength, 400 nm or 800 nm. It is an interesting question what role this state plays in the photoconversion and what the dynamics of the $RH^{*} \rightarrow RH^{**}$ step of photoconversion are. The experiments with 800 nm or 400 nm pulses shown in Fig. 6.7 require a molecule to absorb all photons from one pulse, and hence no time resolution is achieved. In order to separate the excitation of the photoconverting form into excitation to RH^{*} and subsequent excitation to RH^{**}, we employ a two-color experiment where a 400 nm pulse excites the GFP molecules and an 800 nm pulse, delayed by time t, induces photoconversion.

Fig. 6.8 shows the results of such an experiment. To avoid contributions from the absorption of one color only, the individual beam intensities were adjusted so that each of them induced only a small amount of photoconversion. 3 mOD absorbance change for the 800 nm and 6 mOD for the 400 nm beam were observed. For comparison the maximum photoconversion signal arising from both pulses together around $t = 0$ was 22 mOD. In Fig. 6.8 the diffusion calibration has been applied to the data as discussed in section 6.3. As a result, the photoconversion efficiency η is obtained. η describes the fraction of molecules in the interaction volume that are converted with a single 400 nm–800 nm two-pulse sequence. The maximum photoconversion efficiency is $\eta = 3.4 \times 10^{-5}$

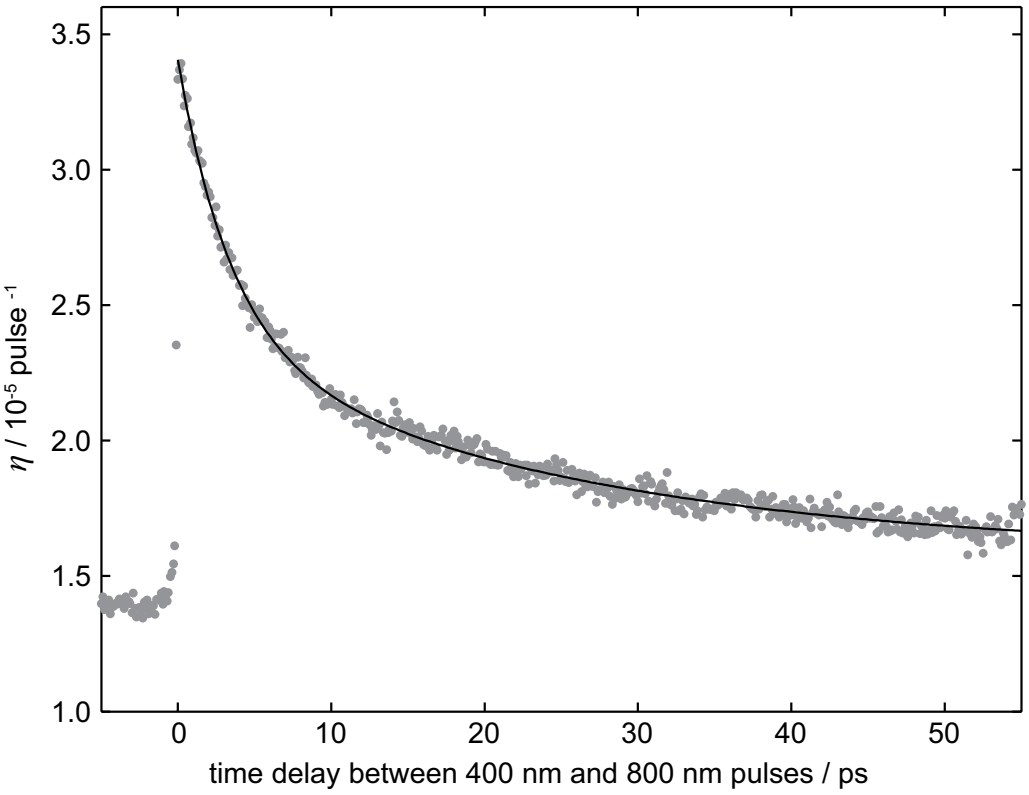

Figure 6.8: Time-resolved two-color experiment on photoconversion of GFP. After initial excitation of RH to RH* with a 400 nm pulse, a 800 nm pulse induces photoconversion, and the diffusion-corrected conversion efficiency (i.e., the calibration was applied) is shown as a function of pump–repump time delay t. The constant offset at negative time delays is due to the photoconversion caused by the single 800 nm and 400 nm pulses.

for $t \approx 0$, which represents an enhancement of a factor of 2.4 over the photoconversion efficiency yielded with the wrong time ordering of the excitation pulses (i.e., 800 nm first, $t < 0$). This clearly shows that there is a cooperative part to the photoconversion, requiring an interaction with the 400 nm pulse first, followed by an interaction with the 800 nm pulse. Therefore we can say that the photoconversion can more easily be achieved (i.e., with less overall pulse energy) when first exciting to RH* and then exciting to the reactive RH**.

By scanning the time delay of the two pulses one can determine how efficient the excitation to RH** is a certain time after the initial excitation to RH*. Fitting a bi-exponential function, $A_0 + A_1 \exp(-t/\tau_1) + A_2 \exp(-t/\tau_2)$, to the data for $t > 0$ yields time constants of $\tau_1 = (3.46 \pm 0.14)$ ps and $\tau_2 = (24.2 \pm 1.7)$ ps with amplitudes of $A_0 = (1.585 \pm 0.015) \times 10^{-5}$, $A_1 = (1.027 \pm 0.027) \times 10^{-5}$, and $A_2 = (0.793 \pm 0.018) \times 10^{-5}$. If the non-cooperative background of 1.4×10^{-5} is subtracted the relative amplitudes ensue as $\tilde{A}_0 = 9.2\%$, $\tilde{A}_1 = 51.3\%$, and $\tilde{A}_2 = 39.5\%$.

Kummer *et al.* [155] measured the fluorescence decay of the protonated RH* form at 450 nm, i.e., the depopulation of RH* of the T203V mutant, with a time resolution of

6 ps. They found time constants of 5.4 ps and 17 ps to be the predominant contribution to the dynamics, with similar relative amplitudes to the ones we measured in the photoconversion experiment. These dynamics of fluorescence relaxation from the RH^* state are the same, within the experimental accuracy, as the ones we find for excitation of the reactive RH^{**} state from RH^*. The deviation of the time constant reported by Kummer *et al.* (5.4 ps) from our time constant (3.46 ps) can likely be attributed to the low time resolution of 6 ps in Kummer's experiment. They also found contributions on longer timescales up to 400 ps adding up to a relative amplitude of $\approx 16\%$. The scanning range of our experiments was limited to 55 ps and the small constant contribution of $\tilde{A}_0 = 9.2\%$ is most likely due to those slow contributions. Therefore, we argue that the excitation to the reactive RH^{**} can only occur close to the Franck-Condon region that was accessed in the initial RH^* excitation step. It is not likely that a later, relaxed species like R_I^{-*} is excited to the reactive state, because in that case, the transient in Fig. 6.8 would rather look like a step function or even exhibit a rise of some picoseconds duration due to the formation of the relaxed forms of GFP in the excited state. Instead we observe that the timescales and amplitudes correspond to those for depopulation of the initially excited RH^*.

6.6 Time-delayed unshaped 400 nm – shaped 800 nm pulse excitation

Photoconversion of GFP is used to mark and track cellular structures under the fluorescence microscope. The insight into the photoconversion process gained through the experiments described in the previous sections can be employed to yield a high photoconversion efficiency. Especially when using high intensities through tight focusing of femtosecond pulses this marking of structures can be induced efficiently. In the light of this application, the question as to whether the photoconversion efficiency can be further improved through femtosecond pulse shaping is very interesting and will be addressed in this section.

The setup used for the time-resolved GFP experiments (Fig. 6.4) includes a pulse shaper in the path of the 800 nm beam, thus it is simple to measure the photoconversion yield as a function of pulse shape of the 800 nm pulses and time-delay between 400 nm and 800 nm pulses. Again, the separation of the photoconversion process starting from the neutral RH ground state to the photoconverted species R_{pc}^- is achieved through excitation into RH^* and subsequent excitation into the reactive RH^{**} state. The goal is to control the essential step of excitation of the reactive state ($RH^* \rightarrow RH^{**}$) by shaping the 800 nm pulses.

6.6.1 Inducing photoconversion with chirped pulses

First we studied the effect of chirped pulses by changing the second order coefficient ϕ'' (or b_2) of the spectral phase (see Eq. 2.14) and measuring the resulting change of absorbance ΔOD as a function of the time delay between the unshaped 400 nm and the chirped 800 nm pulses. The color-shaded surface in Fig. 6.9 represents the data recorded

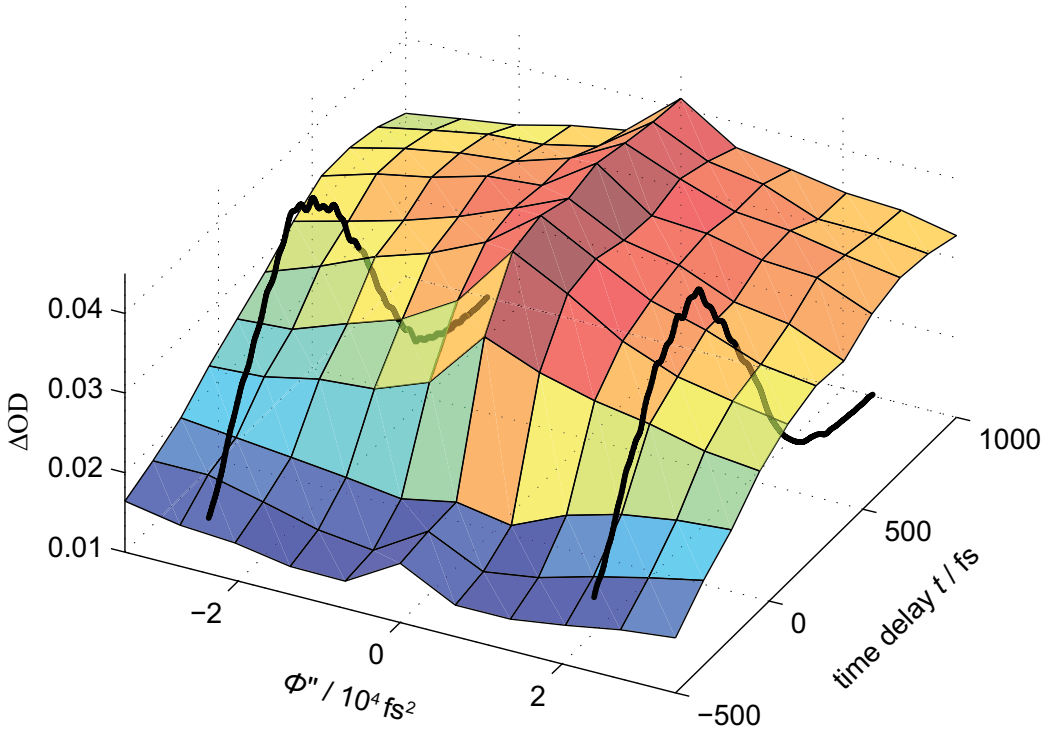

Figure 6.9: Time-delayed chirped-pulse experiments on GFP. Unshaped 400 nm pulses excite the GFP to the RH* state, and time-delayed, chirped 800 nm pulses excite to the reactive RH** state. The change in absorbance is shown as an 11 × 11 surface grid; both the time delay t and the second order spectral phase coefficient ϕ'' was varied. The simulated intensities of the chirped pulses are shown at $\phi'' = \pm 24000$ fs^2 as solid lines (arbitrary units).

at 11 points in each chirp direction and at different time delays. At $\phi'' = 0$ the curve corresponds to the curve of the unshaped 400–800 nm experiment in Fig. 6.8, section 6.5 with a steep rise of the signal around $t = 0$, limited by the instrument resolution and a small signal decline toward $t = 1000$ fs due to the biexponential dynamics determined earlier. The ridge along $\phi'' = 0$ that is also visible at $t < 0$ is due to three photon absorptions of 800 nm and not due to combined action of the 400 nm and 800 nm pulses. At $\phi'' \neq 0$ however, this single pulse effect plays a very minor role.

For nonzero chirp parameters on the other hand, the step at $t = 0$ is somewhat "washed out" and the signal rises more slowly with increasing time delay t. For interpretation of the data the temporal intensity of the shaped 800 nm pulses was simulated using the measured linear laser spectrum and the applied spectral phase. The resulting intensities $I(t)$ are plotted as thick lines in the graph at the chirp parameter values $\phi'' = \pm 24000$ fs^2. A simple interpretation of the two-dimensional data can be gained by considering the transients at each chirp value separately and regarding them as experiments analogous to Fig. 6.8. Then it is clear that using chirped 800 nm pulses the time resolution is worse compared to using unchirped pulses. This effect is independent of molecular dynamics after the excitation to RH* and only a result of the longer pulses that excite to RH**.

One can further model the signal by considering the different contributions of the

chirped pulse time-delayed experiments. We assume that the initial RH state does not absorb at 800 nm at all and that only linear absorption of the 800 nm light after excitation into the RH* state leads to photoconversion. Then the population P_{RH^*} in the RH* state, which is a precondition for photoconversion, can be written as

$$P_{\mathrm{RH}^*,\delta}(t) \propto \theta(t)\ \{A_0 + A_1 \exp(-t/\tau_1) + A_2 \exp(-t/\tau_2)\} \tag{6.22}$$

after excitation with infinitely short 400 nm pulses. Here, the first factor $\theta(t)$ is the Heaviside step function and the second factor is the biexponential function that was used to model the decay of the signal in section 6.5 with the pertaining best parameters A_i and τ_i. In our experiments the employed 400 nm pulses are estimated to have a duration of ≈ 100 fs and to be close to Gaussian shape:

$$I_{400}(t) \propto \exp\left(-\frac{4t^2 \ln 2}{(100\ \mathrm{fs})^2}\right). \tag{6.23}$$

Therefore the population of the excited state RH* can be expressed as the convolution

$$P_{\mathrm{RH}^*}(t) \propto \int_{-\infty}^{\infty} I_{400}(\tau - t)\, P_{\mathrm{RH}^*,\delta}(\tau)\, \mathrm{d}\tau. \tag{6.24}$$

Then, under the assumptions that the efficiency of the RH$^* \rightarrow$ RH** excitation is constant throughout the bandwidth of the 800 nm pulses, that it represents a one-photon transition, and that coherences in the GFP molecule do not play any role, the photoconversion signal $S_{pc}(t)$ as a function of time delay between 400 nm and 800 nm pulses can be modeled by the proportionality

$$S_{pc}(t) \propto \int_{-\infty}^{\infty} I_{800}(\tau - t)\, P_{\mathrm{RH}^*}(\tau)\, \mathrm{d}\tau. \tag{6.25}$$

The intensity $I_{800}(t)$ of the shaped pulses is simulated using the measured laser spectrum and the applied phase mask at the SLM.

For the values $\phi'' = \pm 24000$ fs^2 the simulated signals $S_{pc}(t)$ are compared in Fig. 6.10 to the measured data at these chirp values. In general, simulated and experimental data match well over the range of the time delays studied here. Especially the longer, "washed-out" rise starting at times $t < 0$, in contrast to Fig. 6.8, is reproduced well by the simulation.

It is obvious, however, that over the range of time delays studied here, the measured data for positive chirp (frequency up-chirp) is mostly greater than that for negative chirp (down-chirp). In fact, this can also be seen in the two-dimensional plot of Fig. 6.9 where the transients on the right hand side of $\phi'' = 0$ are slightly higher than on the left hand side. A possible and likely explanation for this asymmetry is an intrapulse dumping process [167–172]: after initial excitation the resulting population in RH* moves along the reaction coordinate – either due to wave-packet motion or due to vibrational relaxation. Therefore, the effective energy gap for transferring the population to the higher excited

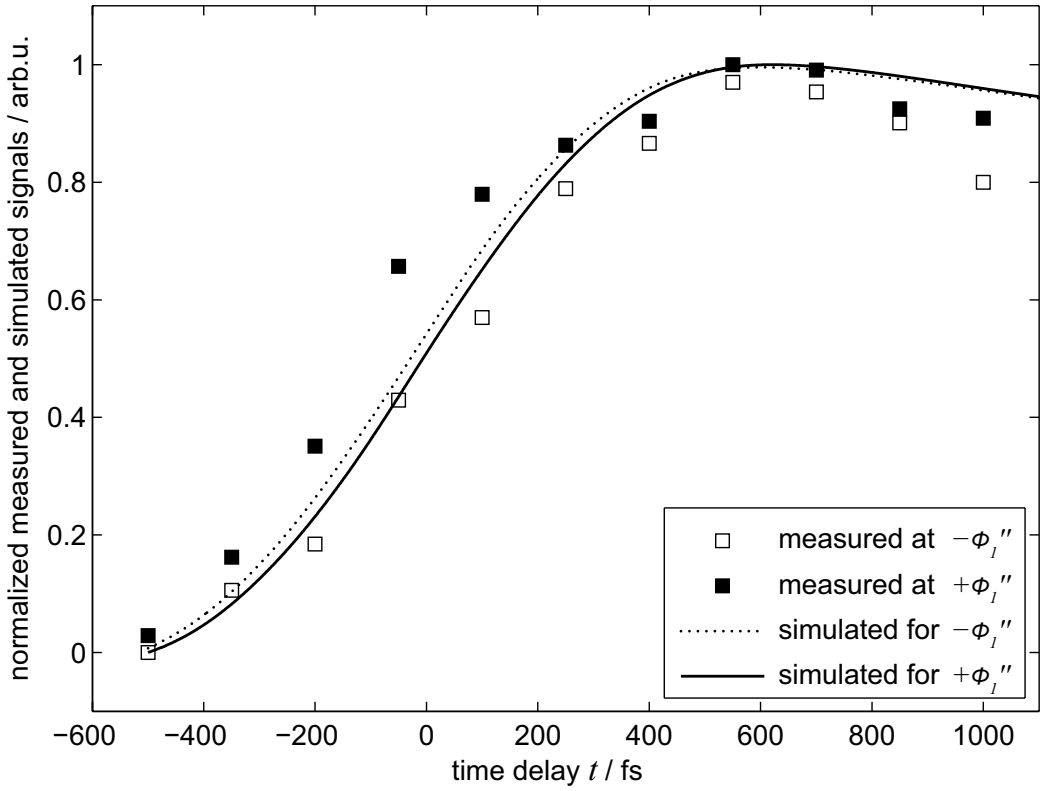

Figure 6.10: Comparison of simulated and measured chirped pulse transients of GFP. The signals $S_{pc}(t)$ at $\phi'' = \pm 24000$ fs^2 are shown as solid and dotted lines and were calculated according to eqns. 6.22–6.24 and normalized. The data of the measured transients at the same chirp values were also normalized and are shown as open squares and filled squares, respectively.

state RH** changes with time and chirped femtosecond laser pulses, depending on their frequency ordering can "follow" this effective energy gap. If the momentary frequency of a laser pulse is resonant with the effective energy gap during the duration of the pulse, not only an excitation RH* $\rightarrow$ RH** is possible but also a dumping of part of the already excited population RH* $\leftarrow$ RH** will occur. This process is called "intrapulse dumping". In effect, the population that remains in the higher state after the pulse depends on the frequency ordering of the pulse. If the energy gap decreases a higher fraction of molecules will end up in the excited state RH** when up-chirped pulses are used. Vice versa, if the energy gap increases, a higher fraction of molecules will end up in the excited state RH** when down-chirped pulses are used. In the theoretical parts of the original works of Cerullo *et al.* [167] and Cao *et al.* [171] the potentials participating in the intrapulse processes were described as displaced harmonic oscillators or a Morse ground state and a dissociative excited state, respectively. Both models imply that the energy gap decreases with time. Here, we deal with a system where the initial state is not a stationary "ground state". The Franck-Condon area on the RH* surface is depopulated rapidly (see also the simple potential energy scheme in Fig. 6.3). Thus it is

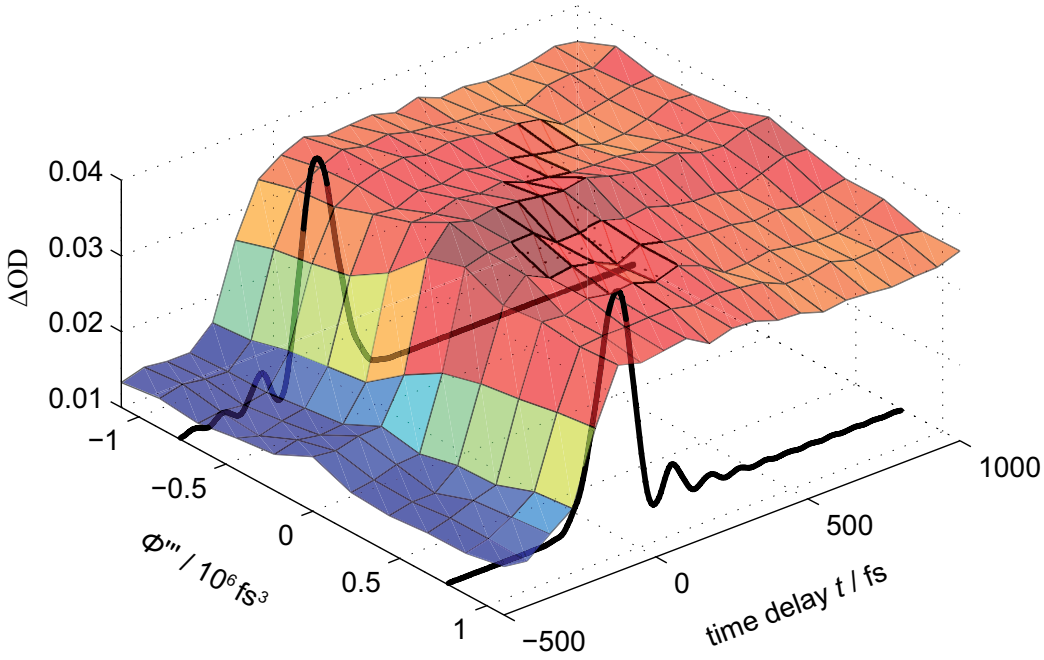

Figure 6.11: Time-delayed third order spectral phase pulses to induce photoconversion of GFP. Unshaped 400 nm pulses excite the GFP to the RH* state, and time-delayed 800 nm pulses, on which a third order phase mask was imprinted with the SLM, excite to the reactive RH** state. The change in absorbance is shown as an 21×11 surface grid with time delay t and the third order spectral phase coefficient ϕ''' as the respective axes. The simulated intensities of the shaped pulses are shown at $\phi''' = \pm 0.77 \times 10^6$ fs^3 as solid lines (arbitrary units).

not clear *a priori* if the energy gap between the RH* and the (unknown) RH** increases or decreases. The tendency in our data that up-chirped pulses are more efficient at inducing the photoreaction, however, provides strong evidence for a picture where the effective energy gap between RH* and RH** decreases on the accessible timescale of our experiment.

6.6.2 Photoconversion using third order phase pulses

In addition to the chirped pulse experiments we also conducted experiments where the third order spectral phase was varied. In contrast to mirror symmetric quadratic phase functions, point symmetric third order phase functions introduce asymmetric temporal pulse intensities (even with symmetric spectra). Experiments analogous to the ones in the previous section but with third order phase-shaped pulses can be expected to exhibit a pronounced asymmetry with respect to $\phi''' = 0$.

Indeed, Fig. 6.11 reveals this kind of asymmetry. Again, the data for $\phi''' = 0$ corresponds to the transient studied in section 6.5. For nonzero ϕ''' the steep rise around $t = 0$ is slightly washed out due to the slightly longer effective duration of the shaped pulses. The simulated intensities of the latter are shown at $\phi''' = \pm 0.77 \times 10^6$ fs^3 as solid lines in the same graph and exhibit postpulses for $\phi''' > 0$ and prepulses for $\phi''' < 0$.

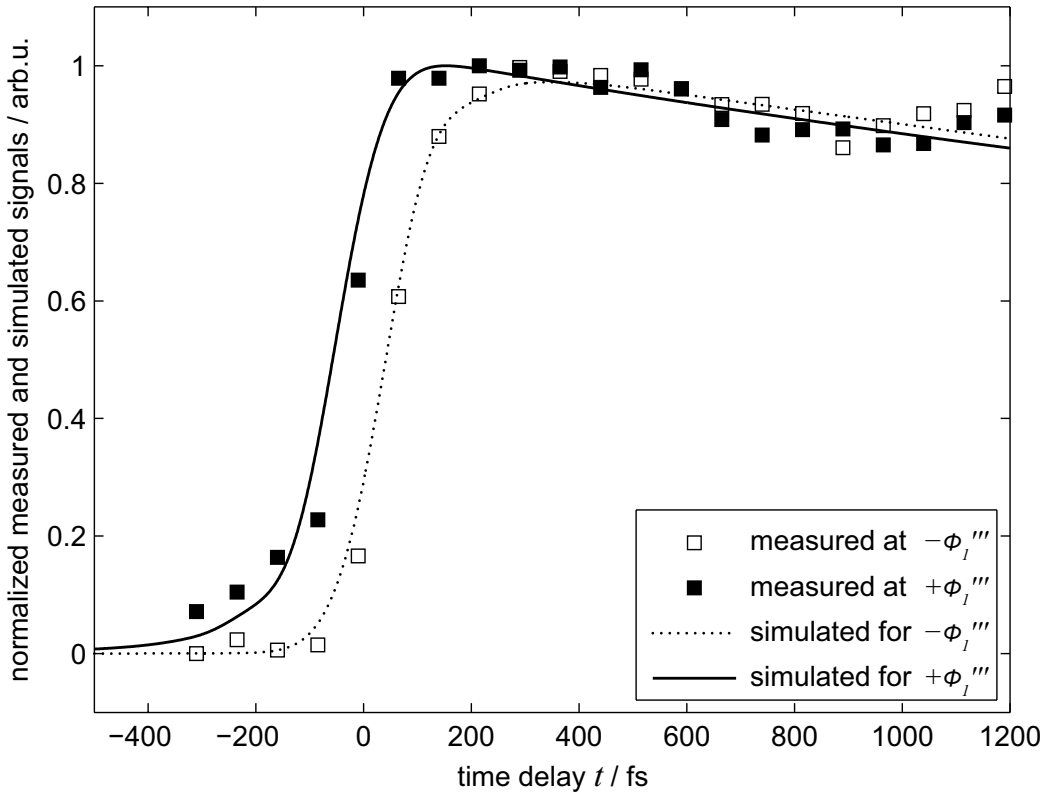

Figure 6.12: Comparison of simulated and measured signals from third order phase shaped 800 nm pulse transients of GFP. The signals $S_{pc}(t)$ at $\phi''' = \pm 0.77 \times 10^6$ fs^3 are shown as solid and dotted lines and were calculated according to eqns. 6.22–6.24 and normalized. The data of the measured transients at the same phase values were also normalized and are shown as open squares and filled squares, respectively. (The data from the experiment was corrected for a common timing offset.)

The photoconversion data reflects this asymmetry with respect to $\phi''' = 0$ in two ways. First, the major fraction of the signal rise occurs at earlier times t for $\phi''' > 0$, whereas negative ϕ''' shift the rise to later times.[1] Second, for positive ϕ''' the initial part of the signal increase starts at early times with a shallow slope, while at negative ϕ''' the signal stays low and then immediately rises sharply. Furthermore, for $\phi''' > 0$ the rise to the final signal level represents a rather sharp edge, whereas for $\phi''' < 0$ there is a shallow positive slope toward the final maximum signal level that is reached a few hundred femtoseconds later compared to $\phi''' > 0$. The final signal levels ($t \gtrsim 500$ fs) do not show any significant asymmetry anymore. Only the previously discussed small ridge due to three 800 nm photon excitation remains. It should be noted that in contrast to the chirped pulse experiments, the third order phase shaped pulses employed here do not have a frequency sweep.

The simple one photon absorption model (eqns. 6.22–6.24 from the previous section) was used to simulate the signal from the third order phase shaped experiment here as

[1] This is easiest to see by following the lines of constant t in the vicinity of the rise in Fig. 6.11.

well. The dotted and solid line in Fig. 6.12 represent the simulated signals at $\phi''' = -0.77 \times 10^6$ fs^3 and $\phi''' = +0.77 \times 10^6$ fs^3 and the open and filled squares are the respective measured data. It is obvious that the simulation reproduces all the features found in the data and discussed above: at earlier times a shallow rise and fast saturation for $\phi''' > 0$ and a later, sharp rise with slower saturation for $\phi''' < 0$. This excellent agreement of simulation and experiment implies that the model is correct and therefore no coherent or higher order effects play any role in this experiment using third order spectral phase masks.

6.7 Conclusions

In this chapter a study on the photoconversion of T203V GFP under femtosecond irradiation starting from the protonated species of the chromophore was presented. Our accumulative setup (see chapter 5) with a sensitivity of $\Delta\text{OD} = 10^{-7}$ was used for the experiments on this system. The photoconversion process was found to be largely governed by an initial excitation to a higher excited state of the chromophore RH**. From there, photoconversion is much more efficient than from the first excited state RH*. This supports earlier suggestions that the decarboxylation reaction of the Glu222 rest follows a Kolbe type mechanism [159] because a higher excited state generally has a higher oxidative potential. To further investigate the role of RH* in the subsequent excitation to the reactive RH** state, we used a time-resolved two-color experiment where a 400 nm pulse excites RH to RH* and a time-delayed 800 nm pulse excites RH* to RH**. The probability of the latter process decreases with time constants very similar to those for the depopulation of RH* previously reported in the literature [155]. Thus, with one 800 nm photon the RH** state can only be reached from the region of the RH* potential energy surface where the initial excitation occurred and, due to the excited state dynamics, RH** can only be reached a few picoseconds after the initial excitation. These results are summarized in an energy level diagram in Fig. 6.13.

While the experiments with unshaped and time-delayed 400 nm and 800 nm pulse excitation allowed us to gain insight into the time scale of a possible excitation from RH* into the photoconverting RH** state, the experiments with phase-shaped and time-delayed 800 nm pulses showed that the second excitation step RH$^{*} \rightarrow$ RH** can be modeled successfully as a simple linear absorption. Both chirped 800 nm pulses and third order phase shaped 800 nm pulses were employed in the experiment. The third order phase experiments revealed that the data can be fully reproduced by the simple linear absorption model. In contrast, positively and negatively chirped 800 nm pulses resulted in a slight asymmetry with respect to unshaped pulses. This suggests that intrapulse dumping plays a small role in the chirped pulse RH$^{*} \rightarrow$ RH** excitation. Furthermore, the down-chirped frequency ordering for suppression of photoconversion indicates that the parts of the potential energy surfaces of RH* and RH** that are populated during the pulse duration approach each other with increasing reaction coordinate so that the effective energy gap decreases with progressing time (compare to Fig. 6.13).

The findings of the studies in this chapter are particularly interesting with respect to the use of GFP in TPA microscopy because the high intensity levels of a typical setup

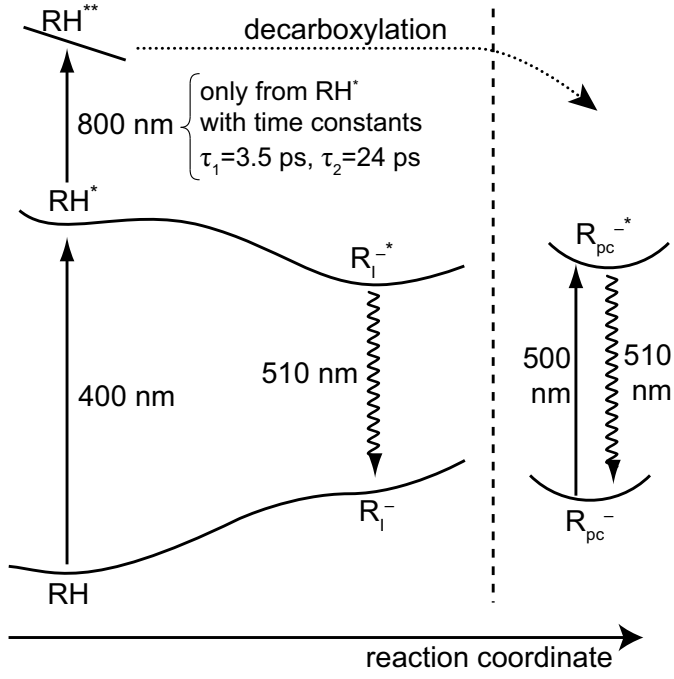

Figure 6.13: Results of our femtosecond studies on the ultrafast photoconversion of GFP. One photon excitation at 400 nm or TPA at 800 nm leads to the excited state RH*. Starting from there, efficient photoconversion can be induced by further excitation into RH**. This excitation is only possible within the first few picoseconds. Additionally, the potential energy surfaces of RH* and RH** are tilted toward each other with increasing reaction coordinate.

using a femtosecond oscillator with tight focusing ($\approx$ 1 μm) are comparable with the intensity levels of our experiments with an amplified laser system and loose focusing. When using 800 nm pulses in a microscopy experiment, the process of ground-state absorption and subsequent excited-state absorption from RH* can be regarded as a resonance-enhanced multiphoton absorption, thus there will always be some photoconversion in microscopy experiments, decreasing the fluorescence signal from 800 nm TPA over time, and also changing the fluorescence lifetimes [161, 166].

7 Applications of the accumulative method to chiral systems

7.1 Introduction

Chirality is a fundamental principle of the structure of molecules. A chiral molecule is defined as a molecule that cannot be matched with its own mirror image. Both mirror images, called enantiomers, have the same chemical bonds and the same constitution but their functional groups are oriented in different spatial directions with respect to the central structure. In an achiral environment both enantiomers exhibit the same reactivity, the same physical and scalar properties and cannot be distinguished chemically. However, all life on earth can be called "chiral" at its most fundamental scale. Almost all known naturally occurring functional peptides consist of only the L enantiomers of amino acids. This phenomenon has been termed the "homochirality" of life. The question why and how the L enantiomers came to be the vastly predominant chiral form in biomolecules is still subject to scientific discussion and investigation [173, 174]. A number of non-biological mechanisms that can lead to a predominance of one enantiomer have been proposed, such as magnetic fields, circularly polarized light, or the effects of chiral elementary particles. All the proposed sources of enantiomeric excess lead to only a very small predominance of one enantiomer and amplification mechanisms of these effects are required to finally lead to the biological homochirality as we find it in nature.

Chemistry on the other hand, strives to find methods for synthesizing chiral compounds, e.g. with biological action for pharmaceutical purposes. Usually, chiral reactants are used in such chemical syntheses because racemic or achiral reactants cannot yield one particular product with enantiomeric selectivity. A synthesis approach which starts from achiral reactants must make use of an external chiral agent in order to selectively yield a single product enantiomer. For the purposes of both industrial synthesis and academic chemical research the chiral agent is usually a chiral reactant or a chiral auxiliary, such as a chiral solvent or a chiral catalyst. Due to the chirality of photons and light in general, chemical chirality can potentially be controlled using tailored light fields to induce photoreactions.

This chapter summarizes the different approaches to chiral photochemistry from the literature with a special emphasis on the use of shaped femtosecond laser pulses to control molecular chirality. A fast and precise polarimeter is presented as a first step toward the combination of the accumulative detection method (introduced in chapter 5) with chiral photochemistry. Finally, potential molecular systems and mechanisms for quantum control experiments on chirality are discussed.

7.2 Chiral asymmetric photochemistry

7.2.1 Continuous-wave circularly polarized light

An approach very different from classic chemistry is the use of light as a chiral external agent [175]. A partially selective synthesis can be achieved through photochemical reactions using circularly polarized light [176–178]. This method for chiral photochemistry exploits the static circular dichroism, i.e. the fact that under illumination with circularly polarized light the extinction coefficient of one enantiomer is slightly different from the extinction of the other enantiomer. In asymmetric synthesis in general, one tries to maximize or minimize the enantiomeric excess (*e.e.*) which is defined as

$$e.e. = \frac{[R] - [S]}{[R] + [S]} \tag{7.1}$$

with the concentrations [R] and [S] of the two enantiomers R and S. The *e.e.* ranges from -1 to +1 for 100% S to 100% R, with 0 for the racemic mixture.

The two most common approaches to direct asymmetric photochemistry are photoderacemization and asymmetric photodestruction. Photoderacemization starts with a racemic mixture of chiral molecules and circularly polarized light is used to excite predominantly one enantiomer which is then transformed to an achiral form. The thermal reverse reaction is not enantioselective and hence, with prolonged irradiation, a stationary state with nonzero enantiomeric excess is reached. Asymmetric photodestruction, on the other hand, creates an enantiomeric excess with circularly polarized light by preferentially exciting and destroying one enantiomer versus the other.

Both approaches are limited by the difference in the extinction coefficients of the two enantiomers. Kuhn *et al.* [179] were the first to unambiguously observe asymmetric photochemistry and to formulate its limits. They defined [180] the anisotropy, g, or Kuhn factor as

$$g = \frac{\epsilon_\mathrm{l} - \epsilon_\mathrm{r}}{\epsilon} \tag{7.2}$$

where $\epsilon = (\epsilon_\mathrm{l} + \epsilon_\mathrm{r})/2$ with the extinction coefficients ϵ_l and ϵ_r for left and right circularly polarized light at the employed wavelength. In the case of photoderacemization CW irradiation leads to a stationary state where $[\mathrm{R}]k_\mathrm{R} = [\mathrm{S}]k_\mathrm{S}$ with the reaction rates $k_\mathrm{R,S}$ which are proportional to the extinction coefficients $\epsilon_\mathrm{R,S}$. Thus, the stationary state of photoderacemization is also characterized by the maximum achievable enantiomeric excess

$$e.e._\mathrm{max} = \pm\frac{g}{2}. \tag{7.3}$$

Since molecules typically have a g factor of less than 10^{-2}, the achievable *e.e.* with circularly polarized CW light is rather low. Similar yet more complicated analyses can be performed for other types of asymmetric photochemistry using circularly polarized light only. These "classical" approaches to enantioselective photochemistry are ultimately limited by the g factor. One can understand the minuteness of the enantiomeric selectivity of these approaches by considering that the circular dichroism is an effect of the interaction of the light field with the molecular magnetic dipole moment and both the magnetic part of the light field and the molecular magnetic dipole are usually very

small. Alternatively, one can explain the small g factor by noting that the chirality of a circularly polarized light field is hardly felt by a molecule because it is much smaller than the wavelength (and thus the period of polarization rotation) of the light.

7.2.2 Controlled asymmetric photochemistry using femtosecond laser pulses

The development and enhancement of femtosecond laser systems triggered renewed interest in optically controlled asymmetric chemistry. In general, the advantage of femtosecond pulses over CW light is that electronic and vibrational dynamics and coherences in the molecule can be exploited. Secondly, non-equilibrium states and wave packets can be prepared and acted upon by femtosecond laser pulses. Controlling the stereochemical properties of molecules and thus chiral photochemistry with femtosecond laser pulses can hence be regarded as an extension to coherent control (e.g. in the schemes of Brumer and Shapiro [181] or Tannor-Kosloff-Rice [182, 183]).

A prerequisite to the theoretical treatment of enantioselective photochemistry is a quantum mechanical formulation of the problem. After the establishment of modern quantum mechanics, Hund was the first to formulate the stability criterion of enantiomers in terms of tunneling times in a one-dimensional double well potential where the wells represent the left and the right handed mirror images [184]. This model explains the existence of enantiomers but for a description of processes involved in an enantioselective photochemical reaction the theoretical formulation has to include the interaction of the molecule with the electric field and describe the dynamics of the system.

In the early 1990's Shapiro and Brumer suggested the use of coherent lasers to break the symmetry of a theoretical model of achiral precursor molecules and yield chiral products [185]. Subsequently, there have been a number of theoretical investigations on the problem of chiral synthesis using short coherent light pulses.

It should be noted that in general the conditions in an experiment will be vastly different from the idealized conditions assumed in theoretical models for quantum control of asymmetric photochemistry. One has to consider the proposed control mechanisms according to their "robustness" to the imperfections of an experiment. There are several prerequisites for a realistic control experiment that one could conduct in a well-equipped femtosecond laboratory and in our laboratory in particular. The precursor molecules will initially be randomly oriented in a racemic mixture. In solution, where one can expect optically detectable *e.e.* yields, the molecules will exhibit energy inhomogeneity due to the relatively strong interaction with the solvent. Finally, all involved laser beams will have a nonuniform spatial profile and a drift of the carrier–envelope phase, especially when using a number of amplification and frequency conversion stages.

A few years after Brumer and Shapiro's suggestion, Salam and Meath [186] presented the strength and duration of circularly polarized pulses as a means to control the excited state populations of right vs. left handed enantiomers in a randomly oriented racemic mixture. This theoretical suggestion exploits the slightly different coupling strengths of circularly polarized light to the two enantiomers of a chiral molecule, i.e., it includes the circular dichroism as an effect of the magnetic dipole moment. As a result of the different couplings the populations of the excited enantiomers display a beating with a

frequency given by the difference in coupling strengths. While this method can in theory yield $e.e. = 100\%$ and is suited for randomly oriented racemic mixtures, it requires very high intensities to cycle the populations of the excited states. It is also very sensitive to fluctuations in pulse duration; e.g. a difference 0.5 fs over a 200 fs pulse inverts the sign of the $e.e.$ The mechanism for chiral control of the model system in Ref. [186] also relies on the absence of any interaction between the molecules with each other or with the environment. Similarly, any inhomogeneities either in the laser beam profile or in the molecular energies would destroy the control selectivity.

In a quantum dynamics simulation on the molecule H_2POSH (phosphinothioic acid) which features a chiral axis (the P–S bond), Fujimura *et al.* [187, 188] applied optimally shaped IR laser pulses with two polarization components to pre-oriented molecules at low temperature. Starting from a racemic superposition state they were able to yield close to 100% enantiomeric excess after irradiation with a multi-polarization multi-pulse laser field of ≈ 50 ps duration. For this result the molecules were fully and rigidly oriented with their P–S bond along the z-axis and only rotation of SH with respect to the rest of the molecule was allowed. The laser propagated along z and had the two polarization components E_x and E_y. In later publications the authors extended the treatment of this molecule to a two-dimensional model retaining the orientation along the P–S bond but also allowing free rotation of the whole molecule about this axis [189]. They also extended their theoretical approach to a density matrix formalism of the enantiomer mixture. When allowing free rotation about the molecular axis the authors find reduced control over the preparation of a pure enantiomeric state. They reached $e.e. \approx 20\%$ after a shaped pulse of 120 ps duration vs. 100% after a shaped pulse of 80 ps duration in the case of the fully rigid orientation. Nevertheless, the fact that a pre-oriented racemic mixture in which rotation of the molecules is allowed can be distilled to a significant enantiomeric excess with shaped laser pulses is an important result.

Shapiro, Brumer, and co-authors advanced their control model to a system with an electronic ground state that has two distinct enantiomeric minima $|\mathrm{D}\rangle$ and $|\mathrm{L}\rangle$ and a common excited electronic state that has an achiral nature. They consider two vibrational states in the electronically excited state ($|1\rangle, |2\rangle$). Three laser pulses are employed to couple $|\mathrm{D}\rangle \leftrightarrow |1\rangle, |2\rangle$ and $|\mathrm{L}\rangle \leftrightarrow |1\rangle, |2\rangle$, and also $|1\rangle \leftrightarrow |2\rangle$ [134]. In this model system the coherent coupling of the levels results in control of the directional population transfer between $|\mathrm{D}\rangle$ and $|\mathrm{L}\rangle$. Quantum chemical simulations on dimethylallene were conducted to determine the required vibronic states for application of this control scenario [190]. The control parameters of the general scenario are pulse duration, pulse shape, pulse frequencies (or detunings), pulse delays, and pulse intensities. The system is highly sensitive to variations of these parameters and $e.e. \approx 1$ can be reached if the same pulse configuration is applied multiple times ("laser distillation"). It should be noted that other groups have shown that the coherent control scheme is only viable if either pre-aligned or pre-oriented precursor molecules are used [191, 192]. The effects of the electric dipole interaction of an achiral laser field (with less than three orthogonal polarization components) with an isotropic ensemble will always amount to a net enantiomeric selectivity of zero.

Bychkov *et al.* [191] modeled the same coherent control mechanism of the 4-level model system $\{|\mathrm{D}\rangle, |\mathrm{L}\rangle, |1\rangle, |2\rangle\}$ as Brumer and Shapiro, without specifying an actual

molecule, however, they studied an isotropic distribution of molecules over the Eulerian angles. In this situation, they showed that in order to "encode" the chiral information into the molecules of the randomly oriented mixture a chiral light field with three orthogonal pulsed polarization components is necessary. Similar to Ref. [134], the control parameters were frequency detuning and pulse separation. The remaining degree of enantioselectivity was found to be $e.e. = 8\%$.

The group of Fujimura circumvented the problem of an initially isotropic distribution by employing a three polarization component electric field as well [192]. However, they pointed out, the criterion that the field be chiral can also be met by a *sequence* of pulses. In such a sequence the first pulse that has for instance z-polarization can prealign the molecules along the z-axis [193] and a subsequent combination of shaped x- and y-polarized pulses can selectively prepare one enantiomeric state with an $e.e.$ of 44% for their model system H_2POSH. Recently, Zhdanov and Zadkov [194] suggested a similar scheme were an enantiomeric purification can be reached by orientation-dependent (pre-)selection of molecules [195] and subsequent symmetry-breaking electric dipole interaction.

Brumer *et al.* extended their coherent control scheme to randomly oriented precursors (or an "unpolarized" ensemble) by also employing three phase-stable, mutually perpendicular electric field components [196]. Their theoretical treatment involves a ten state model including angular momentum and has been applied to 1,3-dimethylallene as a model system [197]. Further, it has been shown that this coherent control scheme remains functional in the presence of collisions and decoherence in a dissipative bath *if* the pertinent timescales are on the order of or longer than the interaction with the control pulses [198, 199].

Methods that are related to stimulated rapid adiabatic passage (STIRAP) [200] were also suggested as control mechanisms with chiral selectivity. Ohta *et al.* [201] studied preoriented racemic molecules that undergo adiabatic passage to a pure enantiomeric state by irradiation with a two-component electric field. The adiabatic parameter is the direction of the changing linearly polarized field. In two different approaches Král *et al.* [202, 203] treated three- and multi-level systems with broken symmetry (chirality). In such a system the "ordinary" STIRAP scheme with laser coupled states $|1\rangle \leftrightarrow |2\rangle$ and $|2\rangle \leftrightarrow |3\rangle$ for population transfer from $|1\rangle$ to $|3\rangle$ can be modified by a third laser to couple $|1\rangle \leftrightarrow |3\rangle$. Then, the two quantum pathways $|1\rangle \leftrightarrow |3\rangle$ and $|1\rangle \leftrightarrow |2\rangle \leftrightarrow |3\rangle$ can interfere with each other and depending on the overall phase complete enantioselectivity can be reached.

Many different quantum control methods using femtosecond or picosecond pulses have been treated theoretically in the literature. While initial models and suggestions were very sensitive to preorientation of molecules, laser intensities, collisions, etc. and therefore hardly viable under real experimental conditions, later approaches included randomly oriented racemic mixtures and dissipative environments. Experimental limitations like spatially varying intensities due to a Gaussian beam profile and drifts in the carrier–envelope phase and the relative phases of the involved laser pulses have not been included in the simulations so far. Nevertheless, the theoretical studies have demonstrated that significant photochemical enantioselectivity can be accomplished. Asymmetric synthesis starting from achiral precursors and using only light as a chiral agent

seems to be feasible with modern ultrafast laser technology.

The question of why no experiment demonstrating quantum control of chirality has been reported up to now can be answered by considering the challenging nature of such an experiment. The accurate determination of the outcome of an experiment, i.e., gaining a measure for the actual enantioselectivity of the applied laser pulse configuration, is a difficult task. In the gas phase the low density of molecules requires a detection method that is sensitive and can distinguish enantiomers on the single molecule level [204]. However, for actual chemical applications a high density of reactants and products is desirable. This is why we chose the solution phase as the medium for enantioselective quantum control experiments. A method for accurate measurements of the outcome of an enantioselective experiment had to be developed. This method has to be sensitive and moderately fast because the expected signals from a quantum control experiment are small and possibly of a transient nature.

7.3 Sensitive and fast polarimeter

There are two optical effects when passing through a chiral medium that could potentially be exploited to measure the *e.e.*: the circular dichroism or the optical rotation. As mentioned before, the circular dichroism is the fact that left and right circularly polarized light have different extinction coefficients for a particular enantiomer. Optical rotation is the fact that left and right circularly polarized light experience slightly different indices of refraction. These two phenomena, circular dichroism (CD) and optical rotation (OR), are fundamentally connected to each other by a Kramers–Kronig relation. Fig. 7.1 shows schematic CD and OR spectra of a chiral molecule in the vicinity of an electronic transition at ω_0. While the circular dichroism is only notable close to ω_0, the OR has significant values at frequencies where there is no absorption. Hence a detection apparatus that exploits the OR to detect the enantiomeric excess can be used at many different wavelengths where no absorption occurs and the actual *e.e.* yield of the experiment is not veiled by potential further photochemistry induced by the light used for the measurement. Therefore, for the design and construction of a setup that can be employed in quantum control and spectroscopy experiments on chiral systems and chiral selectivity we chose to measure the enantiomeric excess via the OR of the sample solution.

The well-known effect of OR on linearly polarized light that passes through a chiral sample is the rotation of the polarization plane. The linearly polarized light can be thought of as consisting of two circularly polarized electric field components, one left and one right handed. Then the propagation through the chiral medium phase-shifts the two components with respect to each other. Addition of these phase-shifted circularly polarized components yields a linearly polarized output field that is rotated by an angle

$$\alpha = [\alpha]_\lambda^T \times M \times l \times e.e. \tag{7.4}$$

where M is the total concentration of both enantiomers and l is the length of propagation through the sample. The quantity $[\alpha]_\lambda^T$, usually given in $^\circ$ ml/g dm, is called the specific

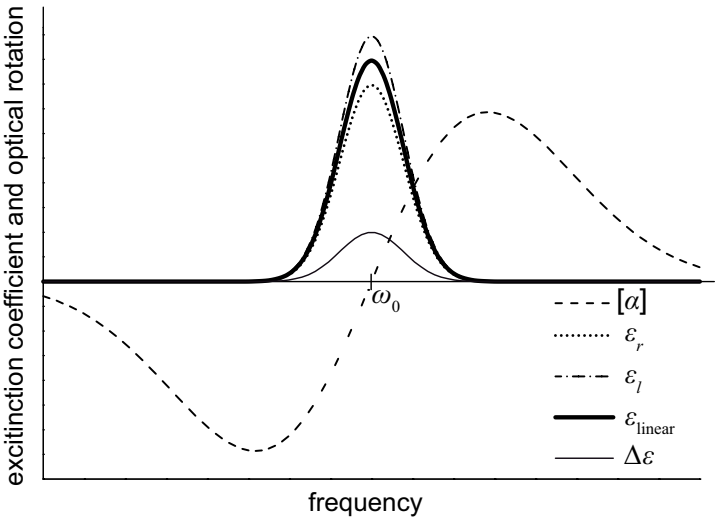

Figure 7.1: Circular dichroism and optical rotation in the vicinity of an optical resonance at ω_0. Figure adapted from Ref. [205].

rotation and depends on the wavelength λ and the temperature T of the solution. It is also solvent specific.

In its simplest and crudest implementation an apparatus for measuring the optical rotation angle, called a polarimeter, consists of a (monochromatic) light source, a polarizer, the sample chamber, an analyzer, and a detector. By rotating the analyzer one can find the rotation angle that the sample introduces. However, in order for α to have a significant value that can be measured in this kind of setup, long interaction lengths of tens of centimeters and high enantiomeric excesses are required. This condition cannot be met in a femtosecond spectroscopy or quantum control experiment because ideally for such an experiment only the laser–solution interaction in the focus of the laser beam is measured and the sample volume that needs to be irradiated is very small. Hence we aimed our efforts at constructing a polarimeter that can detect small optical rotation angles using only a short optical path length. Additionally, the polarimeter setup should be suitable for combination with the accumulative method in order to increase the sensitivity of the chirality detection compared to single pulse experiments and measurements. The sample volume has to be accessible for diverse optical and spectroscopic measurements from many directions because non-chiral-sensitive measurements may need to be combined with the OR measurement and precursor molecules can, for instance, be generated photochemically. Furthermore, the diffusion and possibly the metastable character of the generated chiral species in the accumulative setup requires a fast measurement of the OR on a time scale of less than 1 s.

7.3.1 Polarimeter setup

The criteria for measuring the optical rotation angle resulting from an accumulative quantum control experiment in liquid phase cannot be met by commercially available polarimeters. Within Johannes Buback's Diplom thesis work [205] we have adapted and extended a setup originally presented by Lee and Su [206] to the conditions in our experiment.

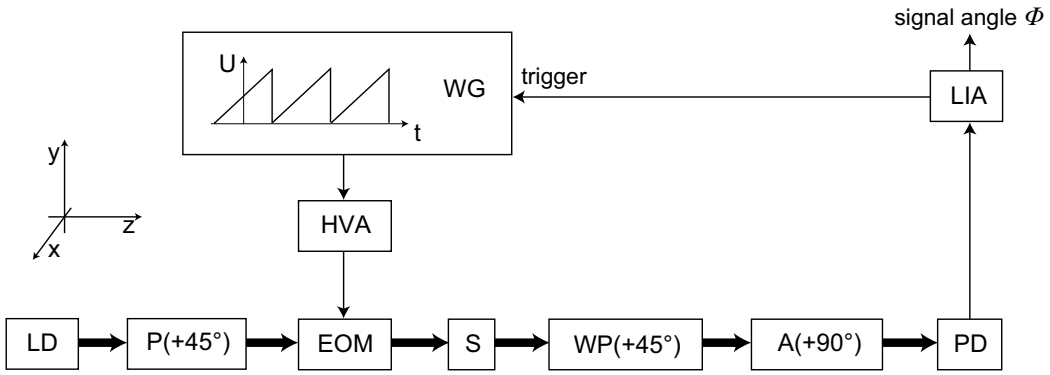

Figure 7.2: Schematics of the fast polarimeter setup for sensitive enantiomeric excess detection. The thick arrows in the bottom of the figure depict the path of the light propagating along the z-axis through the optical setup. Light from a laser diode LD is polarized at +45° by a polarizer P, modulated by the electro-optic modulator (EOM), and passed through a sample S. A δ-wave plate WP oriented at +45° introduces a retardation of close to $n\pi$ with $n = 0, \pm1, \pm2, ...$ Finally, an analyzer A and a photodiode PD are employed to gain the signal $I(t)$ which is compared to a reference oscillation in a lock-in amplifier LIA. The sawtooth wave form driving the EOM is generated in WG and triggered by the internal reference of the LIA.

A schematic diagram of the polarimeter setup is shown in Fig. 7.2. In brief, the setup uses polarization modulated light for heterodyne detection of a phase shift introduced by a chiral sample medium. Additionally it exploits an "angular amplification" mechanism to increase the sensitivity. The principles will be described in detail in sections 7.3.2 and 7.3.3. Light from a laser diode at 405 nm is polarized along the +45° direction by means of a polarizer P. The coordinate system is also defined in Fig. 7.2. The polarization state of the light is then modulated with an electro-optic modulator (EOM) driven by a high voltage amplified (HVA) sawtooth wave sweeping from 0 to 448 V. This corresponds to an optical retardation of 0 to λ along the optical axis of the EOM which is oriented in the x direction (0°). Behind the EOM a chiral sample medium S is placed in the beam path. The δ-wave plate (also called adjustable wave plate or Berek compensator) introduces a retardation of $\delta \approx n\pi$ ($n = 0, \pm1, \pm2, ...$) and is responsible for the angular amplification explained below. Finally, the resulting intensity is detected by a low noise photodiode PD through an analyzing polarizer A. The lock-in amplifier LIA measures the phase angle ϕ of the signal with respect to its internal reference. To guarantee phase-stability of the EOM modulation to the LIA reference, the oscillator output of the LIA is used to trigger the sawtooth waveform generator WG. Alternatively, the waveform generator could be used as an external reference for the LIA, however, this proved to be of lower phase stability than using the internal oscillator of the LIA.

7.3.2 Detected signal I(t)

The expected signal from the described setup (detected by the photodiode PD) can be derived using Jones calculus [207]. Then the phase shift ϕ of the signal $I(t)$ with respect to the LIA reference can be determined and related to the OR of the chiral sample.

We start with the linearly polarized field after the polarizer P:

$$\overrightarrow{E}_{in} = \frac{1}{\sqrt{2}} \begin{pmatrix} 1 \\ 1 \end{pmatrix}. \tag{7.5}$$

This field is then modified by the optical elements EOM, S, WP, and A with the respective Jones matrices

$$\begin{aligned} \mathrm{EOM}(t) &= \begin{pmatrix} \exp \frac{\mathrm{i}\omega t}{2} & 0 \\ 0 & \exp -\frac{\mathrm{i}\omega t}{2} \end{pmatrix} && (7.6) \\ \mathrm{S}(\alpha) &= \frac{1}{2} \begin{pmatrix} \cos\alpha & \sin\alpha \\ -\sin\alpha & \cos\alpha \end{pmatrix} && (7.7) \\ \mathrm{WP}(\delta) &= \mathrm{R}\left(-\pi/4\right) \begin{pmatrix} \exp \frac{\mathrm{i}\delta}{2} & 0 \\ 0 & \exp -\frac{\mathrm{i}\delta}{2} \end{pmatrix} \mathrm{R}\left(\pi/4\right) && (7.8) \\ \mathrm{A} &= \begin{pmatrix} 0 & 0 \\ 0 & 1 \end{pmatrix} && (7.9) \end{aligned}$$

with the rotation matrix

$$\mathrm{R}(\theta) = \begin{pmatrix} \cos\theta & -\sin\theta \\ \sin\theta & \cos\theta \end{pmatrix}. \tag{7.10}$$

Hence the electric field $\overrightarrow{E}_{out}$ at the photodiode results from

$$\overrightarrow{E}_{out}(t) = \begin{pmatrix} E_x \\ E_y \end{pmatrix} = \mathrm{A}\ \mathrm{WP}(\delta)\ \mathrm{S}(\alpha)\ \mathrm{EOM}(t)\ \overrightarrow{E}_{in} \tag{7.11}$$

and the evaluation of the matrix product yields the components $E_x(t) \equiv 0$ and

$$\begin{aligned} E_y(t) = \frac{1}{2\sqrt{2}} \Bigg\{ \exp\left[-\frac{\mathrm{i}}{2}\left(\delta + \omega t\right)\right] \big[\cos\alpha + \exp\left(\mathrm{i}\delta\right)\cos\alpha + \sin\alpha - \exp\left(\mathrm{i}\delta\right)\sin\alpha \\ - \exp\left(\mathrm{i}\omega t\right)\left(-\cos\alpha + \sin\alpha + \exp\left(\mathrm{i}\delta\right)\left(\cos\alpha + \sin\alpha\right)\right)\big] \Bigg\}. \end{aligned} \tag{7.12}$$

Therefore the signal that is measured by the photodiode is given by

$$I(t) = \left|\vec{E}(t)\right|^2 = \frac{1}{2}\left[1 - 2\cos\alpha\cos\delta\cos\left(\omega t\right)\ \sin\alpha + \sin\delta\sin\left(\omega t\right)\right]. \tag{7.13}$$

Using the identity

$$a\sin x + b\cos x = \sqrt{a^2 + b^2}\ \ \sin\left(x + \arctan\frac{b}{a}\right) \tag{7.14}$$

one can rewrite Eq. 7.13 as

$$I(t) = \frac{1}{2}\left[1 - A\sin\left(\omega t - \phi\right)\right]. \tag{7.15}$$

This yields the time-independent amplitude

$$A = \sqrt{\sin^2\delta + \left[\sin\left(2\alpha\right)\ \cos\delta\right]^2} \tag{7.16}$$

and phase

$$\phi = \arctan \frac{\sin(2\alpha)}{\tan \delta}. \tag{7.17}$$

The oscillatory part of Eq. 7.13 is at the same frequency ω as the reference of the lock-in amplifier and the modulation of the EOM. Therefore A and ϕ represent the result of the measurement with the lock-in amplifier. A and ϕ depend on the optical rotation angle α and on the wave plate retardation δ. Due to electronic effects like cable lengths, capacities, and phase shifts at the photodiode detector the actual measured phase is afflicted with a constant offset ϕ_0 even for a non-rotating sample medium ($\alpha = 0$). The offset ϕ_0 can be determined by filling the sample holder with the achiral solvent alone. For Eq. 7.17 to be valid, this offset needs to be subtracted from the lock-in amplifier phase. Then, using a known value of δ, the optical rotation α can be calculated as

$$\alpha = \frac{1}{2} \arcsin(\tan \delta \ \tan \phi). \tag{7.18}$$

7.3.3 Angular amplification

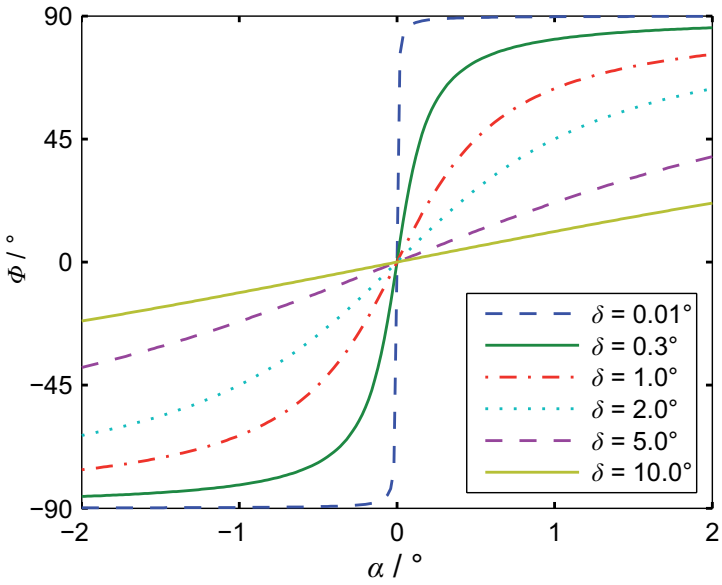

Figure 7.3: Phase ϕ as a function of optical rotation α of the sample. Especially for small retardations δ, the detected phase depends strongly on the optical rotation angle α.

To understand the principles of the polarimeter setup and why it is highly sensitive to small rotation angles we consider the detected phase ϕ as a function of both the wave plate retardation δ and the optical rotation of the sample α. Fig. 7.3 shows the signal phase for small absolute values of α for different settings of the variable wave plate $\delta \gtrsim 0$. It is obvious that the detected phase ϕ increases with increasing α and it also increases with δ approaching 0. Especially for small α, a retardation δ can be chosen such that the measured phase angle ϕ is considerably larger than the angle of the optical rotation α. One can define $M = \phi/\alpha$ as an angular amplification factor. This is plotted on the left hand side of Fig. 7.4 for different values of δ, showing that, depending on the setting of

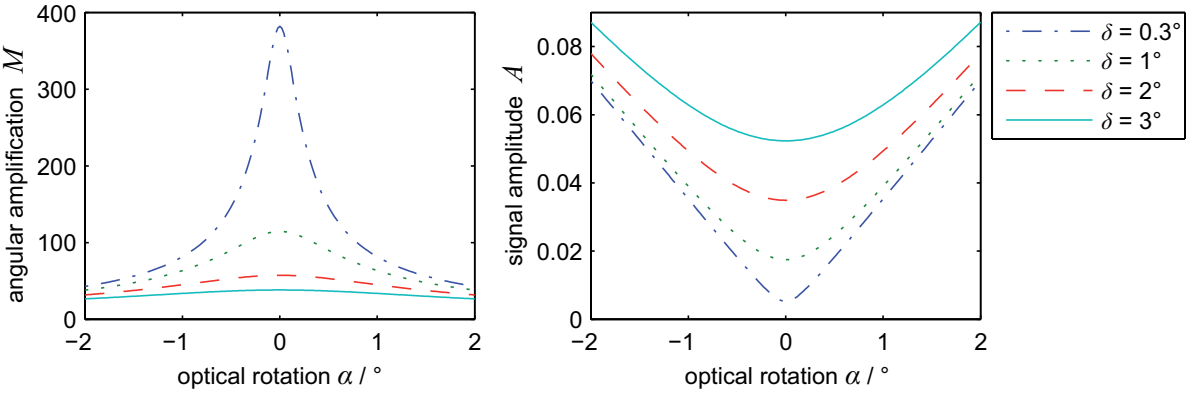

Figure 7.4: Angular amplification and signal amplitude for different waveplate settings. **Left:** The angular amplification $M = \phi/\alpha$ can become very large with $\alpha \approx 0$ and $\delta \approx 0$. **Right:** The signal amplitude decreases when δ approaches $n\pi$ where the angular amplification is largest.

the wave plate, the detected phase ϕ can be orders of magnitude larger than the optical rotation α itself. For small α, ϕ can be expressed as a power series:

$$\phi = \frac{2}{\tan\delta}\,\alpha + \mathcal{O}(\alpha^3). \tag{7.19}$$

Hence, the small-angle amplification factor

$$M = \frac{2}{\tan\delta} \tag{7.20}$$

can theoretically be chosen arbitrarily high by picking $\delta \approx n\pi$ $(n = 0, \pm1, \pm2, ...)$. This effect is the most important principle of the polarimeter setup. In theory, this free choice of angular amplification would allow a measurement of arbitrarily small optical rotations.

There are, however, limitations to choosing the angular amplification. In practice, the setting of the wave plate has an uncertainty and cannot be set arbitrarily close to $\delta = n\pi$. Due to dispersion of the variable wave plate, the bandwidth of the laser diode further introduces a small uncertainty in the actual value of δ. Additionally, the amplitude of the signal decreases with δ approaching $n\pi$. This is illustrated on the right hand side of Fig. 7.4 for the same values of δ as for the amplification on the left hand side. It follows from Eq. 7.16 that for $\alpha \to 0$

$$A = |\sin\delta|. \tag{7.21}$$

In other words, the angular amplification comes at the cost of signal amplitude.[1] For higher angular amplification the photodiode preamplifier and the lock-in amplifier itself must be operated at higher gain which introduces more phase noise, hindering an accurate measurement of ϕ. Therefore, a compromise between the optimal angular amplification (determined by δ) and the signal amplitude needs to be found for every given range of optical rotations that is to be measured.

[1] In fact, this relation can be used to determine the actual retardation δ with a better accuracy than the scale of the Berek compensator would allow for.

7.3.4 Performance of the polarimeter

The resulting experimental angular sensitivity of the polarimeter will be discussed in this section. First an error analysis specifies the theoretical limits of the sensitivity and, second, a measurement determines the experimental sensitivity.

For small α and small δ Eq. 7.18 can be approximated

$$\alpha \approx \frac{1}{2}\ \delta\ \phi \tag{7.22}$$

and the error σ_α in the optical rotation α follows as

$$\begin{aligned}\sigma_\alpha &= \frac{1}{2}\sqrt{\sigma_\phi^2\delta^2 + \sigma_\delta^2\phi^2} \\ &= \frac{1}{2}\sqrt{\sigma_\phi^2\delta^2 + \sigma_\delta^2\frac{4\alpha^2}{\delta^2}}\end{aligned} \tag{7.23}$$

with the uncertainties σ_ϕ and σ_δ in the phase detection and in the Berek retardation setting. In practice δ cannot be chosen arbitrarily small due to the decrease in signal amplitude. The retardation angle has to be chosen as $\delta = n\pi + \Delta\delta$ where $|\Delta\delta| > 2^\circ$ which leads to $A > 3.5\%$ modulation. In the interesting detection regime where $\alpha \ll \delta$, the second term under the square root of Eq. 7.23 can be neglected versus the first term. On the other hand, the first contribution under the square root constitutes the limitation of the angular resolution caused by the lock-in amplifier detection precision. The digital readout precision of the lock-in amplifier is $\sigma_{\phi,\min} = 0.008^\circ$. Hence, if we take $\delta = 2^\circ$ as a realistic example, the limit on the optical rotation precision is given by

$$\sigma_{\alpha,\min} = \frac{1}{2}\ |\sigma_{\phi,\min}\ \delta| = 1.4 \times 10^{-4\circ}. \tag{7.24}$$

This consideration however does not include the fact that σ_ϕ is a function of the amplitude A and thus the retardation δ because the lock-in amplifier will detect more phase noise with decreasing modulation amplitude. The phase noise σ_ϕ in the setup was characterized by a measurement series. The EOM was driven at $\omega = 2\pi \times 30.2$ kHz, the lock-in amplifier time-constant was set to 10 ms, and phase values were read out at a rate of 64 Hz. Then the phase was read out during 1 s (ca. 64 separate values) and the standard deviation was calculated. The procedure was repeated 10 times and the standard deviations were averaged to yield an error as it would occur in a typical fast measurement of an optical rotation after an accumulative chiral photochemistry experiment. δ was set at four different values between 170° and 180° corresponding to values between 0° and 10°. The measured values are shown in table 7.1 along with the resulting angular resolutions $\sigma_\alpha = \sigma_\phi\delta/2$. It is interesting that σ_α remains fairly constant even though the phase noise is considerably larger for smaller retardations. Writing the error in α as

$$\sigma_\alpha = \left|\frac{\sigma_\phi(\delta)}{M(\delta)}\right| \tag{7.25}$$

one can interpret the flatness of σ_α with respect to δ. For $\delta \to 0$ the increasing phase noise σ_ϕ is compensated by a larger angular amplification M. In the range $2^\circ < \delta < 10^\circ$

and under the above mentioned experimental conditions the resolution of the polarimeter is $\alpha_{\mathrm{res}} = \sigma_\alpha = 0.0022°$. It should be noted that the conditions here were chosen such that a measurement can be recorded extremely fast. They are especially well-suited for determining the result of an accumulative experiment with chiral products. The lock-in amplifier time constant $T = 10$ ms is very small and, while it allows a fast measurement of α in $5 \times T = 50$ ms, the angular resolution can be improved significantly by choosing a bigger time constant T to suppress noise more efficiently [205]. The diffusion and reaction dynamics of an accumulative experiment dictate the settings one must choose for an optimal trade-off between measurement speed and precision of the optical rotation angle.

δ / °	σ_ϕ / °	σ_α / °
10	0.03	0.00262
5	0.05	0.00218
3.3	0.075	0.00216
2.4	0.11	0.00230

Table 7.1: Experimental determination of the small angle resolution σ_α. The standard deviation of the lock-in amplifier phase σ_ϕ was measured at four different retardation settings and the resolution in optical rotation results as $\sigma_\alpha = \sigma_\phi \delta/2$.

Comparing our polarimeter setup to commercial polarimeters it is important to note that the single beam setup allows the combination with basically any kind of sample cell and any kind of other spectroscopy in the same setup. Our angular resolution of $\alpha_{\mathrm{min}} = 0.0022°$ rivals the resolution of the best commercial polarimeters, $\alpha_{\mathrm{min}} = 0.002°$, see e.g. Ref. [208]. While these commercial polarimeters have a measurement time of several seconds (e.g. 5 s for Ref. [208]), our polarimeter can determine the optical rotation in a fraction of the time with the same precision or, optionally, with a higher precision at the cost of measurement time.

7.4 Molecular systems and mechanisms for enantioselective quantum control

An experimental demonstration of enantioselective femtosecond quantum control requires not only a suitable detection scheme but also a molecular system that exhibits a photoreaction mechanism that can be controlled by shaped femtosecond pulses. A few systems that potentially fulfill the requirement together with potential experimental realizations will be discussed briefly in the following sections.

7.4.1 Binaphthalene derivatives

1,1'-Binaphthalenes exhibit an intrinsic axial chirality due to steric hindrance from their 2,2' substituents (Fig. 7.5). The potential energy barrier between the two stereoisomers is large so that each configuration is very stable at room temperature. Their specific rotation is large and can be accurately measured in our polarimeter setup. For example, (R)-(+)-1,1'-binaphthyl-2,2'-diamin in dioxane results in a detected phase difference of $\phi = 40°$ [205]. It is known that electronic excitation of binaphthalenes can lead to

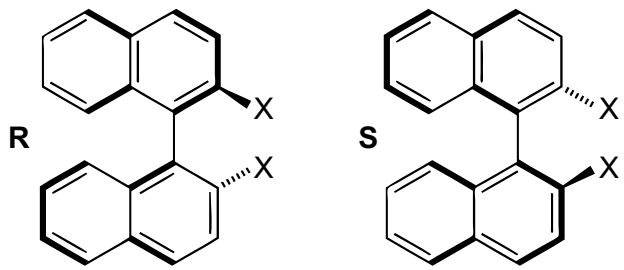

Figure 7.5: R and S forms of 2,2'-substituted 1,1'-binaphtalenes. The amount of steric hindrance depends on the X substituents and results in a nonzero dihedral angle between the two naphthalenes, rendering the molecule axially chiral.

racemization [209]. There has been a recent theoretical study [210] on 1,1'-binaphthalene exploiting multiple pump–dump sequences between the S_0 and S_3 states to convert one enantiomer into the other. Several excitations and periods of propagation on the asymmetric S_0 and S_3 potential energy surfaces lead to an overall isomerization about the inter-ring C–C bond. This process, however, required prealigned binaphthalene molecules and a shaped UV laser with a central wavelength of 154 nm and a large bandwidth.

While the scheme presented by Hoki *et al.* is not feasible with current laser technology, a similar scheme where the pump and dump processes are facilitated via multiphoton processes of shaped near infrared or visible laser pulses might be conceivable. This would also not constitute an actual asymmetric synthesis but it would demonstrate an enantiomer "switching" on a femtosecond to picosecond time scale.

7.4.2 Photochemical helicene formation

Absolute (meaning, starting from achiral reactants) asymmetric chemistry using circularly polarized light has been demonstrated on the photochemical synthesis of helicenes. Hexahelicene was produced from 1-(2-naphthyl)-2-(3-phenanthryl)-ethylene or from 1-(2-benzo[*c*]phenanthryl)-2-phenylethylene [211, 212]. Also higher helicenes like octahelicene ([8]helicene) from 1-(3-phenanthryl)-2-(2-benzo[*c*]phenanthryl)-ethylen [212] and [9-10]helicenes from other bis(arylvinyl) arene precursors have been photochemically produced [213]. The mechanisms of these asymmetric syntheses rely on the natural *cis–trans* isomerism of the ethylene bond of the precursor molecules (see first reaction on the left hand of Fig. 7.6). The *cis* conformer already displays a certain sense of helicity and a strong circular dichroism. Hence, circularly polarized light predominantly excites one enantiomer and the photoinduced ring closure (second step in Fig. 7.6) is selective. An oxidative environment (e.g. I_2 and O_2 in the solution) leads to a complete aromatization and thus to a fixation of the state of helicity (last reaction step in Fig. 7.6).

In the original experiments on these helicene syntheses [211–213] the large circular dichroism of the already transiently helical, yet open ring *cis* forms of the bis(arylvinyl) arenes in the UV was exploited. However, with shaped femtosecond laser pulses one might be able to enhance the enantioselectivity in the following scheme: The *trans–cis* isomerization of the ethylene bond could be influenced such that the rotation is (partially) directional and predominantly *cis* isomers of one helical sense are produced.

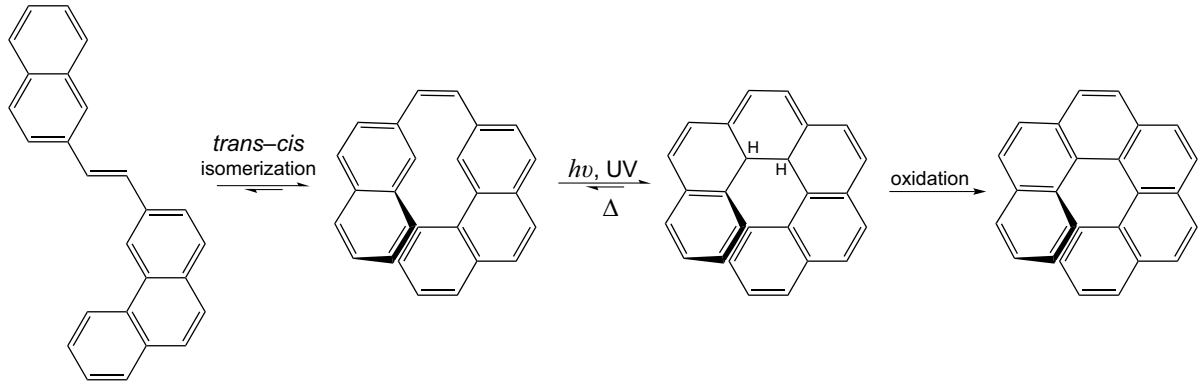

Figure 7.6: Schematics of asymmetric synthesis of hexahelicene using circularly polarized UV light. The helical *cis*-bis(arylvinyl) arene form (second structure) can be selectively excited with circularly polarized UV light to induce a ring closure [211–213]. The presence of iodine and oxygen in the solution facilitates an oxidation which results in the fixation of the helical structure and production of the actual hexahelicene.

Conversely, one of the *cis* enantiomers could be isomerized to the achiral *trans* form. After applying the "control pulses" that accomplish this directional isomerization a "ring-closing" pulse could induce the stabilization of the enantiomers. *cis–trans* isomerizations following femtosecond excitation have been studied extensively [214–216]. Using phase and amplitude shaped 400 nm pulses Vogt *et al.* were even able to control the *cis/trans* ratio of an isomerization of a dye molecule [217]. The mentioned scheme to enantioselectively produce helicenes would additionally require the isomerization to be controlled with a preference in the rotation angle about the ethylene bond. This enantioselective control scheme would have several advantages. Starting with achiral (*trans*) molecules, an actual absolute asymmetric synthesis could be accomplished. Additionally, the specific rotation of helicenes is extremely large ($[\alpha]^{25°C}_{405nm} = -40000°$ for octahelicene [218]) and therefore it should be easy to detect an enantiomeric excess.

7.4.3 Spiropyran/merocyanine chiroptical molecular switches

Photochromic molecular switches have attracted considerable attention in recent years (for a review see, for instance, Refs. [219, 220]). Molecules that change their optical properties upon irradiation with light have a wide and promising field of potential applications such as media for data storage, (q-)bits in quantum computing, and triggers for follow-up reactions, among others. Spiropyrans have interesting photochromic properties. The closed spiropyran form (SP, Fig. 7.7) absorbs in the UV wavelength region only. The open merocyanine form (MC), which absorbs visible light, can be produced photochemically via irradiation of SP with UV light. Hence, the color of the spiropyran compound can be "switched" on. The reverse reaction (SP←MC) can be induced thermally or via irradiation with visible light (thereby "switching" the color "off"). Additionally, the spiro carbon atom is a stereogenic center and the closed SP form exists as two enantiomers R and S. Thus, if it were possible to enantioselectively control the

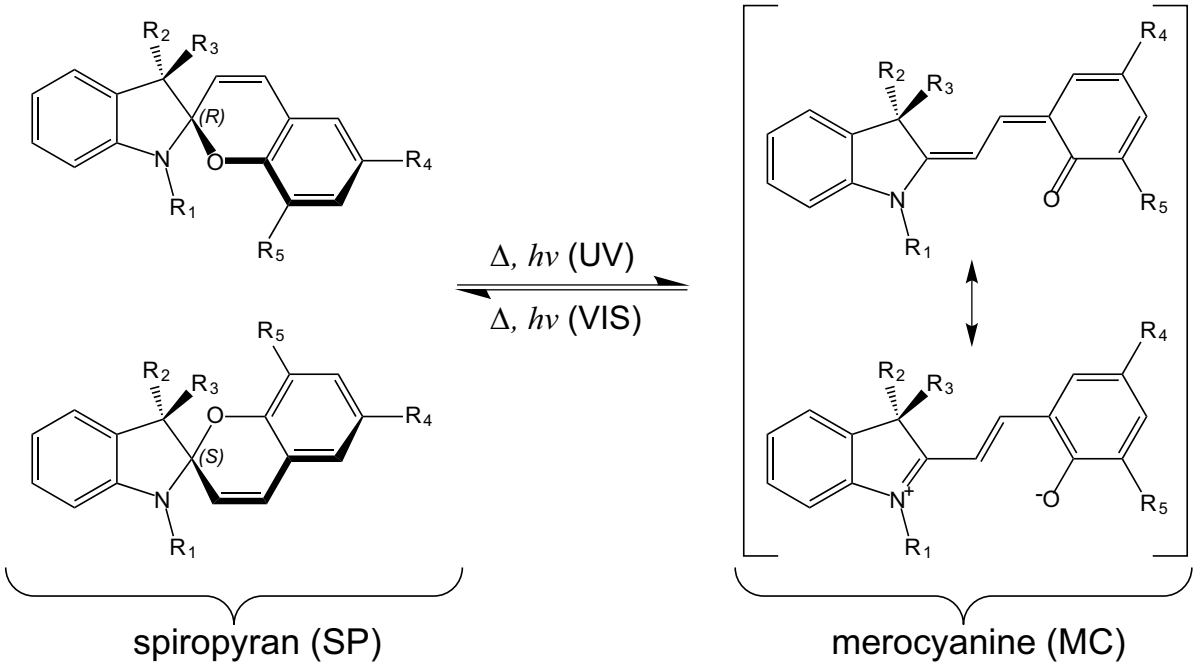

Figure 7.7: Spiropyran/merocyanine as chiroptical molecular switch. The colorless, closed-ring spiro form (SP) absorbs in the UV only. In this form the spiro carbon represents a stereogenic center and the molecule exists as R and S enantiomers. Ring-opening of the usually (depending on the solvent and substituents R_4 and R_5) thermally more stable SP can be induced by irradiance with UV light. The open merocyanine form (MC) has a broad absorption in the VIS and can revert back to SP thermally or photochemically.

MC→SP reaction, the photochromic behavior of spiropyran would not only represent a molecular switch but also a "chiroptical" molecular switch [221] meaning that in addition to the color of the compound, its chirality and hence its optical rotation could be controlled optically.

Using circularly polarized CW light Suzuki *et al.* have shown diastereoselectivity of SP doped into chiral polymer films [222]. Eggers *et al.* have also shown diastereoselectivity on a SP substituted with a chiral side chain [223]. These results however, do not demonstrate absolute asymmetric synthesis because of the initial chirality of the polymer film or of the SP side chain.

However, to accomplish an enantioselective femtosecond control over the SP/MC system a number of prerequisites must be met. For the majority of the SP/MC systems studied in the literature the thermal equilibrium favors the SP form [224]. The actual amount of MC in general depends on solvent, temperature, and substituents. A controlled enantioselective photoreaction must therefore either start from the equilibrium MC or produce it via photochemical ring opening of SP. The former case is somewhat more favorable because it simplifies the experiment and does not require additional UV pulses and delay lines. Additionally, the initial MC product a few pico- to nanoseconds after photoinduced ring opening is vibrationally very hot which might hinder selectivity of a subsequent control pulse to close the spiro ring again.

In the literature, the SP→MC ring-opening reaction has been studied in detail on the femto- to nanosecond timescale [225–228]. The authors of these publications used the spiropyran derivatives with thermal stability on the SP side of the reaction and only studied the ultrafast ring opening which corresponds to the switching "on" of the color (positive photochromism). For the 6-nitro spiropyran derivative ($R_1 = R_2 = R_3 = CH_3$, $R_4 = NO_2$, $R_5 = H$) it was found that excitation of spiropyran to the S_1 state leads to fast intersystem crossing to a triplet state and subsequent ring opening and isomerization [227, 228]. For unsubstituted spiropyran and 6-hydroxy-substituted spiropyran ($R_1 = R_2 = R_3 = CH_3$, $R_4 = H/OH$, $R_5 = H$) on the other hand, it was found that the ring opening occurs via the singlet manifold only and also leads to a distribution of MC isomers within a few picoseconds [225, 226].

With regard to the goal of accomplishing a femtosecond absolute asymmetric synthesis we are more interested in the ring closure reaction leading to the chiral SP form. As mentioned before, this can be studied either on photochemically derived (transient) MC or on substituted SP/MC systems with thermally stable MC. The former experiment on the common 6-nitro spiropyran showed that excitation of the MC form leads to isomerization in the excited state and there was no conclusive evidence for ring closure on the picosecond timescale [229]. In contrast, experiments on 6,8-dinitro spiropyran ($R_1 = R_2 = R_3 = CH_3$, $R_4 = R_5 = NO_2$), for which MC is the thermally more favorable and stable form, revealed that an efficient ring closure mechanism is present [230]. This excited state reaction possibly involves isomerization and leads to ring closure within a few picoseconds with a quantum efficiency of $\Phi \lesssim 0.44$. A further advantage of the 6,8-dinitro derivative is the high thermal stability of each of the forms in solution, MC *and* SP [231, 232]. Hence, this particular compound seems to be a promising candidate for chiral control experiments.

The ring closure reaction (as well as the ring opening reaction) is intrinsically related to the different isomers of the merocyanine form and a fair number of different pathways arise from the combinations of isomers for both the ring opening and the ring closing reactions. Fig. 7.8 shows an overview of the *cis-trans* isomers of the MC form. The dihedral angles α, β, and γ around the conjugated double bonds of the methine bridge connecting the indoline and the pyran moiety are labeled for the top left structure in the figure. Each of the three bonds can have a *cis* (C) or *trans* (T) configuration corresponding to angles of 0° or 180°, respectively, and this results in 8 isomeric structures. The structures in the left column are the most stable isomers in solution; in particular it has been found that the TTC isomer is the predominant structure in solution and only a small fraction of TTT is present [233, 234]. The energies for other isomers like CTC and CTT have also been calculated in theoretical studies [234, 235], however, in equilibrated solutions of MC at room temperature they seem to play a negligible role. The isomers in the right column of Fig. 7.8 are all somewhat unfavorable because of steric hindrance. Even small substituents R_{1-3} like CH_3 will impede the formation of an all planar MC as can be seen from the drawn structures. Nevertheless, isomers similar to TCC and CCC are important transient structures for pathways to ring closure because in those isomers the oxygen comes in close proximity of the spiro carbon atom.

The three angles α, β, and γ can be visualized as three spatial dimensions (Fig. 7.9). The *cis/trans* isomers are located at the nodes of a lattice with a periodicity of 360°

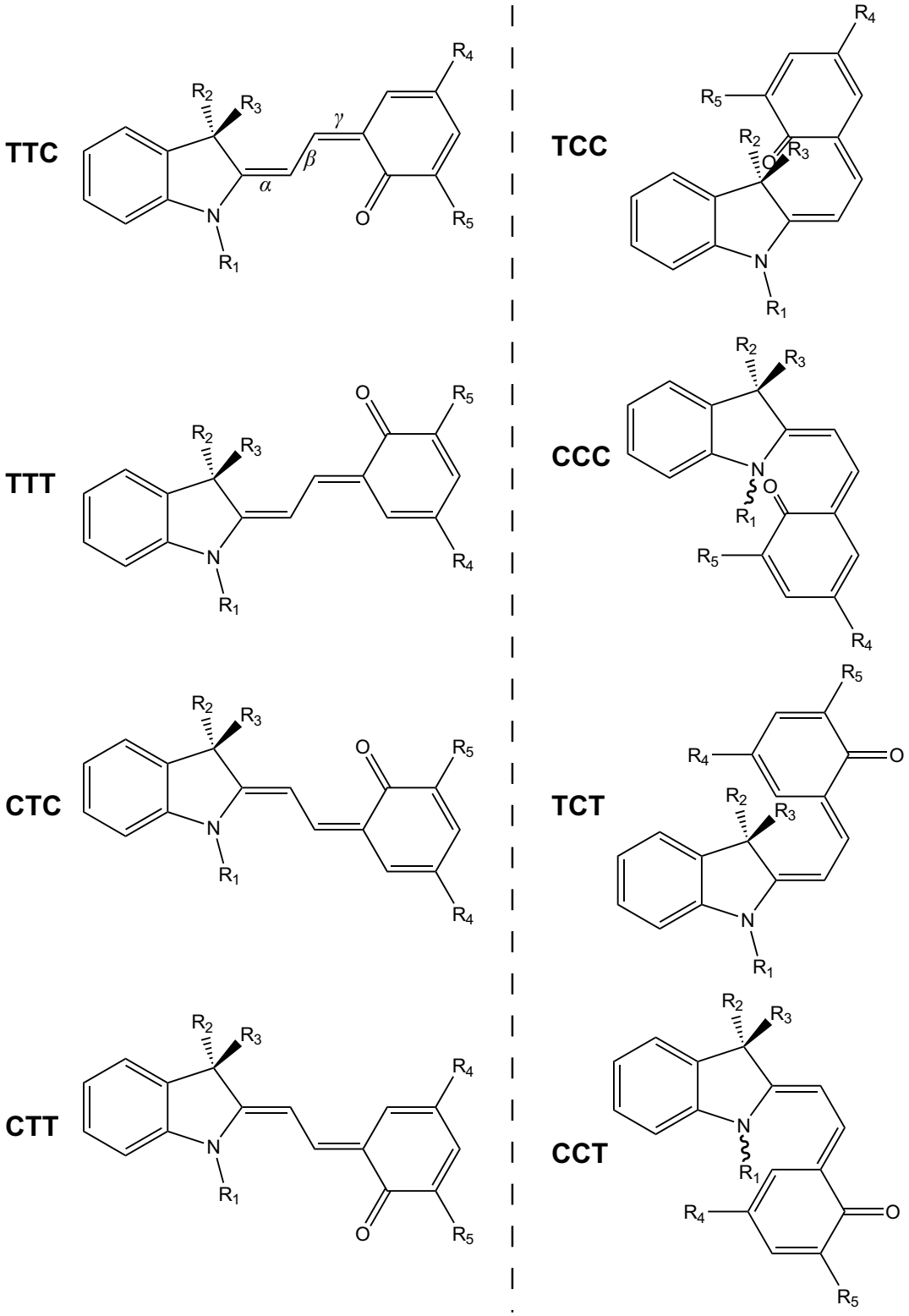

Figure 7.8: *cis/trans* isomers of merocyanine. Left hand side: isomers with no steric hindrance. In thermal equilibrium mostly TTC and a small fraction of TTT is present. Right hand side: isomers with steric hindrance. Especially the TCC and CCC isomers are important for pathways to ring closure to SP.

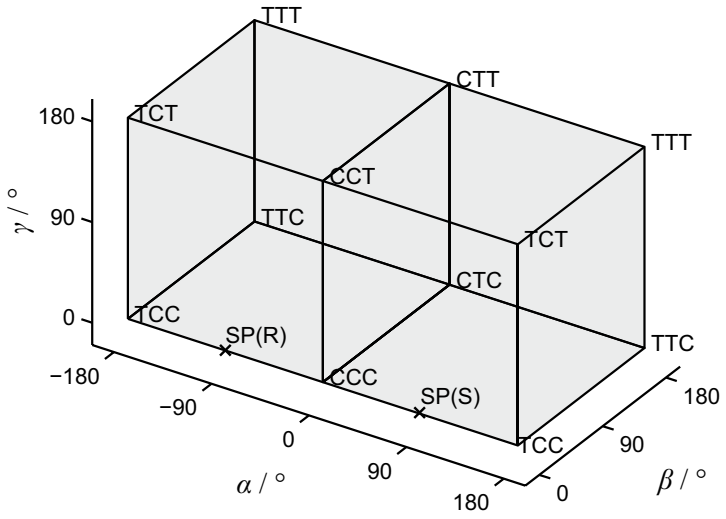

Figure 7.9: Visualization of MC/SP isomers. The *cis* (C) and *trans* (T) configurations are the nodes of a lattice spanning the three dimensional space of the three dihedral angles α, β, and γ around the methine bridge bonds [225].

in each dimension. 12 representative nodes are drawn in Fig. 7.9 for illustration and labeled with their isomeric configurations. The closed SP form can roughly be located between the CCC and TCC isomers of MC because the indoline and the pyran moiety are perpendicular to each other in the SP form, i.e., $|\alpha| \approx 90°$, and the β and γ bonds both must be in their *cis* configurations. The handedness of the SP form is determined by α (compare e.g. structure of CCC in Fig. 7.8). In this lattice picture one can imagine the different possible reactions like ring opening and ring closure as actual paths connecting the initial with the final state. Ring closure, for example, can be pictured as a pathway that connects the most stable MC isomer TTC with one chiral form of SP. Obviously, the most important isomerization for ring closure is the rotation around the central bond. This rotation has been suggested to occur with a small energy barrier in the electronically excited state of MC [230]. While the angle β must change from 180° to close to 0° or 360°, depending on the sense of rotation, the steric hindrance of configurations similar to the TCC isomer imposes a barrier to reformation of a planar MC form. At the same time, when β is not in a planar configuration, the steric effects of the R_2 and R_3 substituents will distort the potential energy surface with respect to α and rotation around this bond will be biased away from the R_2 and R_3 substituents. Therefore it seems that for the simplest pathway from TTC MC to ring closure sketched here the decisive step is the *trans–cis* isomerization of the central methine bond. Depending on the sense of rotation (180°→0° or 180°→360°) the production of one enantiomer will be favored over the other. A quantum control experiment aiming to achieve asymmetric synthesis must then mainly control the sense of rotation around the central bond.

The described scheme is of course very simplified and in reality there are more degrees of freedom that contribute to the ring-closure reaction than just the three angles. To describe the dynamics of a photoinduced ring closure, full quantum chemical simulations that include the electronically excited state are needed. A study on a simple model system found a conical intersection seam leading from the MC S_1 state to the SP S_0 state [236]. However, the system has to be modeled in greater detail because the substituents influence the properties of the SP/MC compounds decisively [237]. Other

studies have included an electronically excited state but where not conducted on the interesting case of dinitro-substituted SP $R_4 = R_5 = NO_2$ [235].

In summary, spiropyran/merocyanine systems are very interesting for absolute asymmetric synthesis. They have several advantages and particularly interesting properties. The two-way photochromism potentially allows photochemical ring opening and ring closing. Absolute asymmetric synthesis on the ultrafast timescale might be accomplished with this system. While the MC form is achiral, photoinduced ring closure can lead to the chiral SP form. The produced enantiomeric excess is stable on a timescale of hours because thermal racemization was found to be slow in nonpolar solvents [238]. Finally, a valuable advantage in terms of the technical realization of a quantum control experiment is that the main absorption bands of MC are in the visible region. The pulse generation and shaping techniques (especially polarization pulse shaping) that are available in the visible are more advanced than UV polarization pulse shaping techniques [239].

7.5 Summary

Asymmetric photochemistry is a field that is interesting both for its applications and for fundamental scientific research. In particular the use of shaped femtosecond pulses might allow to break the limitations that CW light imposes on asymmetric photochemistry. Extensive theoretical studies have shown possibilities to do so, however, an experiment demonstrating their realization has not been reported to date. One of the obstacles on the route to chiral quantum control is the difficulty to reliably determine the success of such an experiment. As a first step toward an enantioselective quantum control experiment we have designed and constructed a polarimeter that can detect the optical rotation of a solution at 405 nm with a resolution of 2.2×10^{-3} ° in only a few tens of milliseconds. This setup will be combined with the accumulation technique to yield very high enantiomeric sensitivity. Further, we have reviewed a number of potential molecular systems for a chiral control experiment. The 6,8-dinitro-substituted spiropyran seems to be the most promising system. Ultrafast photoinduced ring closure of this spiropyran has been reported to occur upon excitation with visible light. Thus, the system could potentially be controlled by polarization-shaped pulses from our NOPA and LC pulse shaper. The goal of such an experiment is not only the control of the ring closure but, more specifically, the enantioselective production of the closed spiropyran form. The pathway to enantioselectivity would mainly involve the selective induction of an excited state *trans–cis* isomerization of the open-ring merocyanine form with a certain sense of rotation. As next steps toward the realization of the outlined goal, we are conducting transient absorption spectroscopy on this merocyanine/spiropyran system to determine the dynamics of the ring closure more precisely and to find good spectroscopic signatures of the ring closure. Following the acquisition of this information, attempts can be made to control the isomerization of MC in the excited state in terms of yield and rotational sense, leading to the final goal of femtosecond photoinduced absolute asymmetric synthesis.

Controlling absolute asymmetric synthesis of spiropyran with shaped femtosecond pulses would not only be an interesting result on this particular system. It would also

provide experimental proof that femtosecond laser control of chirality is possible, which is currently a controversially discussed topic. This possibility to control chirality with laser pulses would extend quantum control in a fundamental way. It would open up routes to laser-induced synthesis that starts from achiral precursors and enantioselectively yields chiral products.

8 Summary

Changes in a molecular system can be caused by interaction with an external field or by intrinsic couplings. Ultrafast spectroscopy techniques permit the observation of such changes on the femtosecond timescale. Many well-established techniques have been applied to different types of reactions and a large number of molecular systems have been studied. Methods, such as transient absorption spectroscopy, have managed to reveal even the ultrafast dynamics that represent the initial steps of chemical reactions. To obtain insight into the fundamental inter- and intramolecular couplings that effect the dynamics of a photoreaction, optical coherent two-dimensional spectroscopy was developed in recent years.

The focus of this work was on the advancement of ultrafast spectroscopic techniques. A new, inherently phase-stable setup for the measurement of two-dimensional spectra was presented. The relaxation of the experimental requirements compared to previous setups simplifies the application of two-dimensional spectroscopy greatly. Another spectroscopic method that focuses on photoinduced reactions with stable products has also been developed within this work. This novel accumulative detection method is highly sensitive to small photoproduct yields and can be combined with many types of conventional time-resolved techniques.

As a prerequisite for the experiments presented in this thesis, ultrabroadband femtosecond laser pulses in the visible spectral region were produced. The pulses were generated by a noncollinear optical parametric amplifier and a liquid crystal pulse shaper was used for compression. This combination results in broadband visible pulses with spectral components ranging from 500 nm to 750 nm and less than 17 fs duration. The pulse characterization is obtained at the sample position in the experimental setup. Varying amounts of dispersion can be compensated with the pulse shaper and control over the spectral phase and amplitude, or, over the polarization state can be achieved. This provides tailored pulses as versatile tools for spectroscopy and quantum control experiments. The primary application of these pulses in this thesis was two-dimensional spectroscopy.

Optical two-dimensional spectroscopy, as the analogue of two-dimensional nuclear magnetic resonance, is a femtosecond spectroscopy method that permits the direct visualization of couplings and energy transfer between different chromophores. To date, the requirement of phase stability of four femtosecond pulses used for this method imposed considerable difficulties on experimental realizations of optical two-dimensional spectroscopy. In particular, laser pulses in the visible wavelength region for measuring electronic couplings demanded severe precautions to meet the phase stability requirements. One goal of this thesis was to improve the applicability of two-dimensional spectroscopy in all spectral regimes. To this end, the pairwise manipulation of the excitation pulses, first used in combination with diffractive optic beam splitters by Miller [117], was

described theoretically and shown to be generally applicable without further restrictions such as diffractive optics. The results of the theoretical considerations can be expressed as follows. Pairwise manipulation only requires the pulse arrival times to be kept constant to a fraction of the *pulse duration*. Conventional setups, in contrast, require these times to be constant to a fraction of the carrier frequency *oscillation period*. Thus the pairwise beam manipulation provides a significant relaxation of the phase stability requirements. A simple experimental setup based on these considerations was presented. This setup uses only conventional metallic beam splitters and delay stages. No active or diffractive elements are required. In a series of experiments it was demonstrated that the setup is phase-stable on all timescales that are relevant for a two-dimensional spectroscopy experiment. A two-dimensional spectrum of the dye Nile Blue was recorded with broadband visible excitation to demonstrate the functionality of the novel setup. There are many promising applications of the new setup in the near future. For example, intramolecular vibronic coupling can be visualized in electronic two-dimensional spectra measured at low temperatures. Another promising application is the design of new materials for organic solar cells. The timescale and efficiency of energy transfer of these new compounds can be measured and evaluated with the help of electronic two-dimensional spectroscopy.

Besides advancing two-dimensional spectroscopy as a femtosecond diagnostic tool, this thesis also focused on the spectroscopic measurement of stable products resulting from photochemical reactions. A new technique for detecting stable photoproducts with extremely high sensitivity was developed. The accumulation of the products resulting from the interaction of the sample with several femtosecond laser pulses allows a precise measurement, even if a single pulse exhibits a low efficiency for initiating the photochemical reaction. In the solution phase this product accumulation occurs on a similar timescale as diffusion of products and reactants. Thus, for a quantitative measurement one must correct for the diffusion. A phenomenological model for the diffusion and accumulation was found and the outcome of an experiment using the accumulative detection method can be expressed as the efficiency of a single pulse. A number of demonstration experiments on the bleaching of a dye solution showed the applicability of the method to femtosecond spectroscopy and quantum control experiments.

A showcase experiment that used the newly developed accumulative detection method was conducted on the ultrafast permanent photoconversion of the green fluorescent protein. In the regular photocycle of this protein, the protonated ground state species absorbs one photon at 400 nm. Subsequent excited state proton transfer leads to a green fluorescing intermediate state and the initial form of the chromophore is restored by reprotonation in the electronic ground state. Alternatively, with a low quantum efficiency, decarboxylation of the Glu222 residue in the protein results in photoconversion, which is the permanent alteration of the optical properties of the protein. The accumulative detection method is ideally suited for studying the photoconversion reaction and changes of absorbance as low as $\Delta\mathrm{OD} = 10^{-7}$ per laser pulse could be detected in the experiments presented here. Previously, the photoconversion process was thought to occur from the singly excited state. In this thesis conclusive evidence was presented that under femtosecond excitation conditions efficient photoconversion occurs from a higher excited state. Time-resolved two-color experiments revealed that this higher state can

only be reached via further excitation of the singly excited state from the vicinity of the initial Franck-Condon excitation. Additionally, information about the effective energy gap between the potential energy surfaces of the singly and the higher excited state was obtained in an experiment that employed shaped femtosecond laser pulses for the second excitation step. The findings presented in this thesis are particularly relevant to applications using the green fluorescent protein in two-photon absorption microscopy. Care must be exercised to suppress unwanted photoconversion in this type of microscopy that is omnipresent in the life sciences.

The accumulative detection method that was developed in this thesis was extended to chiral photochemistry. Even though in recent years quantum control methods have been applied very successfully to various types of photoinduced reactions, enantiomeric selectivity or even absolute asymmetric synthesis have not yet been reported. As a first step toward this goal a polarimeter setup was built to detect small enantiomeric excesses fast and reliably. This setup can be combined with the accumulation product detection method to determine the outcome of a quantum control experiment with high enantiomeric sensitivity. The most promising molecular system for such an attempt at femtosecond controlled chiral photochemistry is the spiropyran/merocyanine compound where a ring closure from the merocyanine to the spiropyran form can result in two enantiomers. Control over which form is produced could potentially be achieved by controlling the excited state isomerization of merocyanine. Experiments using polarization-shaped laser pulses on this system are planned.

This thesis presented developments in two areas of ultrafast spectroscopy. With the newly developed accumulative detection method the femtochemistry of reactions with incredibly low quantum efficiencies can be investigated. This will facilitate studies of photochemical reactions that were previously impossible to detect. The presented setup for two-dimensional spectroscopy relaxes the phase stability requirements by providing an inherent stabilization mechanism. Additionally, the novel setup is simple to implement. Thus the presented technique can stimulate a more wide-spread use of two-dimensional spectroscopy for unraveling molecular couplings and energy transfer.

Zusammenfassung

Veränderungen in einem molekularen System können durch Wechselwirkungen mit einem externen Feld oder durch intrinsische Kopplungen verursacht werden. Techniken der Ultrakurzzeitspektroskopie ermöglichen die Beobachtung solcher Veränderungen auf der Femtosekundenzeitskala. Viele etablierte Techniken wurden bereits auf verschiedene Typen von Reaktionen angewandt und viele molekulare Systeme wurden untersucht. Methoden wie die transiente Absorptionsspektroskopie haben es ermöglicht, selbst die ultraschnellen Dynamiken, welche die ersten Schritte von chemischen Reaktionen darstellen, zu enthüllen. Um einen Einblick in die fundamentalen inter- und intramolekularen Kopplungen, die die Dynamik von Photoreaktionen beeinflussen, zu erhalten, wurde in den vergangenen Jahren die optische kohärente zweidimensionale Spektroskopie entwickelt.

Der Schwerpunkt dieser Arbeit lag in der Weiterentwicklung von Spektroskopietechniken. Ein neuer, inhärent phasenstabiler Aufbau zur Messung von zweidimensionalen Spektren wurde vorgestellt. Die Lockerung der experimentellen Anforderungen im Vergleich zu vorherigen Aufbauten vereinfacht die Anwendung der zweidimensionalen Spektroskopie wesentlich. Eine andere spektroskopische Technik, die auf photoinduzierte Reaktionen mit stabilen Produkten ausgerichtet ist, wurde ebenfalls im Rahmen dieser Arbeit entwickelt. Diese neuartige akkumulative Detektionsmethode ist sehr empfindlich auf geringe Photoproduktausbeuten und kann mit vielen Arten von konventionellen zeitaufgelösten Techniken kombiniert werden.

Als Voraussetzung für die in dieser Arbeit präsentierten Experimente wurden ultrabreitbandige Femtosekundenlaserpulse im sichtbaren Spektralbereich erzeugt. Die Pulse wurden von einem nichtkollinearen optisch-parametrischen Verstärker produziert und ein flüssigkristallbasierter Pulsformer wurde zur Kompression verwendet. Diese Kombination stellt breitbandige sichtbare Laserpulse mit Spektralkomponenten von 500 bis 750 nm und weniger als 17 fs Dauer zur Verfügung. Die Pulscharakterisierung wird an der Stelle der Probe im experimentellen Aufbau vorgenommen. Verschieden starke Dispersion auf dem Weg dorthin kann mit dem Pulsformer kompensiert werden und die spektrale Phase und Amplitude oder die Polarisation kann kontrolliert werden. Somit stehen maßgeschneiderte Pulse als vielseitiges Werkzeug in der Spektroskopie und Quantenkontrolle zur Verfügung. In dieser Arbeit war die Hauptanwendung dieser Pulse die zweidimensionale Spektroskopie.

Die optische zweidimensionale Spektroskopie, das Analogon der zweidimensionalen Kernspinresonanzspektroskopie, ist eine Methode in der Femtosekundenspektroskopie, die eine direkte Visualisierung von Kopplungen und Energietransfer zwischen verschiedenen Chromophoren ermöglicht. Bisher hat das Erfordernis der Phasenstabilität zwischen den für diese Methode verwendeten vier Femtosekundenpulsen die experimentellen Realisierungen von optischer zweidimensionaler Spektroskopie wesentlich erschwert.

Insbesondere bei der Verwendung von sichtbaren Laserpulsen zur Messung von elektronischen Kopplungen waren ausgefeilte Maßnahmen gefragt, um dem Anspruch der Phasenstbilität gerecht zu werden. Ein Ziel dieser Arbeit war es, die Anwendung der zweidimensionalen Spektroskopie in allen Spektralbereichen zu vereinfachen. Zu diesem Zwecke wurde hier die paarweise Manipulation von Anregungspulsen, welche ursprünglich von Miller [117] in Verbindung mit diffraktiven Strahlteilern verwendet wurde, theoretisch beschrieben. Es wurde gezeigt, dass die paarweise Manipulation von Pulsen allgemein anwendbar ist, ohne weitere Einschränkungen wie die Verwendung von diffraktiven Optiken. Die Ergebnisse der theoretischen Beschreibung können wie folgt ausgedrückt werden. Durch die paarweise Manipulation müssen die Ankunftszeiten der Pulse nur bis auf einen Bruchteil der *Pulsdauer* konstant gehalten werden. Im Gegensatz dazu müssen bei konventionellen Aufbauten diese Zeiten bis auf einen Bruchteil der *Oszillationsperiode* der Trägerwelle konstant gehalten werden. Damit bedeuted die paarweise Manipulation von Anregungspulsen eine signifikante Lockerung der Phasenstabilitätsanforderungen. Ein einfacher experimenteller Aufbau, der auf diesen Überlegungen beruht, wurde vorgestellt. Dieser Aufbau nutzt nur konventionelle metallische Strahlteiler und Verzögerungsstrecken. Aktive oder diffraktive Elemente sind nicht nötig. In einer Reihe von Experimenten wurde gezeigt, dass der Aufbau auf allen Zeitskalen, die für ein zweidimensionales Spektroskopieexperiment relevant sind, phasenstabil ist. Um die Funktionalität des neuen Aufbaus zu demonstrieren, wurde ein zweidimensionales Spektrum des Farbstoffes Nil Blau mit breitbandiger Anregung im sichtbaren Spektralbereich aufgenommen. Es gibt viele vielsprechende Anwendungen des neuen Aufbaus in der nahen Zukunft. So können zum Beispiel intramolekulare vibronische Kopplungen mit elektronischen zweidimensionalen Spektren bei niedrigen Temperaturen visualisiert werden. Eine weitere aussichtsreiche Anwendung ist das Design von neuen Materialien für organische Solarzellen. Die Zeitskala und Effizienz von Energietransfer in diesen neuen Stoffen kann mit Hilfe der elektronischen zweidimensionalen Spektroskopie gemessen und beurteilt werden.

Neben der Weiterentwicklung der zweidimensionalen Spektroskopie bestand ein weiterer Schwerpunkt dieser Arbeit in der spektroskopischen Messung von stabilen Produkten, die aus photochemischen Reaktionen stammen. Eine neuartige Technik zur hochsensitiven Bestimmung von stabilen Photoprodukten wurde entwickelt. Die Anhäufung (Akkumulation) von Photoprodukten durch die Wechselwirkung der Probe mit mehreren Femtosekundenpulsen ermöglicht eine präzise Messung auch dann, wenn ein einzelner Laserpuls nur eine geringe Effizienz beim Auslösen der chemischen Reaktion aufweist. In Lösung findet diese Produktanhäufung auf ähnlicher Zeitskala wie die Diffusion der Edukte und Produkte statt. Daher muss die Diffusion für eine quantitative Analyse mit einbezogen werden. Ein phänomenologisches Modell für Diffusion und Anhäufung wurde gefunden und das Messergebnis eines Experiments mit der akkumulativen Messmethode kann als die Effizienz eines einzelnen Pulses angegeben werden. Eine Reihe von Demonstrationsexperimenten zum Photobleichen einer Farbstofflösung zeigte die Anwendbarkeit der Methode in Bezug auf Femtosekundenspektroskopie und Quantenkontrolle.

Ein Experiment zur ultraschnellen permanenten Photokonversion des grün fluoreszierenden Proteins (GFP) stellt ein Musterbeispiel dar, bei dem die neuentwickelte akkumulative Messmethode angewandt wurde. Im regulären Photozyklus dieses Proteins

absorbiert die protonierte Grundzustandsspezies ein Photon bei 400 nm. Unmittelbar darauf folgend führt ein Protonentransfer im angeregten Zustand zu einem grün fluoreszierenden Zwischenzustand und die ursprüngliche Form des Chromophores wird durch Reprotonierung im Grundzustand wieder hergestellt. Alternativ dazu, jedoch mit einer geringen Quanteneffizienz, führt die Decarboxylierung des Glu222-Rests im Protein zur Photokonversion mit einer permanenten Änderung der optischen Eigenschaften des Proteins. Die akkumulative Detektionsmethode ist ideal dazu geeignet, die Photokonversionsreaktion zu beobachten. Absorptionsänderungen von nur $\Delta\mathrm{OD} = 10^{-7}$ konnten bei den hier beschriebenen Experimenten gemessen werden. Bisher wurde geglaubt, dass die Photokonversion vom einfach angeregten Zustand ausgeht. In dieser Arbeit wurden dagegen schlüssige Beweise dafür präsentiert, dass bei Anregung mit Femtosekundenpulsen eine effiziente Photokonversion aus einem höher angeregten Zustand stattfindet. Zeitaufgelöste Experimente mit Pulsen zwei verschiedener Farben zeigten, dass dieser höher angeregte Zustand vom einfach angeregten Zustand aus nur erreicht werden kann durch weitere Anregung in der Nähe der ursprünglichen Franck-Condon-Anregung. Weiterhin wurden in einem Experiment, bei dem geformte Laserpulse für den zweiten Anregungsschritt eingesetzt wurden, Informationen über den effektiven Energieabstand der Potentialflächen des einfach und des höher angeregten Zustandes gewonnen. Die Befunde, die in dieser Arbeit präsentiert wurden, sind besonders relevant für Anwendungen des grün fluoreszierenden Proteins in der Zweiphotonenabsorptionsmikroskopie. Bei dieser in den Biowissenschaften omnipräsenten Mikroskopiemethode muss darauf geachtet werden, dass unerwünschte Photokonversion nicht zu stark hervortritt.

Die in dieser Arbeit entwickelte akkumulative Messmethode wurde für die Anwendung auf chirale Photochemie erweitert. Obwohl die Methoden der Quantenkontrolle in den vergangenen Jahren sehr erfolgreich auf verschiedene Arten von Photoreaktionen angewandt wurden, ist in der Literatur keine Enantiomerenselektivität oder gar absolute asymmetrische Synthese beschrieben worden. Als erster Schritt auf dieses Ziel zu wurde ein Polarimeter gebaut, welches kleine Enantiomerenüberschüsse schnell und zuverlässig messen kann. Dieser Aufbau kann mit der Produktanhäufung kombiniert werden, um das Ergebnis eines Quantenkontrollexperiments mit hoher Sensitivität zu bestimmen. Das vielversprechendse molekulare System für solch einen Versuch der ultraschnellen kontrollierten chiralen Photochemie ist das Spiropyran/Merocyanin-System, in dem ein Ringschluss des Merocyanins zur Spiropyranform zwei Enantiomeren bilden kann. Kontrolle darüber, welche der beiden Formen produziert wird, könnte eventuell durch eine Kontrolle der Isomerisierung des Merocyanins im angeregten Zustand erreicht werden. Experimente an diesem System mit polarisationsgeformten Laserpulsen sind geplant.

In dieser Arbeit wurden Entwicklungen der Ultrakurzzeitspektroskopie in zwei Bereichen vorgestellt. Mit der neuen akkumulativen Detektionsmethode kann die Femtochemie von Reaktionen mit äußerst geringen Quanteneffizienzen untersucht werden. Dies sollte Untersuchungen von photochemischen Reaktionen, die bisher nicht messbar waren, ermöglichen. Der vorgestellte Aufbau für zweidimensionale Spektroskopie erleichtert die Anforderungen an die Phasenstabilität durch seinen inhärenten Stabilisierungsmechanismus. Zusätzlich ist dieser Aufbau einfach zu realisieren. Daher kann die präsentierte Technik eine weitere Verbreitung der zweidimensionalen Spektroskopie stimulieren, womit Energietransfer und Kopplungen in Molekülen weiter entschlüsselt werden können.

Bibliography

[1] J.-C. Diels and W. Rudolph.
Ultrashort Laser Pulse Phenomena.
Optics and Photonics, second edition. Academic Press (October 2006).

[2] G. Sansone, E. Benedetti, F. Calegari, C. Vozzi, L. Avaldi, R. Flammini, L. Poletto, P. Villoresi, C. Altucci, R. Velotta, S. Stagira, S. D. Silvestri, and M. Nisoli.
Isolated Single-Cycle Attosecond Pulses.
Science **314**, 443–446 (October 2006).

[3] A. M. Weiner.
Femtosecond pulse shaping using spatial light modulators.
Review of Scientific Instruments **71**, 1929–1960 (May 2000).

[4] J. R. Lakowicz.
Principles of Fluorescence Spectroscopy.
Third edition. Springer, New York (September 2006).

[5] P. Maine, D. Strickland, P. Bado, M. Pessot, and G. Mourou.
Generation of ultrahigh peak power pulses by chirped pulse amplification.
IEEE Journal of Quantum Electronics **24**, 398–403 (February 1988).

[6] National Instruments.
LabVIEW 8.5.1 Professional Development System.

[7] T. Brixner, N. H. Damrauer, P. Niklaus, and G. Gerber.
Photoselective adaptive femtosecond quantum control in the liquid phase.
Nature **414**, 57–60 (November 2001).

[8] D. Wolpert.
Quantum Control of Photoinduced Chemical Reactions.
Doctoral thesis, Universität Würzburg (2008).

[9] F. Langhojer, D. Cardoza, M. Baertschy, and T. C. Weinacht.
Gaining mechanistic insight from closed loop learning control: The importance of basis in searching the phase space.
The Journal of Chemical Physics **122**, 014102–10 (2005).

[10] T. C. Weinacht, R. Bartels, S. Backus, P. H. Bucksbaum, B. Pearson, J. M. Geremia, H. Rabitz, H. C. Kapteyn, and M. M. Murnane.
Coherent learning control of vibrational motion in room temperature molecular gases.
Chemical Physics Letters **344**, 333–338 (August 2001).

[11] J. M. Geremia, W. Zhu, and H. Rabitz.
Incorporating physical implementation concerns into closed loop quantum control experiments.
Journal of Chemical Physics **113**, 10841–10848 (December 2000).

[12] D. Meshulach, D. Yelin, and Y. Silberberg.
Adaptive ultrashort pulse compression and shaping.
Optics Communications **138**, 345–348 (June 1997).

[13] D. Yelin, D. Meshulach, and Y. Silberberg.
Adaptive femtosecond pulse compression.
Optics Letters **22**, 1793–1795 (December 1997).

[14] T. Baumert, T. Brixner, V. Seyfried, M. Strehle, and G. Gerber.
Femtosecond pulse shaping by an evolutionary algorithm with feedback.
Applied Physics B: Lasers and Optics **65**, 779–782 (December 1997).

[15] T. Brixner, M. Strehle, and G. Gerber.
Feedback-controlled optimization of amplified femtosecond laser pulses.
Applied Physics B: Lasers and Optics **68**, 281–284 (February 1999).

[16] T. Brixner and G. Gerber.
Quantum control of gas-phase and liquid-phase femtochemistry.
ChemPhysChem **4**, 418–438 (April 2003).

[17] M. Dantus and V. V. Lozovoy.
Experimental Coherent Laser Control of Physicochemical Processes.
Chemical Reviews **104**, 1813–1860 (April 2004).

[18] A. E. Eiben and J. E. Smith.
Introduction to Evolutionary Computing.
Springer, Berlin (2003).

[19] D. Wolpert, M. Schade, F. Langhojer, G. Gerber, and T. Brixner.
Quantum control of the photoinduced Wolff rearrangement of diazonaphthoquinone in the condensed phase.
Journal of Physics B: Atomic, Molecular and Optical Physics **41**, 074025 (2008).

[20] P. Tuchscherer, C. Rewitz, D. V. Voronine, F. J. G. de Abajo, W. Pfeiffer, and T. Brixner.
Analytic coherent control of plasmon propagation in nanostructures (2009).

[21] M. Aeschlimann, M. Bauer, D. Bayer, T. Brixner, S. Cunovic, F. Dimler, A. Fischer, F. J. G. de Abajo, V. Myroshnychenko, W. Pfeiffer, M. Rohmer, C. Schneider, F. Steeb, C. Strüber, and D. V. Voronine.
Simultaneous spatial and temporal control of optical nearfields at metal nanostructures (2009).

[22] D. Wolpert, M. Schade, and T. Brixner.
Femtosecond midinfrared study of the photoinduced Wolff rearrangement of diazonaphthoquinone.
Journal of Chemical Physics **129**, 094504–10 (2008).

[23] S. Karg.
Transiente Absorptionssepktroskopie im sichtbaren Spektralbereich.
Diplomarbeit, Universität Würzburg (2009).

[24] R. W. Boyd.
Nonlinear Optics.
Third edition. Academic Press (April 2008).

[25] J. D. Jackson.
Classical Electrodynamics.
Third edition. Wiley (August 1998).

[26] V. G. Dmitriev, G. G. Gurzadyan, and D. N. Nikogosyan.
Handbook of Nonlinear Optical Crystals.
First edition. Springer-Verlag Berlin and Heidelberg GmbH & Co. K (1991).

[27] A. V. Smith.
SNLO.

[28] R. R. Alfano and S. L. Shapiro.
Emission in the Region 4000 to 7000 Å Via Four-Photon Coupling in Glass.
Physical Review Letters **24**, 584 (March 1970).

[29] I. Buchvarov, A. Trifonov, and T. Fiebig.
Toward an understanding of white-light generation in cubic media - polarization properties across the entire spectral range.
Optics Letters **32**, 1539–1541 (June 2007).

[30] S. A. Kovalenko, A. L. Dobryakov, J. Ruthmann, and N. P. Ernsting.
Femtosecond spectroscopy of condensed phases with chirped supercontinuum probing.
Physical Review A **59**, 2369 (March 1999).

[31] B. von Vacano, W. Wohlleben, and M. Motzkus.
Actively shaped supercontinuum from a photonic crystal fiber for nonlinear coherent microspectroscopy.
Optics Letters **31**, 413–415 (February 2006).

[32] M. K. Reed, M. K. Steiner-Shepard, M. S. Armas, and D. K. Negus.
Microjoule-energy ultrafast optical parametric amplifiers.
Journal of the Optical Society of America B **12**, 2229–2236 (November 1995).

[33] G. Cerullo and S. D. Silvestri.
Ultrafast optical parametric amplifiers.
Review of Scientific Instruments **74**, 1–18 (2003).

[34] J. A. Giordmaine and R. C. Miller.
Tunable Coherent Parametric Oscillation in $LiNbO_3$ at Optical Frequencies.
Physical Review Letters **14**, 973–976 (1965).

[35] T. J. Driscoll, G. M. Gale, and F. Hache.
Ti:sapphire second-harmonic-pumped visible range femtosecond optical parametric oscillator.
Optics Communications **110**, 638–644 (September 1994).

[36] G. M. Gale, M. Cavallari, T. J. Driscoll, and F. Hache.
Sub-20-fs tunable pulses in the visible from an 82-MHz optical parametric oscillator.
Optics Letters **20**, 1562–1564 (July 1995).

[37] E. Riedle, M. Beutter, S. Lochbrunner, J. Piel, S. Schenkl, S. Spörlein, and W. Zinth.
Generation of 10 to 50 fs pulses tunable through all of the visible and the NIR.
Applied Physics B: Lasers and Optics **71**, 457–465 (2000).

[38] T. Wilhelm, J. Piel, and E. Riedle.
Sub-20-fs pulses tunable across the visible from a blue-pumped single-pass noncollinear parametric converter.
Optics Letters **22**, 1494–1496 (October 1997).

[39] G. Cerullo, M. Nisoli, and S. D. Silvestri.
Generation of 11 fs pulses tunable across the visible by optical parametric amplification.
Applied Physics Letters **71**, 3616–3618 (December 1997).

[40] O. E. Martinez.
Pulse distortions in tilted pulse schemes for ultrashort pulses.
Optics Communications **59**, 229–232 (September 1986).

[41] J. Hebling.
Derivation of the pulse front tilt caused by angular dispersion.
Optical and Quantum Electronics **28**, 1759–1763 (December 1996).

[42] S. Akturk, X. Gu, E. Zeek, and R. Trebino.
Pulse-front tilt caused by spatial and temporal chirp.
Optics Express **12**, 4399–4410 (2004).

[43] A. Shirakawa, I. Sakane, and T. Kobayashi.
Pulse-front-matched optical parametric amplification for sub-10-fs pulse generation tunable in the visible and near infrared.
Optics Letters **23**, 1292–1294 (1998).

[44] A. Shirakawa, I. Sakane, M. Takasaka, and T. Kobayashi.
Sub-5-fs visible pulse generation by pulse-front-matched noncollinear optical parametric amplification.
Applied Physics Letters **74**, 2268–2270 (April 1999).

[45] A. Baltuska, T. Fuji, and T. Kobayashi.
Visible pulse compression to 4 fs by optical parametric amplification and programmable dispersion control.
Optics Letters **27**, 306–308 (March 2002).

[46] A. Baltuska and T. Kobayashi.
Adaptive shaping of two-cycle visible pulses using a flexible mirror.
Applied Physics B: Lasers and Optics **75**, 427–443 (October 2002).

[47] M. R. Armstrong, P. Plachta, E. A. Ponomarev, and R. J. D. Miller.
Versatile 7-fs optical parametric pulse generation and compression by use of adaptive optics.
Optics Letters **26**, 1152–1154 (2001).

[48] G. Cerullo, M. Nisoli, S. Stagira, and S. D. Silvestri.
Sub-8-fs pulses from an ultrabroadband optical parametric amplifier in the visible.
Optics Letters **23**, 1283–1285 (1998).

[49] C. Manzoni, D. Polli, and G. Cerullo.
Two-color pump-probe system broadly tunable over the visible and the near infrared with sub-30 fs temporal resolution.
Review of Scientific Instruments **77**, 023103–9 (February 2006).

[50] R. Huber, H. Satzger, W. Zinth, and J. Wachtveitl.
Noncollinear optical parametric amplifiers with output parameters improved by the application of a white light continuum generated in CaF_2.
Optics Communications **194**, 443–448 (July 2001).

[51] R. L. Fork, C. V. Shank, C. Hirlimann, R. Yen, and W. J. Tomlinson.
Femtosecond white-light continuum pulses.
Optics Letters **8**, 1–3 (1983).

[52] W. Zinth and H.-J. Körner.
Physik, Optik, Quantenphänomene und Aufbau der Atome, volume 3.
Third edition. Oldenbourg (1998).

[53] J. yuan Zhang, J. Y. Huang, H. Wang, K. S. Wong, and G. K. Wong.
Second-harmonic generation from regeneratively amplified femtosecond laser pulses in BBO and LBO crystals.
Journal of the Optical Society of America B **15**, 200–209 (1998).

[54] M. K. Reed, M. S. Armas, M. K. Steiner-Shepard, and D. K. Negus.
30-fs pulses tunable across the visible with a 100-kHz Ti:sapphire regenerative amplifier.
Optics Letters **20**, 605–607 (March 1995).

[55] P. Baum, S. Lochbrunner, L. Gallmann, G. Steinmeyer, U. Keller, and E. Riedle.
Real-time characterization and optimal phase control of tunable visible pulses with a flexible compressor.
Applied Physics B: Lasers and Optics **74**, s219–s224 (June 2002).

[56] P. Baum, S. Lochbrunner, and E. Riedle.
Zero-additional-phase SPIDER: full characterization of visible and sub-20-fs ultraviolet pulses.
Optics Letters **29**, 210–212 (2004).

[57] C. Iaconis and I. A. Walmsley.
Spectral phase interferometry for direct electric-field reconstruction of ultrashort optical pulses.
Optics Letters **23**, 792–794 (May 1998).

[58] T. Kobayashi and A. Baltuska.
Sub-5 fs pulse generation from a noncollinear optical parametric amplifier.
Measurement Science and Technology **13**, 1671–1682 (2002).

[59] O. Nahmias, O. Bismuth, O. Shoshana, and S. Ruhman.
Tracking Excited State Dynamics with Coherent Control: Automated Limiting of Population Transfer in LDS750.
Journal of Physical Chemistry A **109**, 8246–8253 (September 2005).

[60] D. J. Kane and R. Trebino.
Characterization of arbitrary femtosecond pulses using frequency-resolved optical gating.
IEEE Journal of Quantum Electronics **29**, 571–579 (February 1993).

[61] R. Trebino, K. W. DeLong, D. N. Fittinghoff, J. N. Sweetser, M. A. Krumbügel, B. A. Richman, and D. J. Kane.
Measuring ultrashort laser pulses in the time-frequency domain using frequency-resolved optical gating.
Review of Scientific Instruments **68**, 3277–3295 (1997).

[62] R. Trebino.
Frequency-Resolved Optical Gating: The Measurement of Ultrashort Laser Pulses.
First edition. Springer (August 2002).

[63] R. Trebino and D. J. Kane.
Using phase retrieval to measure the intensity and phase of ultrashort pulses: frequency-resolved optical gating.
Journal of the Optical Society of America A **10**, 1101 (May 1993).

[64] S. Akturk, M. Kimmel, P. O'Shea, and R. Trebino.
Measuring spatial chirp in ultrashort pulses using single-shot Frequency-Resolved Optical Gating.
Optics Express **11**, 68–78 (2003).

[65] S. Akturk, M. Kimmel, P. O'Shea, and R. Trebino.
Measuring pulse-front tilt in ultrashort pulses using GRENOUILLE.
Optics Express **11**, 491–501 (March 2003).

[66] A. Baltuska, M. S. Pshenichnikov, and D. A. Wiersma.
Amplitude and phase characterization of 4.5-fs pulses by frequency-resolved optical gating.
Optics Letters **23**, 1474–1476 (1998).

[67] A. Baltuska, M. S. Pshenichnikov, and D. A. Wiersma.
Second-harmonic generation frequency-resolved optical gating in the single-cycle regime.
IEEE Journal of Quantum Electronics **35**, 459–478 (April 1999).

[68] K. W. DeLong.
Femtosoft Technologies FROG 3.2.2.

[69] G. Taft, A. Rundquist, M. M. Murnane, I. P. Christov, H. C. Kapteyn, K. W. DeLong, D. N. Fittinghoff, M. A. Krumbugel, J. N. Sweetser, and R. Trebino.
Measurement of 10-fs laser pulses.
IEEE journal of selected topics in quantum electronics **2**, 575–585 (September 1996).

[70] P. W. Milonni and J. H. Eberly.
Lasers.
First edition. Wiley-Interscience (October 1988).

[71] J. N. Sweetser, D. N. Fittinghoff, and R. Trebino.
Transient-grating frequency-resolved optical gating.
Optics Letters **22**, 519–521 (April 1997).

[72] E. B. Treacy.
Compression of picosecond light pulses.
Physics Letters A **28**, 34–35 (October 1968).

[73] E. B. Treacy.
Optical pulse compression with diffraction gratings.
IEEE Journal of Quantum Electronics **QE 5**, 454–458 (September 1969).

[74] R. L. Fork, O. E. Martinez, and J. P. Gordon.
Negative dispersion using pairs of prisms.
Optics Letters **9**, 150–152 (May 1984).

[75] R. Szipocs, K. Ferencz, C. Spielmann, and F. Krausz.
Chirped multilayer coatings for broadband dispersion control in femtosecond lasers.
Optics Letters **19**, 201 (February 1994).

[76] G. Cerullo, M. Nisoli, S. Stagira, S. D. Silvestri, G. Tempea, F. Krausz, and K. Ferencz.
Mirror-dispersion-controlled sub-10-fs optical parametric amplifier in the visible.
Optics Letters **24**, 1529–1531 (November 1999).

[77] P. Baum, M. Breuer, E. Riedle, and G. Steinmeyer.
Brewster-angled chirped mirrors for broadband pulse compression without dispersion oscillations.
Optics Letters **31**, 2220–2222 (July 2006).

[78] O. E. Martinez.
Matrix formalism for pulse compressors.
IEEE Journal of Quantum Electronics **24**, 2530–2536 (1988).

[79] T. Löhrig.
Planung und Realisierung eines Aufbaus zur Formung ultrabreitbandiger fs-Laserpulse im sichtbaren Spektralbereich.
Diplomarbeit, Universität Würzburg (2007).

[80] J. J. Field, C. G. Durfee III, J. A. Squier, and S. Kane.
Quartic-phase-limited grism-based ultrashort pulse shaper.
Optics Letters **32**, 3101–3103 (November 2007).

[81] E. Zeek, K. Maginnis, S. Backus, U. Russek, M. Murnane, G. Mourou, H. Kapteyn, and G. Vdovin.
Pulse compression by use of deformable mirrors.
Optics Letters **24**, 493–495 (April 1999).

[82] E. Zeek, R. Bartels, M. M. Murnane, H. C. Kapteyn, S. Backus, and G. Vdovin.
Adaptive pulse compression for transform-limited 15-fs high-energy pulse generation.
Optics Letters **25**, 587–589 (April 2000).

[83] OKO Tech.
Product datasheet "Linear deformable mirrors" (August 2008).

[84] P. Baum, S. Lochbrunner, and E. Riedle.
Tunable sub-10-fs ultraviolet pulses generated by achromatic frequency doubling.
Optics Letters **29**, 1686–1688 (July 2004).

[85] D. Zeidler, T. Hornung, D. Proch, and M. Motzkus.
Adaptive compression of tunable pulses from a non-collinear-type OPA to below 16 fs by feedback-controlled pulse shaping.
Applied Physics B: Lasers and Optics **70**, S125–S131 (June 2000).

[86] A. M. Weiner, D. E. Leaird, J. S. Patel, and J. R. Wullert.
Programmable shaping of femtosecond optical pulses by use of 128-element liquid crystal phase modulator.
IEEE Journal of Quantum Electronics **28**, 908–920 (1992).

[87] P. Tian, D. Keusters, Y. Suzaki, and W. S. Warren.
Femtosecond Phase-Coherent Two-Dimensional Spectroscopy.
Science **300**, 1553–1555 (June 2003).

[88] B. J. Pearson and T. C. Weinacht.
Shaped ultrafast laser pulses in the deep ultraviolet.
Optics Express **15**, 4385–4388 (April 2007).

[89] S.-H. Shim, D. B. Strasfeld, E. C. Fulmer, and M. T. Zanni.
Femtosecond pulse shaping directly in the mid-IR using acousto-optic modulation.
Optics Letters **31**, 838–840 (March 2006).

[90] S.-H. Shim, D. B. Strasfeld, and M. T. Zanni.
Generation and characterization of phase and amplitude shaped femtosecond mid-IR pulses.
Optics Express **14**, 13120–13130 (December 2006).

[91] T. Brixner and G. Gerber.
Femtosecond polarization pulse shaping.
Optics Letters **26**, 557–559 (April 2001).

[92] T. Brixner.
Adaptive femtosecond quantum control.
Doctoral thesis, Universität Würzburg (October 2001).

[93] J. Paye and A. Migus.
Space-time Wigner functions and their application to the analysis of a pulse shaper.
Journal of the Optical Society of America B **12**, 1480–1490 (1995).

[94] M. M. Wefers and K. A. Nelson.
Space-time profiles of shaped ultrafast optical waveforms.
IEEE Journal of Quantum Electronics **32**, 161–172 (1996).

[95] P.-A. Blanche, P. Gailly, S. Habraken, P. Lemaire, and C. Jamar.
Volume phase holographic gratings: large size and high diffraction efficiency.
Optical Engineering **43**, 2603–2612 (November 2004).

[96] J.-K. Rhee, T. S. Sosnowski, T. B. Norris, J. A. Arns, and W. S. Colburn.
Chirped-pulse amplification of 85-fs pulses at 250 kHz with third-order dispersion compensation by use of holographic transmission gratings.
Optics Letters **19**, 1550–1552 (October 1994).

[97] J. A. Arns, W. S. Colburn, and S. C. Barden.
Volume phase gratings for spectroscopy, ultrafast laser compressors, and wavelength division multiplexing.
In R. E. Fischer and W. J. Smith (Eds.), *Proceedings of SPIE*, volume 3779, pp. 313–323 (July 1999).

[98] T. A. Shankoff.
Phase Holograms in Dichromated Gelatin.
Applied Optics **7**, 2101–2105 (October 1968).

[99] T. Brixner, G. Krampert, P. Niklaus, and G. Gerber.
Generation and characterization of polarization-shaped femtosecond laser pulses.
Applied Physics B: Lasers and Optics **74**, s133–s144 (June 2002).

[100] T. Brixner.
Kohärente Kontrolle von Photodissoziationsreaktionen mit optimal geformten ultrakurzen Laserpulsen.
Diplomarbeit, Universität Würzburg (July 1998).

[101] C. B. Schwarz.
Erzeugung, Charakterisierung und Formung ultrabreitbandiger Femtosekunden-Laserpulse im sichtbaren Spektralbereich.
Diplomarbeit, Universität Würzburg (February 2009).

[102] V. Seyfried.
Beobachtung und Kontrolle molekularer Dynamik durch Femtosekundenlaserpulse.
Doctoral thesis, Universität Würzburg (1998).

[103] K. Lazonder, M. S. Pshenichnikov, and D. A. Wiersma.
Easy interpretation of optical two-dimensional correlation spectra.
Optics Letters **31**, 3354–3356 (November 2006).

[104] S. Mukamel.
Principles of Nonlinear Optical Spectroscopy.
New edition. Oxford University Press, USA (April 1999).

[105] D. M. Jonas.
Two-dimensional femtosecond spectroscopy.
Annual Review of Physical Chemistry **54**, 425–463 (2003).

[106] M. Cho.
Coherent Two-Dimensional Optical Spectroscopy.
Chemical Reviews **108**, 1331–1418 (April 2008).

[107] L. Lepetit, G. Chériaux, and M. Joffre.
Linear techniques of phase measurement by femtosecond spectral interferometry for applications in spectroscopy.
Journal of the Optical Society of America B **12**, 2467–2474 (1995).

[108] S. M. Gallagher, A. W. Albrecht, J. D. Hybl, B. L. Landin, B. Rajaram, and D. M. Jonas.
Heterodyne detection of the complete electric field of femtosecond four-wave mixing signals.
Journal of the Optical Society of America B **15**, 2338–2345 (1998).

[109] J. D. Hybl, A. F. Albrecht, and D. M. Jonas.
Two-dimensional Fourier transform electronic spectroscopy.
Journal of Chemical Physics **115**, 6606–6622 (October 2001).

[110] T. Brixner, T. Mancal, I. V. Stiopkin, and G. R. Fleming.
Phase-stabilized two-dimensional electronic spectroscopy.
Journal of Chemical Physics **121**, 4221–4236 (2004).

[111] U. Selig.
Kohärente 2D Spektroskopie bei breitbandiger Anregung im sichtbaren Spektralbereich.
Diplomarbeit, Universität Würzburg (July 2007).

[112] J. D. Hybl, A. W. Albrecht, S. M. G. Faeder, and D. M. Jonas.
Two-dimensional electronic spectroscopy.
Chemical Physics Letters **297**, 307–313 (November 1998).

[113] P. Hamm, M. Lim, and R. M. Hochstrasser.
Structure of the Amide I Band of Peptides Measured by Femtosecond Nonlinear-Infrared Spectroscopy.
Journal of Physical Chemistry B **102**, 6123–6138 (1998).

[114] S. Woutersen and P. Hamm.
Structure Determination of Trialanine in Water Using Polarization Sensitive Two-Dimensional Vibrational Spectroscopy.
Journal of Physical Chemistry B **104**, 11316–11320 (2000).

[115] O. Golonzka, M. Khalil, N. Demirdoven, and A. Tokmakoff.
Vibrational anharmonicities revealed by coherent two-dimensional infrared spectroscopy.
Physical Review Letters **86**, 2154–2157 (2001).

[116] T. Brixner, I. V. Stiopkin, and G. R. Fleming.
Tunable two-dimensional femtosecond spectroscopy.
Optics Letters **29**, 884–886 (2004).

[117] M. L. Cowan, J. P. Ogilvie, and R. J. D. Miller.
Two-dimensional spectroscopy using diffractive optics based phased-locked photon echoes.
Chemical Physics Letters **386**, 184–189 (March 2004).

[118] A. A. Maznev, K. A. Nelson, and J. A. Rogers.
Optical heterodyne detection of laser-induced gratings.
Optics Letters **23**, 1319–1321 (1998).

[119] G. D. Goodno, G. Dadusc, and R. J. D. Miller.
Ultrafast heterodyne-detected transient-grating spectroscopy using diffractive optics.
Journal of the Optical Society of America B **15**, 1791–1794 (June 1998).

[120] A. Nemeth, F. Milota, T. Mancal, V. Lukes, H. F. Kauffmann, and J. Sperling.
Vibronic modulation of lineshapes in two-dimensional electronic spectra.
Chemical Physics Letters **459**, 94–99 (June 2008).

[121] A. Nemeth, F. Milota, J. Sperling, D. Abramavicius, S. Mukamel, and H. F. Kauffmann.
Tracing exciton dynamics in molecular nanotubes with 2D electronic spectroscopy.
Chemical Physics Letters **469**, 130–134 (February 2009).

[122] S.-H. Shim, D. B. Strasfeld, Y. L. Ling, and M. T. Zanni.
Multidimensional Ultrafast Spectroscopy Special Feature: Automated 2D IR spectroscopy using a mid-IR pulse shaper and application of this technology to the human islet amyloid polypeptide.
Proceedings of the National Academy of Sciences **104**, 14197–14202 (September 2007).

[123] E. M. Grumstrup, S.-H. Shim, M. A. Montgomery, N. H. Damrauer, and M. T. Zanni.
Facile collection of two-dimensional electronic spectra using femtosecond pulse-shaping Technology.
Opt. Express **15**, 16681–16689 (2007).

[124] T. Hornung, J. C. Vaughan, T. Feurer, and K. A. Nelson.
Degenerate four-wave mixing spectroscopy based on two-dimensional femtosecond pulse shaping.
Opt. Lett. **29**, 2052–2054 (2004).

[125] J. C. Vaughan, T. Hornung, K. W. Stone, and K. A. Nelson.
Coherently Controlled Ultrafast Four-Wave Mixing Spectroscopy.
Journal of Physical Chemistry A **111**, 4873–4883 (2007).

[126] T. Zhang, C. Borca, X. Li, and S. Cundiff.
Optical two-dimensional Fourier transform spectroscopy with active interferometric stabilization.
Optics Express **13**, 7432–7441 (2005).

[127] V. Volkov, R. Schanz, and P. Hamm.
Active phase stabilization in Fourier-transform two-dimensional infrared spectroscopy.
Optics Letters **30**, 2010–2012 (2005).

[128] A. W. Albrecht, J. D. Hybl, S. M. G. Faeder, and D. M. Jonas.
Experimental distinction between phase shifts and time delays: Implications for femtosecond spectroscopy and coherent control of chemical reactions.
Journal of Chemical Physics **111**, 10934–10956 (December 1999).

[129] M. K. Yetzbacher, N. Belabas, K. A. Kitney, and D. M. Jonas.
Propagation, beam geometry, and detection distortions of peak shapes in two-dimensional Fourier transform spectra.
Journal of Chemical Physics **126**, 044511–19 (2007).

[130] D. Egorova, M. F. Gelin, and W. Domcke.
Analysis of cross peaks in two-dimensional electronic photon-echo spectroscopy for simple models with vibrations and dissipation.
The Journal of Chemical Physics **126**, 074314–11 (February 2007).

[131] R. S. Judson and H. Rabitz.
Teaching lasers to control molecules.
Physical Review Letters **68**, 1500 (March 1992).

[132] P. Nuernberger, G. Vogt, T. Brixner, and G. Gerber.
Femtosecond quantum control of molecular dynamics in the condensed phase.
Physical chemistry chemical physics : PCCP **9**, 2470–97 (May 2007).

[133] J. R. Taylor.
An Introduction to Error Analysis: The Study of Uncertainties in Physical Measurements.
Second edition. University Science Books (March 1997).

[134] M. Shapiro, E. Frishman, and P. Brumer.
Coherently Controlled Asymmetric Synthesis with Achiral Light.
Physical Review Letters **84**, 1669 (February 2000).

[135] D. Axelrod, D. E. Koppel, J. Schlessinger, E. Elson, and W. W. Webb.
Mobility measurement by analysis of fluorescence photobleaching recovery kinetics.
Biophysical Journal **16**, 1055–1069 (September 1976).

[136] J. Caesar, S. Sherlock, S. Shaldon, L. Chiandussi, and L. Guevara.
Use of indocyanine green in measurement of hepatic blood flow and as a test of hepatic function.
Clinical Science **21**, 43 (1961).

[137] W. Holzer, M. Mauerer, A. Penzkofer, R.-M. Szeimies, C. Abels, M. Landthaler, and W. Baumler.
Photostability and thermal stability of indocyanine green.
Journal of Photochemistry and Photobiology B: Biology **47**, 155–164 (December 1998).

[138] A. Assion, T. Baumert, M. Bergt, T. Brixner, B. Kiefer, V. Seyfried, M. Strehle, and G. Gerber.
Control of Chemical Reactions by Feedback-Optimized Phase-Shaped Femtosecond Laser Pulses.
Science **282**, 919–922 (October 1998).

[139] K. I. Willig, R. R. Kellner, R. Medda, B. Hein, S. Jakobs, and S. W. Hell.
Nanoscale resolution in GFP-based microscopy.
Nature Methods **3**, 721–723 (2006).

[140] E. Betzig, G. H. Patterson, R. Sougrat, O. W. Lindwasser, S. Olenych, J. S. Bonifacino, M. W. Davidson, J. Lippincott-Schwartz, and H. F. Hess.
Imaging Intracellular Fluorescent Proteins at Nanometer Resolution.
Science **313**, 1642–1645 (September 2006).

[141] G. H. Patterson and J. Lippincott-Schwartz.
A Photoactivatable GFP for Selective Photolabeling of Proteins and Cells.
Science **297**, 1873–1877 (September 2002).

[142] J. J. van Thor, T. Gensch, K. J. Hellingwerf, and L. N. Johnson.
Phototransformation of green fluorescent protein with UV and visible light leads to decarboxylation of glutamate 222.
Nature Structural Biology **9**, 37–41 (2002).

[143] R. Y. Tsien.
The green fluorescent protein.
Annual Review of Biochemistry **67**, 509–546 (November 2003).

[144] D. C. Prasher, V. K. Eckenrode, W. W. Ward, F. G. Prendergast, and M. J. Cormier.
Primary structure of the Aequorea victoria green-fluorescent protein.
Gene **111**, 229–233 (February 1992).

[145] C. W. Cody, D. C. Prasher, W. M. Westler, F. G. Prendergast, and W. W. Ward.
Chemical structure of the hexapeptide chromophore of the Aequorea green-fluorescent protein.
Biochemistry **32**, 1212–1218 (February 1993).

[146] M. Ormö, A. B. Cubitt, K. Kallio, L. A. Gross, R. Y. Tsien, and S. J. Remington.
Crystal Structure of the Aequorea victoria Green Fluorescent Protein.
Science **273**, 1392–1395 (September 1996).

[147] F. Yang, L. G. Moss, and G. N. Phillips.
The molecular structure of green fluorescent protein.
Nat Biotech **14**, 1246–1251 (October 1996).

[148] M. Chalfie, Y. Tu, G. Euskirchen, W. W. Ward, and D. C. Prasher.
Green fluorescent protein as a marker for gene expression.
Science **263**, 802–805 (February 1994).

[149] M. Chattoraj, B. A. King, G. U. Bublitz, and S. G. Boxer.
Ultra-fast excited state dynamics in green fluorescent protein: Multiple states and proton transfer.
Proceedings of the National Academy of Sciences **93**, 8362–8367 (August 1996).

[150] K. Winkler, J. Lindner, V. Subramaniam, T. M. Jovin, and P. Vöhringer.
Ultrafast dynamics in the excited state of green fluorescent protein (wt) studied by frequency-resolved femtosecond pump-probe spectroscopy.
Physical Chemistry Chemical Physics **4**, 1072–1081 (2002).

[151] H. Lossau, A. Kummer, R. Heinecke, F. Pollinger-Dammer, C. Kompa, G. Bieser, T. Jonsson, C. M. Silva, M. M. Yang, D. C. Youvan, and M. E. Michel-Beyerle.
Time-resolved spectroscopy of wild-type and mutant Green Fluorescent Proteins reveals excited state deprotonation consistent with fluorophore-protein interactions.
Chemical Physics **213**, 1–16 (December 1996).

[152] D. Stoner-Ma, A. A. Jaye, P. Matousek, M. Towrie, S. R. Meech, and P. J. Tonge.
Observation of Excited-State Proton Transfer in Green Fluorescent Protein using Ultrafast Vibrational Spectroscopy.
Journal of the American Chemical Society **127**, 2864–2865 (March 2005).

[153] J. T. M. Kennis, D. S. Larsen, I. H. M. van Stokkum, M. Vengris, J. J. van Thor, and R. van Grondelle.
Uncovering the hidden ground state of green fluorescent protein.
Proceedings of the National Academy of Sciences **101**, 17988–17993 (December 2004).

[154] J. Wiehler, G. Jung, C. Seebacher, A. Zumbusch, and B. Steipe.
Mutagenic Stabilization of the Photocycle Intermediate of Green Fluorescent Protein(GFP).
ChemBioChem **4**, 1164–1171 (2003).

[155] A. D. Kummer, J. Wiehler, H. Rehaber, C. Kompa, B. Steipe, and M. E. Michel-Beyerle.
Effects of Threonine 203 Replacements on Excited-State Dynamics and Fluorescence Properties of the Green Fluorescent Protein (GFP).
Journal of Physical Chemistry B **104**, 4791–4798 (May 2000).

[156] J. J. van Thor, G. Zanetti, K. L. Ronayne, and M. Towrie.
Structural Events in the Photocycle of Green Fluorescent Protein.
Journal of Physical Chemistry B **109**, 16099–16108 (August 2005).

[157] J. J. van Thor, G. Y. Georgiev, M. Towrie, and J. T. Sage.
Ultrafast and Low Barrier Motions in the Photoreactions of the Green Fluorescent Protein.
Journal of Biological Chemistry **280**, 33652–33659 (September 2005).

[158] J. J. van Thor and J. T. Sage.
Charge transfer in green fluorescent protein.
Photochemical and Photobiological Sciences **5**, 597–602 (2006).

[159] A. F. Bell, D. Stoner-Ma, R. M. Wachter, and P. J. Tonge.
Light-Driven Decarboxylation of Wild-Type Green Fluorescent Protein.
Journal of the American Chemical Society **125**, 6919–6926 (June 2003).

[160] G. Jung, J. Wiehler, and A. Zumbusch.
The Photophysics of Green Fluorescent Protein: Influence of the Key Amino Acids at Positions 65, 203, and 222.
Biophysical Journal **88**, 1932–1947 (March 2005).

[161] G. Jung, M. Werner, and M. Schneider.
Efficient Photoconversion Distorts the Fluorescence Lifetime of GFP in Confocal Microscopy: A Model Kinetic Study on Mutant Thr203Val.
ChemPhysChem **9**, 1867–1874 (2008).

[162] C. Xu, R. M. Williams, W. Zipfel, and W. W. Webb.
Multiphoton excitation cross-sections of molecular fluorophores.
Bioimaging **4**, 198–207 (1996).

[163] A. Volkmer, V. Subramaniam, D. J. S. Birch, and T. M. Jovin.
One- and Two-Photon Excited Fluorescence Lifetimes and Anisotropy Decays of Green Fluorescent Proteins.
Biophysical Journal **78**, 1589–1598 (March 2000).

[164] M. Schneider, S. Barozzi, I. Testa, M. Faretta, and A. Diaspro.
Two-Photon Activation and Excitation Properties of PA-GFP in the 720-920-nm Region.
Biophysical Journal **89**, 1346–1352 (August 2005).

[165] S. Habuchi, M. Cotlet, T. Gensch, T. Bednarz, S. Haber-Pohlmeier, J. Rozenski, G. Dirix, J. Michiels, J. Vanderleyden, J. Heberle, F. DeSchryver, and J. Hofkens.
Evidence for the Isomerization and Decarboxylation in the Photoconversion of the Red Fluorescent Protein DsRed.
Journal of the American Chemical Society **127**, 8977–8984 (June 2005).

[166] M. Cotlet, P. M. Goodwin, G. S. Waldo, and J. H. Werner.
A Comparison of the Fluorescence Dynamics of Single Molecules of a Green Fluorescent Protein: One- versus Two-Photon Excitation.
ChemPhysChem **7**, 250–260 (2006).

[167] G. Cerullo, C. J. Bardeen, Q. Wang, and C. V. Shank.
High-power femtosecond chirped pulse excitation of molecules in solution.
Chemical Physics Letters **262**, 362–368 (November 1996).

[168] C. J. Bardeen, V. V. Yakovlev, K. R. Wilson, S. D. Carpenter, P. M. Weber, and W. S. Warren.
Feedback quantum control of molecular electronic population transfer.
Chemical Physics Letters **280**, 151–158 (November 1997).

[169] C. J. Bardeen, V. V. Yakovlev, J. A. Squier, and K. R. Wilson.
Quantum Control of Population Transfer in Green Fluorescent Protein by Using Chirped Femtosecond Pulses.
Journal of the American Chemical Society **120**, 13023–13027 (December 1998).

[170] C. J. Bardeen, J. Cao, F. L. H. Brown, and K. R. Wilson.
Using time-dependent rate equations to describe chirped pulse excitation in condensed phases.
Chemical Physics Letters **302**, 405–410 (March 1999).

[171] J. Cao, J. Che, and K. R. Wilson.
Intrapulse Dynamical Effects in Multiphoton Processes: Theoretical Analysis.
Journal of Physical Chemistry A **102**, 4284–4290 (June 1998).

[172] B. D. Fainberg.
Nonperturbative analytic approach to the interaction of intense ultrashort chirped pulses with molecules in solution: Picture of "moving" potentials.
Journal of Chemical Physics **109**, 4523–4532 (1998).

[173] W. A. Bonner.
The origin and amplification of biomolecular chirality.
Origins of Life and Evolution of Biospheres **21**, 59–111 (March 1991).

[174] W. A. Bonner.
Chirality and life.
Origins of Life and Evolution of Biospheres **25**, 175–190 (June 1995).

[175] Y. Inoue and V. Ramamurthy (Eds.).
Chiral Photochemistry.
Molecular and supramolecular photochemistry. Dekker, New York (August 2004).

[176] H. Rau.
Asymmetric photochemistry in solution.
Chemical Reviews **83**, 535–547 (October 1983).

[177] Y. Inoue.
Asymmetric photochemical reactions in solution.
Chemical Reviews **92**, 741–770 (July 1992).

[178] M. Avalos, R. Babiano, P. Cintas, J. L. Jiménez, J. C. Palacios, and L. D. Barron.
Absolute Asymmetric Synthesis under Physical Fields: Facts and Fictions.
Chemical Reviews **98**, 2391–2404 (November 1998).

[179] W. Kuhn and E. Braun.
Photochemische Erzeugung optisch aktiver Stoffe.
Naturwissenschaften **17**, 227–228 (April 1929).

[180] W. Kuhn.
The physical significance of optical rotatory power.
Transactions of the Faraday Society **26**, 293–308 (1930).

[181] P. Brumer and M. Shapiro.
Control of unimolecular reactions using coherent light.
Chemical Physics Letters **126**, 541–546 (May 1986).

[182] D. J. Tannor and S. A. Rice.
Control of selectivity of chemical reaction via control of wave packet evolution.
Journal of Chemical Physics **83**, 5013–5018 (November 1985).

[183] D. J. Tannor, R. Kosloff, and S. A. Rice.
Coherent pulse sequence induced control of selectivity of reactions: Exact quantum mechanical calculations.
Journal of Chemical Physics **85**, 5805–5820 (November 1986).

[184] F. Hund.
Zur Deutung der Molekelspektren. III.
Zeitschrift für Physik A Hadrons and Nuclei **43**, 805–826 (November 1927).

[185] M. Shapiro and P. Brumer.
Controlled photon induced symmetry breaking: Chiral molecular products from achiral precursors.
The Journal of Chemical Physics **95**, 8658–8661 (December 1991).

[186] A. Salam and W. J. Meath.
On the control of excited state relative populations of enantiomers using circularly polarized pulses of varying durations.
The Journal of Chemical Physics **106**, 7865–7868 (May 1997).

[187] Y. Fujimura, L. González, K. Hoki, J. Manz, and Y. Ohtsuki.
Selective preparation of enantiomers by laser pulses: quantum model simulation for H_2POSH.
Chemical Physics Letters **306**, 1–8 (June 1999).

[188] Y. Fujimura, L. González, K. Hoki, D. Kröner, J. Manz, and Y. Ohtsuki.
From a Racemate to a Pure Enantiomer by Laser Pulses: Quantum Model Simulations for H_2POSH.
Angewandte Chemie International Edition **39**, 4586–4588 (2000).

[189] K. Hoki, Y. Ohtsuki, and Y. Fujimura.
Locally designed pulse shaping for selective preparation of enantiomers from their racemate.
The Journal of Chemical Physics **114**, 1575–1581 (2001).

[190] D. Gerbasi, M. Shapiro, and P. Brumer.
Theory of enantiomeric control in dimethylallene using achiral light.
The Journal of Chemical Physics **115**, 5349–5352 (2001).

[191] S. Bychkov, B. Grishanin, and V. Zadkov.
Laser synthesis of chiral molecules in isotropic racemic media.
Journal of Experimental and Theoretical Physics **93**, 24–32 (July 2001).

[192] K. Hoki, L. González, and Y. Fujimura.
Quantum control of molecular handedness in a randomly oriented racemic mixture using three polarization components of electric fields.
The Journal of Chemical Physics **116**, 8799–8802 (May 2002).

[193] H. Stapelfeldt and T. Seideman.
Colloquium: Aligning molecules with strong laser pulses.
Reviews of Modern Physics **75**, 543 (April 2003).

[194] D. V. Zhdanov and V. N. Zadkov.
Absolute asymmetric synthesis from an isotropic racemic mixture of chiral molecules with the help of their laser orientation-dependent selection.
Journal of Chemical Physics **127**, 244312–16 (December 2007).

[195] D. Zhdanov, B. Grishanin, and V. Zadkov.
Orientational selection of molecules in combined laser and electrostatic fields.
Journal of Experimental and Theoretical Physics **103**, 335–345 (2006).

[196] E. Frishman, M. Shapiro, D. Gerbasi, and P. Brumer.
Enantiomeric purification of nonpolarized racemic mixtures using coherent light.
The Journal of Chemical Physics **119**, 7237–7246 (October 2003).

[197] D. Gerbasi, P. Brumer, I. Thanopulos, P. Kral, and M. Shapiro.
Theory of the two step enantiomeric purification of 1,3 dimethylallene.
Journal of Chemical Physics **120**, 11557–11563 (June 2004).

[198] E. Frishman, M. Shapiro, and P. Brumer.
Optical purification of racemic mixtures by 'laser distillation' in the presence of a dissipative bath.
Journal of Physics B: Atomic, Molecular and Optical Physics **37**, 2811–2821 (2004).

[199] D. Gerbasi, M. Shapiro, and P. Brumer.
Theory of "laser distillation" of enantiomers: Purification of a racemic mixture of randomly oriented dimethylallene in a collisional environment.
Journal of Chemical Physics **124**, 074315–9 (February 2006).

[200] N. V. Vitanov, T. Halfmann, B. W. Shore, and K. Bergmann.
Laser-induced population transfer by adiabatic passage techniques.
Annual Review of Physical Chemistry (October 2001).

[201] Y. Ohta, K. Hoki, and Y. Fujimura.
Theory of stimulated Raman adiabatic passage in a degenerated reaction system: Application to control of molecular handedness.
The Journal of Chemical Physics **116**, 7509–7517 (May 2002).

[202] P. Král and M. Shapiro.
Cyclic Population Transfer in Quantum Systems with Broken Symmetry.
Physical Review Letters **87**, 183002 (October 2001).

[203] P. Král, I. Thanopulos, M. Shapiro, and D. Cohen.
Two-Step Enantio-Selective Optical Switch.
Physical Review Letters **90**, 033001 (2003).

[204] T. Müller, K. B. Wiberg, and P. H. Vaccaro.
Cavity Ring-Down Polarimetry (CRDP): A New Scheme for Probing Circular Birefringence and Circular Dichroism in the Gas Phase.
Journal of Physical Chemistry A **104**, 5959–5968 (June 2000).

[205] J. Buback.
Hochsensitive Spektroskopie chiraler Systeme.
Diplomarbeit, Universität Würzburg (December 2007).

[206] J.-Y. Lee and D.-C. Su.
Improved common-path optical heterodyne interferometer for measuring small optical rotation angle of chiral medium.
Optics Communications **256**, 337–341 (December 2005).

[207] E. Hecht.
Optics.
Fourth edition. Addison Wesley (August 2001).

[208] Rudolph Research.
AUTOPOL IV Automatic Polarimeter.
http://www.rudolphresearch.com/polarimeters/autopol_iv.php.

[209] M. Irie, K. Yoshida, and K. Hayashi.
Laser photolysis study of the photoracemization of 1,1'-binaphthyl.
Journal of Physical Chemistry **81**, 969–972 (1977).

[210] K. Hoki, S. Koseki, T. Matsushita, R. Sahnoun, and Y. Fujimura.
Quantum control of molecular chirality: Ab initio molecular orbital study and wave packet analysis of 1,1'-binaphthyl.
Journal of Photochemistry and Photobiology A: Chemistry **178**, 258–263 (March 2006).

[211] H. Kagan, A. Moradpour, J. F. Nicoud, G. Balavoine, and G. Tsoucaris.
Photochemistry with circularly polarized light. Synthesis of optically active hexahelicene.
Journal of the American Chemical Society **93**, 2353–2354 (May 1971).

[212] W. J. Bernstein, M. Calvin, and O. Buchardt.
Absolute asymmetric synthesis. I. Mechanism of the photochemical synthesis of nonracemic helicenes with circularly polarized light. Wavelength dependence of the optical yield of octahelicene.
Journal of the American Chemical Society **94**, 494–498 (1972).

[213] A. Moradpour, H. Kagan, M. Baes, G. Morren, and R. H. Martin.
Photochemistry with circularly polarized light - III : Synthesis of helicenes using bis(arylvinyl) arenes as precursors.
Tetrahedron **31**, 2139–2143 (1975).

[214] J. A. Syage, W. R. Lambert, P. M. Felker, A. H. Zewail, and R. M. Hochstrasser.
Picosecond excitation and trans-cis isomerization of stilbene in a supersonic jet: Dynamics and spectra.
Chemical Physics Letters **88**, 266–270 (May 1982).

[215] R. J. Sension, S. T. Repinec, A. Z. Szarka, and R. M. Hochstrasser.
Femtosecond laser studies of the cis-stilbene photoisomerization reactions.
Journal of Chemical Physics **98**, 6291–6315 (April 1993).

[216] S. Takeuchi, S. Ruhman, T. Tsuneda, M. Chiba, T. Taketsugu, and T. Tahara.
Spectroscopic Tracking of Structural Evolution in Ultrafast Stilbene Photoisomerization.
Science **322**, 1073–1077 (November 2008).

[217] G. Vogt, G. Krampert, P. Niklaus, P. Nuernberger, and G. Gerber.
Optimal Control of Photoisomerization.
Physical Review Letters **94**, 068305 (February 2005).

[218] R. H. Martin and M. J. Marchant.
Resolution and optical properties ([α]max, ORD and CD) of hepta-, octa- and nonahelicene.
Tetrahedron **30**, 343–345 (1974).

[219] G. H. Brown (Ed.).
Photochromism.
Techniques of chemistry. Wiley-Interscience, New York (1971).

[220] B. L. Feringa (Ed.).
Molecular switches.
Wiley-VCH, Weinheim (2001).

[221] B. L. Feringa, R. A. van Delden, N. Koumura, and E. M. Geertsema.
Chiroptical Molecular Switches.
Chemical Reviews **100**, 1789–1816 (2000).

[222] Y. Suzuki, K. Ozawa, A. Hosoki, and K. Ichimura.
Reversible change in the optical rotatory power of poly(L-glutamate) thin film induced by photochromism of a spiropyran.
Polymer Bulletin **17**, 285–291 (March 1987).

[223] L. Eggers and V. Buss.
A Spiroindolinopyran with Switchable Optical Activity.
Angewandte Chemie International Edition **36**, 881–883 (1997).

[224] V. I. Minkin.
Photo-, Thermo-, Solvato-, and Electrochromic Spiroheterocyclic Compounds.
Chemical Reviews **104**, 2751–2776 (May 2004).

[225] N. P. Ernsting and T. Arthen-Engeland.
Photochemical ring-opening reaction of indolinespiropyrans studied by subpicosecond transient absorption.
Journal of Physical Chemistry **95**, 5502–5509 (1991).

[226] J. Z. Zhang, B. J. Schwartz, J. C. King, and C. B. Harris.
Ultrafast studies of photochromic spiropyrans in solution.
Journal of the American Chemical Society **114**, 10921 (1992).

[227] A.-K. Holm, M. Rini, E. T. J. Nibbering, and H. Fidder.
Femtosecond UV/mid-IR study of photochromism of the spiropyran 1',3'-dihydro-1',3',3'-trimethyl-6-nitrospiro[2H-1-benzopyran-2,2'-(2H)-indole] in solution.
Chemical Physics Letters **376**, 214–219 (July 2003).

[228] A.-K. Holm, O. F. Mohammed, M. Rini, E. Mukhtar, E. T. J. Nibbering, and H. Fidder.
Sequential Merocyanine Product Isomerization Following Femtosecond UV Excitation of a Spiropyran.
Journal of Physical Chemistry A **109**, 8962–8968 (October 2005).

[229] C. J. Wohl and D. Kuciauskas.
Excited-State Dynamics of Spiropyran-Derived Merocyanine Isomers.
Journal of Physical Chemistry B **109**, 22186–22191 (December 2005).

[230] J. Hobley, U. Pfeifer-Fukumura, M. Bletz, T. Asahi, H. Masuhara, and H. Fukumura.
Ultrafast Photo-Dynamics of a Reversible Photochromic Spiropyran.
Journal of Physical Chemistry A **106**, 2265–2270 (March 2002).

[231] U. Pfeifer, H. Fukumura, H. Misawa, N. Kitamura, and H. Masuhara.
Enzyme-like activity of albumins on the thermal back reaction of a photochromic spirobenzopyran.
Journal of the American Chemical Society **114**, 4417–4418 (1992).

[232] I. Willner, R. Blonder, and A. Dagan.
Reversible Optical Recording by a Dinitrophenol Antibody-Catalyzed Ring Opening of 6,8-dinitro Spiropyran.
Journal of the American Chemical Society **116**, 3121–3122 (1994).

[233] J. Hobley and V. Malatesta.
Energy barrier to TTC-TTT isomerisation for the merocyanine of a photochromic spiropyran.
Physical Chemistry Chemical Physics **2**, 57–59 (2000).

[234] G. Cottone, R. Noto, and G. L. Manna.
Theoretical study of spiropyran-merocyanine thermal isomerization.
Chemical Physics Letters **388**, 218–222 (April 2004).

[235] Y. Sheng, J. Leszczynski, A. A. Garcia, R. Rosario, D. Gust, and J. Springer.
Comprehensive Theoretical Study of the Conversion Reactions of Spiropyrans: Substituent and Solvent Effects.
Journal of Physical Chemistry B **108**, 16233–16243 (September 2004).

[236] I. Gómez, M. Reguero, and M. A. Robb.
Efficient Photochemical Merocyanine-to-Spiropyran Ring Closure Mechanism through an Extended Conical Intersection Seam. A Model CASSCF/CASPT2 Study.
Journal of Physical Chemistry A **110**, 3986–3991 (March 2006).

[237] M. Minami and N. Taguchi.
Effects of substituents on the indoline ring on the negative photochromic properties of spirobenzopyran derivatives.
Chemistry Letters **25**, 429 (1996).

[238] J. Hobley, V. Malatesta, R. Millini, L. Montanari, and W. O. Parker.
Proton exchange and isomerisation reactions of photochromic and reverse photochromic spiropyrans and their merocyanine forms.
Physical Chemistry Chemical Physics **1**, 3259–3267 (1999).

[239] R. Selle, P. Nuernberger, F. Langhojer, F. Dimler, S. Fechner, G. Gerber, and T. Brixner.
Generation of polarization-shaped ultraviolet femtosecond pulses.
Optics Letters **33**, 803–805 (April 2008).

Acknowledgements

At the conclusion of this work I would like to express my gratitude everybody who helped in one way or another. Excellent team work and productive scientific collaborations were the crucial ingredients for the success of the research projects. The studies leading up to this work, the projects presented here, and finally the thesis itself would not have been possible without the support I received from inside and outside of the academic environment. I am grateful for the technical, financial, and moral support that I received from various individuals and organizations.

Here I would like to thank explicitly:

- Prof. Dr. Tobias Brixner for giving me the opportunity to work in this field of research. He has always provided me with helpful advice and encouragement. New ideas and open discussions were always nurtured in his research group. He allocated the appropriate funding to back the projects and ideas. He also never hesitated to allow his students to participate in conferences and to introduce them to the scientific community. His overall support and the inspirational atmosphere in his group allowed this work to succeed.

- Frank Dimler for his great contributions to all the projects from the beginning of our graduate studies. The scientific discussions with him and the input concerning the projects and related topics were most valuable for the prolific working environment during the last few years. During long "lab nights" his company made even the hardest work an enjoyable experience.

- Ulrike Selig for her enthusiasm for 2D spectroscopy. Her ideas and positive attitude were the driving force in countless instances when problems arose and had to be solved.

- Johannes Buback for the resourcefulness that he provided for even the most challenging projects like the polarimeter and chiral systems. His tireless efforts to improve the apparatus, the measurement methods, and experiments in general are unparalleled.

- Tatjana Löhrig for her valuable help with designing and building the pulse shaper and characterizing the pulses.

- Dr. Patrick Nürnberger for his profound knowledge of everything related to femtochemistry. His wide interest and the discussions with him provided many impulses for various projects.

- Prof. Dr. Gregor Jung for his steady support during the development of the accumulation technique and for his expertise and helpful contributions to the green fluorescent protein project.
- Dr. Daniel Wolpert for his work on the infrared project and for extracurricular activities.
- Dr. Reimer Selle for his interesting work on UV pulse shaping and for discussions on many topics.
- Dr. Gerhard Vogt for sharing his experience with the laser system and ultrafast spectroscopy.
- Dr. Susanne Fechner for contributing her pulse shaping expertise and her cheerful personality.
- Robert Spitzenpfeil, Christoph Schwarz, and Peter Popp for providing reliable and well-equipped computer facilities in Experimentelle Physik 1 and Physikalische Chemie 1.
- Dr. Gerhard Krampert for his resourceful design of optomechanics.
- Prof. Dr. Thomas Weinacht for his kind support during my master's studies at Stony Brook.
- Dr. David Cardoza for the enjoyable and successful laboratory times at Stony Brook.
- Prof. Dr. Gustav Gerber for sparking my interest in femtochemistry and supporting me throughout my studies of physics in Würzburg, during the master's program at Stony Brook, and in Experimentelle Physik 1 back in Würzburg.
- The Research Training School 1221 (GRK 1221) on the "Control of Electronic Properties of Assemblies of pi-Conjugated Molecules" for financial support and research training events, classes, and talks.
- The Emmy Noether program of the Deutsche Forschungsgemeinschaft for financial support.
- The State of Bavaria for a stipend according to the Bayerisches Begabtenförderungsgesetz during my studies in Würzburg and Stony Brook.
- The Wilhelm und Else Heraeus Förderprogramm of the Deutsche Physikalische Gesellschaft for funding participations in the spring meetings of the DPG.
- The colleagues from the laboratory next door in Experimentelle Physik 1 for sharing some resources and providing a friendly atmosphere.
- Everybody from Experimentelle Physik 1 who has not been mentioned here for providing the great team spirit and the enjoyable working atmosphere.

- Everybody from the physical chemistry department for the warm welcome of our group and the substantial support during and after the move of the laboratory.
- All members of the machine shops and electronic shops in both the physics and physical chemistry departments. Their genuine creativity was indispensable for the apparatus used in the scientific projects.
- The administrative staff for helping with various tasks, foremost Monika Seifer, Diep Phan, Helga Schwark in the physics department and Andrée Meyer in the physical chemistry department.
- Frank Dimler, Eliza-Beth Lerch, Ulrike Selig, and Johannes Buback for diligent and critical proof-reading of this thesis.
- Eliza-Beth for her love, support, and understanding through the ups and downs of frustration and excitement with my scientific projects.
- My family for always supporting me, for giving me the opportunity to pursue a higher education and encouraging me throughout the years. My grandparents Josef and Sieglinde have steadily helped me in many ways. From my early childhood on my mother Ingrid was never demanding, yet always encouraged me to achieve high goals.